The Imaging Capabilities of Ground Penetrating Radar for the Detection of Buried Anti-Personnel Landmines

Dissertation
zur Erlangung des akademischen Grades
Doktoringenieur (Dr.-Ing.)

von Dipl.-Wirtsch.-Ing. Alexander Teggatz
geb. am 24. April 1979 in Magdeburg

genehmigt durch die
Fakultät für Elektrotechnik und Informationstechnologie
der Otto-von-Guericke-Universität Magdeburg

Gutachter:
Prof. Dr. Abbas Omar (FEIT/IESK)
Prof. Dr. Jürgen Nitsch (FEIT/IGET)
Dr. Martin Dohlus (DESY/MPY)

Promotionskolloquium am 19. März 2008

Schriftliche Erklärung

Ich erkläre hiermit, dass ich die vorliegende Arbeit ohne unzulssige Hilfe Dritter und ohne Benutzung anderer als der angegebenen Hilfsmittel angefertigt habe. Die aus fremden Quellen direkt oder indirekt übernommenen Gedanken und Informationen sind als solche kenntlich gemacht. Insbesondere habe ich nicht die Hilfe einer kommerziellen Promotionsberatung in Anspruch genommen. Dritte haben von mir weder unmittelbar noch mittelbar geldwerte Leistungen für Arbeiten erhalten, die im Zusammenhang mit dem Inhalt der vorgelegten Dissertation stehen. Die Arbeit wurde bisher weder im Inland noch im Ausland in gleicher oder ähnlicher Form als Dissertation eingereicht und ist als Ganzes auch noch nicht veröffentlicht.

Alexander Teggatz

Acknowledgement

I gratefully would like to acknowledge the outstanding support of all people who, by many different means, provided help, advice and encouragement to me.
First and foremost, I would like to thank my supervisor Prof. Dr.-Ing. Abbas S. Omar for the opportunity to become a member of his group at the Institute for Electronics, Signal Processing and Communications at the Otto-von-Guericke University. Prof. Omar supported me continously with his profound knowledge and his big experience. His helpful suggestions and our interesting discussions illustrate his enthusiasm and help to encourage young scientists to contribute to the scientific community.
To the same extend, I sincerely thank the leader of the research group for Ground Penetrating Radar Dr.-Ing. Andreas Jöstingmeier. Without his constant support, his technical and personal guidance, his patience and his willingness to correct countless technical publications this work would have never been completed.
Moreover, I would like to thank Dr.-Ing. Tobias Meyer, Dipl.-Ing. Michael Anis, Dipl.-Ing. Nikolaos Spiliotis, M. Sc. Ayan K. Bandyopadhyay and other members of the research group for their frequent suggestions, the provided knowledge and experiences and, especially, for the support of all measurement activities.
Of course, I am grateful to my parents for their love and support which means so much to me. Finally, I would like to thank Anja, my beloved wife and source of inspiration, who I owe so much for making this effort possible. Without her love, encouragement and her understanding this manuscript would not exist.

Abstract

Anti-Personnel (AP) landmines are considered as a problem of global proportions and it is estimated that about 60-70 million AP landmines are scattered within at least 70 countries all over the world. Many of the mines are made without metal so that detection methods based on electromagnetic induction (EMI) often tend to fail. A promising concept for the detection of buried nonmetallic objects is the ground penetrating radar (GPR) which originates from geophysical techniques.
The investigations in the context of this thesis cover different important aspects of GPR. A novel approach for the 3D field simulation of a complete GPR environment will be proposed which not only allows to study the fundamental principles of GPR but will also be utilized for the systematic verification of antenna concepts in the context of GPR applications. Finally, the important problem of focusing the raw data of GPR measurements will be addressed and two different focusing concepts will be investigated using both, field simulations and measurements.

Anti-Personen (AP) Landminen werden als Problem globalen Ausmaßes betrachtet. Es wird geschätzt, dass es weltweit ungefähr 60-70 Million AP Landminen verteilt in mehr als 70 Ländern gibt. Viele Minen werden inzwischen ohne Metall hergestellt, so dass ihre Detektion auf Basis von elektromagnetischer Induktion (EMI) häufig versagt, während das sogenannte bodendurchdringende Radar (engl. Ground Penetrating Radar, GPR) für die Detektion von vergrabenen nichtmetallischen Objekten gut geeignet ist. GPR hat seinen Ursprung im Bereich der Geophysik.
Die Untersuchungen im Rahmen dieser Arbeit betreffen unterschiedliche wichtige Aspekte von GPR Systemen. Zunächst wird eine neue Methode zur 3D Feldimulation eines kompletten Systems vorgestellt. Diese erlaubt nicht nur die Untersuchung grundlegender Prinzipien von GPR, sondern auch für die systematische Verifizierung verschiedener Antennenkonzepte, die im Rahmen von GPR Anwendungen verwendet werden. Schließlich wird das Problem der Fokussierung der Rohdaten einer GPR Messung diskutiert. Dafür werden zwei unterschiedliche Fokussierkonzepte sowohl mit Feldsimulationen als auch anhand realer Messungen untersucht.

Contents

Nomenclature

CONSTANTS

ϵ_0	permittivity of vacuum	$8.854 \cdot 10^{-12}$ As/(Vm)
μ_0	permeability of vacuum	$4\pi \cdot 10^{-7}$ Vm/(As)
c_0	speed of light in vacuum	$\approx 2.997924 \cdot 10^8$ m/s
Z_0	intrinsic impedance of free space	$= \sqrt{\mu_0/\epsilon_0} = 376.73\ \Omega$
π	mathematical constant pi	≈ 3.1415926

OPERATORS

$\nabla\cdot$	divergence operator
$\nabla\times$	curl operator
$\mathbf{x}$	vector x
$\mathbf{x}^T$	transpose of vector x
$\lvert\mathbf{x}\rvert$	absolute value of vector x
$\mathbf{X}$	matrix X
$\Re(z)$	real part of z
$\Im(z)$	imaginary part of z

SYMBOLS

$\mathbf{E}$	electric field strength	[V/m]
$\mathbf{H}$	magnetic field strength	[A/m]
$\mathbf{D}$	electric displacement density	[As/m^2]
$\mathbf{B}$	magnetic flux density	[Vs/m^2]
$\mathbf{J}$	electric current density	[A/m^2]

$\mathbf{k}$	wave number vector	[1/m]
$\mathbf{n}$	unit vector in direction of $\mathbf{k}$	–
k_0	wave number in free space	[1/m]
k_z	transversal component of $\mathbf{k}$ in free space	[1/m]
$k_{z\eta}$	transversal component of $\mathbf{k}$ in a medium	[1/m]
ρ	electric charge density	[As/m^3]
σ	electric conductivity	[A/(Vm)]
α	attenuation coefficient (real part of γ)	[1/m]
β	phase coefficient (imaginary part of γ)	[1/m]
γ	propagation coefficient	[1/m]
d	geometrical range or distance	[m]
$\boldsymbol{\nu}$	two-dimensional transverse component	[m]
f	frequency	[1/s]
δ_{range}	range resolution	[m]
$\delta_{spatial}$	spatial resolution	[m]
δ_{time}	time domain resolution	[s]
ω	angular frequency	[rad/s]
λ	wavelength	[m]
ϵ	permittivity	[As/(Vm)]
ϵ_r	relative permittivity	–
ϵ_r'	real part of the relative permittivity	–
ϵ_r''	imaginary part of the relative permittivity	–
μ	permeability	[Vm/(As)]
μ_r	relative permeability	–
μ_r'	real part of the relative permeability	–
μ_r''	imaginary part of the relative permeability	–
$\tan\delta_e$	loss tangent for dielectric losses	–
$\tan\delta_m$	loss tangent for magnetic losses	–
θ_b	angle of illumination	–
η	index of refraction	–
υ	degree of efficiency	–
ς	radar cross section	–
Γ	reflection coefficient	–
$\mathscr{T}$	transmission coefficient	–

T	pulse duration, time interval	[s]
B	frequency bandwidth	[Hz]
P_{acc}	accepted average peak power	[W]
P_t	average peak power at transmitter output	[W]
P_r	average peak power at receiver output	[W]
$\mathscr{P}_t$	average peak power density at target object	[W/m^2]
$\mathscr{P}_i$	average peak power density at receiver	[W/m^2]
L_t	power losses of transmitter	–
L_r	power losses of receiver	–
L_{rt}	radiation losses of transmitter	–
L_{rr}	radiation losses of receiver	–
L_{ch}	losses of transmitting channel	–
D_t	directivity of transmitting antenna	–
D_r	directivity of receiving antenna	–
S_{match}	S-parameter of 'match' standard measurement	–
S_{short}	S-parameter of 'short' standard measurement	–
S_{offset}	S-parameter of 'offset' standard measurement	–
S_{corr}	S-parameter corrected using the calibration	–
E_D	directivity error of one-port error model	–
E_S	source match error of one-port error model	–
E_R	reflection tracking error of one-port error model	–

ABBREVIATIONS

AP	Anti-Personnel (Landmine)
APS	Automatic Positioning System
AT	Anti-Tank (Landmine)
CW	Continuous Wave
CAD	Computer-Aided Design
CST	Computer Simulation Technology GmbH
DBS	Doppler Beam Sharpening
DEM	Digital Elevation Model
DNT	Dinitrotoluene $C_6H_3(NO_2)_2CH_3$
DUT	Device Under Test

NOMENCLATURE

EMI	Electromagnetic Induction
FMCW	Frequency Modulated Continuous Wave
FDTD	Finite Difference Time Domain
FIT	Finite Integration Technique
FPGA	Field Programmable Gate Array
GEMA	Gesellschaft f. elektroakustische u. mech. Apparate
GPR	Ground Penetrating Radar
GPS	Global Positioning System
ICBL	International Campaign to Ban Landmines
InSAR	Interferometric Synthetic Aperture Radar
IRA	Impulse Radiating Antenna
MoM	Method of Moments
MRI	Magnetic Resonance Imaging
MWS	CST Microwave Studio Package
NRL	Naval Research Laboratory
NQR	Nuclear Quadrupole Resonance
NMR	Nuclear Magnetic Resonance
PEC	Perfect Electric Conductor
RADAR	Radio Detection And Ranging
RAF	Royal Air Force
RCS	Radar Cross Section
ROC	Receiver Operating Characteristic
R&S	Rohde & Schwarz GmbH & Co. KG
SAR	Synthetic Aperture Radar
SFCW	Stepped Frequency Continuous Wave
SNR	Signal to Noise Ratio
TEM	Transverse Electromagnetic
TLM	Transmission Line Model
TNT	Trinitrotoluene $C_6H_2(NO_2)_3CH_3$
UN	United Nations
UWB	Ultra-Wideband
UXO	Unexploded Ordnance
VB	Visual Basic
VNA	Vector Network Analyzer

List of Figures

Chapter 1

Introduction

1.1 The Global Landmine Crisis

According to the UN the threat of Anti-Personnel (AP) landmines represents a crisis of global proportions. Due to the confusion of warfare the exact number of landmines is unknown. However, it is estimated that more than 60-70 million landmines are scattered within at least 70 countries around the world [Var07b]. More than 350 different kinds of AP mines have been produced by more than 50 countries. Mine affected territories include countries such as Afghanistan, Angola, Bosnia, Cambodia, Egypt, Eritrea, Iraq, Laos, Somalia, Sri Lanka and Sudan. Each year approximately 26000 people are affected by landmines. Typical injuries include blindness, burns, destroyed limbs and shrapnel wounds. The victims of AP landmines often suffer from amputations and long hospital stays or, even worse, die immediately or shortly after the explosion because they cannot reach sufficient medical care in time.
While the costs for the production of a single AP mine typically do not exceed 5 dollar the costs to remove one landmine are estimated to be up to 1000 dollar and the costs for surgical care and for the fitting of an artificial limb often exceed 3000 dollar [Var07b]. Furthermore, landmines always have a long-term effect on people and their environment. Landmines stand in the way of efforts to restore post-war societies to normal life. Long after the conflict itself ended the landmines threat consumes a huge amount of money that could be used more effectively and hidden landmines have an impact on virtually every aspect of life in the mine-affected countries. A study of the social costs of landmines in Afghanistan, Bosnia-Herzegovina, Cambodia, and Mozambique revealed that up to 85 percent of households had daily

activities affected by landmines. Unless removed and destroyed, landmines create huge social costs, vast numbers of internally displaced persons, impede the economic recovery, prevent the delivery of government services, create conditions for diseases, and encourage the continued militarization of post-conflict societies [Var98].

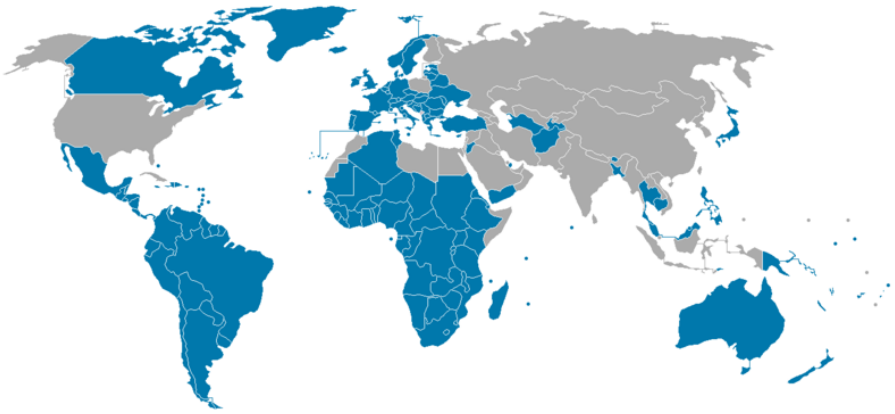

Figure 1.1: Signatories of the Ottawa Treaty as of February 2007.

The Ottawa Treaty from 1999 also known as the 'Convention on the Prohibition of the Use, Stockpiling, Production and Transfer of Anti-Personnel Mines and on their Destruction' bans the use of AP mines around the world. The Treaty prohibits the manufacture, trade and use of AP mines, obliges countries to destroy stockpiles within four years, clear their own territory within ten years and urges governments to help poorer countries clear land and assist landmine victims. By the end of February 2007 155 countries have joined the Ottawa Treaty with 2 countries that have signed but not yet ratified. However, the 40 countries who have still not signed include the United States of America, Russia, China, Pakistan, Egypt, Israel and India. The countries where mines are still used include Burma, Burundi, Columbia, India, Iraq, Pakistan, Philippines, Russia (Chechnya), Somalia, Sudan and Nepal and 13 countries produce or reserve the right to produce anti-personnel mines and somewhere between 190 million and 200 million anti-personnel mines are still stockpiled by states which did not signed the Ottawa Treaty. The mine producers are from Asia (Burma, China, India, Nepal, North Korea, South Korea, Pakistan, Singapore, and Vietnam), from the Middle East (Iran), from the Americas (Cuba and United States) and from Europe (Russia). Moreover, military non-state groups and actors continue to produce AP landmines in conflict societies [Var07a].

1.2 Methods of Landmine Detection

1.2.1 Standards and Definitions

The UN standard for humanitarian demining defines a 99.6 percent probability of clearance. This standard leads to a high rate of so-called false alarms since all sensors and methods have to be adjusted to the highest possible sensitivity. The detailed specifications for a mine detecting device are defined by a receiver operating characteristic (ROC) that relates the probability of detection with the rate of false alarms. Military demining differs from humanitarian demining in two ways. In war times it is often sufficient to enforce a path through an existing mine field. Often this is done by mechanical devices like diggers or rollers mounted on armored vehicles. Moreover, for military demining a higher casualty risk is accepted and the demanded probability of detection and successful clearance is lowered. In the following section various techniques for the detection of buried landmines will be discussed according to informations that have been derived from [BG97] and [ML$^+$03].

1.2.2 Manual and Mechanical Methods

The most common techniques for the detection of AP landmines are manual ones. Using so-called prodders, which are rigid sticks of metal about 25 cm long, the deminer scans the soil at a shallow angle of typically 30 degree. Each time an unusual object is detected, the miner checks the contour, which indicates whether the object is a landmine. Though highly effective, the prodding method is slow and dangerous. The deminer might encounter mines that have moved or have been placed so that they are triggered by prodding especially in hard and rocky soil. Thus, one serious accident occurs for every 1000 mines removed. New designs of rotary prodders which allow for a better penetration with lower force in combination with an acoustic classification have been proposed, e.g. in [Rus02; SvD$^+$03]. According to the definition of military demining the army requires a mine clearance device that is able to clear fast and safe known minefields or areas that are suspected to be mine-affected. Mechanical mine-clearing devices such as the 'Minebreaker' [Var06e] have been successfully applied for mine clearance, whereby clearance efficiency and safety have been proven to be sufficient. Previously, the 'Keiler', an armored clearing vehicle has been used for that purpose. However, this device is a tactical vehicle

that is meant to breach through minefields for military objectives. The 'Minebreaker' provides a safety lane with a width of 4.7 m and is milling the ground in the lane down to up to a depth of 50 cm, whereby both, AP mines and Anti-Tank (AT) mines, are supposed to be destroyed mechanically or by explosion. A similar concept has been realized for the 'Minewolf' [Var06f]. However, 'Minebreaker' and 'Minewolf' (Fig. 1.2) with a total weight of 47 tons, respectively, 26 tons cannot be deployed easily and are not suited for difficult terrains and extreme soil conditions. Moreover, unconfirmed reports claim, that some AP mines remain active and are only buried underneath the cleared soil where it will be even harder to detect them.

Figure 1.2: 'Minebreaker' (left) and 'Minewolf' (right) mine-clearing vehicles.

1.2.3 Electromagnetic Induction

Electromagnetic induction (EMI) is the working principle of all metal detectors. EMI detectors include a transmitter and a receiver coil. Electric currents that flow in the transmitter coil radiate a primary magnetic field that penetrates the surrounding medium and any nearby metallic object. A time changing primary magnetic field will induce so-called eddy currents in the buried object and these currents radiate a secondary magnetic field that is picked up by the receiver coil. EMI detectors are often classified into two broad categories, namely, continuous wave and pulse induction. EMI detectors for landmine detection have been applied for the first time in World War I, were further developed during World War II and have been routinely used to detect landmines since then [Bau99]. The use of EMI to detect conducting objects is well established in other application areas such as mineral

exploration, nondestructive testing, treasure hunting, or food processing. A modern metal detector can detect extremely small quantities of metal under various soil and other environmental conditions. The effective rate of area coverage depends on many factors, which include the search halo of the detector, the frequency of occurrence of metal fragments and actual landmines and the operating procedure employed. The most obvious and serious limitation of these detectors used to detect buried landmines is the fact that they are metal detectors. They are very sensitive and can detect tiny metal fragments as small as a couple of millimeters in length and less than a gram in weight. An area to be demined is usually littered with a large number of such metal fragments and other metallic debris of various sizes. This results in a high rate of false alarms since a metal detector cannot currently distinguish between the metal in a landmine and that in a harmless fragment. Moreover, many common AP mines have almost no metal parts except for the small striker pin and even recently proposed EMI methods tend to fail completely [Var07a].

1.2.4 Infrared and Hyperspectral Methods

Infrared, respectively hyperspectral imaging methods utilize electro-optical sensor systems and have been proposed to be possible candidates for the detection of buried landmines [Lun01]. For the imaging with an infrared or hyperspectral sensors broadband techniques with up to 20 frequency bands are taken into account in order to perform reflective and thermal measurements [SH99; KS$^+$99]. Moreover, it is possible to process the polarization information of the scattered light within these bands which also allows for the detection of buried or surface laid anti-personnel mines. Infrared imaging sensors respond to the electromagnetic or thermal radiation in a sensor-specific wavelength range. A large part of the solar energy incident on soil is absorbed and leads to a heating of the soil. As a result of this heating, the soil emits thermal radiation detectable by a thermal infrared sensor. Infrared System are referred to as passive, if they receive the thermal emission from buried targets, respectively as active, if an artificial source is applied. Polarimetric systems process the polarization of the scattered light and either use the sun or the sky for illumination or an active source such as a laser. The sensor systems can be used from a considerable standoff distance and provide information on different mine properties. However, only few AP mine detecting approaches have been reported and the obtained signatures tend to be highly dependent on environmental conditions.

1.2.5 Acoustic-to-Seismic Coupling

A detection of landmines that utilizes the coupling of acoustic and seismic effects is based on the ability of sound to penetrate the ground and excite resonances in buried target objects. Sound produced in the air efficiently couples into the first 50 cm of the soil because of the porous nature of natural ground resulting in acoustic vibrations that are sensitive to the presence of buried mines. The basic idea of the acoustic-seismic approach is to excite low frequency vibrations of buried objects and measure the surface vibration signatures above them using remote sensing techniques. The excitation of a mine and the surrounding soil is achieved using acoustic or seismic waves. The remote sensing is realized with microwave, ultrasonic and laser Doppler vibrometers [SX99; SX01]. The use of acoustic-to-seismic coupling for the detection of landmines exploits new phenomena that have not been explored for such a purpose before. A landmine is an artificial object that is acoustically much more compliant than any kind of soil. Moreover, such nonporous objects offer additional contrast to the porous soil in the presence of the acoustic wave which results in a high-vibration contrast between the soil and the buried target object. However, this technique is still in an early stage and needs to be further evaluated experimentally.

1.2.6 X-Ray Backscatter Methods

X-ray backscattering can be used to produce images of subsurface objects, and hence to identify mines. It is analogous to the more widespread method of passing X-rays through an object, but instead detects the small amount of reflected radiation, which is in proportion to the density of the material. By scanning one or more narrow beams of X-rays a 2D or 3D subsurface image can be created. The technique is intended for the real-time detection of landmines using physically large systems with significant power requirements, although AP mines have been imaged as well. Low power systems using radiation sources of X-rays and deconvolution techniques instead of narrow collimated beams have also been proposed. The systems which have been developed are supposed to produce a 2D image with cm resolution. However, the technique reveals problems due to the shallow penetration of the X-rays into soil and the small percentage of energy which is backscattered. Moreover, the system complexity, a high sensitivity to soil topography, and safety aspects due to the use of ionising radiation complicate mine detection approaches [Var07c].

1.2.7 Neutron and Nuclear Techniques

The detection of landmines using nuclear techniques has been proposed continuously and studied intensely. Nuclear techniques look at either a return of the natural radioactive radiation, which is characteristic of explosive components that are found in soil e.g., nitrogen or carbon, or a characteristic intensity change of the scattered radiation between soil and explosives. Radiation methods are essentially anomaly detectors, which means they detect inhomogeneities in the medium and inclusions in addition to mines. Virtually every conceivable nuclear reaction has been examined, but after considering different factors such as selectivity, sensitivity, probability of detection, false alarm rate, soil absorption, processing time, limitations due to fundamental physics, and technical limitations such as size, weight, power and the availability of sources and detectors, only a few have potential for mine detection. Reports about the examination of nuclear reactions for the detection of buried landmines can be found in the literature e.g. in [Mol86; MF+03].

1.2.8 Nuclear Quadrupole Resonance

The nuclear quadrupole resonance (NQR) is an electromagnetic method that operates in the frequency range of 0.5 MHz to 5 MHz. It is a very new technology and the first practical deployments have been reported recently [GB+01]. NQR is a magnetic resonance phenomenon closely related to nuclear magnetic resonance (NMR) and its offspring, magnet resonance imaging (MRI). A large static magnetic field with a strength up to 20 T orients the nuclei so that slightly more are in the low energy state which means aligned parallel to the static field than are in the higher state oriented opposed to the field. The population difference that can be obtained corresponds to a weak diamagnetism of the nuclear spins, with a classical magnetization vector aligned along the static magnetic field. The magnetic field corresponding to this nuclear diamagnetism can be observed by applying a resonant radio frequency pulse at right angles to the static field, causing the magnetization to rotate away from the axis of the static magnetic field. The magnetization then precesses freely in the static field, at the so-called Larmor frequency, and this time-dependent flux induces a weak voltage in a radio-frequency pickup coil perpendicular to the static field. This induced signal is the NMR signal. Despite small variations in the underlying physical relations NQR utilizes the same concept as MRI.

1.2.9 Biological Sensor Methods

If the explosive package of mines could be detected directly the detection of any other type of clutter, such as shrapnel and metal fragments, could be eliminated. Trained dogs sniff out explosives vapors in the air above or near buried objects with incredible accuracy. However, dog training is an extremely difficult and time-consuming process that last up to three years. Moreover, the dog handler and the dog have to perform with perfect matching [Var05a]. As an interesting alternative honeybees offer the potential of using biological organisms to search wide areas for the presence of explosives and landmines [RB$^+$02; Dev02]. The use of bees is analogous to dogs for mine clearance, except that a colony of tens of thousands of bees can be trained in about one hour to fly over and search a field for explosives, does not require a leash, and will not set off any mines. Like dogs, bees can be trained to search for either the odors of explosives or suites of these chemicals. Initial tests indicate that bees are capable of detecting these odors at concentrations below those detectable by most instruments and match the odor sensitivity of dogs.

Figure 1.3: Minedogs and dog handler perform landmine detection.

Another example of a living system that responds to explosives and provides the operator with an identifiable signal to identify the explosive residue over wide areas is the microbial mine detection. A common soil microorganism has been genetically engineered to recognize explosives such as DNT and TNT and respond to it by producing a fluorescent protein [FBM00]. The bacteria are sprayed over a field and will contact the explosive. As fluorescent protein is produced and the bacteria become detectable using any of several fluorescence detection techniques.

1.2.10 Ground Penetrating Radar

The concept of ground penetrating radar (GPR) which is also referred to as georadar, ground probing radar, or subsurface radar originates from geophysical techniques. Similar to seismic measurements which make use of acoustic waves, electromagnetic waves are applied in order to image the subsurface [Dan04; Ulr82]. The historical steps which led to modern GPR are illustrated in 1.3. Since then GPR has been applied successfully for geologic [DA89; PM93; LL95; MLM98; GH$^+$04], hydrologic [ACR91; KC99; SD$^+$01; GPR04], engineering [WM$^+$93; BMN98; Mai00; ES$^+$05], archaeological [DBT78; Dan00; WH04], or petroleum [KE90] applications.
However, GPR can be also applied for the detection of buried AP landmines as it will be studied in this thesis. In case of a metallic mine, GPR senses the electrical inhomogeneities of the metal in the presence of a less conducting surrounding soil, but it can also be applied to sense the electrical inhomogeneities caused by dielectric landmines without any metal content. However, it is important to note, that GPR is not a landmine sensor but an electrical contrast sensor and subsurface clutter can result in scattering signatures comparable to that of a landmine. Changing soil properties can significantly affect the obtained reflections for the case of dielectric mines. Other subsurface inhomogeneities, such as rocks, roots, surface roughness, and soil inhomogeneities also yield a signature, which has to be taken into account for the signal processing. It has already been shown, that the received signal is often very weak, which implies that the reflection that is caused by the buried landmine is very small [Dan04]. Moreover, strong reflections which are referred to as ground bounce can typically be obtained at the air-soil interface. If a landmine is buried at a shallow depth, the often weak landmine signature can be covered by the strong ground-bounce return. It will be shown that the bandwidth of the radar significantly affects the imaging resolution and, thus, the ability to detect buried objects.
In conclusion, there is significant potential for improvements of GPR. As it will be addressed by the state-of-the-art review in 1.4 recent achievements of electromagnetic modeling allow to study the various interconnections in GPR, such as antenna design and positioning, bandwidth and resolution, properties of the soil or signal processing. The potential to realize significant improvements in GPR can only be obtained by an investigation of this complex relations [ML$^+$03]. This thesis addresses the imaging capabilities of a GPR for the detection of buried AP landmines and takes the influence of all components of such a system into account.

1.3 A Brief History of Radar and GPR

1.3.1 Development of Radar Systems

The basic principles of radar were already known from the early days of Heinrich Rudolph Hertz' research into radio phenomena in the 1880s. Although several attempts were made to develop useful radar systems, mainly to assist in avoidance of dangerous ship collisions, it was not until the beginning of World War II that the radar technology became practically useful and attained the prominence, that it holds nowadays. In the following section a brief summary will be given according to [Bro77; Swo86; Olh88; Sko90; Edd93; Gue97] in order to illustrate several important historical steps which finally led to the development of modern radar systems.
In 1904, Christian Huelsmeyer applied for a patent for his telemobiloscope [Hue04] in Düsseldorf, Germany. The telemobiloscope was a transmitter-receiver system for the detection of distant metallic objects by means of electrical waves and was designed as an anti-collision device for ships. It mainly consisted of a spark gap aimed using a multipole antenna. When a reflection was picked up by the two straight antennas attached to the separate receiver, a bell sounded. The system was able to detected the presence of ships in a distance up to 3 km. However, no practical application followed, although Guglielmo Marconi, widely credited as the 'Inventor of Radio', suggested an angle-only radar for ship collision avoidance [Wei03]. In 1922, Albert H. Taylor and Leo C. Young of the U.S. Naval Research Laboratory (NRL) noticed while conducting communication experiments that a wooden ship in the Potomac River was interfering with their signals. Thus, they had demonstrated the first continuous wave (CW) interference radar with separated antennas for the transmitter and the receiver which could already detect precisely the presence of the considered target object, but neither its correct location nor its velocity.
The next step was the introduction of pulsed radar systems. In 1925, the first short-pulse echo from the ionosphere was observed on a cathode ray tube by G. Breit and M. Tuve of John Hopkins University. During 1934 the first photo of a short-pulse echo from an aircraft was made by Robert M. Page. In 1936, the first pulse radar of the NRL was demonstrated successfully at a range of 4 km on a small airplane flying up and down the Potomac River. Within three month the range was extended to 40 km. However, the radar was based on low frequency signals, and thus required very large antennas which made it impractical for in-flight applications.

One of leading expert in the development of modern radar in Germany between 1928 and 1940 was Hans Eric Hollmann. In 1928, he started a company called GEMA with Hans-Karl von Willisen and Paul-Günther Erbslöh, which built the first radar in 1934 for naval use. It used a 50 cm wavelength and could find ships up to 10 km away. By 1935 they had developed two different radar systems. For naval use, the 'Seetakt' system, operated at a frequency of 375 MHz and a land based radar called 'Freya' operated at a frequency of 250 MHz. The german company Telefunken set up a radar business in 1933 based on Hollmann's work and developed the 'Würzburg' radar. During the war the 'Freya' and the highly directional 'Würzburg' worked in pairs. While the 'Freya' radar spotted the incoming aircraft the 'Würzburg' radar system could calculate the range and the height of the identified target object.
The first operational radar systems that was installed in the UK in 1937 was the 'Chain Home' system. It was designed by Sir Robert Watson-Watt and played a critical role in the Battle of Britain, pinpointing the location of German raids and allowing the Royal Air Force (RAF) to concentrate its forces rather than having to search the enemy aircraft by patrolling. The 'Chain Home' station operated at a frequency of 22 MHz and any aircraft in a distance up to 150 km could be spotted under good weather conditions. The United States installed a first operational shipborne radars, the 'XAF', on the battleship USS New York. It had a surface search range of 20 km and an air search range of 140 km. In 1942, the acronym RADAR (Radio Detection and Ranging) was established by the U.S. Navy and replaced earlier acronyms that were used by the British and the Germans.

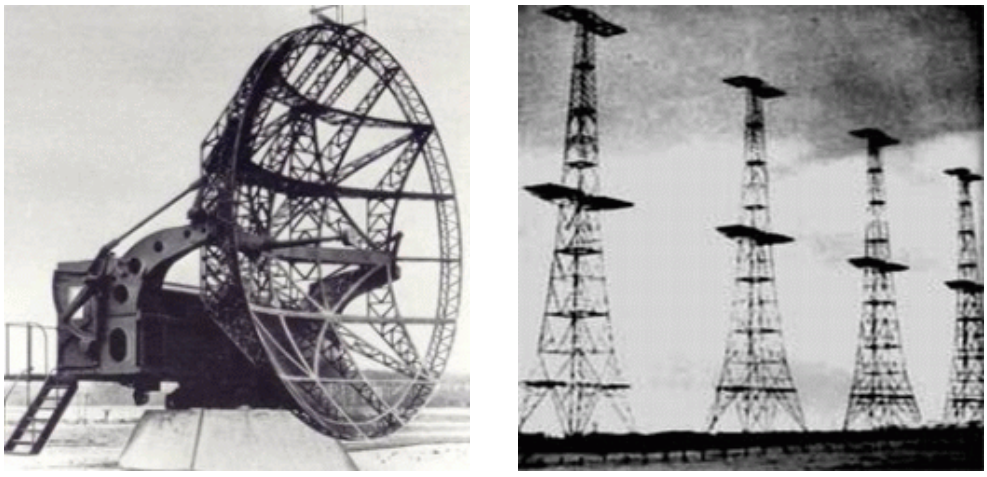

Figure 1.4: 'Würzburg' system and 'Chain Home' masts [Var06d].

1.3.2 Development of GPR Systems

From the early beginnings the development of GPR took place in parallel to the development of radar and in 1910, only six years after Huelsmeyer applied for a patent and performed experiments with anti-collision devices for ships, Heinrich Loewy adapted the concept to locate orebody and ground-water occurrences by means of reflected electromagnetic waves [Loe10]. This idea let to the assignation of a german patent for Gotthelf Leimbach and Heinrich Loewy the same year [LL10]. Herein the authors describe a technique which utilizes a number of boreholes filled with pairs of sending and receiving antennas in order to survey an unknown area. Hence, a rough picture of the ground structure could be reconstructed if the alignment of the boreholes is varied and the attenuation between sending and receiving antennas is obtained. For many applications the borehole radar concept is necessary in order to achieve the best possible coupling between the antenna and the ground [LS02].
The second technique of Leimbach and Loewy utilizes surfaces mounted antennas to determine the distance between the common plane of source and receiver and the reflecting layer. This has been done by by varying the frequency and meanwhile observing the resulting maximum and minimum field strength patterns which result from the interference between the transmitted surface and subsurface EM waves [LL11]. With the introduction of pulsed radar systems in the mid-1920s certain specific drawbacks of CW based systems could be eliminated and it was possible to determine precisely the distance, respectively, the depth of a reflecting plane.
The first GPR survey was performed in Austria in 1929 to sound the depth of a glacier [Ste29; Ste30]. However, the technology was largely forgotten until in the 1950s U.S. Air Force planes crashed in Greenland, because their radars were seeing through the ice layer and misread the altitude. This started investigations into the ability of radar to see into the subsurface not only for ice sounding but also for mapping subsurface properties and the water table. In 1967, a system comparable to Stern's original glacier radar was proposed, built and flown to the moon as part of the Surface Electrical Properties Experiment of Apollo 17 [SS$^+$72]. In 1972, Rex Morey and Art Drake founded the company Geophysical Survey Systems Inc. and started to sell commercial GPR systems for the first time [Mor74]. Since then many field applications and research reports could be recognized all over the world. Today there are over 300 patents related to GPR and several companies are developing commercial equipment or are offering a complete GPR survey service.

1.4 Objectives and the State of the Art

1.4.1 Starting Point of the Investigation

The potential of GPR for the detection of nonmetallic AP landmines and Unexploded Ordnances (UXO) in general has been already addressed in 1.2.10 and a state of the art survey reveals many reports about the successful applications of ultra-wideband GPR systems for such purposes. The forward-looking GPR in [SD+00] utilizes a frequency range from 50 MHz to 1.2 GHz for the detection of UXO, whereas the pulse-based system in [AG+02] is meant to be used for the detection of AP landmines in the frequency range from 100 MHz to 1.2 GHz. In [BW+00] a GPR system has been introduced as a stepped-frequency radar covering the frequency range from 500 MHz to 1.8 GHz. Later the frequency range has been extended up to 4 GHz [BW+02]. The results of the MINETEST report [Dea01] demonstrate the successful application of project-funded prototypes, that all utilize a sensor fusion concept for the detection of AP landmines, namely, MACADAM, INFIELD, HOPE [Rot02] and DEMAND [Sac04]. All of these prototypes combine different sensors in order to detect the buried AP landmines. However, it can be found that the GPR unit is always one of the most important parts of a sensor fusion systems [BSC99].
So far, the discussed GPR systems utilize frequencies below 3 GHz or 4 GHz exclusively. Often this is explained by the fact that the losses inside of the soil and, thus, the corresponding penetration depth increases if the frequency increases limiting the applicability of such a system. Furthermore, one should keep in mind that it is technically more complicated and usually also more expensive to generate and propagate higher frequencies, especially for the case of pulse-based GPR systems which are operated exclusively in the time domain. However, it should be noted, that in 2002 the U.S. Federal Communications Commission defined a frequency mask according to which all GPR systems must be operated with their 10 dB bandwidth below 960 MHz or in the frequency band from 3.1 GHz to 10.6 GHz [Var02] which contradicts the operating frequency range for most of the proposed systems.
Consequently, in this thesis the imaging capabilities of GPR for the detection of buried AP landmines will be investigated systematically and without any prejudice. The main objectives of the thesis that can be found in the following sections illustrate how all important aspects of the problem are taken into account.

1.4.2 3D EM Field Simulation of a GPR

Using methods of electromagnetic field simulation in combination with recent computer technology allows simulating electrically large problems, such as a complete GPR environment. In general, GPR simulations are very helpful for a detailed understanding of the underlying physical concepts, because it is possible to study the effect of different parameter of the GPR system systematically. Moreover, the simulation of a complete GPR environment allows to investigate different antenna configurations in the ground in advance to the fabrication of first prototypes.
Several approaches for the electromagnetic simulation of a GPR can be found in the literature. In [Tra96] the application of an analytical one-dimensional transmission line model for the simulation of a GPR yields interesting results. However, most approaches utilize numerical techniques to simulate the GPR problem in two or three dimensions. One of the first FDTD description of a fully three-dimensional GPR which has been described in [BS96; BS98] is utilized to investigate a separated-aperture sensor that consists of two parallel dipole antennas above a dry, loamy soil. Similar approaches that can be found in [GO00; GO01; KB04] take also lossy and heterogeneous soil materials into account and have been successfully utilized for different investigations in the context of GPR. In [LH01] a modular approach is described which, however, takes only an analytical description of the antenna into account. The simulation method in [KWR02] assumes the excitation by a quasi-plane wave instead of real antenna. Moreover, the transmitting antenna is assumed to be placed in the farfield of the receiving antenna, which is usually not the case for a quasi-monostatic GPR system. In [GG$^+$04] a hybrid simulation technique is proposed which utilizes both, finite differences and the method of moments (MoM). In conclusion, however, all of the discussed methods are limited to simple geometries or take other significant simplifications into account. Moreover, the specialized FDTD-codes are difficult to modify and cannot be extended easily to alternative geometries. Thus, none of the previous techniques allows to simulate a realistic GPR environment. In the context of this thesis a method will be presented which uses all features of the FIT-based commercial field simulation CST Microwave Studio (MWS) for the simulation of a complete GPR setup. Because the large number of varying geometries during a complete GPR scan demands for an automation of the GPR simulation the proposed method allows to automate the process of the antenna movement above the considered ground by means of an ActiveX control.

1.4.3 Investigation of Antennas for GPR

The antenna is the crucial hardware part of a GPR system because the imaging quality, respectively the resolution of the imaging system strongly depends on the radiation characteristics of the antenna. The antenna parameters that are effecting the system include the bandwidth of operating frequencies, the radiation pattern, the phase center location, the gain and the radiation efficiency. Moreover, the polarization, the corresponding polarization diversity and different effects of self-clutter which are also known as ring-down or reverberation have to be taken into account [LC+03]. Such ring-down events which occur due to an impedance mismatch at the aperture of the antenna could be misinterpreted as multiple reflections [RGD00] and therefore have to be avoided right from the beginning of the design process.
In the past a variety of antennas has been proposed for GPR applications, such as Vivaldi antennas [CB+04], resistively loaded antennas [MS99; Eid00], single and crossed dipoles [BE98; GD+00], bow-tie antennas [LYL01; Yar04], dielectric rod antennas [YC05], logarithmic or Archimedean spiral antennas [Lim03; CB+04; TJ05], tapered antennas [LYL00; CJ+06], double-ridged TEM horn antennas [YL00] or impulse radiating antennas [RZG98; FB01]. Some of these antennas have been already utilized for decades while others are brand new and still under development.
It shows, that many of the previous antennas have been designed exclusively under freespace conditions. In a GPR, however, the antenna has to meet different requirements and GPR antennas cannot be optimized without taking the GPR environment into account. First of all the soil area which is supposed to be illuminated by the GPR is often located in the nearfield region of the antenna, which has to be considered, see [MH04; LY+05]. Moreover, the reflection at the air-soil interface usually appears much stronger than the reflection at the target object itself. This problem is a systematic one and has to be included right from the beginning in the process of optimizing an antenna. In [MN98] the successful implementation of a Brewster angle configuration has been reported which allows to eliminate the air-surface reflection by applying a certain inclination angle to transmitting and receiving antenna. Unfortunately the size of the GPR system increases significantly, because the inclination angle of the antennas demands a certain distance between them which increases with higher permittivities of the soil. Moreover, it is very difficult to apply such a setup if the dielectric properties of the soil medium are not constant or completely unknow as it is the case for most field measurements.

In this thesis the GPR system is supposed to be applied for the detection of small-sized buried objects such as UXO or AP landmines. Therefore, certain requirements of the antenna system can be identified: As it will be explained in 2.2.6 the antenna must utilize an ultra-wideband frequency range in order to achieve the necessary spatial resolution which is inevitable for the detection of such small-sized objects. Recently, there have been proposals of adaptive antennas, which have to be placed close to ground [LYL04; LYL05]. However, it is often very difficult to obtain the correct properties of the soil. Also it has been found that a certain distance between the surface of the soil and the antenna increases the performance of focusing techniques due to the influence of the incident angles of the transmitted wave.
The different designs of ultra-wideband antennas which will be considered in the context of this thesis need to be investigated using the 3D EM field simulation of a GPR environment as it is proposed in chapter 3. Thus it will be possible to study the potential of each antenna to be used for GPR. Some of the antennas which will be discussed are of-the-shelf designs such as the log-periodic dipole antenna or different standard gain horn antennas. Others will be modified from existing designs such as the double-ridged TEM horn antenna or are designed completely new as it is the case for the Orion-type IRA. To the best of the authors knowledge none of the existing approaches utilizes the same level of integration for the antenna design as the the one which will be presented in the context of this thesis.

1.4.4 Focusing by Synthetic Aperture

The important problem of focusing the raw results of monostatic or bistatic GPR measurements has been been addressed frequently. Such processing techniques have been proposed to significantly improve the spatial resolution of the imaging systems. Using focusing, it is possible to compensate for the non-perfect radiation characteristics of the illuminating antenna. Because of the different historical origins one has to distinguish between two major groups of focusing algorithms. On the one hand processing techniques which originate from seismic applications, e.g. the Stolt migration [Sto78] or the Phase-shift migration [GS84], have been adapted for GPR applications, e.g. in [BO91; PL99; BEH00; KW$^+$03; PO04; vGS00; SK04]. All migration techniques, in general, try to concentrate the scattered reflection signature of the electromagnetic inhomogeneities such as a buried landmine in the origin of this reflection in order to increase the contrast of the radar image.

Synthetic aperture radar (SAR) techniques, however, originate from airborne or spaceborne imaging applications and have been adapted for the focusing of GPR images, e.g. in [JM94; JLM96; SD+00; MvG02; MY02; OLL04]. The methods which are applied in the time domain or the frequency domain combine the results of various measurements at different antenna positions. Thus, a synthetic aperture is generated which is much larger than the utilized physical antenna, see 5.
Most of the proposed SAR algorithms for GPR assume a two layer geometry which consist of an air layer above a homogeneous soil layer and utilize optical ray paths methods to determine the angle of refraction at the air-soil interface. Theoretically, the refraction and the dispersion of the wave can be compensated if the dielectric permittivity profile of the soil could be estimated accurately such as it it proposed in [FG02]. However, in reality many of the suggested focusing concepts still suffer from unpredictable effects due to reflection, refraction and dispersion and often the soil properties and the permittivity profile in the subsurface cannot be estimated correctly. Moreover, the three-dimensional focusing of a certain region within the soil is computational expensive and therefore very time-consuming which contradicts the ideal case of real-time image processing. Consequently, some approaches utilize only a limited number of focusing planes at different depth for which a constant velocity is assumed in order to combine the results subsequently [HS00; SF05] or place a single focusing plane in the depth where the target objects are assumed to be located, e.g. in [MN98], which reduces the computational efforts. Nonetheless, the required profile of the permittivity in the subsurface is often not available.
In this thesis a SAR focusing method will be investigated that allows to discard most of the discussed constraints or even turns them into advantages as it is the case with the refraction at the air-soil interface. It will be shown that only a single focusing plane which is placed directly at the surface of the soil has to be taken into account for the focusing of the complete data volume. Thus, it is possible to reduce the three-dimensional problem of focusing every point in the lower half-space to a two-dimensional one. Consequently, the difficult prediction of the soil properties can be omitted and in addition the computational efficiency can be increased significantly. It will be verified by both, numerical field simulations and experimental measurements, that the focusing problem can be simplified as suggested, because the application of the SAR focusing exclusively on the surface of the soil leads to proper focused field distribution within a certain region below the surface.

1.5 Organization of the Thesis

This thesis is organized according to the main objectives which have been addressed in the previous section. Every chapter can be understood as a representation of one aspect of the overall research work. Another characteristic of the work is the frequent utilization of figures that has been found to be very useful for the presentation of complex results and relations. The outline of the thesis will be as follows:
Chapter 2 gives a brief review of the fundamental relations which are needed for the description of the propagation of waves. Moreover, different important aspects for the theoretical description and classification of radar system are addressed.
In chapter 3 a novel approach for the 3D EM field simulation of a complete GPR environment is proposed. This complete GPR problem includes the antenna, a homogeneous soil brick and a target object which has been buried inside of this soil brick. For this approach all features of a commercial simulation software are utilized by an ActiveX remote control. The discussion includes the definition of realistic soil structures, realistic target objects and the integration of different antennas.
Chapter 4 addresses the development of antennas in the context of GPR applications. The design and the electromagnetic radiation characteristics of the different types of antenna are investigated and the prototypes are integrated in the proposed field simulation of a GPR in order to verify their ability for such applications.
In chapter 5 the important problem of focusing the raw data of GPR measurements is addressed. The analytical derivation of the discussed SAR focusing algorithm and the real implementation of the algorithm will be discussed and verified. Moreover, different theoretical and practical limitations of the SAR focusing are investigated systematically using both, analytical and numerical simulation techniques.
In contrast to the SAR focusing concept chapter 6 addresses the focusing using a physical dielectric lens. All important aspects of the lens design, such as the definition of the dimensions and the correct placement of the lens will be investigated and the lens concept will be verified by 3D simulations and measurements.
Chapter 7 addresses the results of several experimental GPR measurements which have been accomplished in the context of this thesis in order to investigate different aspects of the practical application of GPR. Therefore, two prototype GPR systems have been designed, constructed and verified experimentally, namely, a fully automated laboratory GPR and a mobile GPR setup for outdoor measurements.
Finally, the results of the research work are summarized in chapter 8.

Chapter 2

Fundamental Relations

2.1 Propagation of Electromagnetic Waves

2.1.1 Maxwell's Equations

Maxwell's equations, a set of four equations developed by James C. Maxwell in 1865 [Max65], describe the temporal and spatial behavior of electric and magnetic fields, namely, the generation of magnetic fields by currents and changing electric fields in equation (2.1), the generation of electric fields by changing magnetic fields in equation (2.2), the generation of electric fields by electric charges in equation (2.3), respectively, the experimental absence of magnetic monopoles in equation (2.4).

$$\nabla \times \mathbf{E} = -j\omega\mathbf{B} \tag{2.1}$$

$$\nabla \times \mathbf{H} = j\omega\mathbf{D} + \mathbf{J} \tag{2.2}$$

$$\nabla \cdot \mathbf{D} = \rho \tag{2.3}$$

$$\nabla \cdot \mathbf{B} = 0 \tag{2.4}$$

In addition, the material equations (2.5)-(2.7) describe the electric and magnetic behavior of the surrounding medium with respect to different physical properties.

$$\mathbf{J} = \sigma \cdot \mathbf{E} \tag{2.5}$$

$$\mathbf{D} = \epsilon \cdot \mathbf{E} \tag{2.6}$$

$$\mathbf{B} = \mu \cdot \mathbf{H} \tag{2.7}$$

2.1.2 Permittivity and Permeability

It is well known, that the microscopic interactions inside of a material which exists due to an electromagnetic field can only be described by macroscopic values, namely, dielectric permittivity, magnetic permeability, and electric conductivity. The dielectric permittivity $\epsilon = \epsilon_0 \cdot \epsilon_r = \epsilon_0 \cdot (\epsilon_r' - j\epsilon_r'')$ is a complex function having real and imaginary components. The real portion of ϵ_r is usually expressed as the dielectric constant ϵ_r', which is the ratio of the electric-field storage capacity of a material to that of free space, whereas the imaginary portion of ϵ_r is usually expressed as dielectric loss ϵ_r'' representing the attenuation. Although dielectric losses are small if the conductivity of a material is low and the dielectric constant is typically the primary component of dielectric permittivity, dielectric losses have to be taken into account. Consequently, equation (2.2) can be reformulated according to [Col92].

$$\begin{aligned} \nabla \times \mathbf{H} &= j\omega\mathbf{D} + \mathbf{J} && (2.8)\\ &= j\omega\epsilon_0\epsilon_r\mathbf{E} + \sigma\mathbf{E} && (2.9)\\ &= j\omega\epsilon_0 \left[\epsilon_r' - j\left(\epsilon_r'' + \frac{\sigma}{\omega\epsilon_0}\right)\right]\mathbf{E} && (2.10)\\ &= j\omega\epsilon_0\epsilon_r'\mathbf{E} + (\omega\epsilon_0\epsilon_r'' + \sigma)\,\mathbf{E} && (2.11) \end{aligned}$$

Herein $\epsilon_r'' + \sigma/\omega\epsilon_0$ may be considered as the effective imaginary part of the dielectric permittivity or $\omega\epsilon_0\epsilon_r'' + \sigma$ as the total effective conductivity. Dielectric permittivity, magnetic permeability, and electric conductivity are frequency dependent and can vary strongly over the frequency range [Pow97]. However, their behavior is often assumed to be relatively consistent over the considered range of operating frequencies. The loss tangent $\tan\delta_e$ is a characteristic parameter which describes the losses of a dielectric material and is calculated using the following equation.

$$\tan\delta_e = \frac{\omega\epsilon_r'' + \sigma}{\omega\epsilon_r'} \qquad (2.12)$$

Any measurement of $\tan\delta_e$ always includes the effects of a finite conductivity σ. However, at microwave frequencies ω becomes large and as a consequence $\omega\epsilon_r''$ is usually much larger than σ which subsequently can be neglected.

The magnetic permeability μ, which represents the magnetic field divided by the magnetic field strength, is the product of the permeability of free space μ_0 and relative magnetic permeability μ_r. As in the electric case, attenuation cause μ to be a complex parameter with a negative imaginary part which denotes as $\mu = \mu_o \cdot (\mu_r' - j\mu_r'')$. Consequently, the magnetic loss tangent $\tan\delta_m$ denotes as

$$\tan\delta_m = \frac{\mu_r''}{\mu_r'} \tag{2.13}$$

Both, dielectric and magnetic materials, are referred to as isotropic if the produced polarization does not depend on the direction of the applied electric and magnetic field, respectively. Otherwise they will be referred to as anisotropic materials.

2.1.3 Plane Wave Assumption

An elementary solution of the wave equations can be derived if only plane waves in a homogeneous, isotropic medium are considered [Col92]. The concept of plane waves is fictional because it assumes that there is no fall off of intensity as the wave propagates away from its source and that it continuously maintains planar wave fronts. However, a spherical wave at some distance from its source can be considered planar over a certain dimension with an insignificant $1/\mathbf{r}$ decrease in intensity. Thus the plane wave concept is a practical simplification for waves interacting with objects and all spherical waves can be described by overlapping plane waves as follows.

$$\mathbf{E} = E_0 e^{-j\mathbf{k}\cdot\mathbf{r}+j\omega t} \tag{2.14}$$

$$\mathbf{H} = H_0 e^{-j\mathbf{k}\cdot\mathbf{r}+j\omega t} \tag{2.15}$$

The constant-phase surfaces given by $\mathbf{k}\cdot\mathbf{r} = const$ are planes and the field $\mathbf{E}$ does not vary on a constant-phase plane. The vector $\mathbf{k}$ may also be written as $\mathbf{k} = \mathbf{n}k_0$, where $\mathbf{n}$ is a unit vector in the direction of $\mathbf{k}$ and k_0 is the magnitude of $\mathbf{k}$ in freespace. For lossy cases $j\mathbf{k} = \mathbf{n}\cdot(\alpha + j\beta)$ which adds an attenuation constant α and a phase constant β to the sinusoidal temporal and spacial variation in equations (2.14) and (2.15), respectively. For reasons of simplification we allow for $r = \mathbf{n}\cdot\mathbf{r}$. Hence, the propagation of a plane wave in the positive direction of r reads as

$$\mathbf{E} = E_0 e^{-\alpha r} e^{j(\omega t - \beta r)} \tag{2.16}$$

$$\mathbf{H} = H_0 e^{-\alpha r} e^{j(\omega t - \beta r)} \tag{2.17}$$

It should be mentioned, that the term plane wave is also used to describe waves that are approximately plane waves in a localized region of space. For example, an antenna produces a field that is approximately a plane wave in its far-field region.

2.1.4 Dielectric Interfaces

It is assumed that the half-space $z \geq 0$ is filled with dielectric medium with a permittivity ϵ. A TEM wave is assumed incident from the region $z \leq 0$. Without loss the xy axis may be oriented so that the unit vector $\mathbf{n}_1$ which specifies the direction of incidence lies in the xz plane. It is convenient to solve this problem for two special cases, namely, with parallel polarization, where the electric field of the incident wave is coplanar with the plane of $\mathbf{n}_1$ and the interface normal and lies in the xz plane, and perpendicular polarization, where the electric field of the incident wave is perpendicular to the plane of incident as it has been defined by $\mathbf{n}_1$ with an interface normal along the y axis. An incident TEM wave with arbitrary polarization can always be decomposed into a sum of perpendicular and parallel polarized waves. The two polarizations are analyzed separately because the reflection and transmission coefficients to be defined, are different for the two cases [Col92]. According to Fig. 2.1 the incident TEM wave can be described as follows.

$$\mathbf{E}_i = \mathbf{E}_1 e^{-jk_0 \mathbf{n}_1 \cdot \mathbf{r}} \tag{2.18}$$

$$\mathbf{H}_i = Y_0 \mathbf{n}_1 \times \mathbf{E}_i \tag{2.19}$$

A certain part of the incident power will be reflected, and the remaining part will be transmitted into the dielectric medium. Let the reflected wave be

$$\mathbf{E}_r = \mathbf{E}_2 e^{-jk_0 \mathbf{n}_2 \cdot \mathbf{r}} \tag{2.20}$$

$$\mathbf{H}_r = Y_0 \mathbf{n}_2 \times \mathbf{E}_r \tag{2.21}$$

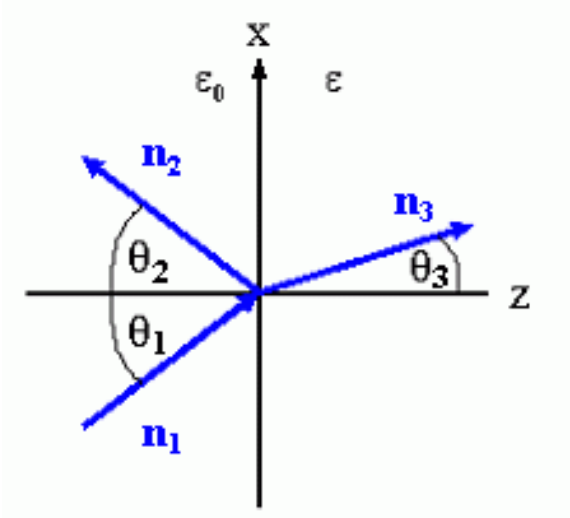

Figure 2.1: Plane wave incident on a dielectric interface.

where $\mathbf{n}_2$ and $\mathbf{E}_2$ are to be determined. In the dielectric medium the solution for a TEM wave is the same as that in free space, but with ϵ_0 replaced by ϵ. Thus, the parameter $k = \omega\sqrt{\mu_0\epsilon} = \eta k_0$ and $Y = \sqrt{\epsilon/\mu_0} = \eta Y_0$ are used, where $\eta = \sqrt{\epsilon_r}$ is the index of refraction. The transmitted wave can be expressed by

$$\mathbf{E}_t = \mathbf{E}_3 e^{-jk\mathbf{n}_3\cdot\mathbf{r}} \tag{2.22}$$

$$\mathbf{H}_t = Y_0\mathbf{n}_3 \times \mathbf{E}_t \tag{2.23}$$

with $\mathbf{n}_3$ and $\mathbf{E}_3$ as yet unknown. The boundary conditions that are to be applied are the continuity of the tangential components of the electric and the magnetic field at the interface plane which is only possible if the fields on adjacent sides of the boundary have the same variation with respect to x and y. Hence, the propagation phase constant along x must be the same for all waves.

$$k_0 n_{1x} = k_0 n_{2x} = k n_{3x} = \eta k_0 n_{3x} \tag{2.24}$$

Since n_{1y} was chosen as zero, it follows that $n_{2y} = n_{3y} = 0$. Equation (2.24) gives

$$\sin\theta_1 = \sin\theta_2 \tag{2.25}$$

$$\sin\theta_1 = \eta\sin\theta_3 \tag{2.26}$$

These two equations are usually referred to as the well-known Snell's law of reflection (2.25) and refraction (2.26), respectively, with θ_1 denoting the angle of incident, θ_2 the angle of reflection and θ_3 the angle of refraction. The so-called Fresnel coefficients for the reflection Γ_1 and the transmission $\mathscr{T}_1$ of the incident wave in case of parallel polarization can be determined by the following equations.

$$\Gamma_1 = \frac{\left(\epsilon_r - \sin^2\theta_1\right)^{1/2} - \epsilon_r\cos\theta_1}{\left(\epsilon_r - \sin^2\theta_1\right)^{1/2} + \epsilon_r\cos\theta_1} \tag{2.27}$$

$$\mathscr{T}_1 = \frac{2\eta\cos\theta_1}{\left(\epsilon_r - \sin^2\theta_1\right)^{1/2} + \epsilon_r\cos\theta_1} \tag{2.28}$$

It is important to note that Γ_1 vanishes for an angle of incidence $\theta_1 = \theta_b$, which is referred to as the so-called Brewster angle, where all the incident power is transmitted into the dielectric medium. The calculation of the Brewster angle for a certain interface depends on the permittivity of the medium, respectively, the index of refraction and from equation (2.27) the following condition can be derived.

$$\epsilon_r - \sin^2\theta_b = \epsilon_r^2\cos^2\theta_b \tag{2.29}$$

$$\sin\theta_b = \left(\frac{\epsilon_r}{\epsilon_r + 1}\right)^{1/2} \tag{2.30}$$

For perpendicular polarization the roles of electric and magnetic fields are interchanged so that the electric field has only a y component. However, the fields can still be expressed in the form given by (2.18)-(2.23), but with $\mathbf{E}_1$, $\mathbf{E}_2$ and $\mathbf{E}_3$ having y components only. As in the previous case, the boundary conditions must hold for all values of x and y on the $z = 0$ plane and Snell's law of reflection (2.25) and refraction (2.26) must be satisfied. Thus, the Fresnel reflection and transmission coefficients, Γ_2 and $\mathscr{T}_2$, for the case of perpendicular polarization of the incident wave can be calculated according to the following expressions.

$$\Gamma_2 = \frac{\cos\theta_1 - \left(\epsilon_r - \sin^2\theta_1\right)^{1/2}}{\left(\epsilon_r - \sin^2\theta_1\right)^{1/2} + \cos\theta_1} \tag{2.31}$$

$$\mathscr{T}_1 = \frac{2\cos\theta_1}{\left(\epsilon_r - \sin^2\theta_1\right)^{1/2} + \cos\theta_1} \tag{2.32}$$

As an example for a given interface between freespace and a material with a permittivity of $\epsilon_r = 3$ the variation of Γ and T has been illustrated in Fig. 2.2 for both, parallel and perpendicular polarization of the incident field. The incident angle θ_1 has been is varied from 0 degree to 90 degree. For such a configuration the Brewster angle can be calculated according to equation (2.30) to be 60 degree. As it can be obtained from the figure a notable difference between both cases is the nonexistence of a Brewster angle for the case of perpendicular polarization.

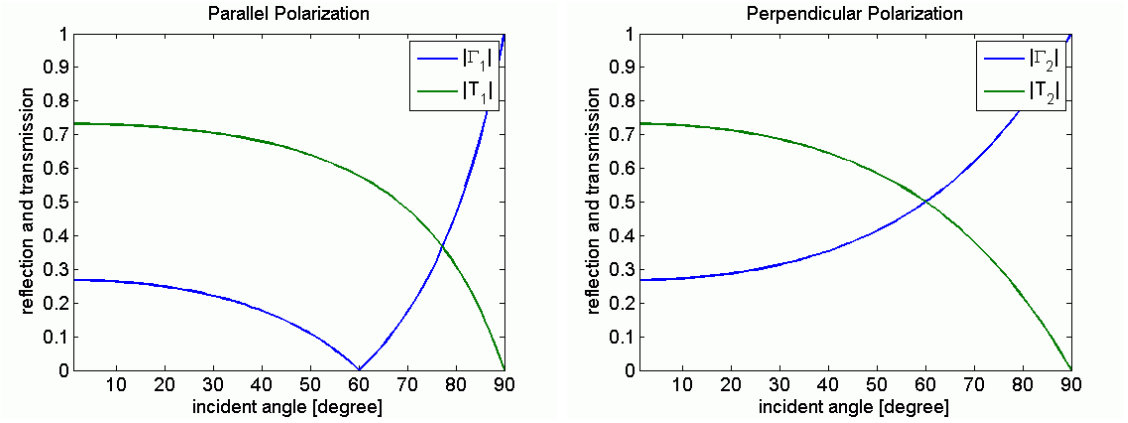

(a) parallel polarization (b) perpendicular polarization

Figure 2.2: Reflection and transmission for varying incident angle.

This has to be considered if for certain applications the reflection coefficient should be minimized by choosing the Brewster angle for the incident wave, which leads to a maximum transmission at the dielectric interface as it has been proposed [MN98]. However, such a concept might become impractical if the difference of the refraction indices at the interface becomes larger and larger, because the corresponding Brewster angle and the extension of a corresponding transceiver system would increase beyond any practical limitations. Moreover, any variation of the permittivity or a rough surface would significantly decrease the quality of the approach.

2.2 Theory of Radar Systems

2.2.1 Radar Categorization

In general, the transmitting and the receiving station can exist at the same location, which is either called a quasi-monostatic radar if the distance between the transmitter and receiver is equal to zero, or is referred to as a monostatic radar if a single antenna performs both transmit and receive duty. If the transmitter and receiver station have separate locations the system is called bistatic, see [BGJ03]. If a radar system involves one or more transmitting stations and more than one receiving station it is referred to as multistatic radar. The different concepts for the spatial distribution of transmitter and receiver fulfill different requirements. It is important to note, that more receivers will not automatically increase the amount of information about a target, respectively, a device under test (DUT). Radars can also be typed according to their waveform. A continuous wave (CW) type transmits continuously. Moreover, the signal can contain frequency modulation (FMCW) or create the resulting signal as a combination of monochromatic steps through a certain band of frequencies, referred to as stepped frequency continuous wave (SFCW). When the transmitted waveform is pulsed in the time domain the system is called pulsed radar. In analogous manner, one can distinguish between active and passive radars which are types with and without a transmitter, respectively [Edd93].

2.2.2 Transmitted Waveform

The waveform transmitted by the radar is denoted by $s(t)$ and defined as the signal at the output terminals of the transmitter. In todays radar systems the radar signal $s(t)$ may contain modulation of both its amplitude and frequency with time. The general form of $s(t)$ can be written as

$$s(t) = a(t)cos\left[\omega_0 t + \theta(t) + \phi_0\right] \tag{2.33}$$

where $a(t)$ represents the amplitude modulated envelope of the transmitted signal, $\theta(t)$ is a phase term due to frequency modulation, and ϕ_0 is a certain arbitrary phase angle. In some radar analysis it is convenient to treat ϕ_0 as a random phase angle. In most cases it is, however, considered as a certain phase constant [Pee98].

2.2.3 Transmitted Power

The output of the transmitter can be modeled as an equivalent circuit comprised of a source of voltage $s(t)$ in series with an output impedance, denoted by Z. For an impedance-matched load of Z^* across the output terminals the available instantaneous power can be expressed by the following equation.

$$P_{ai} = \frac{s^2(t)}{4\Re(Z)} = \frac{a^2(t)}{8\Re(Z)} \{1 + cos[2\omega_o t + 2\theta(t) + 2\phi_o\}] \tag{2.34}$$

As the cosine term in (2.34) behaves almost as a pure cosine for any single period of the carrier frequency ω_0 it is nearly zero, when averaged over any carrier's period. Thus the average peak transmitted power, denoted by P_t, can be obtained if the available instantaneous power is averaged over one cycle of the carrier and $s(t)$ has its maximum amplitude. It is expressed by the following equation.

$$P_t = \frac{1}{4\Re(Z)} \left[\text{cycle-averaged } s^2(t)\right]_{max} = \frac{[a^2(t)]_{max}}{8\Re(Z)} \tag{2.35}$$

For a pulsed radar P_t is evaluated at the maximum of the envelope of the pulse function, whereas for a continuous wave signal with constant amplitude P_t will have the same value for all times within the period. The available average transmitted power, denoted by P_{av}, is defined as available instantaneous power averaged over a given time interval T_R. Hence, P_{av} can be described as follows.

$$P_{av} = \frac{1}{4\Re(Z)\,T_R} \int_{-T_R/2}^{T_R/2} s^2(t)dt \tag{2.36}$$

In a pulsed radar T_R is the pulse repetition period, and the average power over one period is the same as the average power over any integral number of periods if the transmitted pulses are the same in each interval. For normalized versions of P_{av} equation (2.36) does not contain the factor $1/T_R$. For continuous-wave radar, $a(t)$ and $\theta(t)$ my both be periodic functions and T_R can be taken to be the fundamental period of the two functions. For rectangular pulses P_{av} and P_t are related by the

following equation where the ratio $\frac{T}{T_R}$ denotes the duty factor of the transmitted waveform which can be generalized for other than rectangular pulses [Pee98].

$$P_{av} = \frac{T}{T_R} P_t \tag{2.37}$$

2.2.4 The Radar Equation

The radar equation is not only an equation for the calculation of the range of a radar system, but a versatile tool for the design of a radar system. The performance of a radar is determined by the following characteristic parameter [Lud02].

- radar signal and sampling strategy, often referred to as waveform
- radar subsystems incl. transmitter, antenna, receiver, processing
- radar target with size and fluctuation of its radar cross section
- radar environment: channel losses, attenuation, reflection, noise

The design of a radar system is accomplished iteratively. The parameters which can be effected are varied in such a way, that the demand for the range can be fulfilled while a compromise about all other demands including the cost of the radar system has to be found. In the following the radar equation and the parameter that will effect the design of a radar system will be discussed according to [Pee98].
The desired target reflection signal can be received by the system itself in several ways because monostatic, bistatic or multistatic radar systems may all produce different received signals. However, a single formulation can be used to define the received signal powers in all these systems. Let P_t represent the average peak power output of the transmitter. This power may be reduced by mismatch and losses in microwave elements, such as duplexer, circulators or isolators, and in the transmission line which connects transmitter and antenna. L_t is the power loss from the transmitter to the antenna, where $L_t \geq 1$, the average peak power accepted at the input of the antenna is denoted by P_{acc} which is $P_{acc} = P_t/L_t$. However, not all of this power is radiated by the antenna. Some is lost through heating effects in the structure. This radiation loss of the antenna is denoted by L_{rt} and can be written as $L_{rt} = 1/\upsilon_{rt} \geq 1$ where υ_{rt} denotes the radiation efficiency of the transmitting

antenna. If all the average peak radiated power occurred from a isotropic antenna, the power density of the wave at a distance d_1 would be $P_{rad}/(4\pi d_1^2)$ for a vacuum channel. In the real channel there is an additional one-way power loss on the path from the transmitting antenna to the target due to all channel effects that may occur, denoted by L_{ch1}. Thus an isotropic antenna produces a wave average peak power density at the target that can be described by the following equation.

$$\frac{P_{rad}}{4\pi d_1^2 L_{ch1}} = \frac{P_t}{4\pi d_1^2 L_t L_{rt} L_{ch1}} \tag{2.38}$$

Moreover, a real antenna will increase the power density of the wave at the target because of its directive properties. If the target is at a direction (θ_t, ϕ_t) in spherical coordinates located at the transmitting antenna, the increase is given by the directivity, denoted by $D_t(\theta_t, \phi_t)$. The average peak power density at the target, denoted by $\mathscr{P}_t(d_1, \theta_t, \phi_t)$ is given by the following expression.

$$\mathscr{P}_t(d_1, \theta_t, \phi_t) = \frac{P_t D_t(\theta_t, \phi_t)}{4\pi d_1^2 L_t L_{rt} L_{ch1}} \tag{2.39}$$

When the transmitted wave with an average peak power density of (2.39) crosses the target, the power is scattered by the target in various directions. To account for the power reflected back toward the receiving site, a constant ς, which is called the radar cross section, is associated with the target. The constant, which has the unit of area, when multiplied by $\mathscr{P}_t(d_1, \theta_t, \phi_t)$, corresponds to an equivalent power that is reflected equally in all directions and accounts for the actual available power at the site of the receiver. This average peak power reflected by the target is reduced by the factor $1/(4\pi d_2^2)$ to consider the intensity reduction with range as the reflected wave travels the distance d_2 to the receiving site. Over the path from the target to the receiver there is also a one way channel loss L_{ch2} so that the average peak power density of the wave at the receiving antenna becomes

$$\mathscr{P}_i = \frac{P_t D_t(\theta_t, \phi_t)\varsigma}{(4\pi)^2 d_1^2 d_2^2 L_t L_{rt} L_{ch1} L_{ch2}} \tag{2.40}$$

When the reflected wave crosses the receiving antenna, the effective area of the antenna determines the available received power which reads as $\lambda^2 D_r(\theta_r, \phi_r)/(4\pi L_{rr})$.

Herein λ denotes the wavelength, $D_r(\theta_r, \phi_r)$ denotes the directivity of the receiving antenna and a loss factor is included in order to account for the radiation loss of the receiving antenna which is denoted by L_{rr} and can be written as $L_{rr} = 1/\upsilon_{rr} \geq 1$ where υ_{rr} denotes the radiation efficiency of the receiving antenna. Hence, the average peak signal power available at the output terminals of the receiving antenna can be described by the so-called basic radar equation.

$$P_r = \mathscr{P}_i \frac{\lambda^2 D_r(\theta_r, \phi_r)}{4\pi L_{rr}} = \frac{P_t D_t(\theta_t, \phi_t) D_r(\theta_r, \phi_r) \lambda^2 \varsigma}{(4\pi)^3 d_1^2 d_2^2 L_t L_{rt} L_{ch1} L_{ch2} L_{rr}} \tag{2.41}$$

For equation (2.41) it has been considered that the the directive gain of the receiving antenna is a function of the target direction, (θ_r, ϕ_r), in spherical coordinates located at the receiving antenna. In some cases the maxima of the transmit and receive patterns point directly at the target, with $D_t(\theta_t, \phi_t) = D_t$ and $D_r(\theta_r, \phi_r) = D_r$, representing the directivities of the transmitting and receiving antenna, respectively, and equation (2.41) can be reformulated as follows.

$$P_r = \frac{P_t D_t D_r \lambda^2 \varsigma}{(4\pi)^3 d_1^2 d_2^2 L_t L_{rt} L_{ch1} L_{ch2} L_{rr}} \tag{2.42}$$

Equation (2.41) applies to bistatic and multistatic radars directly. With proper definitions and interpretations, however, it also applies to radars with separated antennas for transmission and reception that are close enough to be considered at the same position (quasi-monostatic) and radars that use the same antenna for transmission and reception (monostatic). Hence, it is possible to replace $d_1 = d_2 = d$ and $L_{ch1} = L_{ch2} = L_{ch}$ so that equation (2.41) reduces to

$$P_r = \frac{P_t D_t(\theta_t, \phi_t) D_r(\theta_t, \phi_t) \lambda^2 \varsigma}{(4\pi)^3 d^4 L_t L_{rt} L_{ch}^2 L_{rr}} \tag{2.43}$$

If the antennas point directly at the target equation (2.43) reduces further to

$$P_r = \frac{P_t D_t D_r \lambda^2 \varsigma}{(4\pi)^3 d^4 L_t L_{rt} L_{ch}^2 L_{rr}} \tag{2.44}$$

For the case of a monostatic setup, with one antenna used for both, transmission and reception, such that $D_t(\theta_t, \phi_t) = D_r(\theta_t, \phi_t) = D(\theta_t, \phi_t)$ and $L_{rt} = L_{rr} = L_{rad}$, equations (2.43) and (2.44), respectively, can be reformulated as follows.

$$P_r = \frac{P_t D^2(\theta_t, \phi_t)\lambda^2 \varsigma}{(4\pi)^3 d^4 L_t L_{rad}^2 L_{ch}^2} \tag{2.45}$$

$$P_r = \frac{P_t D^2 \lambda^2 \varsigma}{(4\pi)^3 d^4 L_t L_{rad}^2 L_{ch}^2} \tag{2.46}$$

For the formulation of (2.46) the substitution $D_t = D_r = D$ has been used, assuming that the directivity D is the same for both, the transmitting and the receiving antenna of the corresponding radar system.

2.2.5 Range Measurement

The measurement of the radial distance between the radar antenna and a target is the basic task of almost all radar systems. It is important to consider that for a specific target range d the estimated traveling time of the wave t_R is corresponding to a total distance $2d$ which is traveled by the wave. Hence, the determination of d which is referred to as single-pulse range measurement reads as follows.

$$d = \frac{c_0 \cdot t_R}{2} \tag{2.47}$$

However, the speed of light in a certain medium differs from than in free space (vacuum). In order to avoid an overestimation of the range of a reflecting target or a certain dielectric boundary the permittivity of the surrounding medium has to be considered. Hence, the determination of d needs to be modified [Dan04].

$$d = \frac{c_0 \cdot t_R}{2\sqrt{\epsilon_r}} \tag{2.48}$$

Further problems such as the determination of a moving targets distance which are addressed by more complicated radar modes of operation such as Doppler processing are irrelevant for a ground penetrating radar with all static objects. Therefore, such radar processing techniques will not be discussed in the context of this thesis.

2.2.6 Resolution of a GPR

An important aspect for the design of radar systems is the achievable resolution. For the case of GPR one has to distinguish between range resolution and spatial resolution. The range resolution, which is also referred to as slant range, vertical or depth resolution is defined in terms of the ability to resolve point targets separated along a line in the direction of radiation. Thereby pulsed radars and SFCW systems yield an equivalent resolution if the spectral shapes are properly defined [LIF94; LI01]. If the received waveform has a bandwidth of B the corresponding impulse response for this waveform would be $sinc(t)$. The resulting time resolution $\delta_{time} = 1/2B$ is given by the width of the mainlobe e.g. at 4 dB below the peak which is a convenient criterion chosen to simplify the formula as it is illustrated in Fig. 2.3.

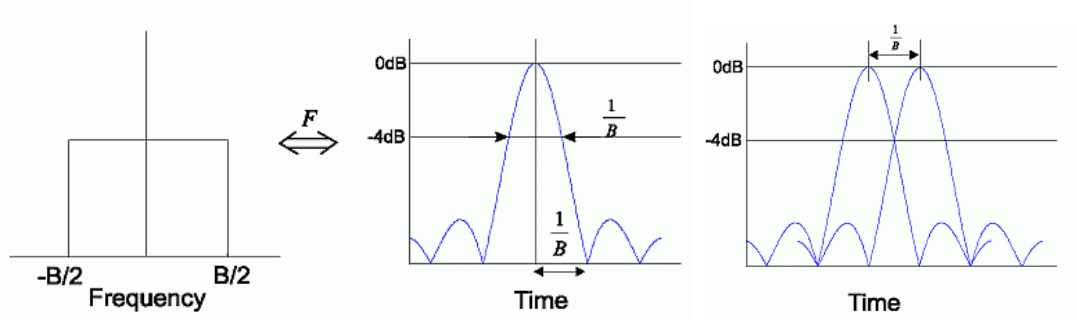

Figure 2.3: Frequency-time relation and resolving distance [LI01].

Hence, for a minimum distance of $1/B$ the impulse response from two targets could be resolved and the range resolution can be obtained according to equation (2.49) [MJ94; SD+98; LI01; vG03]. Herein, the term resolution is used to provide some upper limit to the resolution capability of the waveform, which is only an approximation, with the strong assumption that the target is a point scatterer.

$$\delta_{range} \cong \frac{c}{2B\sqrt{\epsilon_r}} \tag{2.49}$$

The effects of an increasing resolution due to a higher permittivity of the medium and a decreasing bandwidth due to the higher attenuation in such a medium tend to compensate each other so that within certain bounds the range resolution is approximately independent of loss variations within the propagating material [Dan04].

The spatial resolution which is also referred to as lateral, plan or cross range resolution defines the ability to resolve object features or separated targets at a line perpendicular to the direction of radiation. It is depending on the so-called footprint of the antenna, namely, the area A on the surface of the soil that is illuminated, and the corresponding angle of illumination θ_b. Both parameters are related directly to the size and position of the aperture of the antenna. Thus, the spatial resolution can be approximated according to [MJ94; SD+98].

$$\delta_{spatial} \cong 2\sqrt{A} \cong max\left(\frac{\lambda_{min}}{2}, \frac{\lambda_{min}}{2\tan\left(\theta_b/2\right)}\right) \tag{2.50}$$

Many other approaches can be found in the literature that try to estimate the spatial response of the GPR system by different approximations such as in [MN98; MB01; Par01; Dan04]. However, all of these sophisticated techniques relate the spatial resolution to the beam pattern of the antenna, e.g. in Fig. 2.4, which has to be estimated in order to predict the resolving capability of the GPR system.

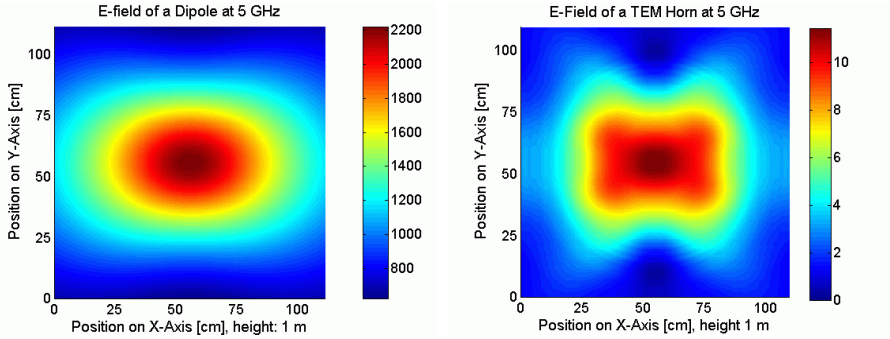

Figure 2.4: E-field for a dipole (left) and a TEM horn antenna (right).

For the selection of the operating frequency and the bandwidth different parameters have to be taken into account, namely, the required resolution, the necessary exploration depth and the expected size of the clutter in the soil medium. While the utilization of lower frequencies increases the penetration depth the spatial resolution can only be increased if higher frequencies are utilized, respectively, the range resolution can be improved if the bandwidth is increased. In general, however, the resolution of a GPR should be limited in advance in order to avoid the detection of small-sized elements which would only decrease the signal-to-noise ratio of the image and complicate the further detection and classification of target objects.

2.2.7 Illustration of GPR Data

The results of GPR can be illustrated in different ways which have been defined in [Dan04]. The normalized amplitude of the received GPR signal at a single antenna position which will be referred to as A-scan is illustrated in Fig. 2.5. An A-scan represents the response of the ground structure at the chosen antenna position.

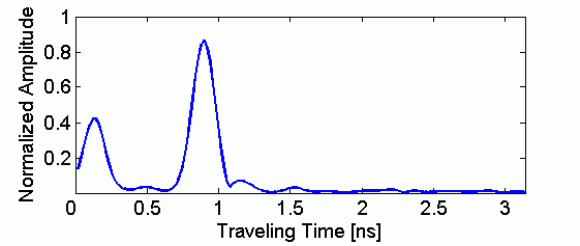

Figure 2.5: Amplitude response for an A-scan of a GPR survey.

A vertical cutting plane through the ground which aligns different A-scans on a linear axis is referred to as B-scan. The B-scan that is illustrated in Fig. 2.6(a) also includes the A-scan in Fig. 2.5 at the position of the white line. If the considered antenna positions are distributed on a 2D plane above the surface a 3D data volume can be created. Hence, it is possible to illustrate virtual B-scans of every cutting plane parallel to the surface of the soil which are also referred to as C-scan. Such a C-scan is illustrated in Fig. 2.6(b) for a depth of 8 cm. Again, the spatial position of the B-scan in Fig. 2.6(a) has been indicated by a white line in Fig. 2.6(b).

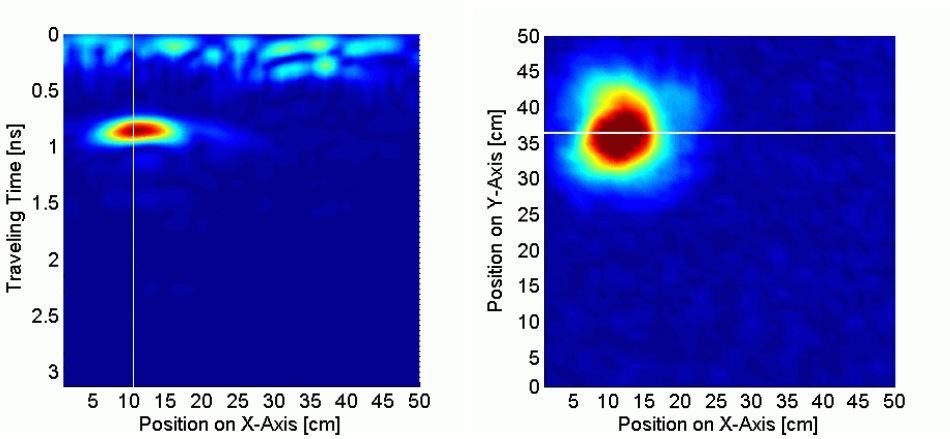

(a) B-scan of a GPR survey

(b) C-scan of a GPR survey

Figure 2.6: Amplitude response for a B-scan and a C-scan of a GPR survey.

Chapter 3

3D EM Field Simulation of GPR

3.1 Introduction

For GPR investigations it is essential to work with data acquired by real measurements. However, there is a strong need for a faster and easier way to investigate different antenna configurations and several different combinations of buried objects in the ground. In the following chapter a field simulation technique will be presented, that allows for the simulation of a complete GPR environment which includes the antenna system, the ground structure and the buried target object. The proposed method utilizes the commercial 3D EM field simulation package CST Microwave Studio (MWS) and introduces the possibility to remote control the antenna movement above the considered ground section. It will be discussed how to solve the problem of necessary changes to the model by means of an ActiveX server control, which allows to control the whole functionality of the simulation tool from an external Win32 application providing a possibility for the automation of the GPR simulation. The definition of electromagnetic soil parameter in the simulation of the GPR will be addressed and the implementation of physical soil properties such as the texture, the structure or the roughness of the surface will be discussed.
Moreover, the flexible integration of different antenna systems and the utilization of different target objects will be illustrated. In order to verify the quality of the GPR simulation results an alternative technique, namely a 1D transmission line simulation method will be introduced. The agreement between the results of both methods illustrates the success of the simulation approach as well as the accuracy of the proposed 3D EM field simulation of a complete GPR environment.

3.2 Definition of Material Properties

3.2.1 Lossless Materials

In CST Microwave Studio several different material properties are considered for a realistic modeling of practical simulation problems. The two preset materials which are available for the simulation are PEC and Vacuum. However, any kind of material can be created using the electromagnetic properties definition menu. Each material is identified by a unique name and can be visualized with individual color and transparency. For example a permittivity of $\epsilon_r = 3$ and a permeability of $\mu_r = 1$ are assigned to the material with the name *Ground*. The red-green-blue color code for the material has been defined and the transparency is set to 85%.

```
invoke(material,'Reset');
invoke(material,'Name','Ground');
invoke(material,'FrqType','hf');
invoke(material,'Type','Normal');
invoke(material,'Epsilon','3.0');
invoke(material,'Kappa','0.0');
invoke(material,'Mue','1.0');
invoke(material,'Color','0.6','0.35','0');
invoke(material,'Transparency','0.85');
invoke(material,'Create');
```

3.2.2 Conductive Materials

In general the materials are either defined as normal, in order to describe isotropic media or take into account the anisotropic behavior of the material. In the following additional material declarations are discussed that consider real ground properties which are inevitable in order to simulate a GPR environment. The introduction of material losses leads to complex values for relative permittivity of the material as it has been explained previously. This means that for the calculation of the material parameters a real and an imaginary part are considered, which both are in general frequency dependent. The losses are described by the dielectric loss angle or its corresponding tangent delta which is calculated using equation (3.1).

Equivalently, the magnetic loss angle and the corresponding magnetic tangent delta are defined by equation (3.2) following the previously given fundamental relations.

$$\varepsilon(\omega) = \varepsilon'(\omega) - j\varepsilon''(\omega) = \varepsilon'(\omega)\left[1 - j \cdot \tan\left(\delta_e(\omega)\right)\right] \tag{3.1}$$

$$\mu(\omega) = \mu'(\omega) - j\mu''(\omega) = \mu'(\omega)\left[1 - j \cdot \tan\left(\delta_m(\omega)\right)\right] \tag{3.2}$$

Consequently, the corresponding tangent delta is given as the negative ratio between imaginary and real part of the complex permittivity or permeability, respectively. Hence, it can be calculated using equations (3.3) and (3.4).

$$\tan(\delta_e) = \frac{\epsilon_r''(\omega)}{\epsilon_r'(\omega)} = -\frac{\Im\left(\epsilon_r(\omega)\right)}{\Re\left(\epsilon_r(\omega)\right)} \tag{3.3}$$

$$\tan(\delta_m) = \frac{\mu_r''(\omega)}{\mu_r'(\omega)} = -\frac{\Im\left(\mu_r(\omega)\right)}{\Re\left(\mu_r(\omega)\right)} \tag{3.4}$$

However, the effect of the magnetic permeability is neglected for the simulation of the ground material and a relative magnetic permeability value of 1 is assumed, which holds true for most sedimentary materials [MB01]. For all general purpose simulations every linear material behavior is described by using the equations (3.3) and (3.4). Nonetheless, CST Microwave Studio includes other versatile possibilities for the definition of lossy materials. One possible definition utilizes the well-known formulation of the conductivity model which denotes as follows.

$$\varepsilon(\omega) = \varepsilon - j\frac{\sigma}{\omega} \tag{3.5}$$

This model realizes a broadband constant conductivity. However, the corresponding tangent delta value of such a conductivity model is highly frequency dependent, as it is illustrated by the red curve in Fig. 3.1. As an alternative an internal dispersive first order Debye model can be fitted to the tangent delta input in order to realize an almost constant tangent value, respectively, to set up a specific tangent delta curve. The green curve in Fig. 3.1 demonstrates the tangent delta dispersive behavior of such a model. It can clearly be seen that this model is less frequency dependent than the tangent delta model for which a constant conductivity is assumed.

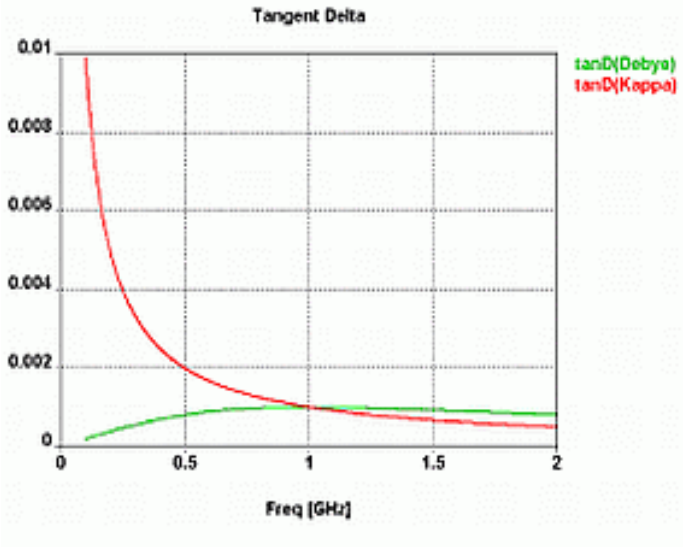

Figure 3.1: Different modeling of the tangent delta behavior [Var06a].

3.2.3 Lossy Metal Materials

In order to simulate the penetration of an electromagnetic field inside a very good but not perfect electrical conductor the lossy metal material type has been defined. This material type is represented by a surface impedance model which offers the possibility to take the skin effect into account without refining the mesh grid distribution for such surfaces. However, the model is physically reasonable only for a specific frequency range, defined by the dimensions of the model and its material properties, namely, the conductivity σ and the permeability μ. Such a material represents a very good conductor, that means a material with a high conductivity, respectively, a high tangent delta which denotes as follows.

$$\tan\left(\delta_e\left(\omega\right)\right) \gg 1 \tag{3.6}$$

Theoretically, this defines an upper limit for valid frequencies. On the other hand the frequency dependent skin depth of the fields δ in equation (3.7) has to be smaller than the thickness d of the corresponding metal solid.

$$\delta = \sqrt{\frac{2}{\omega\mu\kappa}} \tag{3.7}$$

Thus, a limit for the lowest applicable frequency can be defined using an optimized weight *factor* of e.g. approximately 0.2 that has been utilized in equation (3.8).

$$\omega \gg \frac{2}{\mu\kappa \left(factor \cdot d\right)^2} \tag{3.8}$$

Both constraints together theoretically define a valid frequency range which is more than sufficiently large enough for the proposed application. In general, however, the material has to be modeled applying a normal material type in connection with an electric conductivity in order to take lower frequencies into account. Consequently, for broadband simulations the operating frequency range should be split up in two or more intervals. In addition this kind of material can be applied as a boundary condition to suppress unwanted box resonances of the structure model.

3.2.4 Dispersive Materials

In order to consider a frequency dependent material behavior in broadband field simulations the most common models up to second order dispersion can be found in CST Microwave Studio. The available models take into account relaxation and resonance effects. In each case a macroscopic description of the permittivity in the frequency domain represents the underlying microscopic material behavior. The static parameter limit is indicated by the subscript s and the high frequency limit by the infinity symbol. The relaxation process, which is also called first order Debye model is characterized by the following formulation for the relative permittivity. Herein, the variable τ denotes the relaxation time of the process.

$$\varepsilon_r\left(\omega\right) = \varepsilon_\infty + \frac{\left(\varepsilon_s - \varepsilon_\infty\right)}{1 + j\omega\tau} \tag{3.9}$$

The resonance behavior of a material is described by the so-called Lorentz model, which considers the material-field interaction. In CST Microwave Studio the Lorentz model is realized by a second order Debye approach that takes into account the resonance frequency ω_0 and the damping factor δ and reads as follows.

$$\varepsilon_r\left(\omega\right) = \varepsilon_\infty + \frac{\left(\varepsilon_s - \varepsilon_\infty\right)\omega_0^2}{\omega_0^2 + j\omega\delta - \omega^2} \tag{3.10}$$

3.3 Modeling of Realistic Soil Structures

3.3.1 Texture and Structure of Soils

The texture is a geophysical parameter that refers to the relative proportion of sand, silt and clay in a sample of soil. Mineral particles with a diameter smaller than 0.002 mm are called clay. The diameter of silt particles ranges between 0.002 mm and 0.05 mm and sand particles are the largest, with a diameter between 0.05 mm and 2 mm. Particles larger than 2 mm are part of the course fragment of the soil and are neglected unless they exceed 15 percent of the volume [ECS07]. The percentage of each of the particle sizes is used to determine the soil texture class (Fig. 3.2).

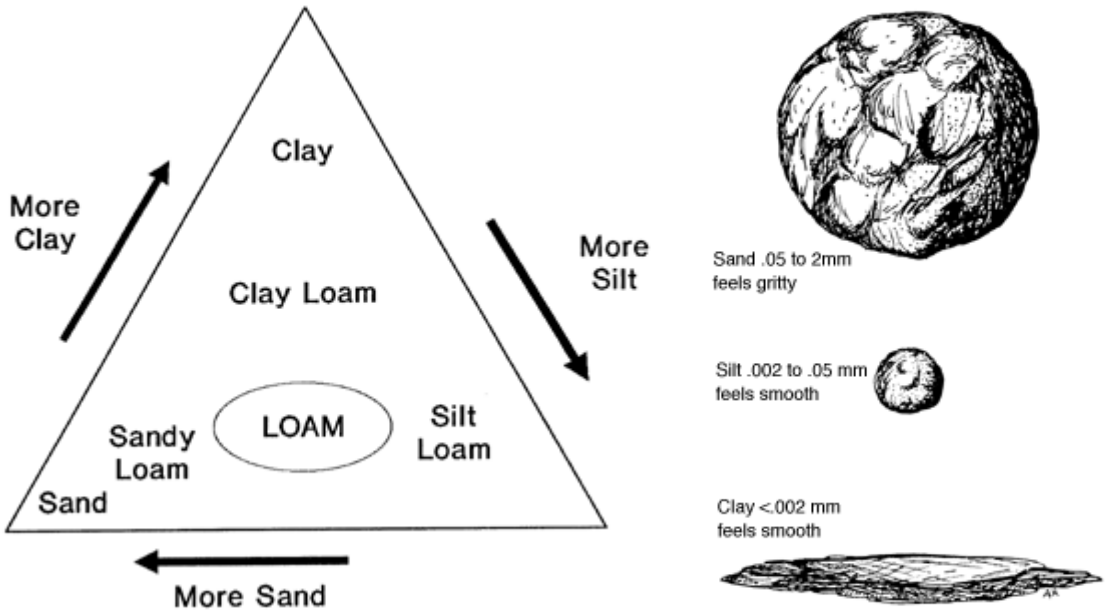

Figure 3.2: Texture class triangle and soil particles [ECS07].

The structure describes how the particles of the soil fit together when they form so-called peds. The shape of the peds determines the structure, that is influencing the drainage, stability, and aeration of the soil and can change over time. The shape of the peds varies strongly depending on the texture, composition and environment. Common soil structure forms are granular, platy, blocky or prismatic peds, which yield different geophysical properties [ECS07]. Thus, the texture and structure of a specific soil allow to predict the corresponding electromagnetic properties.

3.3.2 EM Properties of Soil Materials

Similar to a seismic response, which is a function of the acoustic properties, the response of a GPR is a function of the electromagnetic properties, namely, the dielectric permittivity, the magnetic permeability and the electric conductivity. The dielectric permittivity of the soil medium is directly affecting the velocity of propagation of an electromagnetic wave through the medium, respectively, the reflection and refraction at the interface of the medium. Changes in the dielectric permittivity and electrical conductivity of the soil medium also affect the attenuation of the radar signal. Fine sediments such as silts and clays have a high conductivity and cause high signal attenuation. Thus, the penetration depth is reduced so that GPR is limited to environments of low conductivity [Ulr82; DA89]. The relative magnetic permeability is assumed to be 1 in the context of this thesis which holds true as long as the GPR is not utilized on soil medium with a high iron content such as volcanic soils of Hawaii [IY$^+$07]. Therefore, the knowledge of the permittivity of the soil medium is essential for the definition of GPR surveys and the interpretation of GPR images. Moreover, the permittivity influences the imaging resolution of the GPR system. The measured dielectric constant values for various soils, rocks and minerals can be found in the literature [HU$^+$85; DA89; UB$^+$90; Dan04; Sch96; MB01; HvD$^+$03] and can be utilized for the realistic 3D EM modeling of a complete GPR scenario.
In order to verify the available results for dry sandy soil the permittivity of the soil material which is utilized for the laboratory GPR setup, see 7.2, has been determined by a precise broadband transmission/reflection measurement according to [JMO03; AJO07]. If the permittivity of this soil can be determined precisely it will be possible to compare the results of the 3D EM GPR simulation with the results that are obtained by real laboratory GPR measurements. Therefore, a waveguide has been filled with a sample of the soil material and the scattering parameters have been measured. Using the well-known iteratively inversion technique which has been described in [NR68] it is possible to calculate the complex permittivity from the measured scattering parameter by iterative inversion. Figs. 3.3(a) and 3.3(b) illustrate the results of the real part of the permittivity and the loss tangent. Although the results vary slightly over the frequency range the true value of the complex permittivity can be assumed to be almost constant over the frequency range and can be found by a mean averaging. The resulting permittivity of $\epsilon_r \approx 2.5$ and the loss tangent of 0.01 entirely agree with the results from the literature [Dan04].

The electromagnetic properties of a real soil can be employed for the field simulation of a GPR environment using the MWS constant tangent delta fit model which is based on the previously discussed 1st order Debye model. Herein, the obtained values of both, the relative permittivity and the loss tangent must be assigned to chosen frequency point. Three characteristic frequencies at the start, the center and the end of the operating frequency band, namely, 1 GHz, 5.5 GHz and 10 GHz have been chosen in order to compare the accuracy of the allocation. The comparison of the modeling results and the true values in Figs. 3.4(a) and 3.4(b) reveals the best agreement for the case of an assignment to the center frequency. The deviation from the true value is a systematic characteristic of the 1st order Debye model.

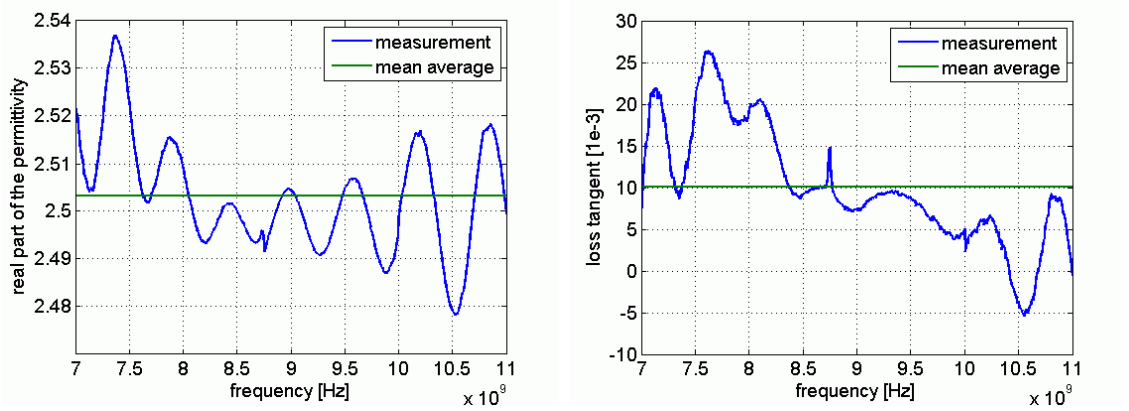

(a) real part of the permittivity (b) corresponding loss tangent

Figure 3.3: Complex permittivity of sandy soil with 0% moisture content.

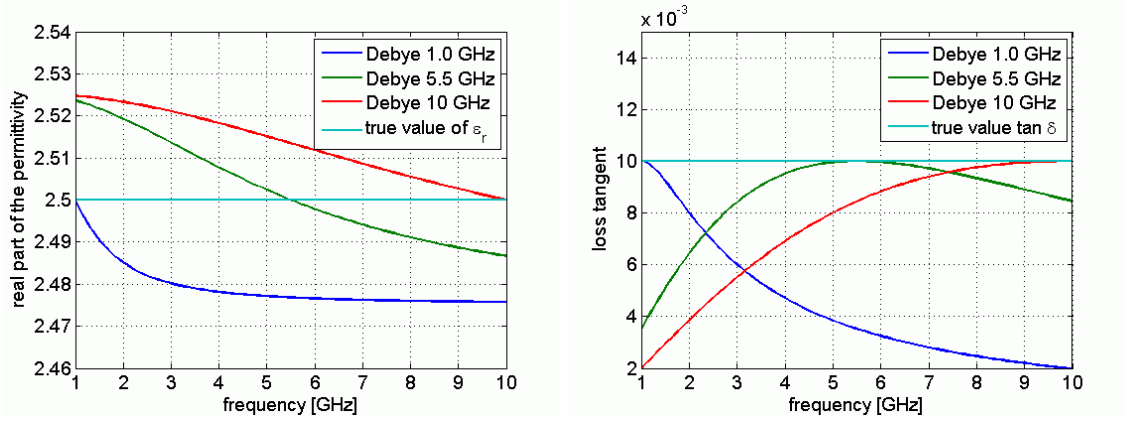

(a) real part of the permittivity (b) corresponding loss tangent

Figure 3.4: 1st order Debye realization of the complex permittivity in MWS.

The proposed 3D EM field simulation of a GPR environment can easily be extended in order to include additional types of soil. However, in the context of this thesis only a limited number of different soil properties could be taken into account. As an example the complex permittivity values of a humid soil with typical dispersive behavior which can be found from [Cur98] have been integrated in the GPR simulation. Figs. 3.5(a) and 3.5(b) illustrate the frequency dependent complex permittivity for this type of soil with a relative moisture content of 21%, respectively, 50%.

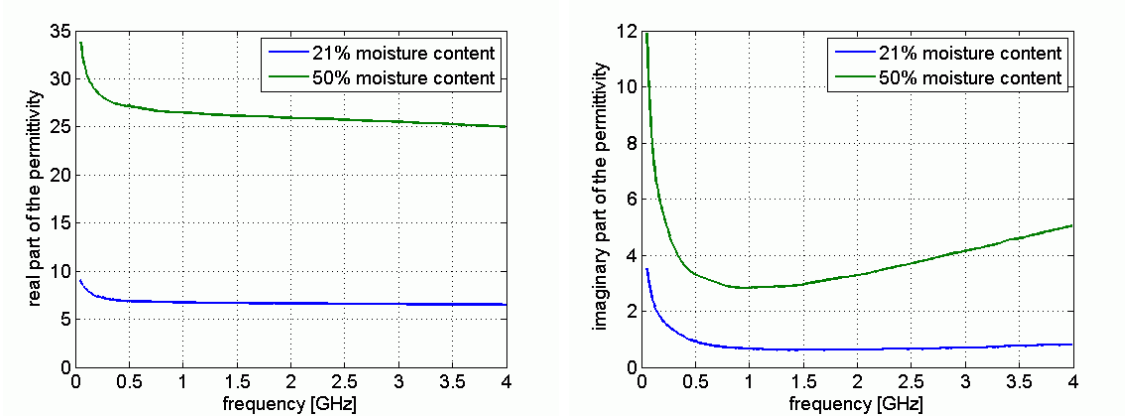

(a) real part of the permittivity

(b) imaginary part of the permittivity

Figure 3.5: Complex permittivity of sandy soil with different moisture content.

In general, however, the dielectric properties of soils and sediments reflect a complex mixture of materials which varies throughout the soil. In rocks and sediments, the dielectric permittivity is primarily a function of mineralogy, porosity, water saturation and frequency. Moreover, it can depend on the geometry of the components and electrochemical interactions [KE90; Kno96]. Variations in each of these parameters can change the effective dielectric constant of the material significantly. Therefore, a forward-modeling technique, namely, the dielectric mixing modeling has been proposed in order to provide a basis for the prediction of the expected dielectric permittivity based on specific input parameters. Numerous dielectric constant mixing models have been proposed in the literature. Most of them fall within four broad categories, namely, effective medium, empirical, phenomenological and volumetric models which are characterized in literature, see [MB01]. The application of dielectric-constant models can be useful for the preparation of a GPR survey in order to predict whether or not a soil mixture will generate measurable reflections and also for the inverse modeling of soil properties from GPR measurements.

3.3.3 Modeling of Surface Roughness

The problem of rough surface scattering has been studied extensively and various formulations of an adequate inverse scattering model can be found in the literature. These analytical approaches take into account a wide range of incident and scattering angles and have shown good results for specified ranges of surface statistics. In [YJL98a; YJL98b] the transmission coefficient is analyzed for a vacuum-dielectric interface. The effect of the surface can be neglected as long as the statistically homogeneous roughness can be assumed to be small in comparison to the utilized wavelength, which, however, holds only true for low frequency GPR systems.
Statistical approaches which can be found in [TR+98; FCK00; KWR02] address the uncertainty of the rough surface modeling and the ambiguity of the underlying inverse scattering problem, whereas in [GHM04] the so-called Gaussian beam summation method will be utilized for the rough surface scattering in order to overcome difficulties which have been encountered using plane-wave approaches. In [KJ02] the scattered radar images of a deterministic Gaussian distributed rough surface have been investigated and existing numerical and analytical models for the description of the rough surface scattering are compared. In [Cas01; Joh02; JB04] different coherent and incoherent scattering effects are demonstrated that can be obtained for rough surface scattering problems. The utilized models match coherent cross sections for normal incidence observation, although the accuracy degrades if multiple scattering effects become more important. Moreover, the modeling of rough surfaces depends on the frequency, the polarization and the antenna pattern. In conclusion, none of the proposed models explains all possible scattering mechanisms and every approximation is limited to a particular combination of the surface structure and the soil parameters due to the highly complex nature of the surface scattering.
Nonetheless, the analytical and numerical results which have been discussed generally indicate that the scattering at rough surfaces can effect the results of a GPR measurement. Therefore, the 3D EM field simulation of a complete GPR environment should also take into account a model of a rough surface. However, it showed that the modeling of a fully Gaussian distributed rough surface increases the computational efforts significantly, because the required mesh grid tends to be very small. Therefore, geometrical approximations, namely, two different versions of a periodic structure of surface waves have been chosen to represent the effects of rough surfaces in the proposed 3D EM field simulation of a complete GPR environment.

The two resulting geometrical models which have been illustrated in Fig. 3.6 utilize sinus-like shaped surfaces. The distance from one surface wave peak to the next one has been chosen to be 3 cm for surface model 1, respectively, 6 cm for surface model 2 with a corresponding wave amplitude of 1.5 cm, respectively, 3 cm. Because the height of the surface is varied only along one axis it is still possible to use a plane of symmetry along this axis. Therefore, the volume of the simulation problem and, thus, the processing time can be reduced significantly. Moreover, it will become much easier to reproduce the suggested surface roughness in the context of real experimental measurements, see 7.2. Fig. 3.7 reveals that the corresponding mesh grid distribution for excitation frequencies up to 18 GHz is still reasonable.

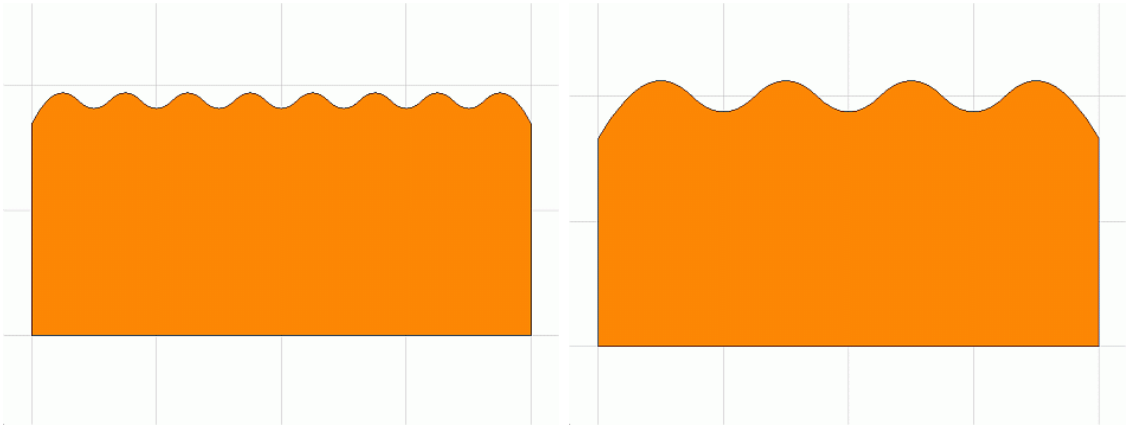

(a) rough surface model 1 (b) rough surface model 2

Figure 3.6: A sinus-like shaped surface for the simulation of rough surfaces.

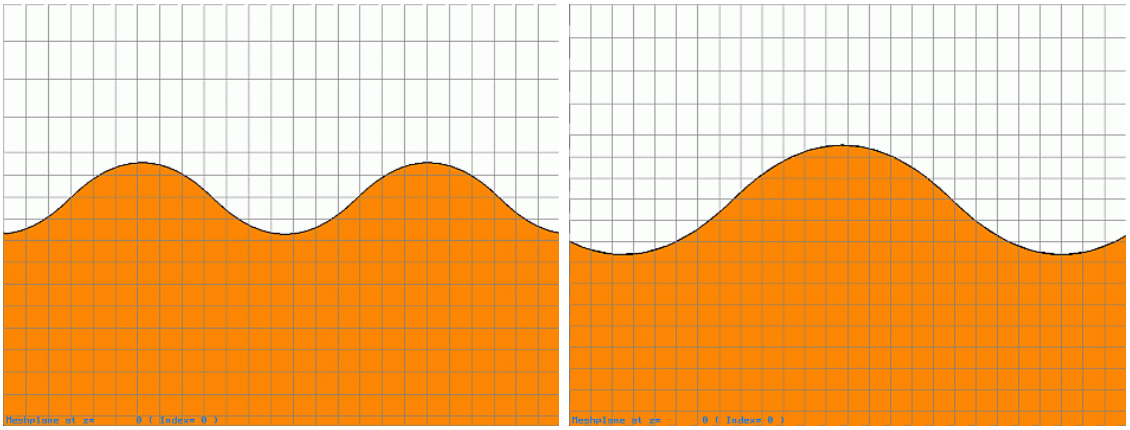

(a) rough surface model 1 (b) rough surface model 2

Figure 3.7: Detailed illustration of the corresponding mesh grid distribution.

3.4 Modeling of Realistic Target Objects

3.4.1 Modeling of Artificial Test Objects

The aim of a GPR system is to detect target objects which have been buried in the ground. In order to simulate a complete GPR the electromagnetic models of such target objects have to be designed and utilized. It has already been stated, that for many typical AP landmines the major signal reflection is created by the layer of air inside of the structure. A first approximation of the chosen target object can be achieved if the electromagnetic properties of air, namely, a permittivity of $\epsilon_r = 1$ and a permeability of $\mu_r = 1$, are assigned to a corresponding geometrical shape. Fig. 3.8 illustrates two examples of such target objects with simple geometry.

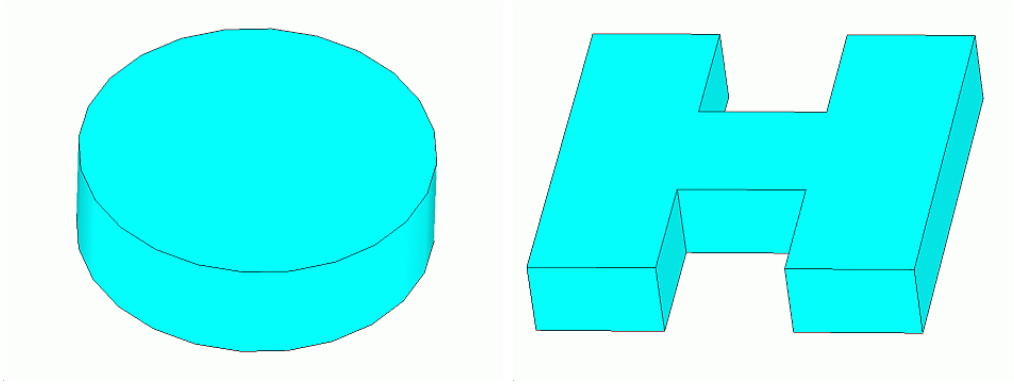

(a) cylindrical object (b) H-shaped object

Figure 3.8: MWS model of target objects with simple geometry.

Fig. 3.8(a) illustrates a cylinder with a diameter of 10 cm and a height of 3 cm. This object has been utilized as a simple model of typical AP mines for many different GPR simulations. The complexity of the geometrical shape can be extended, as it is illustrated in Fig. 3.8(b). The H-shape of this target object has been chosen because a foam material object of the same dimensions has been utilized for different experimental GPR measurements. The total dimensions of the object are 15 cm by 15 cm with an edge length of 5 cm for all subsections. In addition to the air-filled case it is possible to assign different values for the permittivity to the homogeneous target objects in order to investigate the effects of a decreased contrast between the buried object and the surrounding soil for which a permittivity of 2.5 and 3 has been assumed. Thus, different GPR scenarios can be compared, see chapter 4.

3.4.2 Modeling of Typical AP Landmines

In addition, very complex models of real AP landmines have also been taken into account. As an example the detailed model of a PMN mine, see B, with a diameter of 12 cm is illustrated in Fig. 3.9(a). Fig. 3.9(b) illustrates the air-filling inside of the plastic case, whereas Fig. 3.9(c) shows the striking pin which is also made from plastic material. For the GPR simulation the corresponding CAD model is imported and placed inside of the soil. However, it turned out that the utilization of such complex models increases the computational demand significantly, because the corresponding mesh grid must be finer (Fig. 3.9(d)) in comparison to the case of simple geometries. Moreover, it showed that for the fundamental investigation of antenna prototypes in the context of GPR very small object details are not affecting the resulting image. Therefore, mainly simple geometries have been utilized.

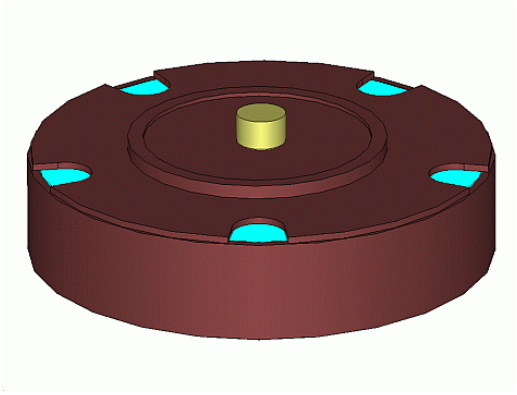

(a) PMN model

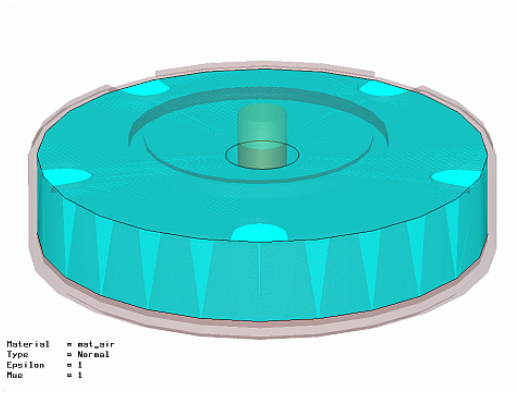

(b) air filling

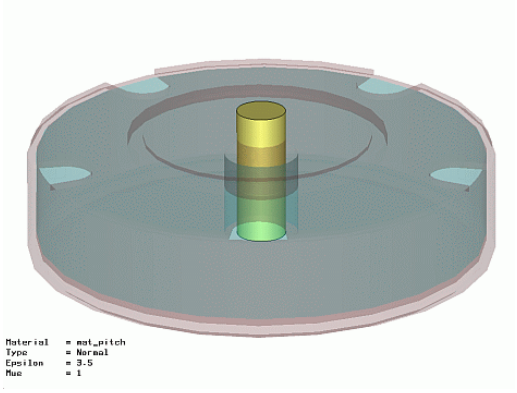

(c) striking pin

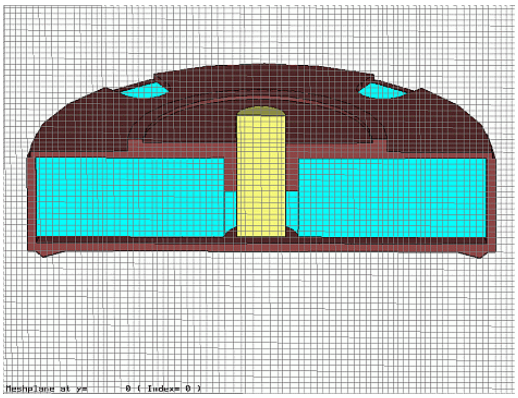

(d) cross section

Figure 3.9: MWS model of a complex PMN Anti-personnel landmine.

3.5 Integration of Different Antennas

So far it has been discussed how a specific soil structure can be created and how the chosen target object is modeled and integrated in this soil structure. However, the most important part of a GPR, namely, the transceiving antenna, has not been considered yet in the context of 3D EM field simulation of a GPR. One of the important reasons for the simulation of a complete GPR environment is the strong need for a possibility to identify antenna designs which yield promising results in the context of GPR prior to the fabrication of a prototype or any experimental measurements. Fig. 3.10 illustrates all antennas that have been investigated in the context of this thesis, namely, standard gain horn antennas, a log-periodic dipole antenna, the Orion-type impulse radiating antenna, the modified Bujanov loop antenna, a modified double-ridged TEM horn antenna and a scaled version of this antenna. The antennas have been modeled and analyzed in CST Microwave Studio, see 4, before they are integrated in the proposed field simulation of a GPR.
The 3D modeling of the antennas is done using the remote control technique, see 3.6, which utilizes a script language in order to access the underlying commands of the field simulation package. Once, the final design has been achieved and the antenna characteristics satisfy the demands for a GPR antenna system, the structure is exported using the SAT-file format which basically describes the geometry of the object. Thus, the number of lines in the corresponding source code can be reduced dramatically. The SAT-file already contains the names and the colors of the different material layers of the antenna. However, the electromagnetic material properties have to be reassigned to the antenna, once it has been imported successfully.
The antenna is always imported at the origin of the modeling space. Thus, it has to be shifted to the chosen position on the x- and the y-axis, respectively, to the correct height above the soil in order to create the final GPR configuration. Although all antennas are ultra-wideband they utilize different bands of operation which has to be taken into account for the GPR configuration. Moreover, an individual waveguide port or a concentrated current element has to be created in order to feed the antenna properly. These parameters and other additional properties are set automatically by a controlling script once the user has chosen the configuration for the GPR simulation, which can be realized by a graphical user interface. Moreover, it is possible to include additional antennas for future investigations. The results of the antenna simulation in the context of a GPR can be found in chapter 4.

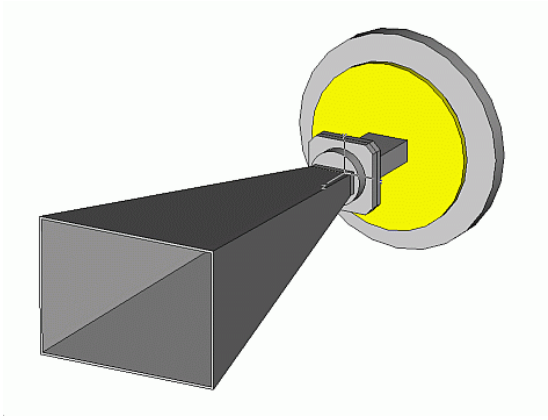

(a) standard gain horn antenna

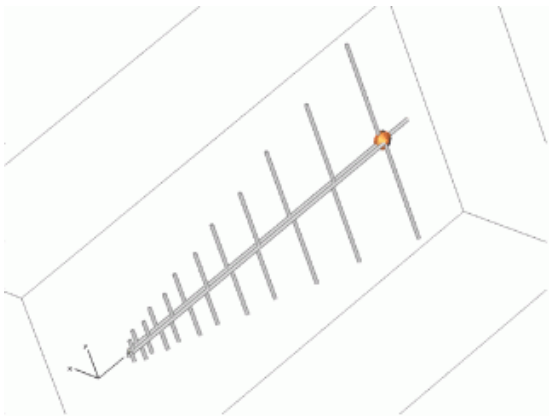

(b) log-periodic dipole antenna

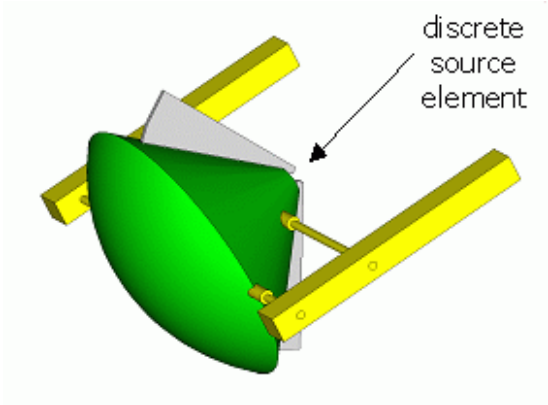

(c) Orion-type IRA

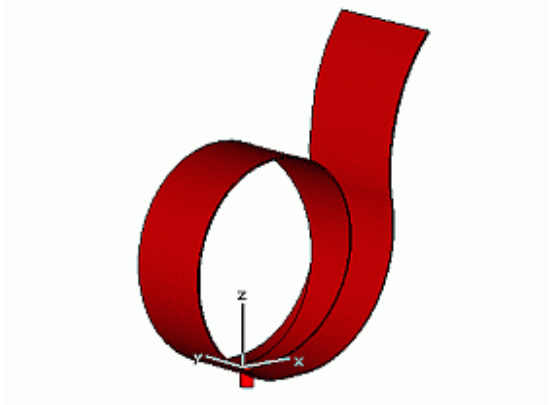

(d) modified Bujanov antenna

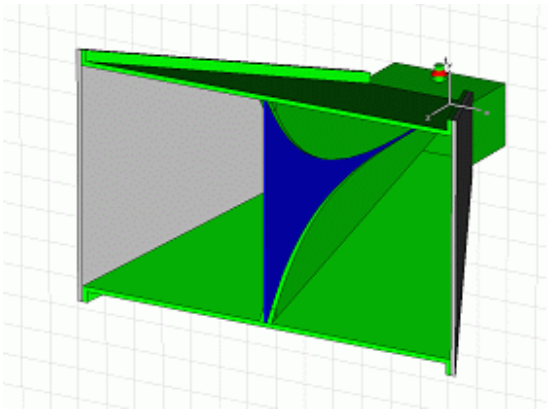

(e) double-ridged TEM horn antenna

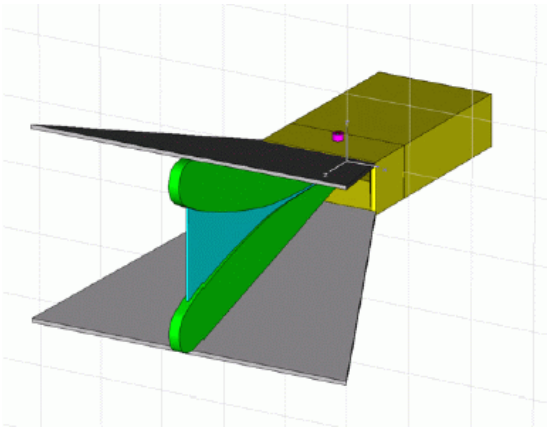

(f) small double-ridged TEM horn

Figure 3.10: 3D EM field simulation models of different antennas.

3.6 Remote Control Technique

The simulation of a GPR environment presented in this thesis uses a technique to controll the 3D EM simulation package CST Microwave Studio by an integrated Visual Basic for Applications (VBA) script which has been suggested in [MJO02]. Hence, it is possible to access all the underlying VBA commands of the program suite from any Win32 application, which allows for remote controlling the corresponding ActiveX elements of the simulation package. After these ActiveX elements have been included, respectively initialized, all underlying functions can be accessed by remote control from another independent Win32 application, e.g. MathWorks Matlab. The embedding of the ActiveX elements can be achieved as illustrated. As an example the ActiveX elements *Application*, *Brick* and *Units* will be embedded.

```
app=actxserver('MWStudio.Application');
brick=actxserver('MWStudio.Brick');
units=actxserver('MWStudio.Units');
```

The label for the ActiveX elements has been chosen to identify the underlying MWS commands. After the Application command has been initialized the blank surface of CST Microwave Studio will start automatically. Every parameter that should be available within the simulation environment can be assigned directly as a part of the corresponding command for the construction of an element using the Matlab command `num2str(x)`. As a result the parameter are assigned directly to the corresponding dimension or value setting option without using the ability to parameterize the simulation. However it might be necessary to assign a certain set of parameter to the parameter list of CST Microwave Studio. This can be done using a command which is included in the ActiveX element *Application*.

```
invoke(app,'StoreDoubleParameter','x_obj',x_object);
invoke(app,'StoreDoubleParameter','y_obj',y_object);
```

As it has been demonstrated before, the Matlab command `invoke` will be used to access the underlying functions of the embedded ActiveX elements. In the command line which is illustrated above the function `StoreDoubleParameter` of the ActiveX element *Application*, that has been labeled `app` declares the variable `x_object` as

`x_obj` in the parameter list of CST Microwave Studio. In the same manner the Matlab variable `y_object` will be declared as `y_obj`. In order to define the dimensions for the units of the distance, the time and the frequency, respectively, the following commands have to be processed. As a general convention the dimensions mm, ns and GHz will be utilized for the simulation in CST Microwave Studio as follows.

```
invoke(units,'Geometry','mm');
invoke(units,'Time','ns');
invoke(units,'Frequency','GHz');
```

The definition of geometrical structure, material parameter, background material, boundary conditions, excitation source, mesh grid configuration and solver parameter can be achieved by groups of invoke commands, that are accessing the different MWS class libraries. Each construction step and every parameter definition results in a history list entry, which can easily be accessed. Hence it is possible to obtain the correct structure and content of all commands that are needed to fulfill the simulation task. These history list items have to be transformed to fulfill all the formal requirements of the Matlab script language. For a certain MWS history list item, e.g. the *Brick* command, the Matlab source code denotes as follows.

```
invoke(brick,'Reset');
invoke(brick,'Name','brick1');
invoke(brick,'Component','Comp1');
invoke(brick,'Material','PEC');
invoke(brick,'Xrange','-30','30');
invoke(brick,'Yrange','-20','20');
invoke(brick,'Zrange','-10','5');
invoke(brick,'Create');
```

Fig. 3.11 illustrates the appearance of such an history list item including the name, the material, the corresponding component and the dimensions on the x, y and z-axis of the corresponding brick object. The illustrated history list item parameter have to be translated in Matlab source code in order to fit the standardized invoke command form, which allows to remote control the simulation environment.

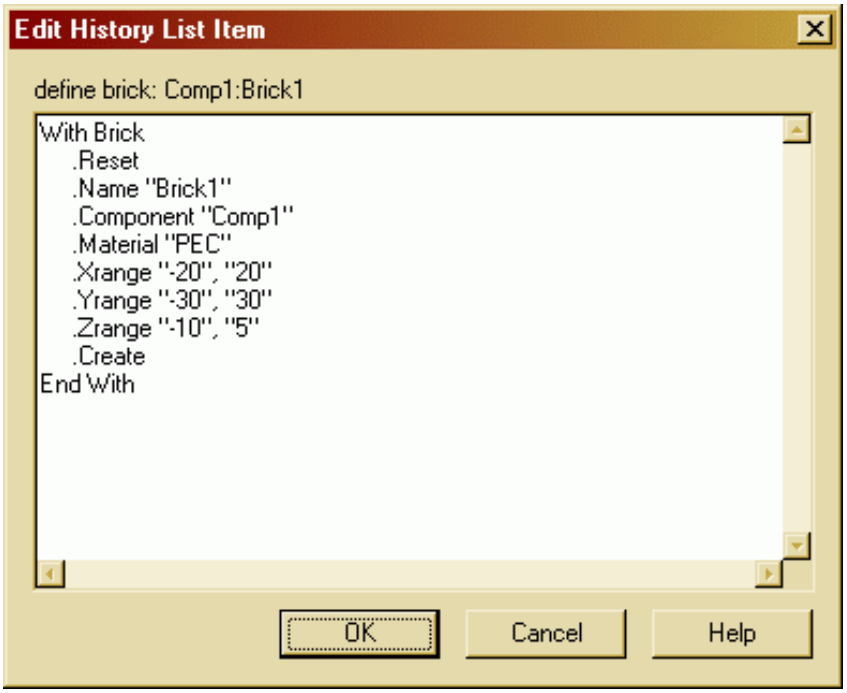

Figure 3.11: Example of a history list item in Microwave Studio.

It is important to note, that none of the previous commands in the *Brick* object example will be processed before the `Create` command in the last line is executed. Then the complete block of commands will be processed and transmitted to the ActiveX client application, namely, the solver of CST Microwave Studio. In a similar way all commands that define the parameter of the MWS simulation environment, e.g. for the mesh generation, the boundary setting, the symmetry options and for the solver, are included in the corresponding Matlab script. To simulate a complete B-Scan or C-Scan data acquisition it is necessary to perform a simulation run for every single antenna position, that is supposed to be taken into account. Hence, it is necessary to rearrange the model for every single simulation run. This repositioning of the antenna above the ground and the data acquisition of the simulation results of a certain antenna position are also controlled by the underlying Matlab script. The repositioning of the antenna results in a program loop, which shifts the parameters for the corresponding position on the x and y-axis and, thus, allows to move the antenna above the soil. After the simulation is solved the resulting signal files are saved using a specified file name. As the next step the field simulation software is reset and started again considering the next grid position of the antenna.

The remote control technique also allows for a controlled feedback of results for automatic model optimization. Moreover, it is possible to solve the GPR simulation problem on different computers at the same time. In order to delete all results and terminate the application the following commands have to be executed.

```
invoke(app,'ResetAll');
invoke(app,'Quit');
```

After the simulation has been completed and the application window has been closed all ActiveX elements that have been embedded must be released completely in order to ensure, that the ActiveX connection can be reestablished for further tasks. As an example the ActiveX elements *Application*, *Brick* and *Units* will be released if the following Matlab source code lines are processed as follows.

```
release(app);
release(brick);
release(units);
```

If the underlying solver application is shut down and opened again several times in a row, which was inevitable once the GPR system has been simulated for a certain antenna position it showed, that the ActiveX connection might fail unexpectedly. Therefore, the proposed concept of remote controlling the client application has been modified by the author in such a way, that the ActiveX connection between Matlab and the MWS solver is opened only once. In between the different simulation runs the solver application remains active and only the parameter are redefined. Thus, the reliability of the remote control has been increased significantly. Moreover, the degree of integration for different parts of the GPR simulation model has to be defined. Previously, the design of a complex structure has been realized by a stepwise processing of all underlying commands which are necessary for the construction of the considered model. However, it is possible to import complete components of the GPR system, namely, the soil brick, the target object and the antenna. This can be done fast and convenient if the proposed file import is combined with a graphical user interface. Thus, even unexperienced users are able to create a GPR scenario which is supposed to be investigated by means of 3D EM field simulation.

3.7 Verification of the GPR Simulation

3.7.1 1D Transmission Line Modeling

For the verification of the field simulation a novel forward radiating Impulse Radiating Antenna, the so called Orion-type IRA, which will be presented in detail in 4.3 has been utilized. The antenna gives superior results concerning the detection of buried objects when it is used together with the calibration technique which is also discussed in 4.3. It is essentially a standard one-port calibration adapted for subsurface detection applications. This GPR setup that includes the antenna structure, the homogeneous soil and the buried object has been simulated using the proposed 3D field simulation of a GPR environment. The investigation has shown that the dimensions of a buried object in the direction normal to the air-soil interface can deviate significantly from its actual size. Such an example is shown in Fig. 3.12(a). The presented B-scan reveals, that the height of the cylinder with a permittivity of $\epsilon_r = 3.5$ which has been buried in a depth of 7 cm is overestimated considering the white rectangle that indicates the actual height of the object. However, it can be estimated correctly for another height as it is shown in Fig. 3.12(b).

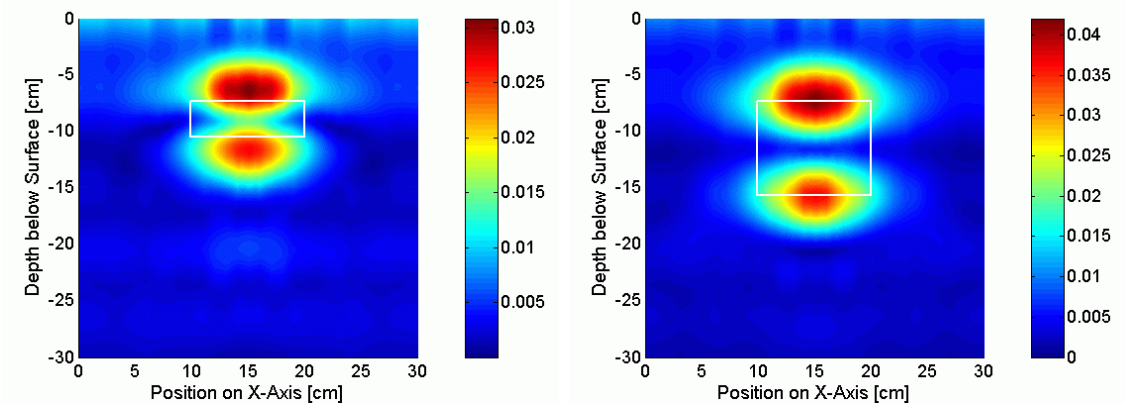

(a) object height 3 cm, $\epsilon_r = 3.5$ (b) object height 8 cm, $\epsilon_r = 3.5$

Figure 3.12: Results of the 3D field simulation for an object with $\epsilon_r = 3.5$.

Therefore, an alternative simulation technique, namely, an analytical 1D transmission line model (TLM), see also [Tra96], will be utilized in order to compare the results of this method with the results of the 3D field simulation. The aim of this investigation is to find out whether the incorrect object can be confirmed using the

proposed two layer TLM. This method allows to calculate the resulting reflection signal that occurs if a homogeneous subsurface object layer with a permittivity of ϵ_{robj} and a length of l_{obj} will be placed in between two homogeneous layers of soil with a permittivity of ϵ_{rsoil}, the transmission line model in Fig. 3.13 has to be analyzed. The object layer is assumed to be terminated by Z_1 at the right-hand side, which represents an unlimited extended soil below the object layer.

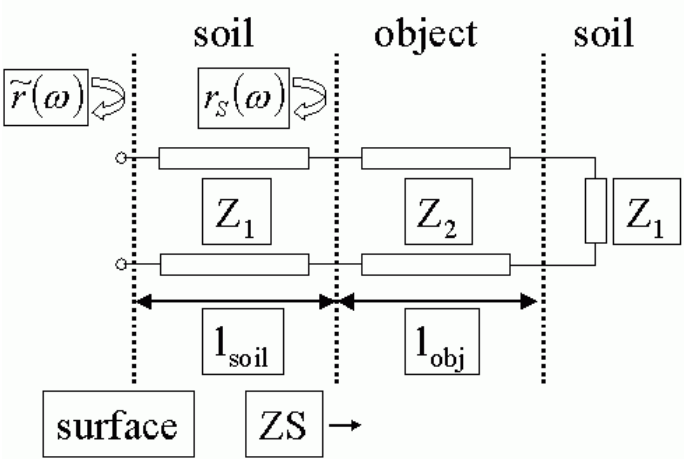

Figure 3.13: Transmission line with object layer inside of a homogeneous soil.

To analyze the above configuration of stacked layers the characteristic impedances of the soil layer and the object layer which are Z_1 and Z_2, respectively, have to be calculated using the following well-known equations (3.11) and (3.12).

$$Z_1 = \frac{Z_0}{\sqrt{\epsilon_{rsoil}}} \tag{3.11}$$

$$Z_2 = \frac{Z_0}{\sqrt{\epsilon_{robj}}} \tag{3.12}$$

According to the TLM theory, the input impedance Z_S that is observed when looking into the object layer from it left-hand side can be calculated by equation (3.13).

$$\frac{Z_S}{Z_2} = \frac{Z_1/Z_2 + j \cdot \tan(\beta_{obj} l_{obj})}{1 + j \cdot Z_1/Z_2 \cdot \tan(\beta_{obj} l_{obj})} \tag{3.13}$$

The reflection directly at the air-soil interface inside of the soil $r(\omega)$ is calculated by equation (3.14). So far it takes into account the interface between object and soil.

$$r(\omega) = r_s(\omega) \cdot e^{-2j\beta_{soil} l_{soil}} = \frac{Z_S - Z_1}{Z_S + Z_1} e^{-2j\beta_{soil} l_{soil}} \tag{3.14}$$

However, the reference plane is still inside of the top soil layer. In order to take the interface effects between the top soil layer and the air layer into account which are described by reflection and transmission coefficient, the reference plane needs to be shifted to the air side of the interface. Hence, the reflection at the surface of the stacked layer at the air side of the interface $\tilde{r}(\omega)$ can be calculated as follows.

$$\tilde{r}(\omega) = \left(\frac{Z_1 - Z_0}{Z_1 + Z_0}\right) + \frac{4 \cdot \left(\frac{Z_1 \cdot Z_0}{Z_1 + Z_0}\right) \cdot r(\omega)}{1 + \left(\frac{Z_1 - Z_0}{Z_1 + Z_0}\right) \cdot r(\omega)} \tag{3.15}$$

In order to compare the results of the transmission line method and the 3D field simulation the same excitation signal is used in both models, namely, a Gaussian amplitude modulation of a carrier exactly at the center frequency of the considered band. The spectrum of the received signal is transformed to the time domain by inverse Fourier Transformation. Finally the carrier is removed by demodulation and the time differences which yield corresponding traveling times can be extracted.

3.7.2 Planar PEC and Dielectric Layers

For the first investigation a PEC reflector layer has been placed in depth d_l below the surface of a homogeneous soil with a permittivity of $\epsilon_r = 3$. The depth d_l below the surface has been varied from between 0 cm up to 80 cm. The traveling time between the surface and the PEC layer can be calculated analytically using equation (2.48). Moreover, for both simulation techniques the time difference can be obtained as the time between the maximum of the reflection at the air-soil interface to the maximum of the reflection at the PEC layer. The estimated time differences are denoted by Δt_{MWS} and Δt_{TLM}, respectively, see Table 3.1. It shows, that the TLM calculation yields exactly the theoretical values of the traveling time according to equation (2.48), whereas it appears slightly overestimated if the results of the 3D field simulation are taken into account as it is illustrated in Fig. 3.14(a).

In order to study how the permittivity of a dielectric layer will effect the differences between both methods another configuration has been investigated. Therefore, a dielectric layer with a height of 8 cm which has been placed in a depth of 7 cm inside of a homogeneous soil with a permittivity of $\epsilon_r = 3$. This configuration equals the case that has been illustrated in Fig. 3.12(b). The layer dimensions have been chosen large enough to justify the assumption of an infinite extension as it is the case for the 1D TLM method. For such a configuration the traveling time from the upper interface between soil and object to the lower interface between object and soil can be calculated again according to equation (2.48), see Table 3.2. The permittivity of the dielectric layer has been varied and it shows that the time difference which has been estimated from the TLM method equals the theoretical calculated values. The resulting time difference which has been obtained equivalently from the 3D field simulation, however, differs significantly from the expected one if the permittivity of the dielectric layer is increased as it has been illustrated in Fig. 3.14(b).
In order to investigate how the volume refinement factor which controls the mesh grid density in the dielectric material effects the accuracy of the 3D field simulation additional configurations with an increased volume refinement have been simulated. Considering the additional results for a permittivity of 10 and 40 in Fig. 3.14(b) with respect to the TLM results it can be revealed, that the accuracy of the 3D EM field simulation using CST Microwave Studio can be increased significantly if the volume refinement factor is chosen sufficiently large enough, see Table 3.3.

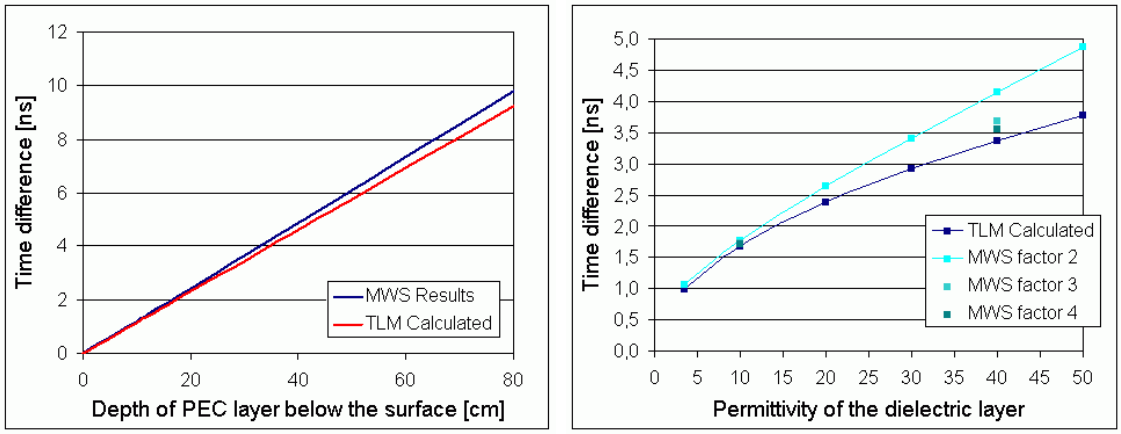

(a) PEC layers (b) dielectric layers

Figure 3.14: Traveling time according to 3D field simulation and TLM.

3.7.3 Estimation of the Object Height

It has already been shown, that the results of the TLM method and the 3D field simulation agree if the simulation parameter are chosen carefully. However, the 3D field simulation of the cylindrical object with a height of 3 cm and a permittivity of $\epsilon_r = 3.5$ which has been placed 7 cm below the surface of the soil with a permittivity of $\epsilon_r = 3$ yields an unexpected height overestimation. The equivalent TLM simulation which equals the A-scan directly above the center of the buried object is shown in Fig. 3.15(a). Herein, the blue curve illustrates the exciting pulse, whereas the green curve represents the reflected signal. The black lines mark the expected reflection centers in the TLM results considering the relations in equation (2.48). Fig. 3.15(a) shows, that the TLM simulation yields also an overestimation of the height of the buried object. Thus, the excellent agreement between the results of the TLM simulation and those using the 3D field simulation which has been achieved confirms the proposed concept of GPR investigation by means of numerical simulation. The overestimation of the height in Fig. 3.12(a) can be revealed again in Fig. 3.15(a). The effect can be explained by destructive and constructive interference of the reflected signal due to discontinuities at the top and the bottom of the buried object. Such phenomena are observed when the height of the buried object is in the range of the distance that an electromagnetic wave travels within the duration of the exciting pulse. For electrically large objects both reflections are well-separated and the size of the object can be determined correctly (Figs. 3.12(b) and 3.15(b)).

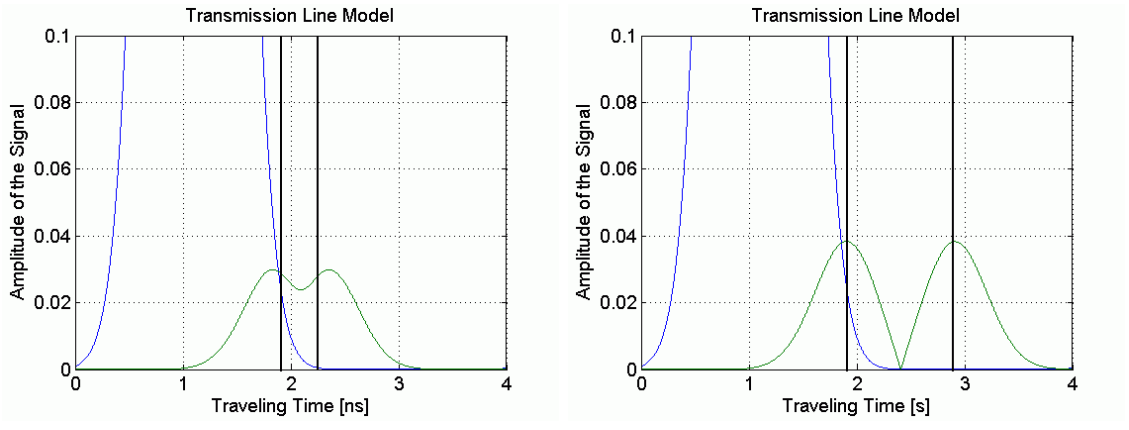

(a) object height 3 cm, $\epsilon_r = 3.5$ (b) object height 8 cm, $\epsilon_r = 3.5$

Figure 3.15: Results of the equivalent TLM method for an object with $\epsilon_r = 3.5$.

Moreover, the same cylindrical objects with a height of 3 cm and 8 cm but with a permittivity of $\epsilon_r = 1$ have been placed in a depth of 7 cm below the surface of the soil with a permittivity of $\epsilon_r = 3$. Again, the 3D field simulation yields unexpected results. Fig. 3.16 illustrates, that instead of two expected reflections, namely, at the top and the bottom interface between the soil and the air filled object which have been indicated by the white rectangle according to equation (2.48), only one large reflection can be obtained. However, this results are completely verified by the results of the TLM method which are shown in Fig. 3.17 and the comparison between both techniques also reveals a very good agreement of the amplitude.

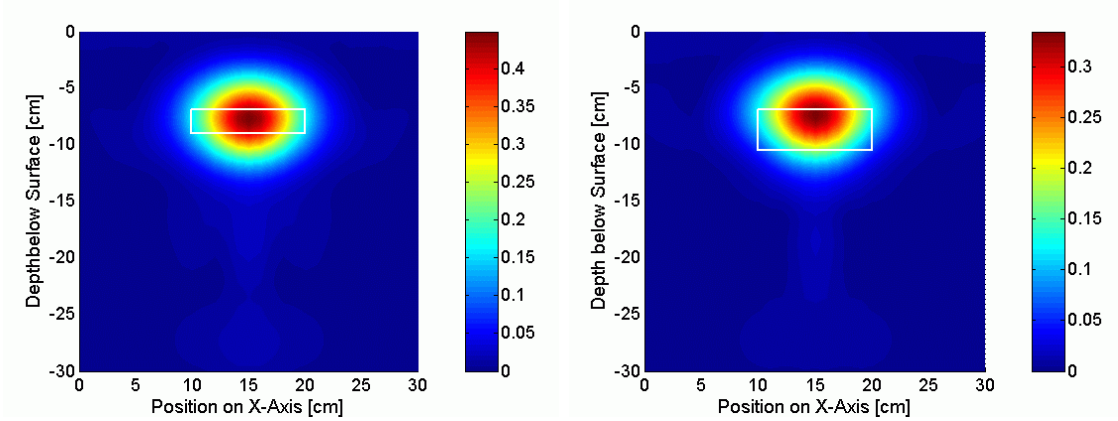

(a) object height 3 cm, $\epsilon_r = 1$ (b) object height 8 cm, $\epsilon_r = 1$

Figure 3.16: Results of the 3D field simulation for an object with $\epsilon_r = 1$.

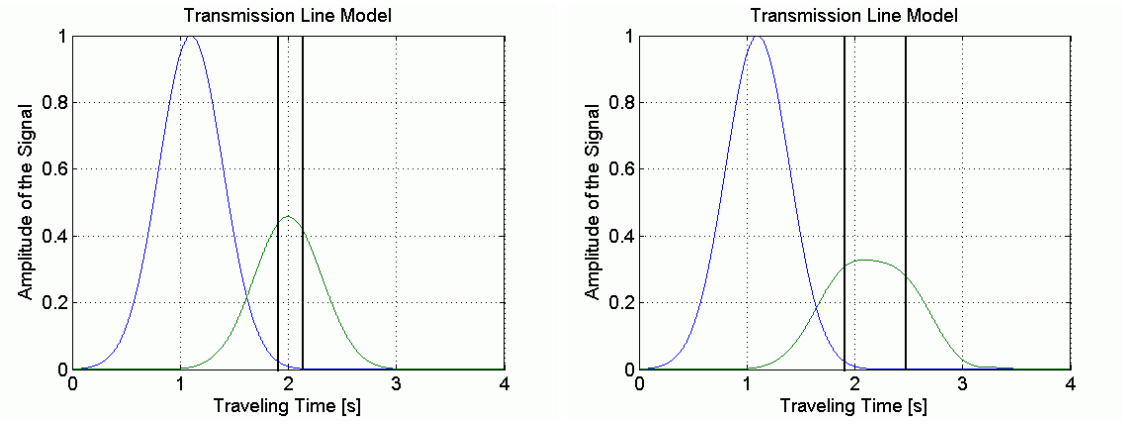

(a) object height 3 cm, $\epsilon_r = 1$ (b) object height 8 cm, $\epsilon_r = 1$

Figure 3.17: Results of the equivalent TLM method for an object with $\epsilon_r = 1$.

Depth below the Surface	Results of MWS	Results of TLM
d_l=00 cm	Δt_{MWS}=0.000 ns	Δt_{TLM}=0.000 ns
d_l=02 cm	Δt_{MWS}=0.240 ns	Δt_{TLM}=0.231 ns
d_l=05 cm	Δt_{MWS}=0.600 ns	Δt_{TLM}=0.578 ns
d_l=07 cm	Δt_{MWS}=0.842 ns	Δt_{TLM}=0.809 ns
d_l=10 cm	Δt_{MWS}=1.207 ns	Δt_{TLM}=1.155 ns
d_l=12 cm	Δt_{MWS}=0.600 ns	Δt_{TLM}=1.386 ns
d_l=15 cm	Δt_{MWS}=1.820 ns	Δt_{TLM}=1.733 ns
d_l=20 cm	Δt_{MWS}=2.422 ns	Δt_{TLM}=2.311 ns
d_l=25 cm	Δt_{MWS}=3.039 ns	Δt_{TLM}=2.889 ns
d_l=30 cm	Δt_{MWS}=3.649 ns	Δt_{TLM}=3.466 ns
d_l=35 cm	Δt_{MWS}=4.258 ns	Δt_{TLM}=4.044 ns
d_l=40 cm	Δt_{MWS}=4.872 ns	Δt_{TLM}=4.622 ns
d_l=80 cm	Δt_{MWS}=9.784 ns	Δt_{TLM}=9.244 ns

Table 3.1: Traveling time according to 3D field simulation and TLM.

Dielectric layer setup	Results of MWS	Results of TLM
ϵ_r=3.5 refinement factor 2	Δt_{MWS}=1.076 ns	Δt_{TLM}=1.005 ns
ϵ_r=10 refinement factor 2	Δt_{MWS}=1.782 ns	Δt_{TLM}=1.688 ns
ϵ_r=20 refinement factor 2	Δt_{MWS}=2.647 ns	Δt_{TLM}=2.387 ns
ϵ_r=30 refinement factor 2	Δt_{MWS}=3.410 ns	Δt_{TLM}=2.923 ns
ϵ_r=40 refinement factor 2	Δt_{MWS}=4.150 ns	Δt_{TLM}=3.375 ns
ϵ_r=50 refinement factor 2	Δt_{MWS}=4.872 ns	Δt_{TLM}=3.774 ns

Table 3.2: Traveling time through a dielectric layer with refinement factor 2.

Dielectric layer setup	Results of MWS	Results of TLM
ϵ_r=10 refinement factor 3	Δt_{MWS}=1.744 ns	Δt_{TLM}=1.688 ns
ϵ_r=10 refinement factor 4	Δt_{MWS}=1.730 ns	Δt_{TLM}=1.688 ns
ϵ_r=40 refinement factor 3	Δt_{MWS}=3.682 ns	Δt_{TLM}=3.375 ns
ϵ_r=40 refinement factor 4	Δt_{MWS}=3.552 ns	Δt_{TLM}=3.375 ns

Table 3.3: Traveling time through dielectric layer with refinement factor 3 and 4.

Chapter 4

Investigation of Antennas for GPR

4.1 Introduction

It has already been discussed that the antenna is the crucial hardware part of a GPR system. The radiation characteristics of the antenna are affecting the performance of the GPR, namely, the quality of the image and the corresponding resolution of the system. Important parameters are its bandwidth of operating frequencies, its radiation pattern, its gain and its radiation efficiency. The following chapter addresses the design and development of different types of GPR antennas.
Some of them are of-the-shelf designs such as the log-periodic dipole antenna or the standard gain horn antenna. Others have been modified from existing designs such as the double-ridged TEM horn and the Bujanov antenna or designed completely new as it is the case for the Orion-type impulse radiating antenna. The antenna characteristics are investigated using both, 3D field simulations and measurements. Moreover, all antennas have been integrated in the proposed simulation of a GPR, see chapter 3, which allows to predict the behavior of the antennas in this context prior to the fabrication of prototypes and measurement experiments.

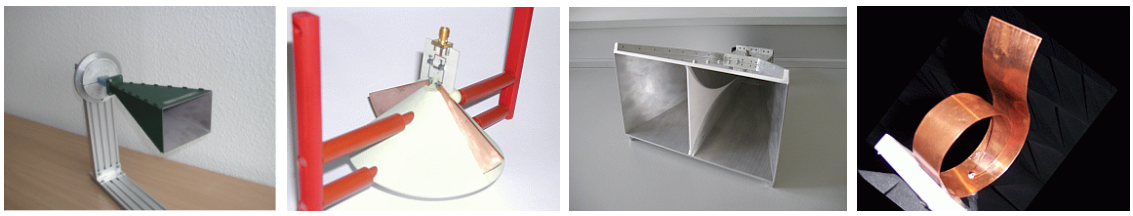

Figure 4.1: Prototypes of the investigated antennas for GPR applications.

4.2 Standard Gain Horn Antenna

4.2.1 Design and Development

Standard gain horn antennas have a wide range of applications, e.g. as transmitting and receiving antennas or for feeding reflectors and they are an important component for antenna gain measurements. The absolute gain of a standard gain horn is calculable from the flare dimensions in Fig. 4.2. Standard gain horns are precision components providing accurate and repeatable gain references and typical gain and bandwidth curves are provided for all standard gain horns [Var05d].

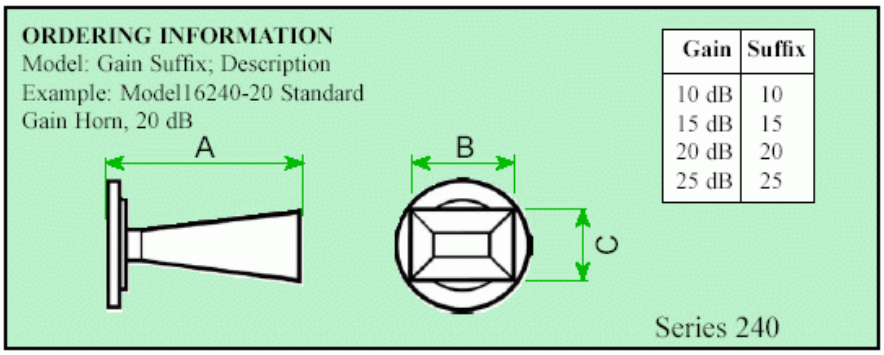

Figure 4.2: Flann standard gain horn antenna dimensions [Var05d]

For the X-band frequency range two different standard gain horn antennas, namely the Flann models 16240-10 (A 76 mm, B 35 mm, C 25 mm, Gain 10 dB) and 16240-20 (A 245 mm, B 109 mm, C 79 mm, Gain 20 dB) have been chosen for GPR applications. In order to achieve a higher gain the 20 dB horn is approximately three times longer than the corresponding 10 dB model. As it is the case for rectangular standard gain horn antennas the transmitted fields are linearly polarized.

4.2.2 Antenna Characteristics

In order to investigate the radiation characteristics of the standard gain horn antenna with a gain of 10 db, respectively, 20 dB both antennas have been simulated by means of 3D EM field simulation. It showed, that the agreement between the results of the simulation and the results of real measurements can be increased significantly, if the holder structure (Fig. 4.3), which is part of the measurement setup is also considered for the simulation model as it is illustrated in Figs. 4.5 and 4.8.

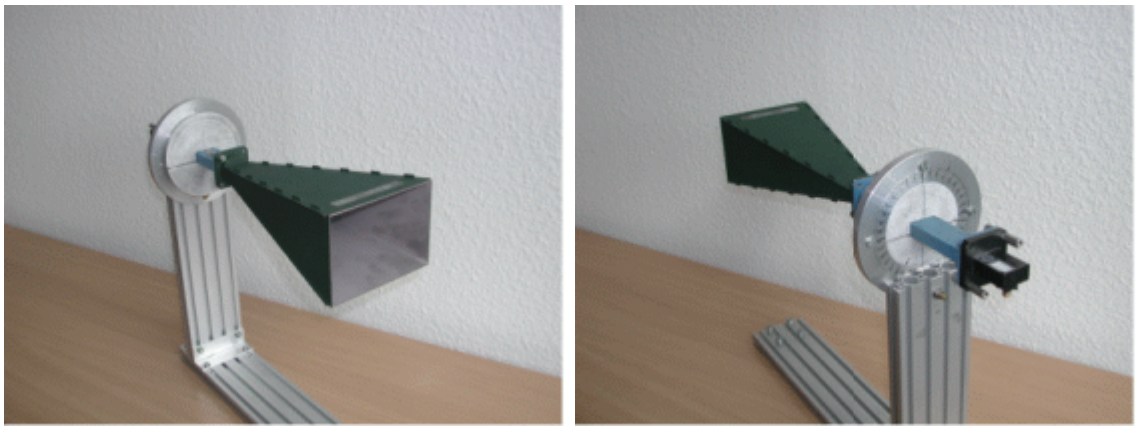

Figure 4.3: 20 dB standard gain horn antenna mounted in the holder.

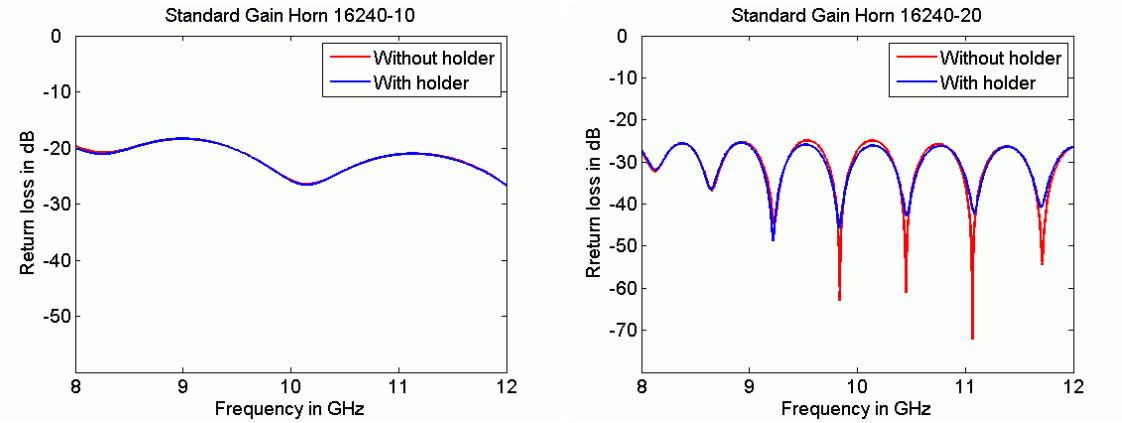

Figure 4.4: Return loss of 10 dB (left) and 20 dB standard gain horn (right).

The 3D field simulation model has been excited by a waveguide port with typical X-band dimensions. As it is illustrated in Fig. 4.4 the 10 dB horn reveals a return loss smaller than -20 dB, whereas the return loss of the 20 dB horn stays below -28 dB. The holder structure causes only a small difference in the simulated return loss characteristic of both standard gain horn antennas. However, the comparison of the E-plane and H-plane results reveals, that there is a significant difference between the simulation with and without holder structure concerning the radiated fields. Figs. 4.6 and 4.7, respectively, Figs. 4.9 and 4.10 illustrate, that the agreement between the results of the measurements and the simulations for directions far away from the main lobe can be increased, if the holder structure is included. All radiation characteristics have been determined at the center frequency, namely at 10 GHz.

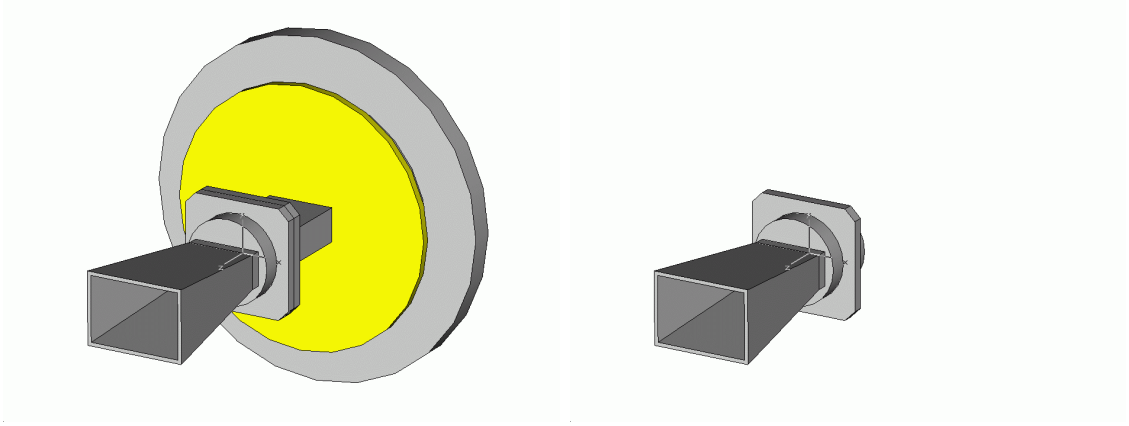

Figure 4.5: MWS model of the 10 dB horn with and without holder structure.

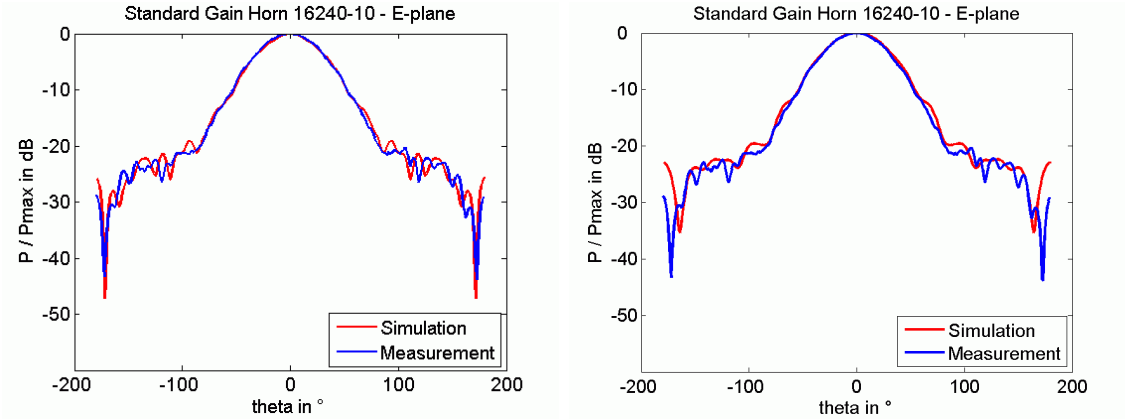

Figure 4.6: E-plane of the 10 dB horn with and without holder (10 GHz).

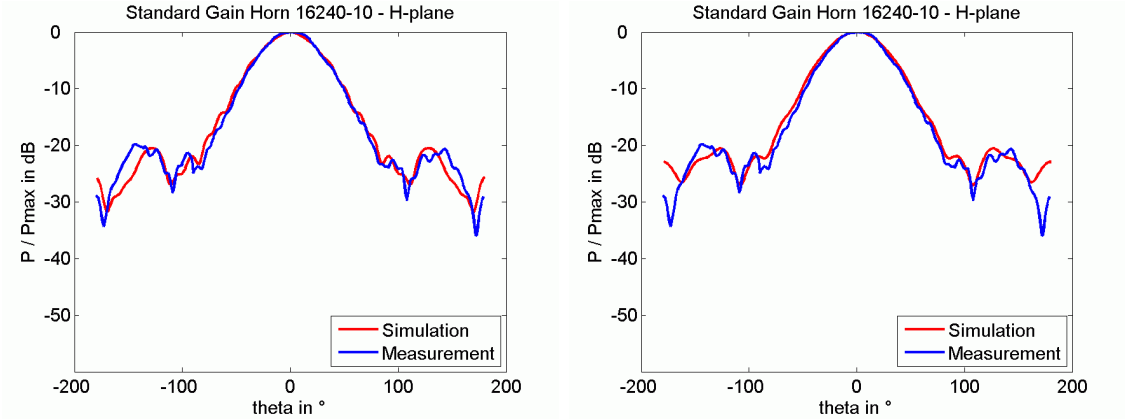

Figure 4.7: H-plane of the 10 dB horn with and without holder (10 GHz).

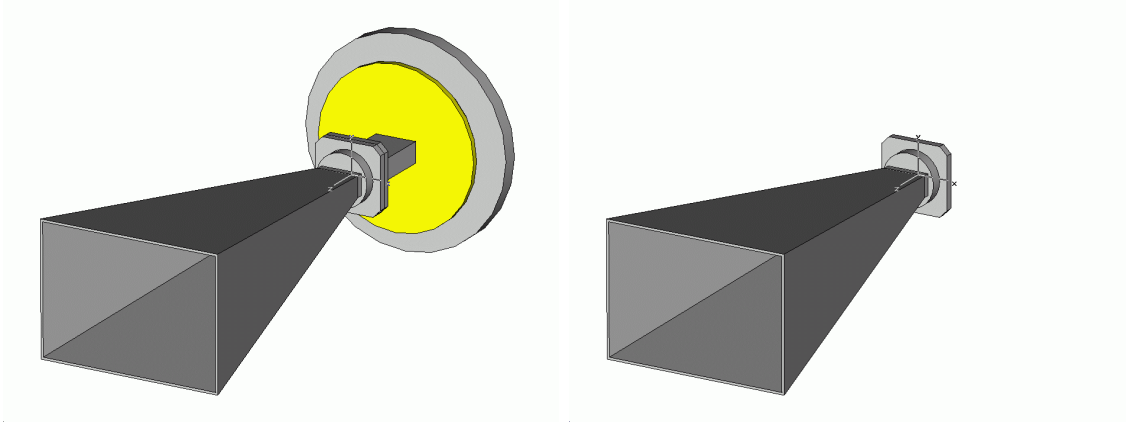

Figure 4.8: MWS model of the 20 dB horn with and without holder structure.

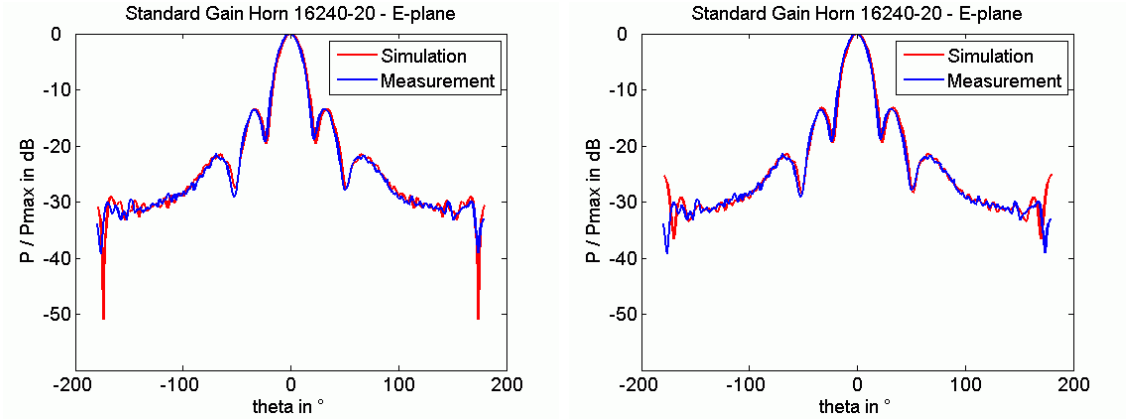

Figure 4.9: E-plane of the 20 dB horn with and without holder (10 GHz).

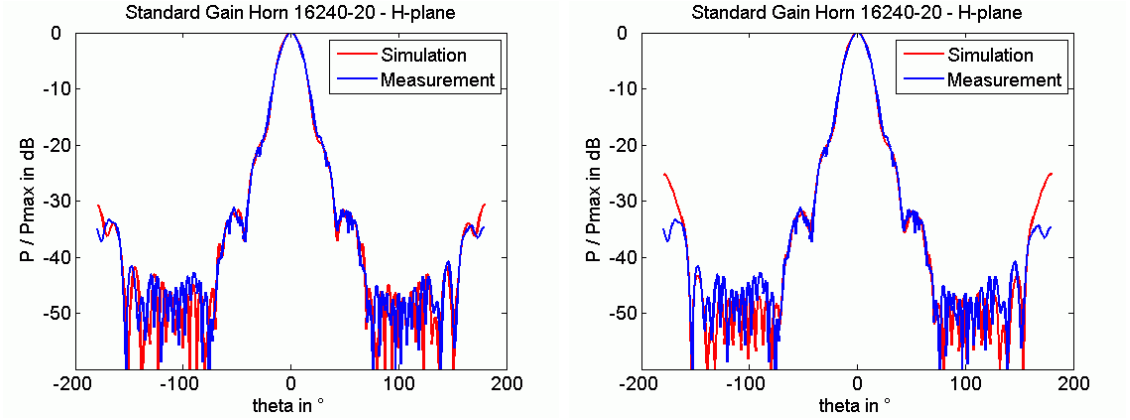

Figure 4.10: H-plane of the 20 dB horn with and without holder (10 GHz).

In order to validate the results of the 3D field simulation, the return loss of both standard gain horn antennas has been measured using a vector network analyzer in the extended X-band frequency range, namely, from 7 GHz to 13 GHz. The results in Figs. 4.11 and 4.12 reveal for both antennas a very good agreement between the measurement and the simulation. However, it can be concluded, that the agreement between the results of measurement and simulation decreases significantly, if the necessary number of mesh lines per wavelength is underestimated.

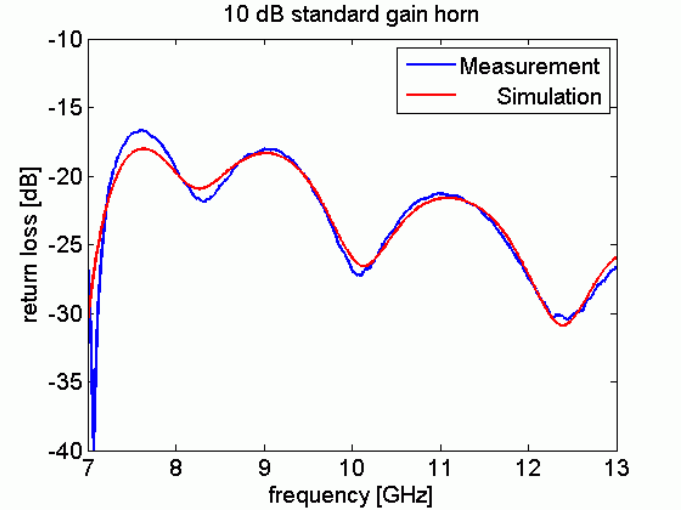

Figure 4.11: Simulated (red) and measured (blue) return loss of the 10 dB horn.

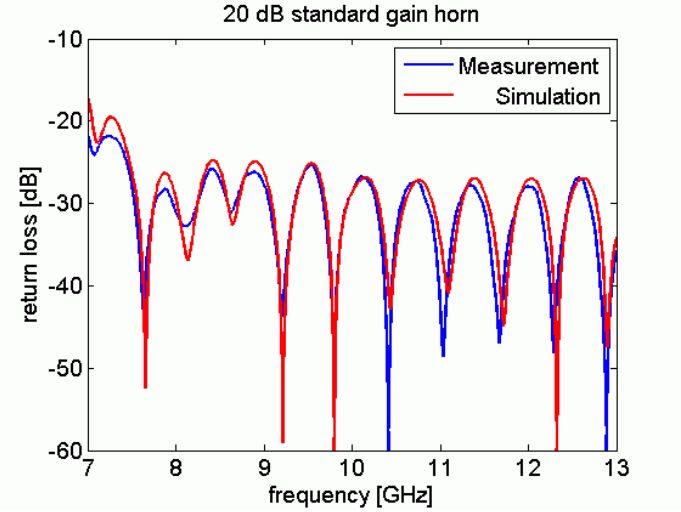

Figure 4.12: Simulated (red) and measured (blue) return loss of the 20 dB horn.

4.2.3 GPR Simulation Results

Fig. 4.13 illustrates how the investigated standard gain horn antennas with a gain of 20 dB has been integrated in the simulation of a GPR environment. The antenna has been placed in a distance of 10 cm above the surface of the homogeneous soil brick for which the permittivity of dry sand, namely, $\epsilon_r = 2.5$ with a loss tangent of 0.01 has been assumed. The dimensions of the soil brick, namely, d_x=60 cm, d_y=20 cm and d_z=20 cm have been chosen large enough in order to avoid interactions between the radiated field and the surrounding boundaries of the model.
The cylindrical target object with a diameter of 10 cm and a height of 3 cm has been aligned parallel to the surface in a depth of 7 cm. Two different scenarios have been considered for the simulation of a B-scan above such a target object. On the one hand an air-filled cylinder with a permittivity of $\epsilon_r = 1.0$ has been assumed which can be understood as a model of the air-gap within a realistic AP mine, see B. The second scenario utilizes a similar object with a permittivity of $\epsilon_r = 3.5$ which has been chosen to be close to that of the ground in order to study the ability of the antenna system to detect target objects with a poor reflectivity. According to the radiation properties of the antenna an operating frequency range from 8 GHz to 12 GHz has been chosen for the simulation and 31 antenna positions on the x-axis across the center of the buried target object are taken into account.

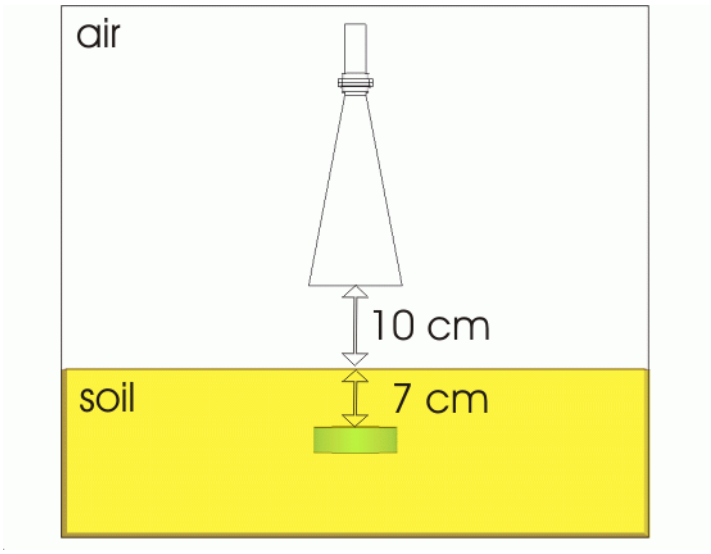

Figure 4.13: Simulation model of a GPR with a 20 dB standard gain horn.

Figs. 4.14 and 4.15 illustrate the results of the two B-scan simulations above a target object with a permittivity of $\epsilon_r = 1.0$, respectively, a target object with a permittivity of $\epsilon_r = 3.5$. Therefore, the 10 dB standard gain horn antenna has been utilized in exactly the same model which has been illustrated in Fig. 4.13 for the case of the 20 dB standard gain horn antenna. All images have been normalized with respect to the maximum amplitude of the case with a target permittivity of $\epsilon_r = 1.0$ which allows to compare the results of both simulations. It shows, that for both cases the buried objects can be clearly identified without a further background subtraction. Moreover, the reflections at the upper and lower interface between the object and the soil can be distinguished which indicates a good depth resolution.

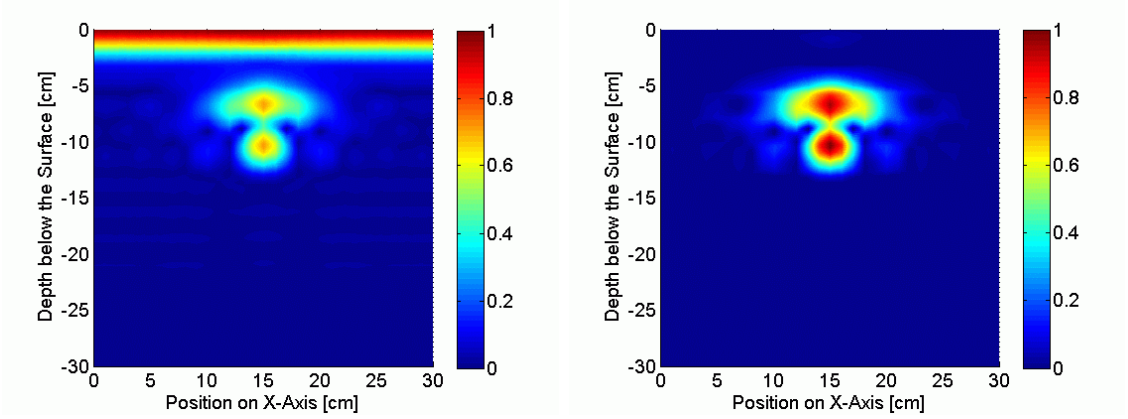

(a) object 1 ($\epsilon_r = 1.0$), no processing (b) additional background subtraction

Figure 4.14: 10 dB standard gain horn above cylindrical object ($\epsilon_r = 1.0$).

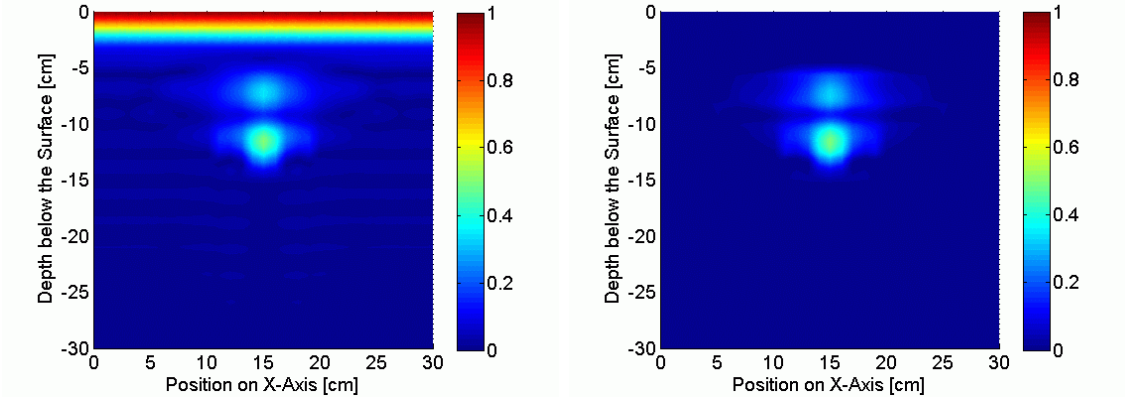

(a) object 2 ($\epsilon_r = 3.5$), no processing (b) additional background subtraction

Figure 4.15: 10 dB standard gain horn above cylindrical object ($\epsilon_r = 3.5$).

For the case of the 20 dB standard gain horn antenna the corresponding results of the two different B-scan simulations above a target object with a permittivity of $\epsilon_r = 1.0$, respectively, a target object with a permittivity of $\epsilon_r = 3.5$ are illustrated in Figs. 4.16 and 4.17. An additional background subtraction has been applied and the images have been normalized with respect to the largest amplitude of the case with a permittivity of $\epsilon_r = 1.0$. Again, the presence of the buried target objects can be clearly revealed form the resulting images. In comparison to the case with the 10 dB standard gain horn antenna the reflection signatures give more evidence of the correct dimensions of the buried target object, namely, a diameter of 10 cm and a height of 3 cm, which can be explained by the higher gain of the antenna.

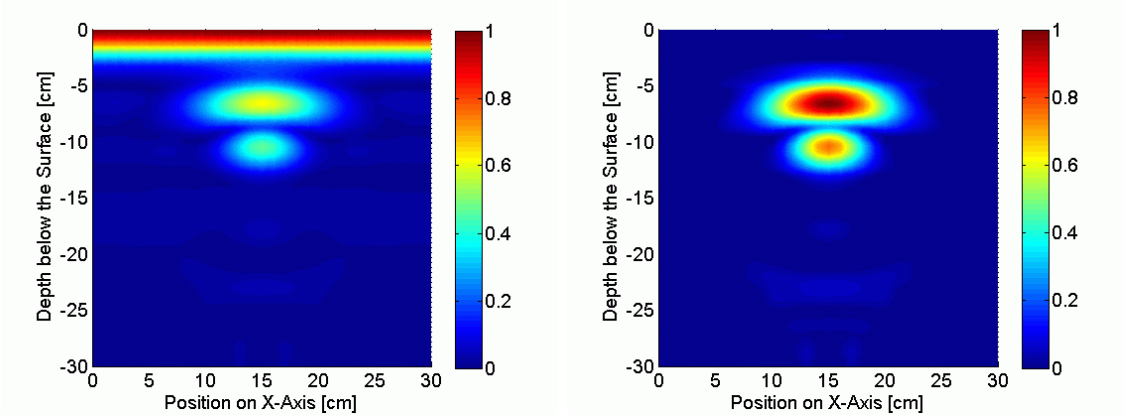

(a) object 1 ($\epsilon_r = 1.0$), no processing (b) additional background subtraction

Figure 4.16: 20 dB standard gain horn above cylindrical object ($\epsilon_r = 1.0$).

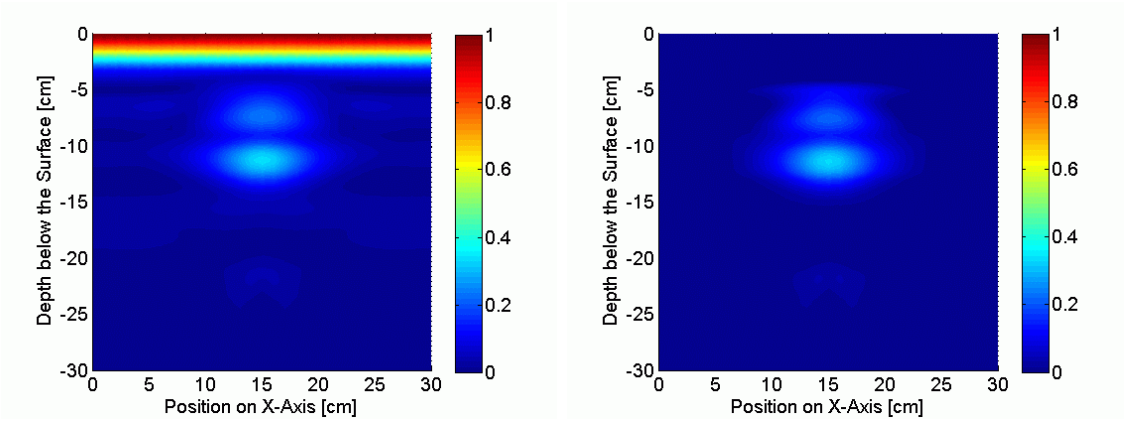

(a) object 2 ($\epsilon_r = 3.5$), no processing (b) additional background subtraction

Figure 4.17: 20 dB standard gain horn above cylindrical object ($\epsilon_r = 3.5$).

4.3 Orion-type Impulse Radiating Antenna

4.3.1 Design and Development

Typically, the reflection at the air-soil interface is stronger than the target reflection itself. This systematic problem has been taken into account right from the beginning in the development of a new type of forward impulse radiating antenna (IRA) which is named Orion-type due to its shape that resembles the Orion star ship. IRAs have already been reported for mine detection applications, e.g. in [FB01]. The novel Orion-type IRA, however, is optimized for the operation close to the air-soil interface with the aim of suppressing reflections from this interface. It will be shown that the antenna gives superior results concerning the detection of buried objects when it is used together with a calibration technique that will also be presented.
The antenna is mainly a forward radiating IRA with two metal arms, embedded in a dielectric material. The permittivity of this dielectric cone has been chosen close to the permittivity of the soil. Thus the overall mismatch due to the interfaces between the antenna and the air, respectively, between the air and the soil can be decreased as the antenna is installed very close to the ground surface. Fig. 4.18 illustrates the utilized 3D EM simulation model and the prototype of the proposed Orion-type IRA including its plastic holder structure and the coaxial SMA connector.

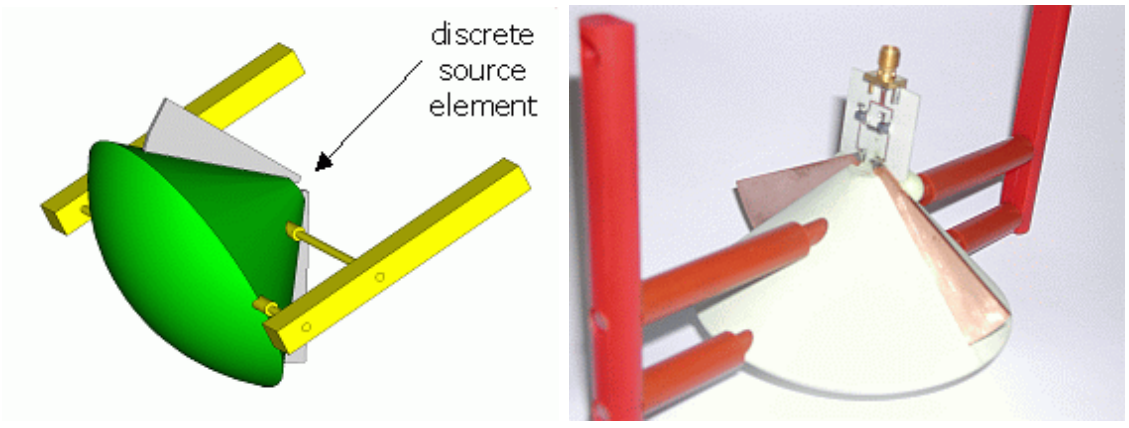

(a) MWS model (b) prototype

Figure 4.18: Orion-type impulse radiating antenna.

The cone of the Orion-type IRA is made of AK4 low loss dielectric material [Var04]. The relative permittivity of this material is almost frequency independent $\epsilon_r = 3.85$

which has been determined by broadband measuring methods [JMO03; AJO07]. The feeding of the antenna in the 3D EM model is realized using a discrete port. However, for feeding the antenna prototype properly it is necessary to use a balun with a step up ratio of 4:1 in order to match the 50 Ohm feeding line impedance to the radiation impedance of the antenna that is about 200 Ohm. Furthermore, the suggested balun structure connects the unsymmetrical coaxial line with the symmetrical antenna structure and eliminates its common mode excitation.

4.3.2 Antenna Characteristics

The free space performance of the Orion-type IRA strongly depends on the operating frequency. Fig. 4.19(a) indicates a poor directivity of the antenna at 1 GHz while Fig. 4.19(a) shows a pencil beam like radiation pattern that has been observed at 5 GHz. Moreover the return loss of the Orion-type IRA has been obtained to be around -5 dB which is quite large compared to that of other antennas which have been optimized for free space operation in the context of this thesis. As a conclusion it can be stated that the free space performance of the Orion-type IRA is inferior to that of other antenna design for GPR which have been investigated in this chapter.

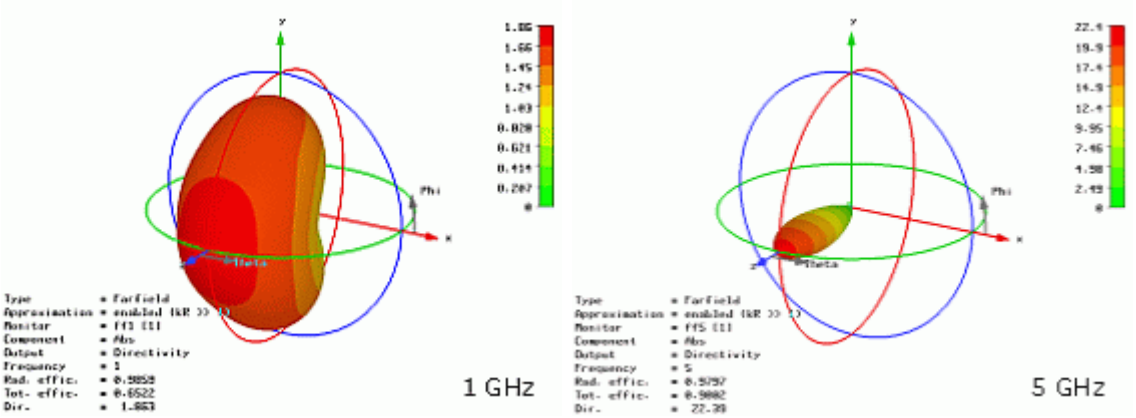

(a) radiation pattern at 1 GHz (b) radiation pattern at 5 GHz

Figure 4.19: Simulated radiation pattern of the Orion-type IRA.

However, it has been found from field simulations that the Orion-type IRA basically illuminates the small area directly below the cone. The wave propagation in this region is in a good agreement to that of a wave traveling along a 1D transmission line. This is important because in order to apply a one-port calibration technique a

1D transmission line model must be valid for the field propagating inside the ground. Fig. 4.20 shows the simulated radiation pattern of the Orion-type IRA at 2 GHz in the presence of homogeneous soil with a permittivity of $\epsilon_r = 2.5$ with a distance of 10 mm between IRA and soil. It shows, that for the propagation of the E-field inside of the soil the behavior of a 1D transmission line model can be assumed. Hence, a well-known one-port calibration procedure can be applied.

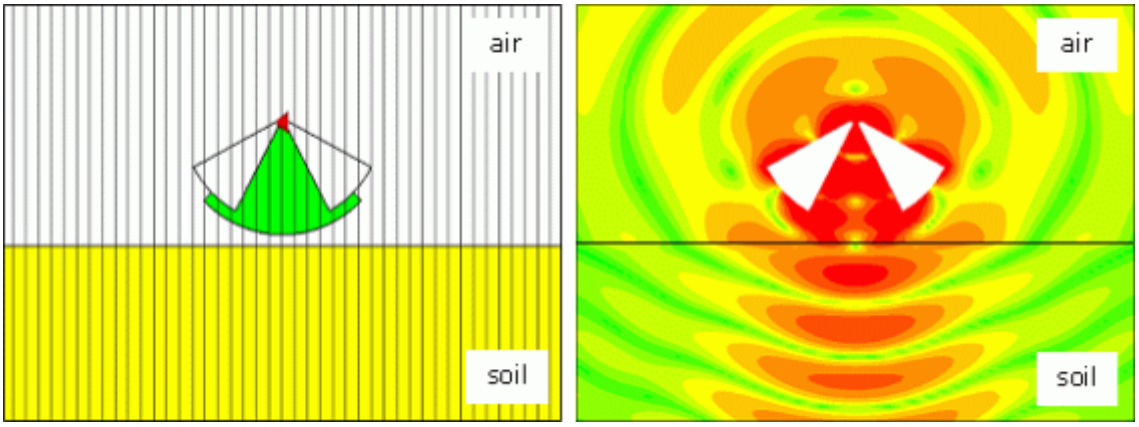

(a) MWS configuration (b) radiation pattern at 2 GHz

Figure 4.20: Simulated radiation pattern in the presence of soil.

4.3.3 Calibration Procedure

In order to apply the suggested one-port calibration one has to take three different calibration standards into account. The well-known technique which is applied is discussed in appendix A.1 and utilizes a match, a short and different offset shorts. Fig. 4.21 illustrates the 3D EM simulation configurations for the realization of these calibration standards. Adapting this procedure to subsurface radar match means that the antenna radiates above the homogeneous ground for which the relative permittivity ϵ_{rsoil} will be assumed. The second standard, which is the short, defines the position of the reference plane. This standard is just a large metal plate located inside the ground at the depth of the reference plane. Since the GPR is used for the detection of targets that are buried within the first 200 mm underneath the surface, the reference plane is placed at the center of this region at a depth of 100 mm. Finally one has to apply different offset shorts. In general, the adequate number of utilized offset short standards depends on the considered frequency range.

The proposed Orion-type IRA antenna has been designed to utilize the frequency range from 1 GHz to 5 GHz which is often referred to be a common frequency range for GPR. Accordingly, two offset shorts with an offset length d_{offset} of 22 mm and 8 mm, respectively, have been chosen. This guarantees that the additional line length which is introduced by the two offsets leads to a phase shift within an interval of $90^o \pm 25^o$ at any frequency in the considered band of operation.

Figure 4.21: Calibration standards - match, short and different offset short.

Hence, the equations of the error terms are sufficiently independent. Moreover, the time domain signals reveal that the antenna mismatch and the air-surface reflection have a stronger effect than the reflections corresponding to the short and the offset short standards. The parameters of the error model, namely, E_D, E_S and E_R are calculated according to the following equations from the corresponding frequency domain calibration data, namely, S_{match}, S_{short} and S_{offset}.

$$E_D = S_{match} \tag{4.1}$$

$$E_S = \frac{(S_{short} - S_{match}) + (S_{offset} - S_{match}) \cdot e^{-i\varphi}}{(S_{offset} - S_{short})} \tag{4.2}$$

$$E_R = (S_{match} - S_{short}) \cdot (1 + E_S) \tag{4.3}$$

The corresponding frequency dependent phase is determined by equation (4.4).

$$\varphi = \pi \cdot \left(1 - f \cdot \left(\frac{4 \cdot d_{offset}\sqrt{\epsilon_r}}{c_0}\right)\right) \tag{4.4}$$

Hence, the error coefficients calculated by equations (4.1)-(4.3) are also frequency dependent. As it is shown in Fig. 4.22(a) all coefficients are continuous as expected at the transition frequency at which the calibration procedure switches from the first offset short to the second one. The measured reflection coefficient, which is denoted by S_{meas}, is corrected by equation (4.5) which yields the calibrated reflection S_{corr}.

$$S_{corr} = \frac{S_{meas} - E_D}{E_R + E_S \cdot (S_{meas} - E_D)} \tag{4.5}$$

Fig. 4.23(a) shows what happens when the above-discussed correction is applied to an air layer located exactly at the position of the reference plane, that has been placed 100 mm underneath the surface of the ground. The antenna mismatch and the surface reflection, that appear in Fig. 4.22(b), are completely eliminated after the application of the calibration procedure. At the same time the target signal, that appears to be weaker than the other reflection signatures in the data without any calibration, can be obtained correctly according to following equation.

$$\Gamma = \frac{\sqrt{\epsilon_{rsoil}} - \sqrt{\epsilon_{r0}}}{\sqrt{\epsilon_{rsoil}} + \sqrt{\epsilon_{r0}}} \tag{4.6}$$

The value of the corrected reflection coefficient is exactly the theoretical one given by equation (4.6), where ϵ_{rsoil} and ϵ_{r0} are the permittivity of the background and the permittivity of the object, respectively. Thus, the depth of the target layer is well-defined with respect to the reference plane. In order to verify the results of the calibration it will be substituted by a simple so-called background subtraction. In this case the term $E_S \cdot (S_{meas} - E_D)$ is considered to be small in comparison to the value of E_R and equation (4.5) can be modified to form equation (4.7).

$$S_{corr} = S_{meas} - E_D = S_{meas} - S_{match} \tag{4.7}$$

If this formulation of an ordinary background subtraction is compared to the formulation in (4.5) it is obvious that the performance of this technique is inferior compared to the results of the complete calibration procedure as it is illustrated in Fig. 4.23. The exclusive application of a background subtraction, see Fig. 4.23(a),

does neither yield the exact depth nor the accurate reflectivity of the buried object. On the other hand Fig. 4.23(b) reveals, that the position of the buried air layer, respectively, the expected amplitude of the reflected signal can be obtained correctly if the proposed calibration is applied. Hence, an ordinary background subtraction is not an adequate equivalent of the suggested one-port calibration procedure which allows to remove both, the antenna mismatch and the air-surface reflection that is dominating the results without calibration, completely. Thus, the subsurface imaging resolution can be improved significantly, even though the proposed Orion-type IRA itself is of inferior performance in comparison to other UWB antennas.

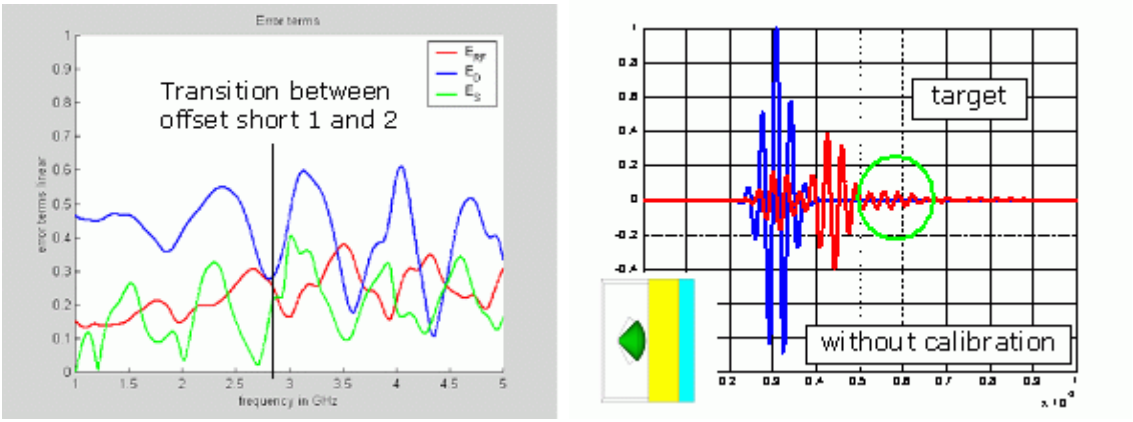

(a) transition of error coefficients (b) no processing

Figure 4.22: Transition of error coefficients and air-layer in 100 mm.

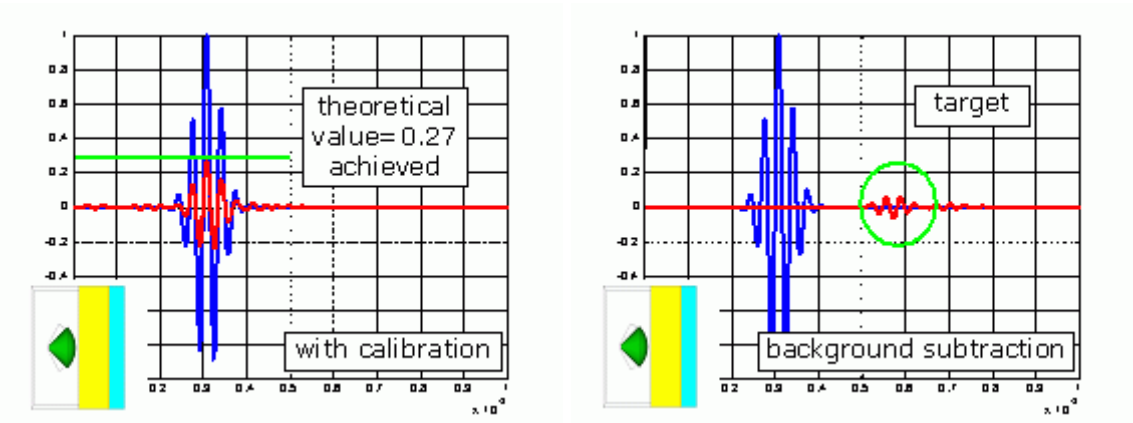

(a) with calibration procedure (b) background subtraction

Figure 4.23: Air-layer in 100 mm - calibration vs. background subtraction.

4.3.4 GPR Simulation Results

An example for the integration of the Orion-type IRA in the simulation of a GPR has been illustrated in Fig. 4.24. The antenna has been placed in a distance of 2 cm above the surface of the homogeneous soil brick with dimensions of d_x=60 cm, d_y=40 cm and d_z=20 cm. For the soil material the properties of dry sand, namely, a permittivity of $\epsilon_r = 2.5$ with a loss tangent of 0.01 have been assumed.
The cylindrical target object with a diameter of 10 cm and a height of 3 cm has again been aligned parallel to the surface in a depth of 7 cm. As before, two different GPR scenarios which utilize an air-filled cylinder with a permittivity of $\epsilon_r = 1.0$, respectively, a similar object with a permittivity of $\epsilon_r = 3.5$ have been taken into account for the simulation of a B-scan with 31 different antenna positions on the x-axis across the center of the target object. An operating frequency range from 1 GHz to 5 GHz has been chosen for the simulation. The normalized results, which are shown in Figs. 4.25 and 4.26, illustrate that the correct shape and position of the buried objects can be identified correctly if the proposed one-port calibration is applied. It also shows, that the upper and the lower reflection which exist due to the permittivity difference between the object and the soil merge for the case with $\epsilon_r = 1.0$ whereas they can clearly be distinguished for the case with $\epsilon_r = 3.5$ which can be explained by constructive and destructive interference, see 3.7.3.

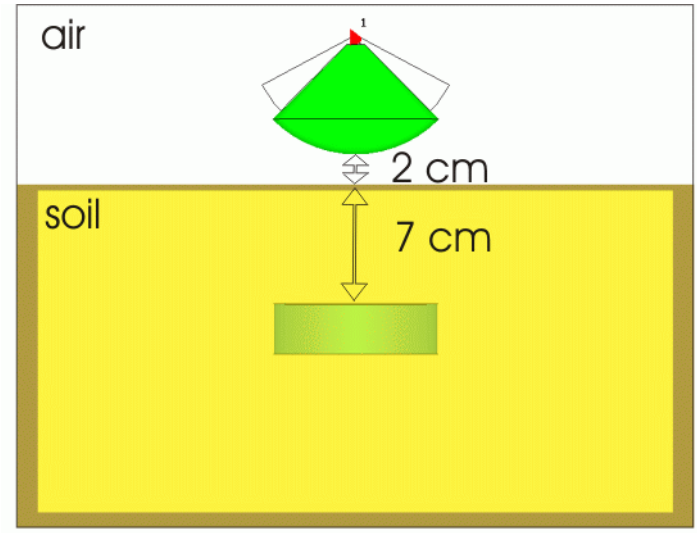

Figure 4.24: Simulation model of a GPR with a Orion-type IRA.

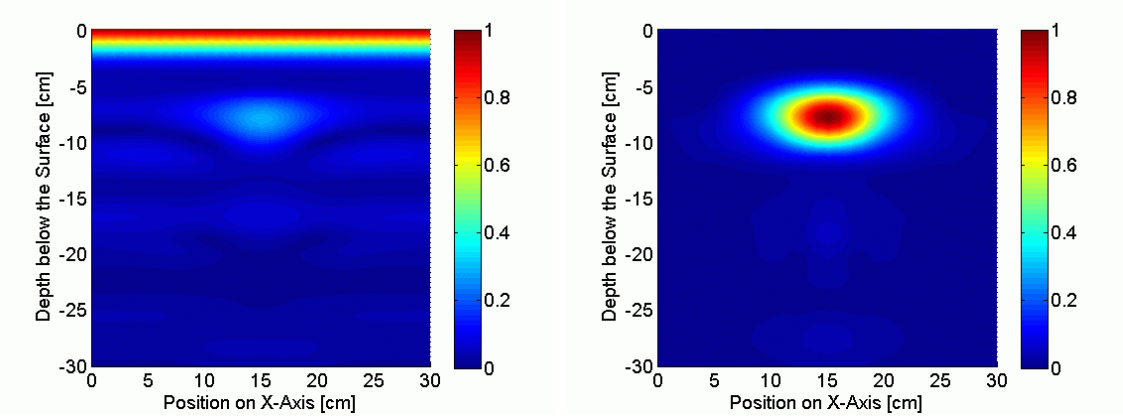

(a) object 1 ($\epsilon_r = 1.0$), no processing (b) additional one-port calibration

Figure 4.25: Orion-type IRA above cylindrical object ($\epsilon_r = 1.0$).

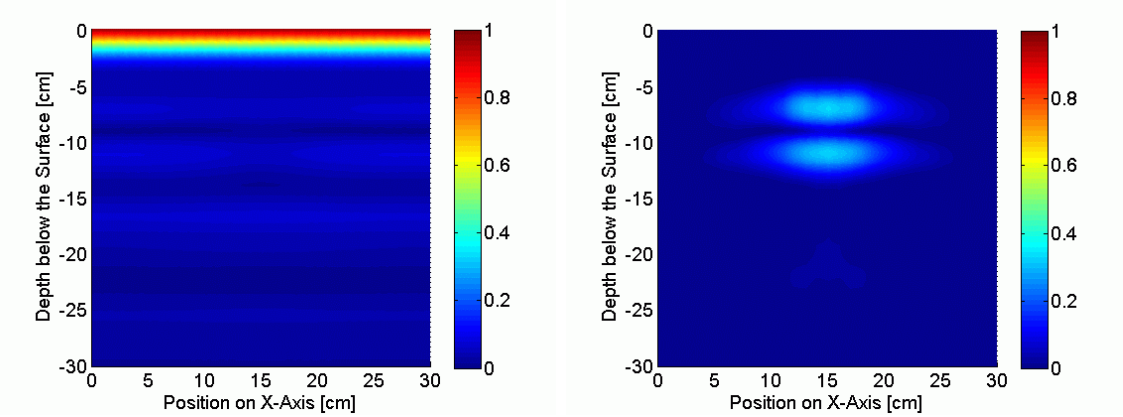

(a) object 2 ($\epsilon_r = 3.5$), no processing (b) additional one-port calibration

Figure 4.26: Orion-type IRA above cylindrical object ($\epsilon_r = 3.5$).

For the GPR simulation of the Orion-type IRA the necessary calculation volume is much smaller than it is the case for other types of antennas. Moreover, the highest operating frequency is only 5 GHz which automatically reduces the necessary number of mesh cells and, thus, the total calculation time of every simulation. Therefore, additional investigations have been done for this type of antenna. Fig. 4.27 illustrates the influence of the inclination angle. The air-filled cylindrical object with a diameter of 10 cm and a height of 3 cm has been rotated in steps of 15 degree. Depending on the orientation of the buried target object which is given by the dotted line in Fig. 4.27 the corresponding B-scans results reveal strong variations.

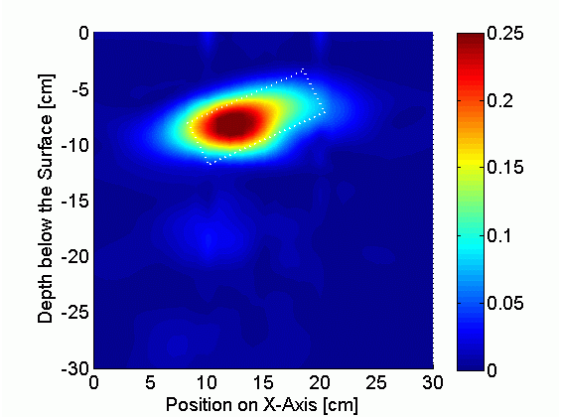

(a) angle of inclination: 15 degrees

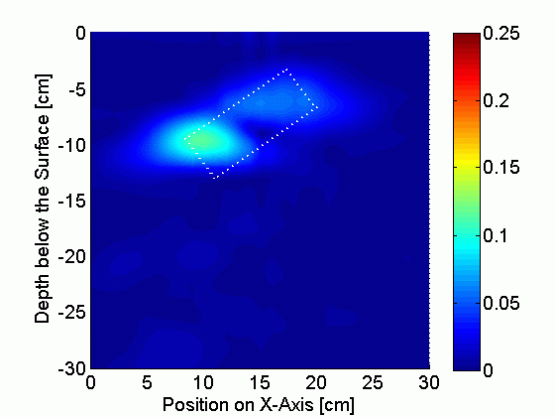

(b) angle of inclination: 30 degrees

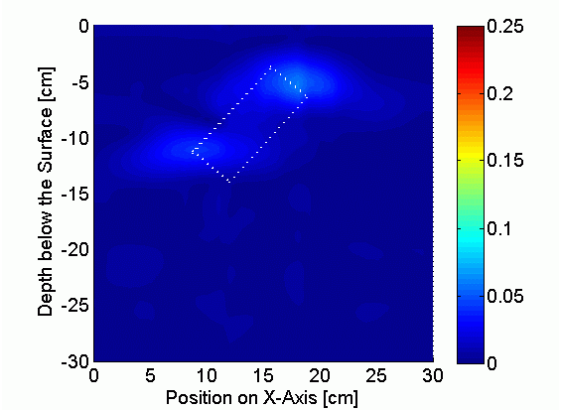

(c) angle of inclination: 45 degrees

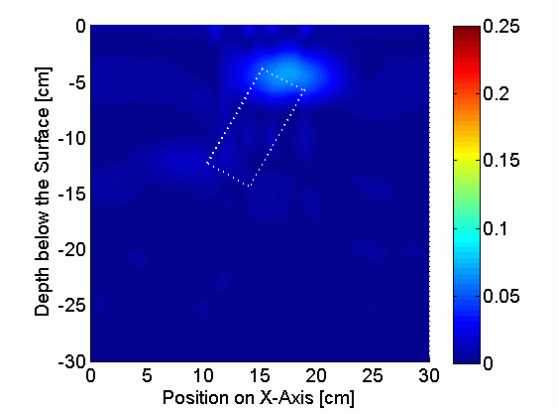

(d) angle of inclination: 60 degrees

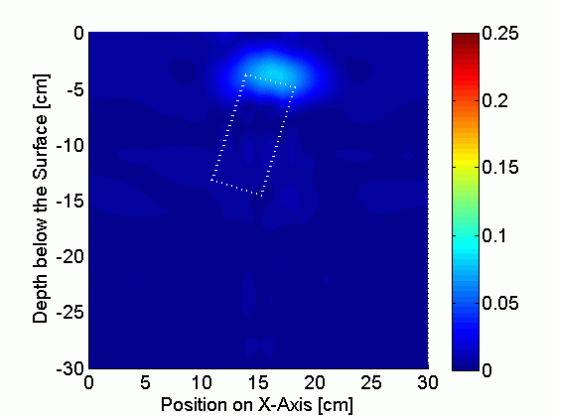

(e) angle of inclination: 75 degrees

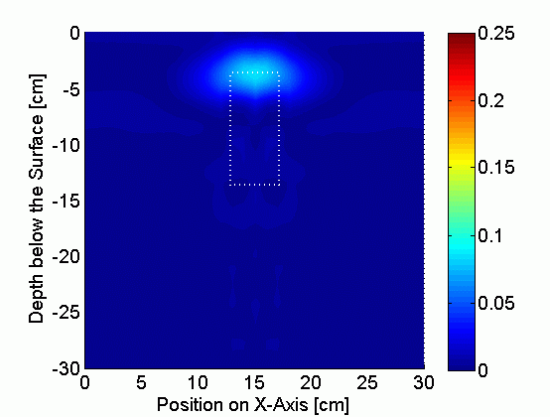

(f) angle of inclination: 90 degrees

Figure 4.27: Orion-type IRA above rotated cylindrical object ($\epsilon_r = 1.0$).

A second example investigates the minimal distance between target objects. The two cylindrical objects in a distance of 4 cm on the x-axis and 2 cm on the z-axis can clearly be distinguished (Fig. 4.28) whereas they start to merge for a distance of 2 cm on the x-axis and 0 cm on the z-axis (Fig. 4.29). Moreover, the simulation results reveal that the amplitude is over- or underestimated after the calibration depending on the relative position to the reference plane. Therefore, the signal amplitude has been corrected for all depth layers with respect to their relative position to the reference plane by multiplying the reflected signal with an interpolated amplitude correction factor that has been taken from reference simulations of a PEC layer.

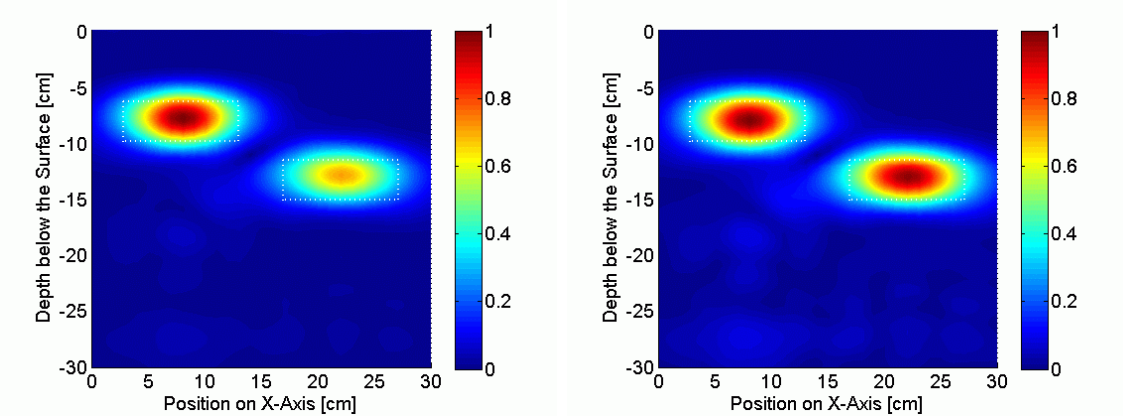

(a) two object case 1, no processing

(b) additional amplitude correction

Figure 4.28: Orion-type IRA above two object case 1 ($\epsilon_r = 1.0$).

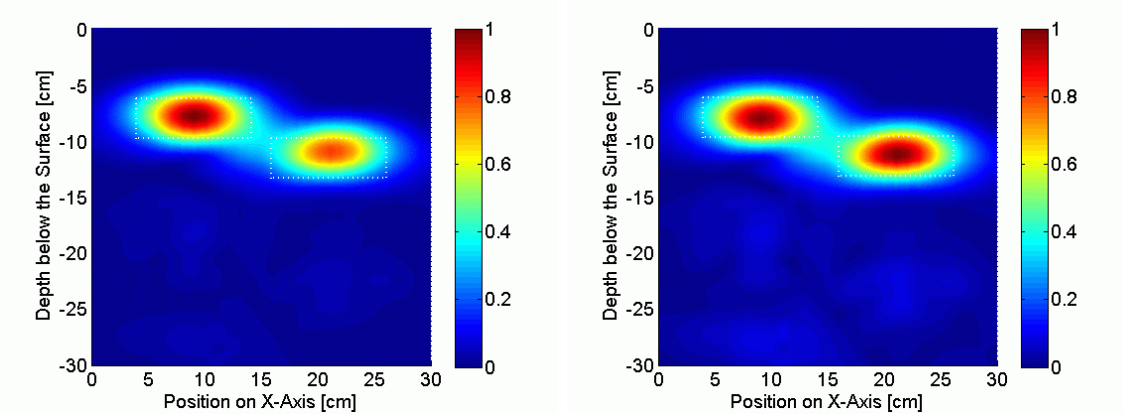

(a) two object case 2, no processing

(b) additional amplitude correction

Figure 4.29: Orion-type IRA above two object case 2 ($\epsilon_r = 1.0$).

4.4 Log-periodic Cylindrical Dipole Antenna

4.4.1 Design and Development

Log-periodic antennas are well-known broadband, unidirectional and narrow-beam antennas that exhibit interesting radiation properties, especially with respect to GPR applications. The impedance and radiation characteristics are regularly repetitive as a logarithmic function of the excitation frequency. A log-periodic dipole antenna (LPDA) consists of individual components which are often dipoles. The length and spacing of these elements increase logarithmically from one end to the other which is the reason for the name of this type of antenna. The antenna is designed in such a way that alternating elements are driven with a phase shift of 180 degree in comparison to the previous dipole element which can be achieved by an alternating connection of the dipoles on the two wires of a balanced transmission line. In the following section the design of a log-periodic antenna will be described according to [Rol06]. The underlying geometry of a log-periodic antenna which has to be specified by a reasonable design procedure is illustrated in Fig. 4.30.

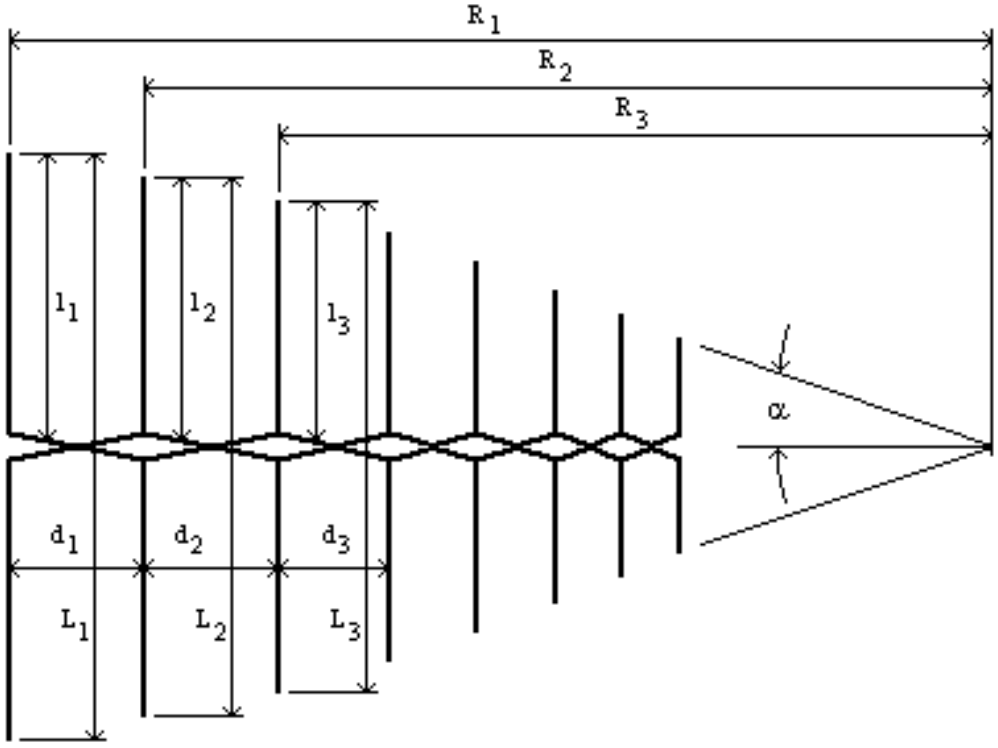

Figure 4.30: Design specifications of a log-periodic dipole antenna [Rol06].

The radiation characteristic of the log-periodic dipole antenna depends on the apex angle α which is denoted according to typical standards and may not be confused with the attenuation factor of a propagating wave. The underlying geometrical relations between α, the graduation factor τ, the length of the n-th dipole L_n, the distance between two elements d_n and the distance of the n-th element to the tip of the antenna R_n can be described by the following equations.

$$\frac{R_1}{L_1} = \frac{R_n}{L_n} = \frac{1}{2 \cdot \tan \alpha} \tag{4.8}$$

The relation between the distances R_n from the tip of the antenna to the n-th dipole can be described by the graduation factor $\tau < 1$ as it is described by equation (4.9).

$$R_n = \tau \cdot R_{n-1} \tag{4.9}$$

This expression can be modified leading to the following explicit formulation for R_n.

$$R_n = \tau^{n-1} \cdot R_1 \tag{4.10}$$

Equations (4.11) and (4.12) can be derived equivalently for the length of the n-th dipole L_n and the distance between the n-th element and the previous one d_n.

$$L_n = \tau^{n-1} \cdot L_1 \tag{4.11}$$
$$d_n = \tau^{n-1} \cdot d_1 \tag{4.12}$$

For a further analysis it is more convenient to relate the distance between the dipoles to the wavelength. The freespace wavelength λ_n of the resonance frequency of the first dipole is approximately 4 times the length of the half dipole $l_n = L_n/2$.

$$\lambda_n \cong 4 \cdot l_n \tag{4.13}$$
$$\frac{d_n}{\lambda_n} \cong \frac{d_n}{4 \cdot l_n} \tag{4.14}$$

Equation (4.14) illustrates, that the distance between the dipole elements of the log-periodic antenna is everywhere over the length of the antenna exactly the same if d_n is related to the wavelength λ_n. The electric periodicity of the log-periodic antenna which is typically denoted by σ in the context of periodic antennas can be calculated by equation (4.15). Together with the values of α and τ this equation is effecting the electric properties of the antenna considerably.

$$\sigma = \frac{d_n}{4 \cdot l_n} = \frac{R_n - R_{n+1}}{4 \cdot l_n} = \frac{R_n\,(1-\tau)}{4 \cdot l_n} = \frac{R_n\,(1-\tau)}{4 \cdot R_n \tan\alpha} = \frac{1-\tau}{4 \cdot \tan\alpha} \tag{4.15}$$

The dependency of the 3 dB beam width on a changing electric periodicity σ is illustrated in Fig. 4.31. It is obvious, that for every value of τ an optimum value of σ can be found and that the directivity of the log-periodic antenna can be improved significantly if the value of graduation factor τ is increased.

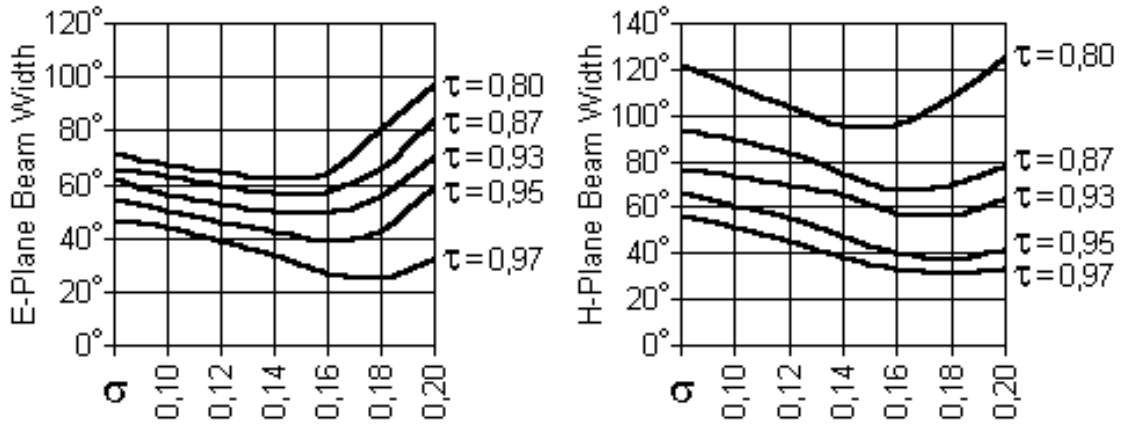

Figure 4.31: 3 dB beam width for E-plane and H-plane [Rol06].

The design parameters have been optimized by 3D EM field simulation. Parameters that have been estimated in the context of a GPR application are the number and dimensions of the dipoles, the design of the apex and the distance between the two coaxial lines and the resistance of the termination. The chosen design with $\alpha = 33.25^o$, $\tau = 0.822$ and $\sigma = 0.149$ which results in 12 dipole elements has been optimized for a frequency range of 1 GHz to 4 GHz in order to meet the demand of a lightweight UWB antenna which could be applied to GPR. A proper design of the apex is important for the performance of the antenna. After an optimization the

diameter of the inner conductor changes from 1.27 mm to 1.8 mm at the position of the apex as it is illustrated in Fig. 4.32. The antenna is matched to 50 Ohm and for the termination of the coaxial feeding line a discrete 70 Ohm resistance is required.

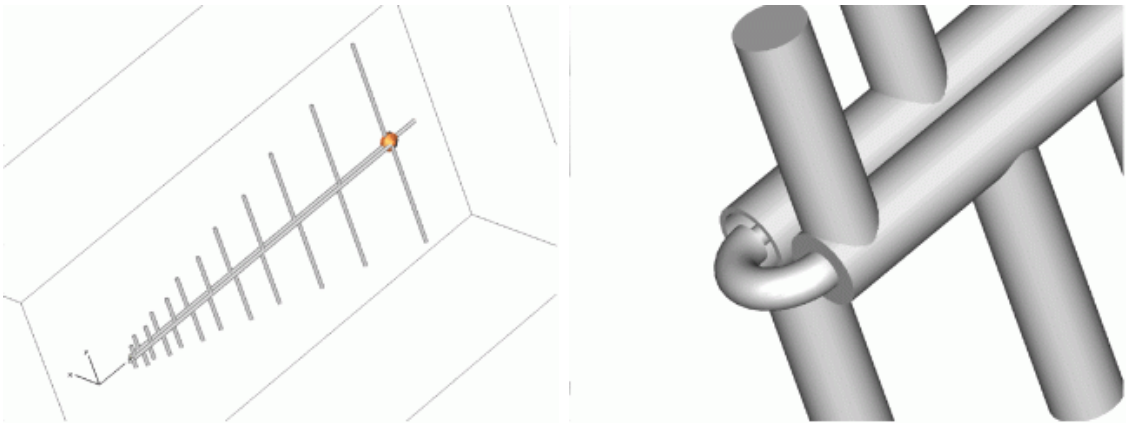

(a) MWS model (b) design of the apex

Figure 4.32: Optimized MWS model of the log-periodic dipole antenna.

4.4.2 Antenna Characteristics

The simulated return loss of the log-periodic antenna is almost -20 dB for the demanded frequency range up to 4 GHz (Fig. 4.33). At higher frequencies it increases significantly. However, the farfield radiation pattern turned out to be almost frequency independent with an average gain of 8 dB (Fig. 4.35). It is well-known, that the phase center of the log-periodic antenna is a function of frequency and is approximately located at the position where the length of a dipole antenna is half a wavelength. At low frequencies only the large dipoles radiate efficiently and therefore it is far away from the tip of the antenna. For higher frequencies it moves towards the tip of the antenna as it is illustrated in Fig. 4.34. The position of this shifting phase center can be calculated. However, it is not sufficient to know the location of the phase center as a function of frequency in order to compensate for the distortion of a transmitted pulse because the length of the feeding line from the reference plane to the active region has also to be taken into account. Since a part of the feeding line is a slow wave structure it is not straight forward to calculate the corresponding time delay. Hence, a proper calibration of the log-periodic antenna would be necessary in order to make use of its wideband characteristics.

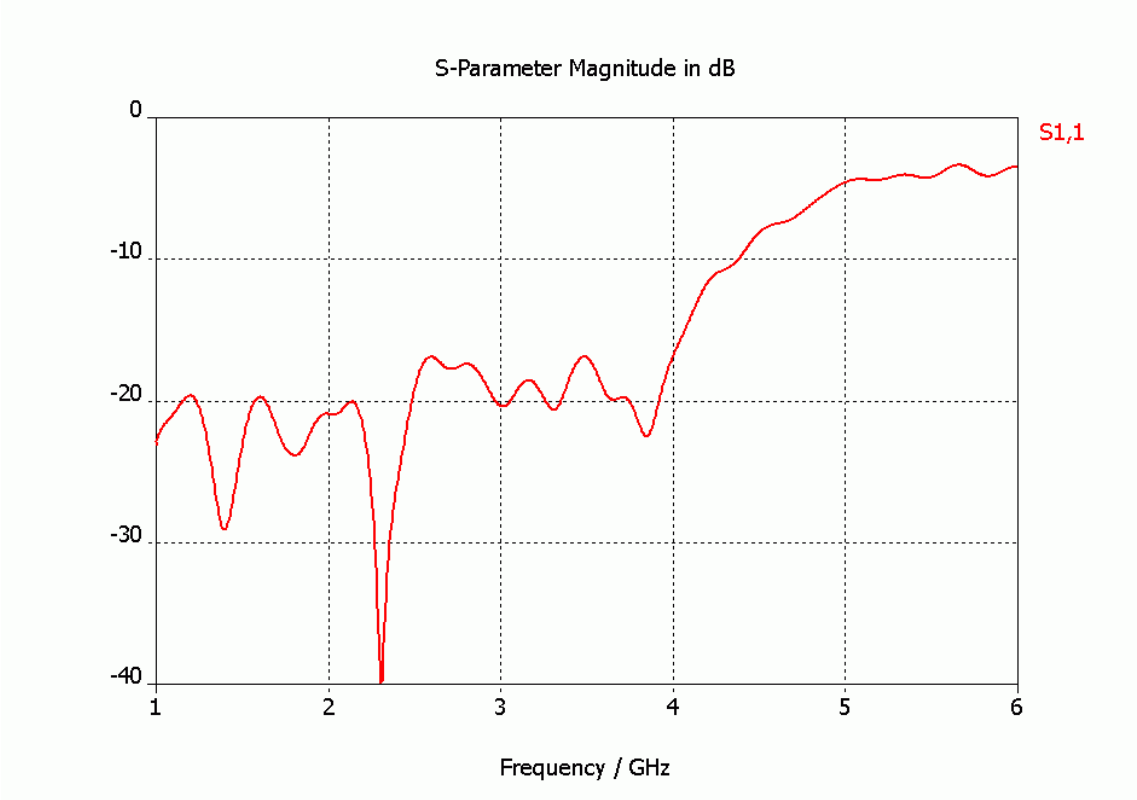

Figure 4.33: Simulated return loss of the log-periodic dipole antenna.

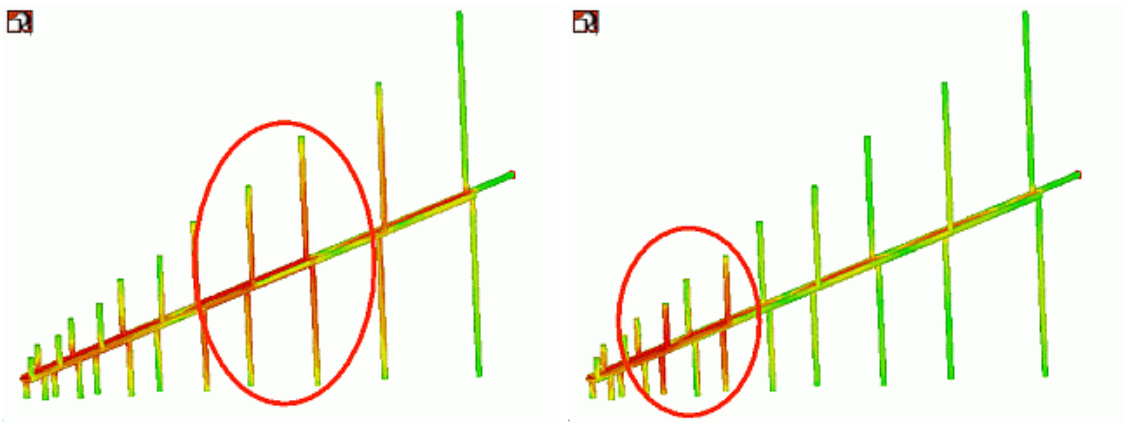

(a) active region at 1 GHz

(b) active region at 2 GHz

Figure 4.34: Distribution of the phase center for different frequencies.

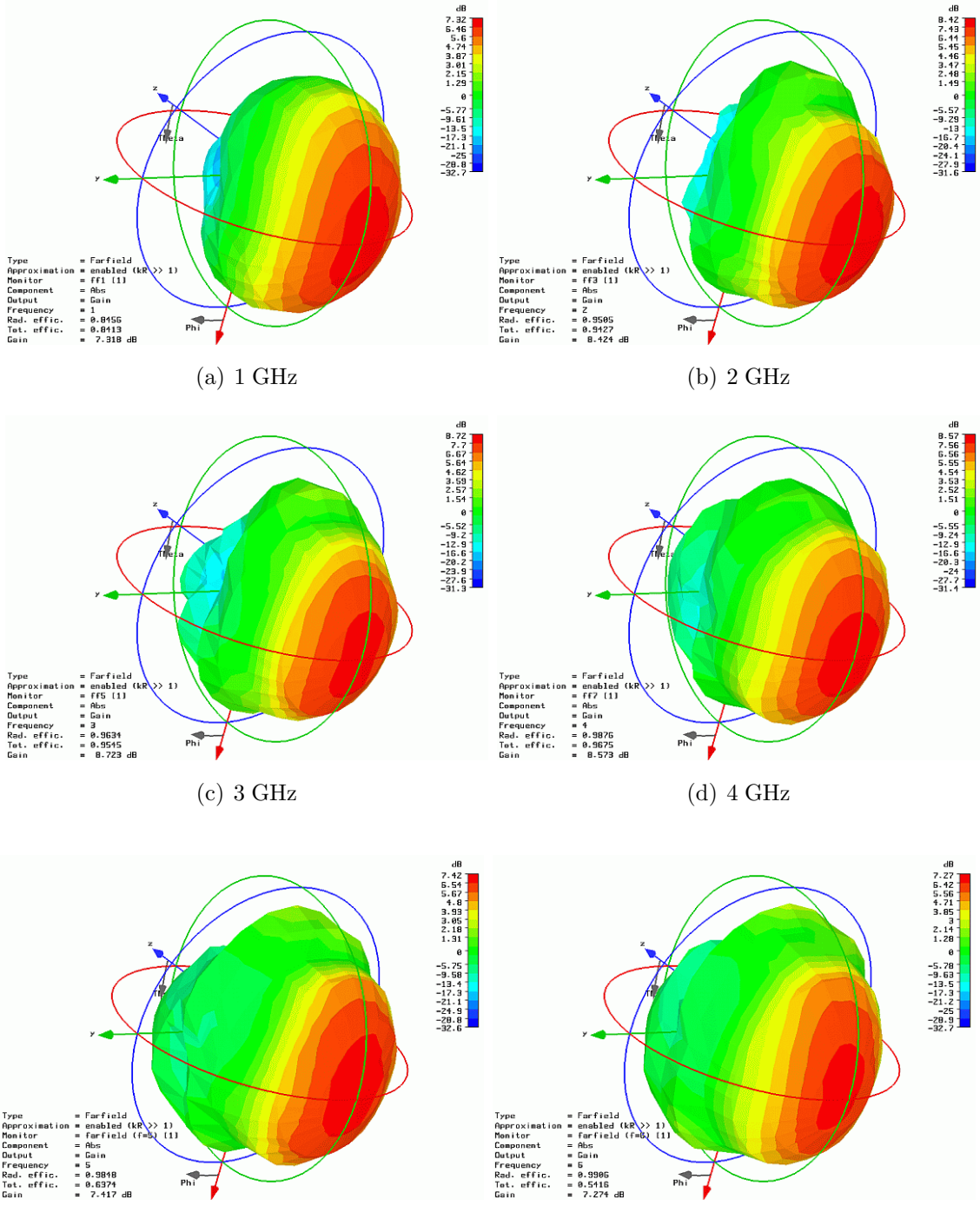

(a) 1 GHz (b) 2 GHz

(c) 3 GHz (d) 4 GHz

(e) 5 GHz (f) 6 GHz

Figure 4.35: Radiation pattern of the log-periodic dipole antenna.

4.4.3 GPR Simulation Results

The corresponding GPR simulation model is illustrated in Fig. 4.36. The LPDA has been placed in a distance of 10 cm above the surface of the homogeneous soil brick with dimensions of d_x=45 cm, d_y=35 cm and d_z=20 cm. For the soil material the permittivity of dry sand, namely, $\epsilon_r = 2.5$ with a loss tangent of 0.01 has been assumed and a cylindrical object with a permittivity of $\epsilon_r = 1.0$, a diameter of 10 cm and a height of 3 cm has been placed in a depth of 7 cm. The simulation of 31 different antenna positions utilizes a frequency range from 1 GHz to 3 GHz.
Fig. 4.37(a) illustrates that without any further processing neither the shape nor the position of the target object can be revealed correctly. The application of background subtraction reveals a typical hyperbolic reflection signature that is shown in Fig. 4.37(b). Theoretically, a hyperbolic reflection signature can be concentrated in the origin of the reflection which allows to reveal the true shape of the reflector, see chapter 5. However, Fig. 4.37(c) illustrates, that the focusing fails, because the phase center of the LPDA is moving together with the active region if the frequency changes. In order to solve the problem the one-port calibration which has been proposed for the Orion-type IRA antenna has also been utilized for the log-periodic antenna. After the calibration standards have been taken into account Fig. 4.37(d) yields both, the shape and the position of the buried object correctly.

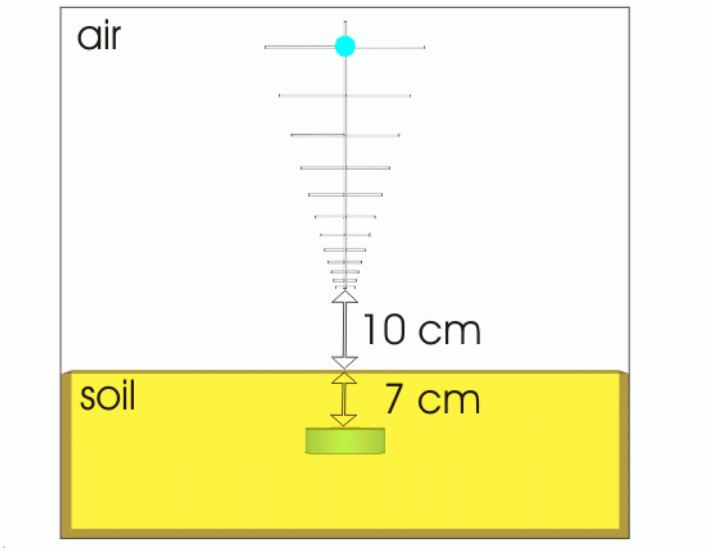

Figure 4.36: Simulation model of a GPR with a log-periodic dipole antenna.

One of the assumptions of a one-port calibration is the propagation of a plane wave. In order to verify, that the soil brick has been chosen large enough to avoid interactions of the propagating field with the surrounding boundaries a convergence study has been conducted. Therefore, additional simulations with an increased soil brick length have been conducted. Although, the simulations converge it can be obtained, that the quality of the calibration strongly depends on the brick dimensions.
From the simulation it can be found, that the frequency range from 1 GHz to 3 GHz yields a poor imaging resolution. Moreover, it is not possible to increase the frequency range any further, because the size of the smallest dipole cannot be decreased due to mechanical limitations. Therefore, the log-periodic dipole antenna has not been fabricated and will not be utilized for future GPR experiments.

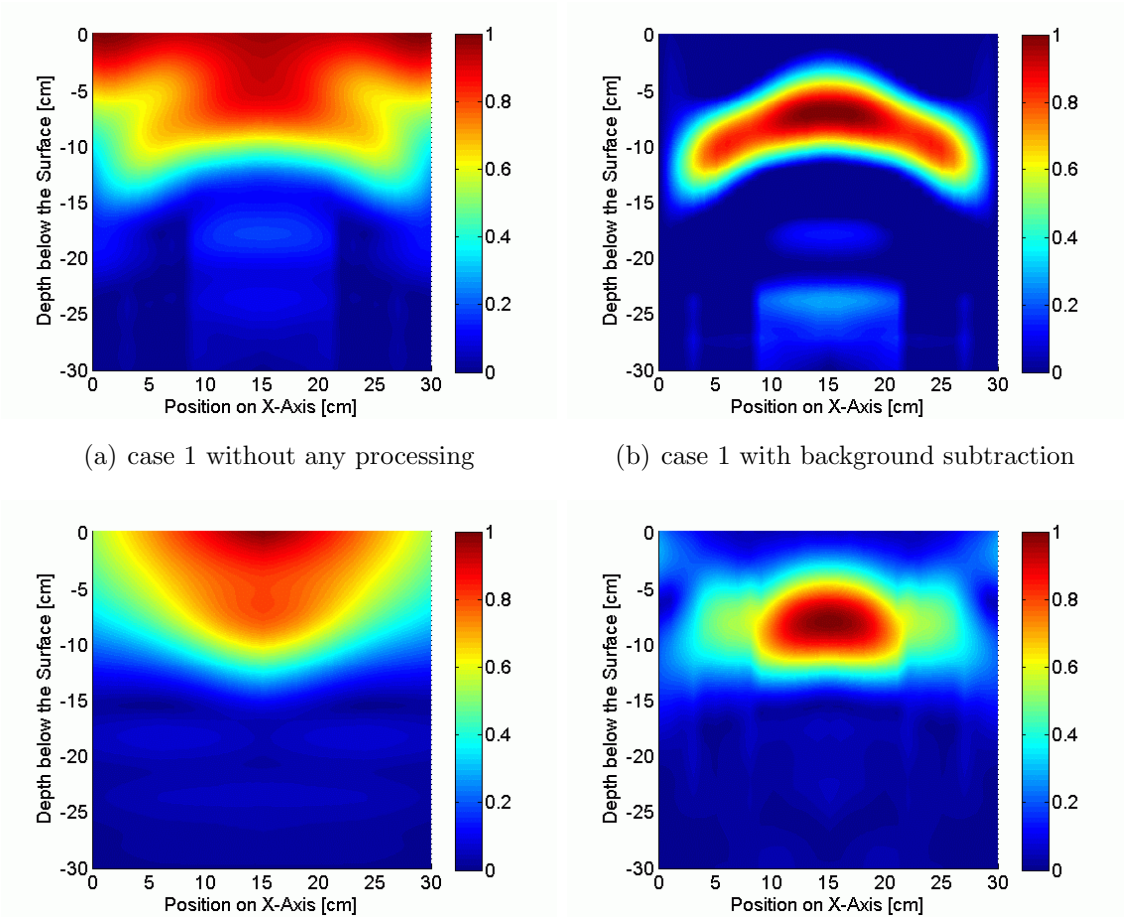

(a) case 1 without any processing

(b) case 1 with background subtraction

(c) case 1 with SAR focusing

(d) case 1 with one-port calibration

Figure 4.37: GPR simulation results of the LPDA 10 cm above the surface.

4.5 Modified Double-ridged TEM Horn Antenna

4.5.1 Design and Development

One of the most common example for a broadband antenna with a reasonable size in comparison to the operating bandwidth that is provided is the double-ridged TEM horn antenna. Such double-ridged TEM horn antennas have been reported [YL00] to be very successful in GPR applications. They fulfill the basic requirements of such a system, namely, a low return loss, a wide frequency band of operation and a reasonable gain. In this contribution we suggest two modifications of the standard double-ridged TEM horn antenna that further improve its performance. Our design goals which are not met by the well-known standard structure are a return loss of less than -10 dB and single main lobe operation in the frequency range from 2 GHz to 10 GHz. The 3D EM field simulation model and a fabricated prototype of the suggested antenna are illustrated in Figs. 4.38(a) and 4.38(b), respectively.

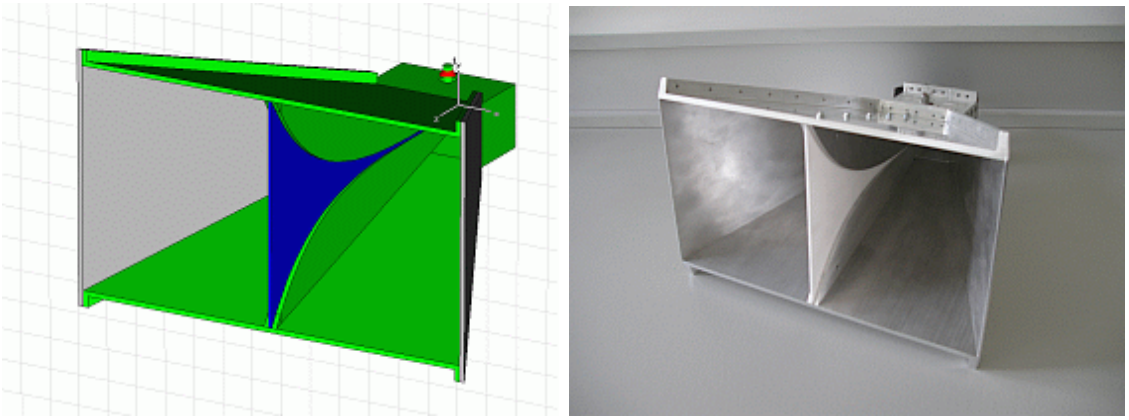

(a) MWS model (b) prototype

Figure 4.38: Modified double-ridged TEM horn antenna.

There are basically two major differences between the suggested antenna design and the standard double-ridged TEM horn antenna like it has been investigated in [BLV03] and [BF$^+$04]. Firstly, the space between the ridges is partially filled with dielectric material in order to decrease the lower frequency limit and by doing so increasing the frequency range of the antenna. At the coaxial feeding line the dielectric homogeneously fills up the gap between the ridges, whereas it has the shape of a wedge at the aperture of the antenna as shown in Fig. 4.39. Thus, the dielectric

filling has the maximum effect where it is needed most, namely, at the feeding point of the TEM horn. At this place the dimensions of the housing are small leading to a quite large lower frequency limit. This constraint can be relaxed by the insertion of the dielectric filling. At the aperture, however, a smooth transition between free space and the antenna is required in order to keep the overall return loss small. This is guaranteed by the wedge shape of the dielectric filling inside the double-ridged TEM horn antenna. The best trade-off between a reasonable average return loss and the maximum extension of the operating bandwidth down to the low frequency end has been obtained for dielectric materials with a moderate relative permittivity like that of Polytetrafluoroethylene (PTFE), known as Teflon, which is close to $\epsilon_r = 2$. Therefore, the dielectric wedge has been made of this material.

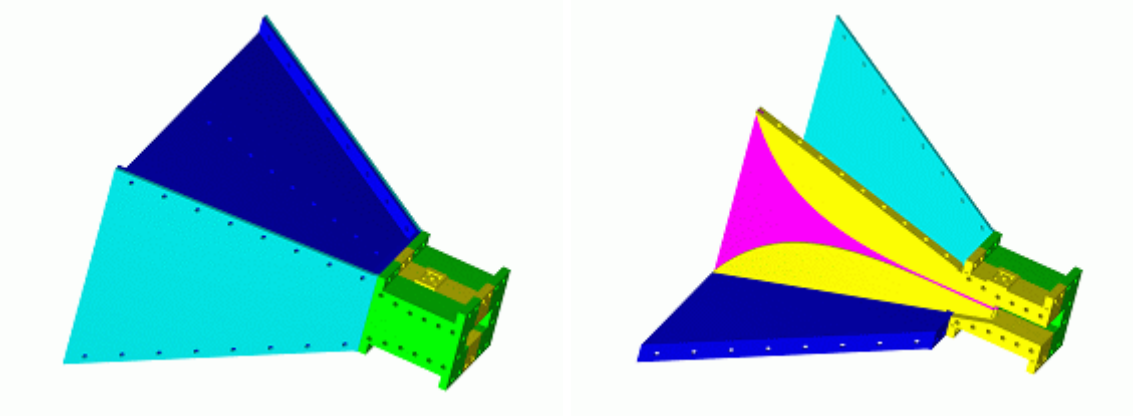

(a) complete structure (b) inner view

Figure 4.39: Shape of the homogeneous dielectric filling (AutoCAD).

As a second modification the suggested TEM horn antenna utilizes an integrated wave absorber where standard TEM horns have a short circuit. By 3D EM simulations it could be obtained that it cannot be avoided that a small portion of the energy is transmitted to the waveguide in the back direction of the antenna. This effect might occur for frequencies higher than 4 GHz where this waveguide starts to support wave propagation. Although the amount of energy transmitted in this direction is quite small it really has a bad impact on the return loss of the antenna. Hence an integrated wave absorber has been suggested in order to get rid of all unwanted reflections. The absorber consists of a double wedge of absorber foam located in a short-circuited waveguide section, as it is illustrated in Fig. 4.40.

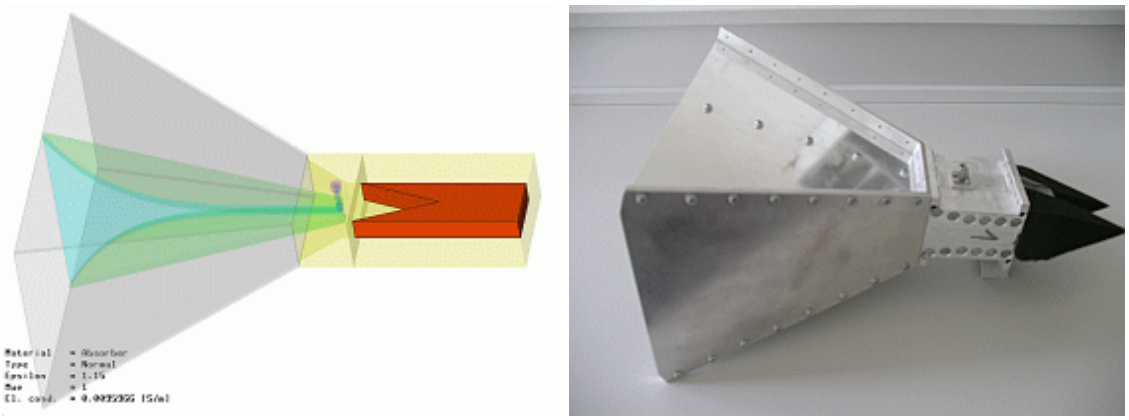

(a) MWS model (b) preliminary realization

Figure 4.40: Absorbing structure at the open end of the waveguide.

4.5.2 Antenna Characteristics

The suggested modifications of the usual TEM horn antenna design do not affect the radiation characteristic significantly. The radiation pattern in Fig. 4.41 illustrate that the single main lobe in the horn axis remains stable up to 10 GHz. At higher frequencies it starts to split into several side lobes pointing in off-axis directions with a dip of 6 dB between them along the main axis, exactly like it has been predicted in [BLV03] and [BF+04]. The directivity varies from 11.9 at 2 GHz up to 45.82 at 10 GHz and is decreasing again after the main lobe starts to split up into two major lobes. Because a single lobe antenna characteristic is required for GPR applications the operating frequency band has been chosen from 2 GHz to 10 GHz.
From Fig. 4.42 it can be revealed that the simulated, respectively, the measured return loss of the suggested new design for the double-ridged TEM horn antenna remains below -10 dB for the chosen frequency range. In addition, Fig. 4.43 illustrates the improved return loss characteristic of the new design in comparison with the well-known original design of a double-ridged TEM horn antenna. With the improved antenna design the important return loss level of -10 dB can be already achieved at 1.8 GHz whereas the original design allows only for a smaller return loss at frequencies higher than 4 GHz. The comparison of the simulated and the measured return loss for the modified double-ridged TEM horn antenna reveals a very good agreement for frequencies below 5 GHz. For higher frequencies, however, the measured return loss of the antenna is even better than the simulated one.

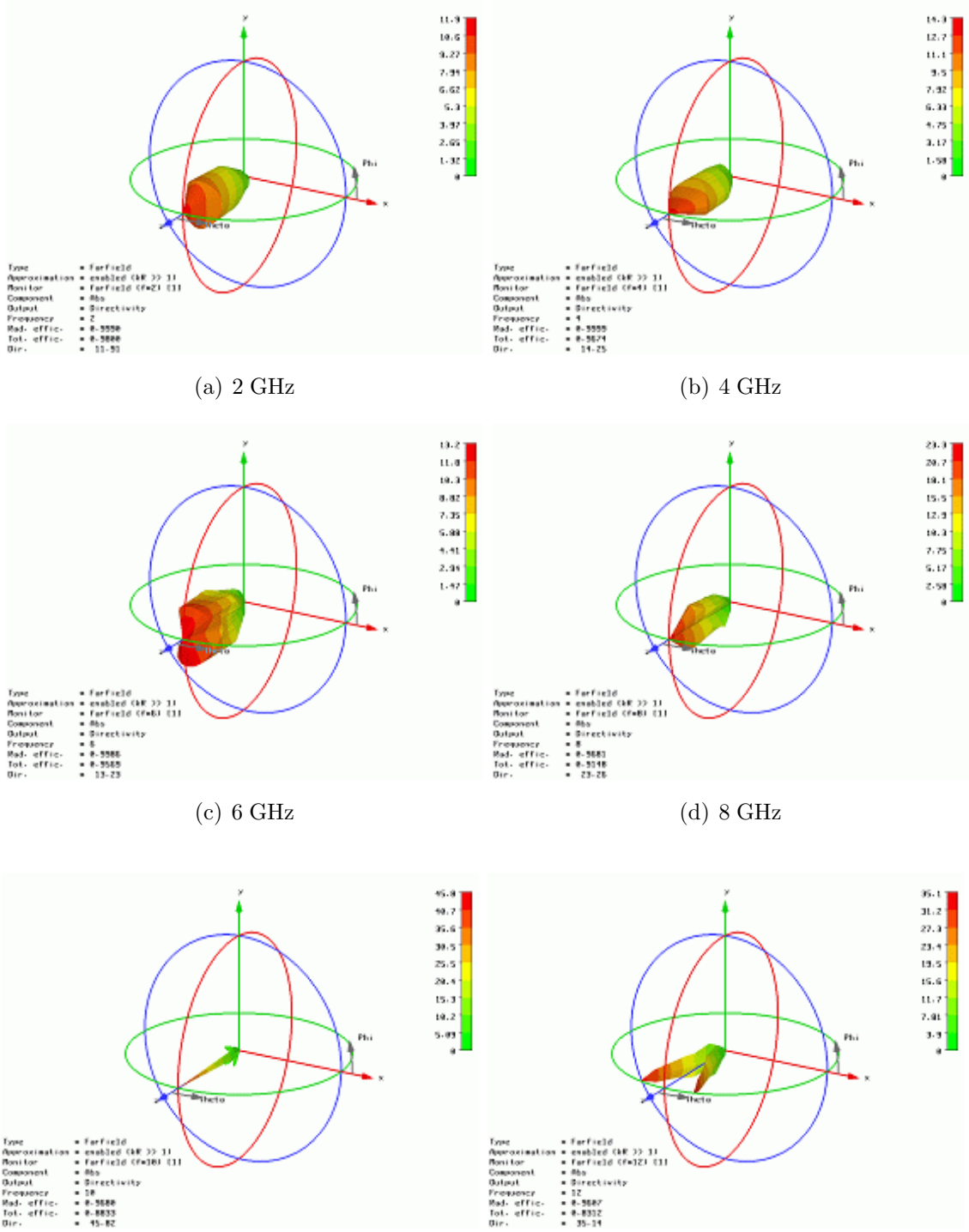

(a) 2 GHz

(b) 4 GHz

(c) 6 GHz

(d) 8 GHz

(e) 10 GHz

(f) 12 GHz

Figure 4.41: Radiation pattern of the modified double-ridged TEM horn.

The difference can be explained by the fact, that the field simulations do neither include dielectric losses nor Ohmic losses. Hence, the return loss of the real double-ridged TEM horn antenna structure is less than the simulated value. The same systematical difference between the results of the simulation and the measurement has been obtained for other types of antennas such as the modified Bujanov antenna or the small TEM horn antenna, which have also been investigated in the context of this thesis. However, the simulation allows to predict the return loss with a reasonable accuracy. In conclusion, the overall characteristics of the modified double-ridged TEM horn antenna fulfill the requirements for GPR completely.

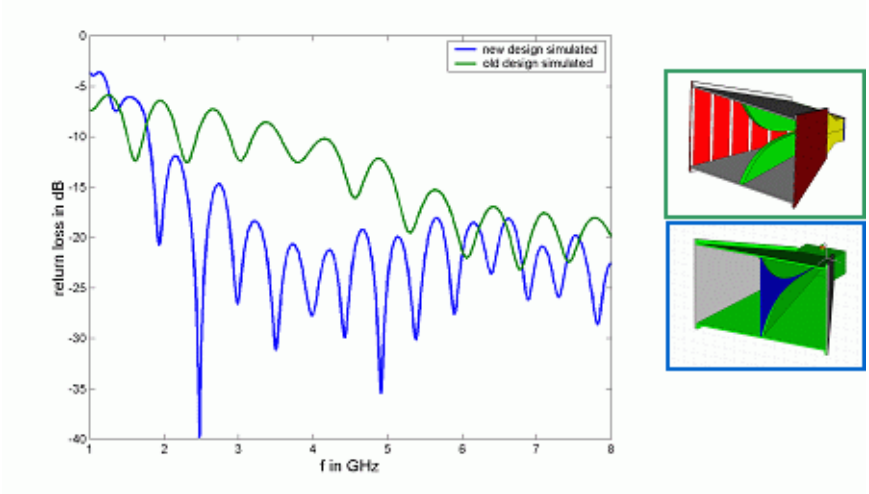

Figure 4.42: Simulated return loss of old design (green) and new design (blue).

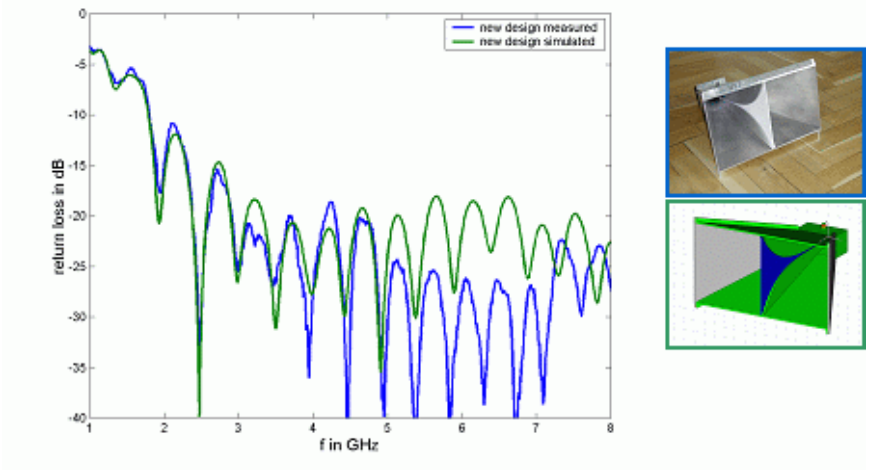

Figure 4.43: Simulated (green) and measured (blue) return loss of new design.

4.5.3 GPR Simulation Results

The integration of the double-ridged TEM horn antenna in the simulation of a GPR has been illustrated in Fig. 4.44. The antenna has been placed in a distance of 10 cm above the surface of the homogeneous soil brick with dimensions of d_x=70 cm, d_y=20 cm and d_z=20 cm. For the soil material the properties of dry sand, namely, a permittivity of $\epsilon_r = 2.5$ with a loss tangent of 0.01 have been assumed.
The cylindrical target object with a diameter of 10 cm and a height of 3 cm has been aligned parallel to the surface in a depth of 7 cm. For the simulation of a B-scan with 31 antenna positions on the x-axis across the center of the buried target object two different scenarios, namely, an air-filled cylinder with a permittivity of $\epsilon_r = 1.0$, respectively, a similar cylinder with a permittivity of $\epsilon_r = 3.5$ have been taken into account. The frequency range has been chosen from 1 GHz to 10 GHz according to the characteristics of the antenna. The results that are shown in Figs. 4.45 and 4.46 have been normalized with respect to the maximum of the amplitude in Fig. 4.45. Although some noisy signals can be recognized which indicates unwanted numerical effects, the shape and the position of the objects can be obtained for both simulations even without background subtraction. Moreover it shows, that the reflections at the top and the bottom of the object can be distinguished easily because the lateral resolution is very high due to the large range of operating frequencies.

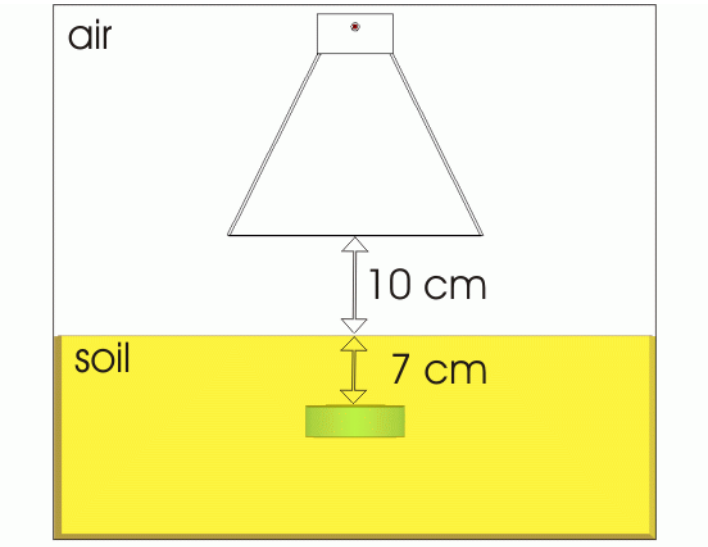

Figure 4.44: Simulation model of a GPR with a double-ridged TEM horn.

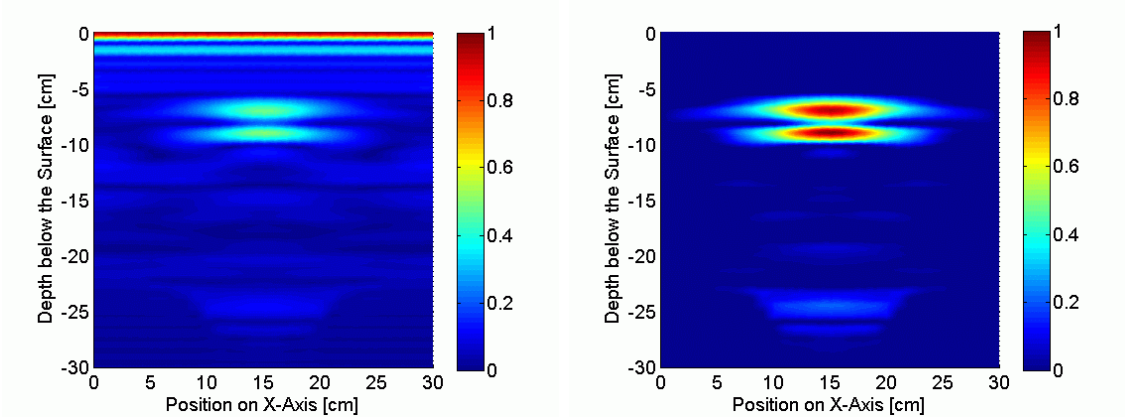

(a) object 1 ($\epsilon_r = 1.0$), no processing (b) additional background subtraction

Figure 4.45: Double-ridged TEM horn above cylindrical object ($\epsilon_r = 1.0$).

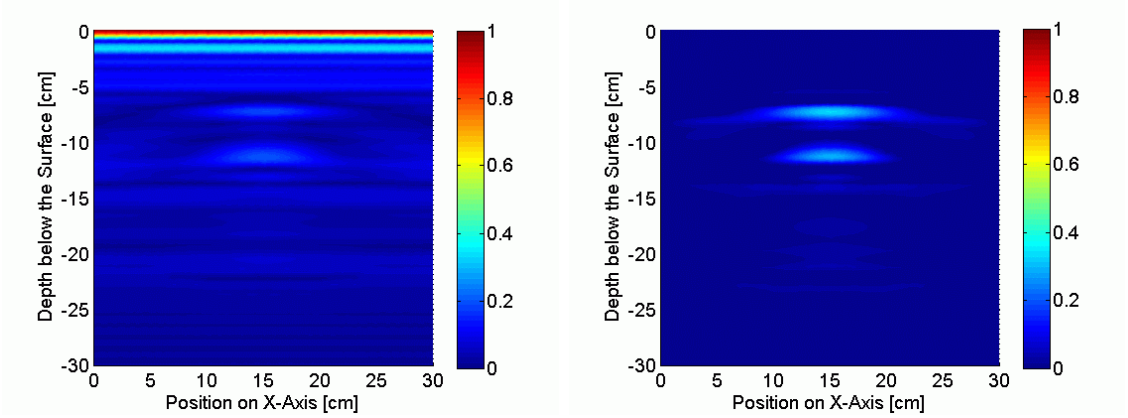

(a) object 2 ($\epsilon_r = 3.5$), no processing (b) additional background subtraction

Figure 4.46: Double-ridged TEM horn above cylindrical object ($\epsilon_r = 3.5$).

After the performance of the double-ridged TEM Horn antenna in the context of a GPR environment has been demonstrated successfully another problem has been investigated. For this case a quasi-monostatic GPR setup with two antennas has been simulated as it is illustrated in Fig. 4.47. The configuration is referred to as quasi-monostatic, because the GPR measurement is performed with a constant distance between the transmitting and the receiving antenna. The results of the quasi-monostatic setup (S_{21}) and of a corresponding single antenna system (S_{22}) are illustrated in Fig. 4.48. It shows, that without any processing the shape of the buried object is slightly overestimated for the quasi-monostatic case, which indicates the larger footprint of such a system in comparison to a monostatic GPR.

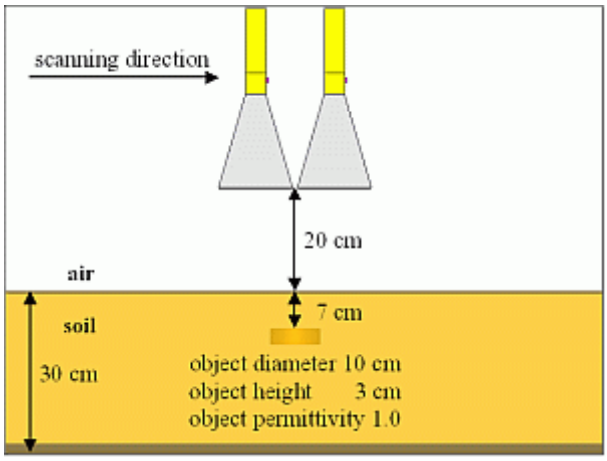

Figure 4.47: Simulation model of a quasi-monostatic GPR setup.

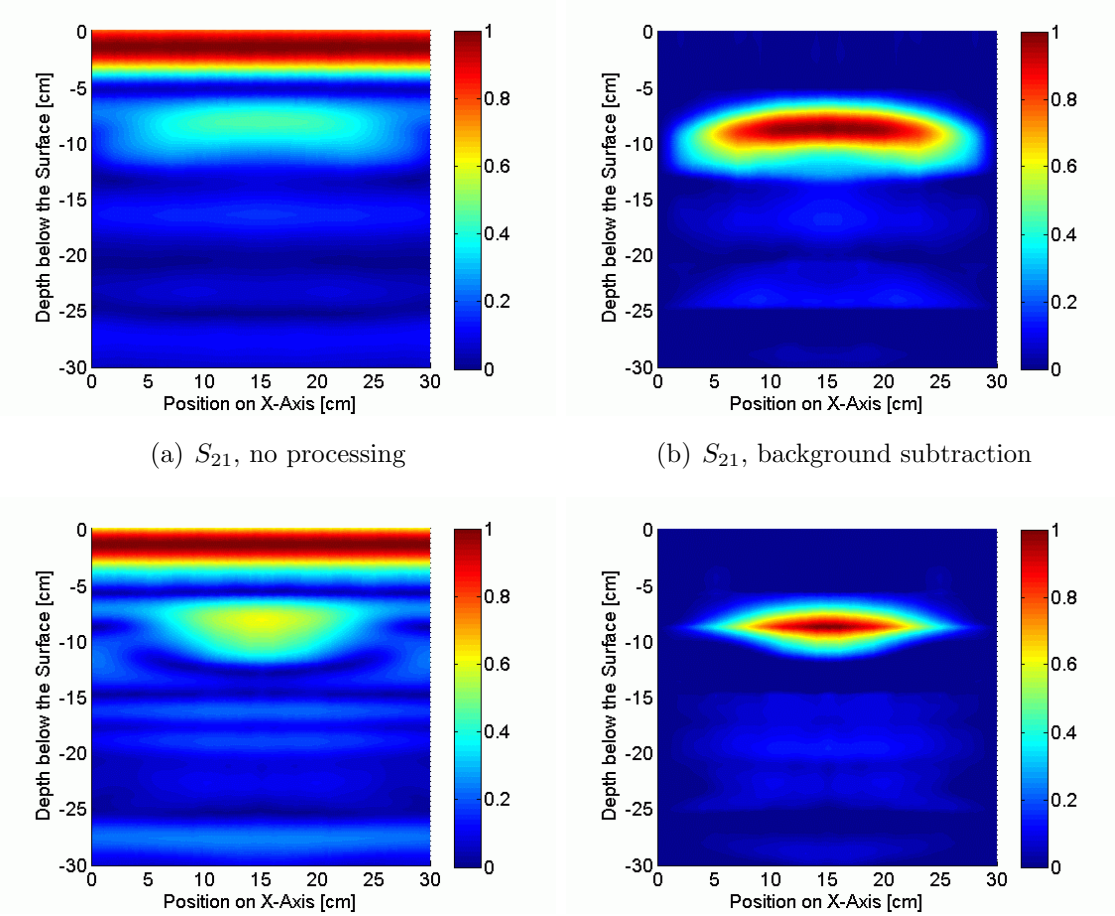

(a) S_{21}, no processing

(b) S_{21}, background subtraction

(c) S_{22}, no processing

(d) S_{22}, background subtraction

Figure 4.48: Quasi-monostatic GPR setup above cylindrical object ($\epsilon_r = 1.0$).

4.6 Small Double-ridged TEM Horn Antenna

4.6.1 Design and Development

Based on the modified TEM horn antenna, see 4.5, the small version of the double-ridged TEM horn antenna has been designed exclusively for GPR applications in the context of this thesis. It is basically the original TEM horn antenna which has been scaled down by a factor of 2 in order to achieve a more compact and lightweight design while maintaining the broad bandwidth of operating frequencies. However, all crucial design parameters have been investigated and optimized in the process in order to increase the performance in terms of operating bandwidth and radiation characteristics. The 3D EM simulation model and the final realization of the suggested antenna are illustrated in Figs. 4.49(a) and 4.49(b), respectively.

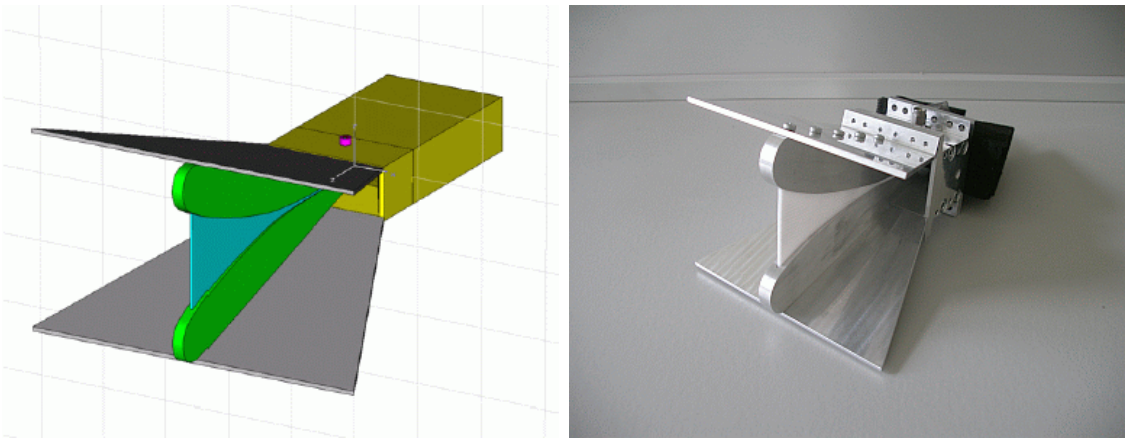

(a) MWS model (b) prototype

Figure 4.49: Small double-ridged TEM horn antenna.

For the scaled version of the double-ridged TEM horn antenna the sidewalls have been removed completely and it could be demonstrated by detailed investigations in [Mal06], that this does not affect the radiation characteristics or the bandwidth of the antenna. As it has been the case for the large version of the double-ridged TEM horn antenna the space between the ridges is partially filled with Teflon with a permittivity close to $\epsilon_r = 2$ in order to decrease the lower frequency limit and, thus, increase the frequency range of the antenna. Moreover, it can be obtained, that a modified shape of the ridges increases the band of operating frequencies to the lower end in comparison to the original design of a TEM horn antenna.

Thus, one general drawback of the down-scaling of any given antenna, namely, the up-scaling of the lowest usable frequency could be partially compensated. Fig. 4.50 illustrates the modified shape of the ridges and the dielectric wedge. The dimensions of the waveguide section of the new antenna have been slightly modified. However, it starts to support wave propagation at higher frequencies and a small portion of the energy is transmitted to the waveguide in the back direction of the antenna. Therefore, the integrated wave absorber which has been already suggested for the large TEM horn antenna in order to get rid of any unwanted reflection has been utilized. The SMA-connector feeding remains unchanged and Fig. 4.51 illustrates the final sketch of the small TEM horn which has been used for the fabrication.

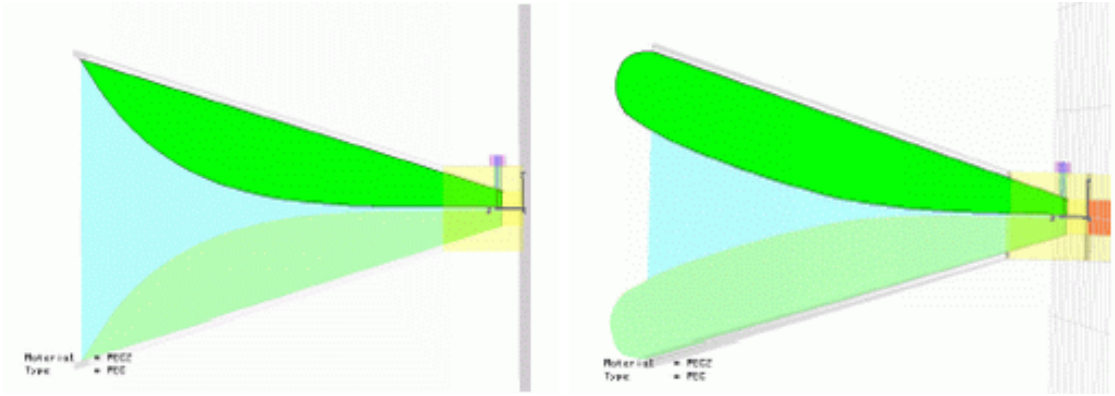

(a) original ridge (b) modified ridge

Figure 4.50: Modification of the geometrical shape of the ridges.

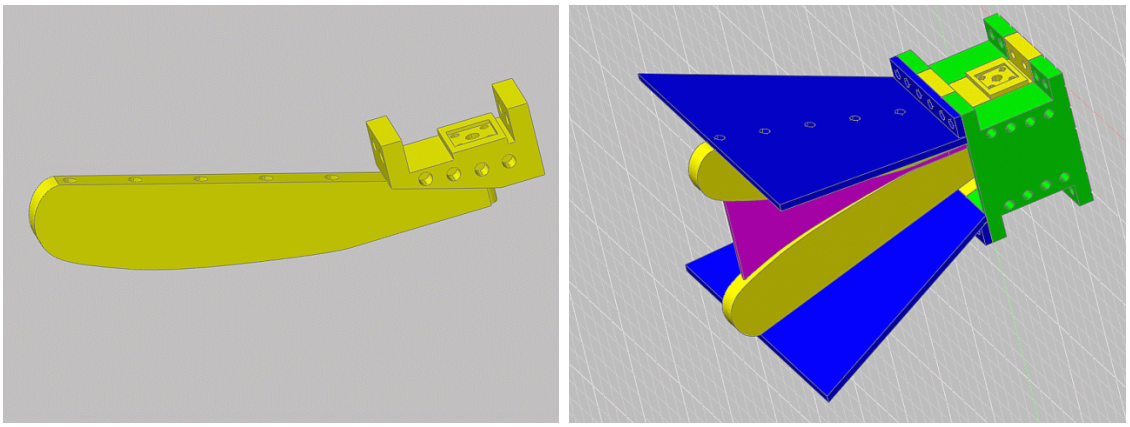

(a) AutoCAD model of the ridge (b) AutoCAD model of TEM horn

Figure 4.51: Final sketch of the small double-ridged TEM horn antenna.

4.6.2 Antenna Characteristics

The simulated and the measured return loss of the small double-ridged TEM horn antenna are compared in Fig. 4.52. As it can be seen the return loss of the antenna is less than -10 dB for frequencies between 3 GHz and 18 GHz. Thus, the lower limit of the frequency range has been increased only slightly in comparison to the large TEM horn antenna which illustrates the success of the bandwidth optimized antenna scaling. In comparison, the results of the simulation and the measurement generally agree. However, it can be obtained that the measured return loss is smaller than the simulated one for frequencies between 6 GHz and 16 GHz. Again, the exclusion of dielectric and Ohmic losses in the simulation leads to the difference between the measured and the simulated return loss exactly as it has been obtained for the large double-ridged TEM horn. The radiation pattern of the small TEM horn antenna which is shown in Fig. 4.53 has also been investigated by 3D EM simulation for different frequencies. The direction of the main lobe remains almost constant for frequencies between 2 GHz and 10 GHz whereas the directivity of the TEM horn antenna increases from 5 up to 46 if the frequency increases. Similar to the original sized double-ridged TEM horn antenna the main lope starts to split for frequencies above 10 GHz which defines the upper limit for the operating frequency range.

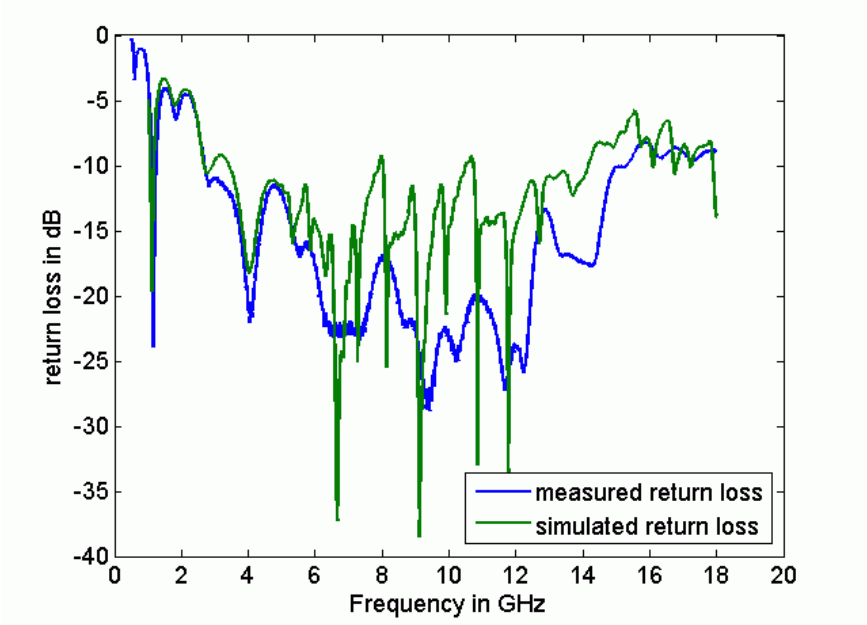

Figure 4.52: Return loss of the small double-ridged TEM horn antenna.

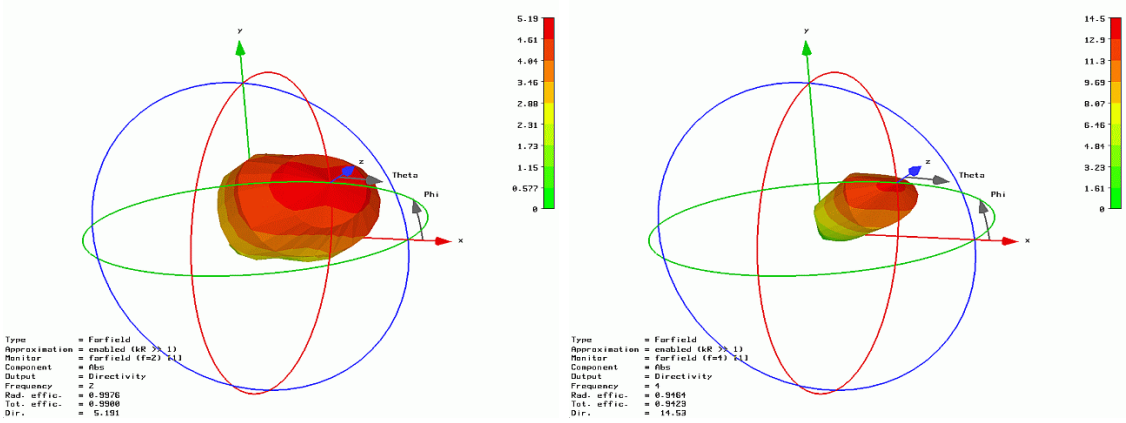

(a) 2 GHz (b) 4 GHz

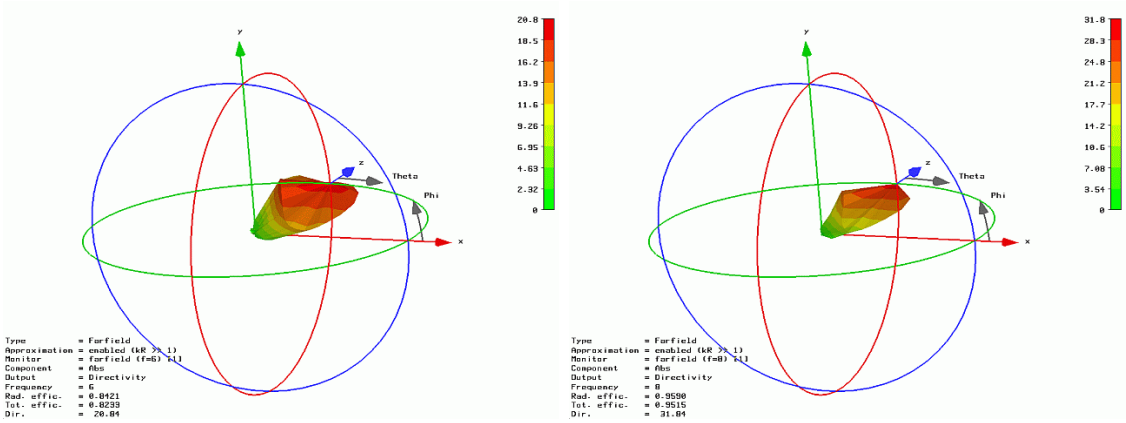

(c) 6 GHz (d) 8 GHz

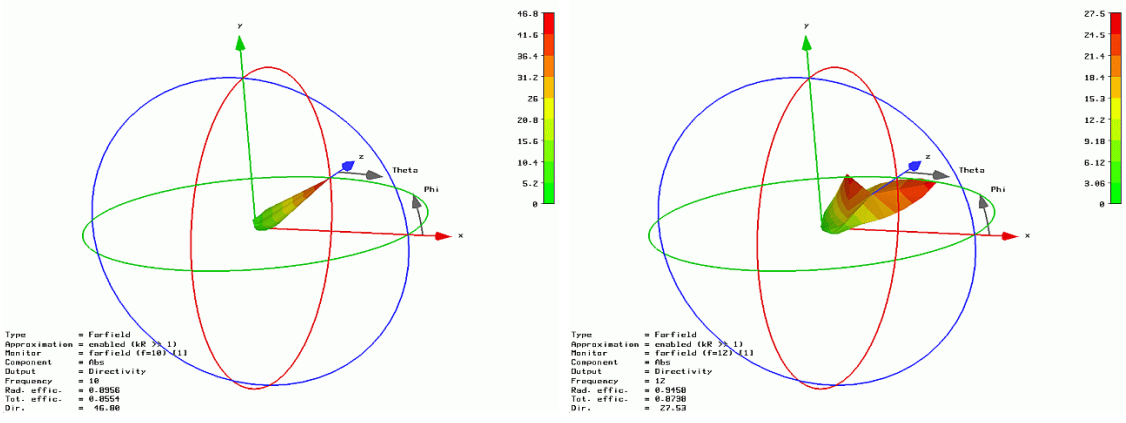

(e) 10 GHz (f) 12 GHz

Figure 4.53: Radiation pattern of the small double-ridged TEM horn antenna.

4.6.3 GPR Simulation Results

The simulation model of the small double-ridged TEM horn antenna in the context of a GPR environment is illustrated in Fig. 4.54. The antenna has been placed in a distance of 10 cm above the surface of the homogeneous soil brick for which the permittivity of dry sand, namely, $\epsilon_r = 2.5$ with a loss tangent of 0.01 has been assumed. The dimensions of the homogeneous soil brick, namely, d_x=60 cm, d_y=20 cm and d_z=20 cm have been chosen large enough in order to avoid any interactions between the radiated field and the surrounding boundaries of the simulation model.
The cylindrical target object with a diameter of 10 cm and a height of 3 cm has been aligned parallel to the surface in a depth of 7 cm. The two different scenarios which have been investigated previously using different antennas have also been considered for the simulation of the small double-ridged TEM horn. On the one hand an air-filled cylinder with a permittivity of $\epsilon_r = 1.0$ has been assumed which represents a model of the air-gap within a realistic AP mine, see B. On the other hand a similar cylindrical object with a permittivity of $\epsilon_r = 3.5$ has been chosen in order to study the response of a target which reveals only a poor reflectivity. According to the radiation properties of the antenna an operating frequency range from 3 GHz to 10 GHz has been chosen for the simulation and 31 different antenna positions on the x-axis across the center of the object are taken into account.

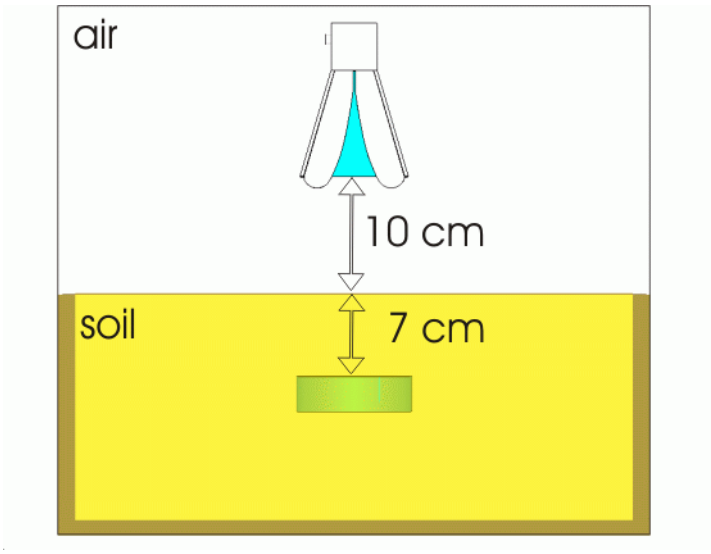

Figure 4.54: Simulation model of a GPR with a small double-ridged TEM horn.

Figs. 4.55 and 4.56 illustrate the results of the two B-scan simulations above target objects with a permittivity of $\epsilon_r = 1.0$, respectively, $\epsilon_r = 3.5$. All images have been normalized with respect to the maximum amplitude of the case with a target permittivity of $\epsilon_r = 1.0$ which allows to compare the results of both simulations. It shows, that the target objects can be clearly recognized even without a further background subtraction. As it has been the case for the Orion-type IRA the reflections at both interfaces between the object and the soil merge for the case with $\epsilon_r = 1.0$ whereas they can clearly be distinguished for the case with $\epsilon_r = 3.5$. This effect can be explained by constructive and destructive interference of the contributing reflected signals at the top and the bottom of the object, see 3.7.3.

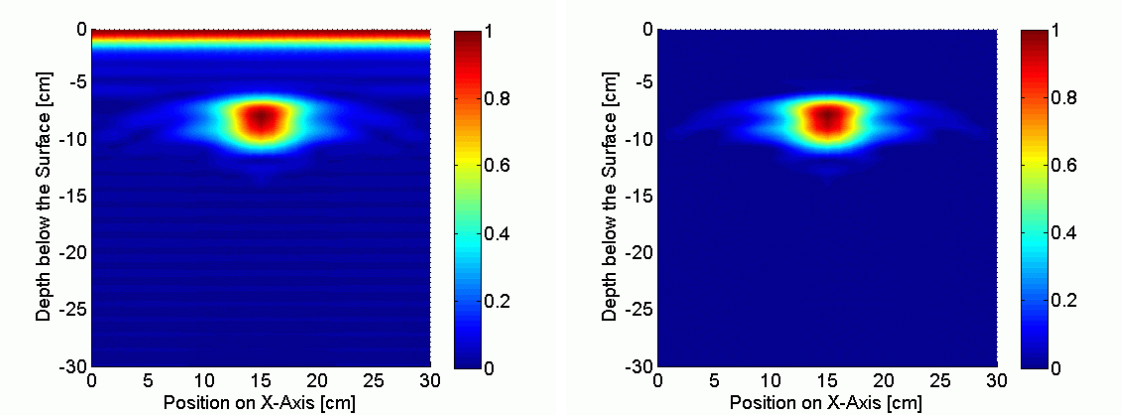

(a) object 1 ($\epsilon_r = 1.0$), no processing (b) additional background subtraction

Figure 4.55: Small double-ridged TEM horn above cylindrical object ($\epsilon_r = 1.0$).

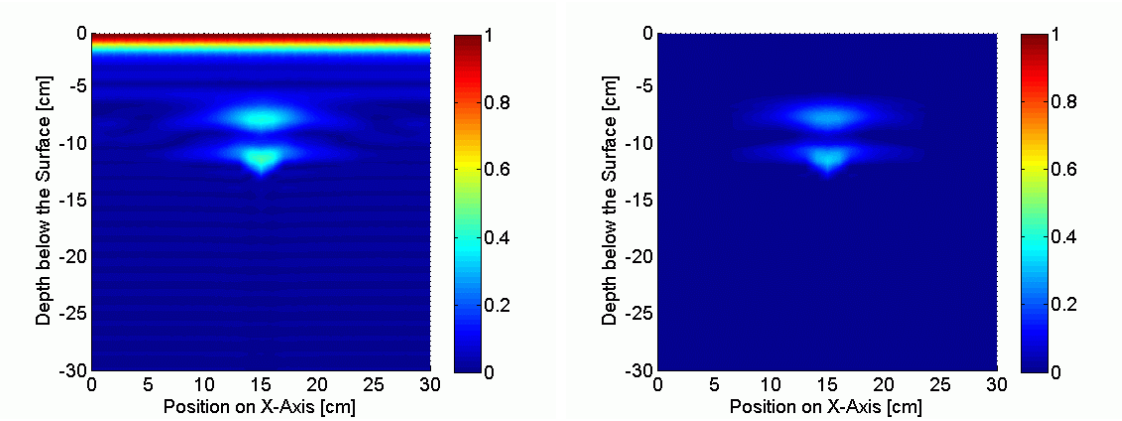

(a) object 2 ($\epsilon_r = 3.5$), no processing (b) additional background subtraction

Figure 4.56: Small double-ridged TEM horn above cylindrical object ($\epsilon_r = 3.5$).

In addition, the small double-ridged TEM horn antenna has been placed in a height of 10 cm above two different rough surfaces which have been introduced in 3.3.3. The well-known cylindrical object with a permittivity of $\epsilon_r = 1.0$ has been buried in a depth of 7 cm below the surfaces for which a peak-peak distance of 3 cm for model 1, respectively, 6 cm for model 2 and a wave amplitude of 1.5 cm, respectively, 3 cm have been assumed, see Fig. 4.57. The results of the corresponding B-scan simulations in Fig. 4.58 illustrate a periodic reflection which represents the peaks of the sinus-like shaped surfaces. The periodic reflection pattern at the low points of the surface, however, can only be identified for the case of surface model 2. It can also be concluded, that the surface roughness effects the reflection signature of the buried object. Nonetheless, it can still be easily identified in both cases.

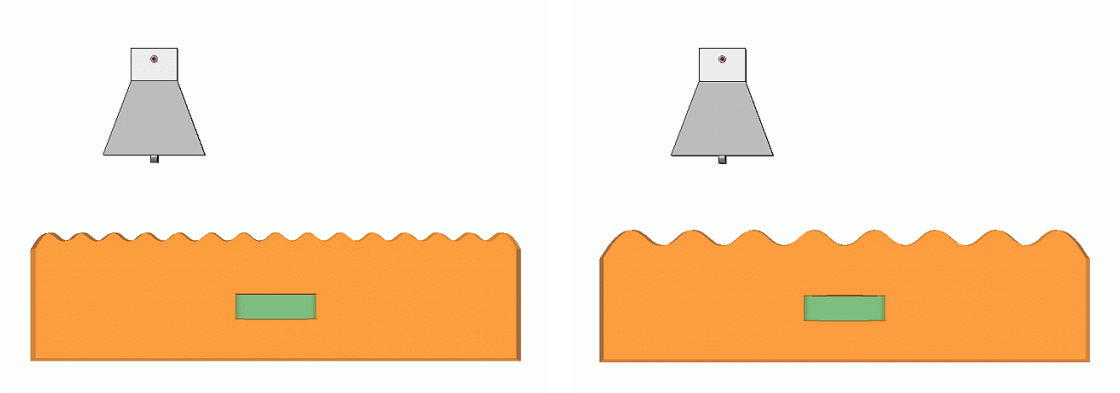

(a) rough surface model 1 (b) rough surface model 2

Figure 4.57: Small double-ridged TEM horn above surface roughnesses.

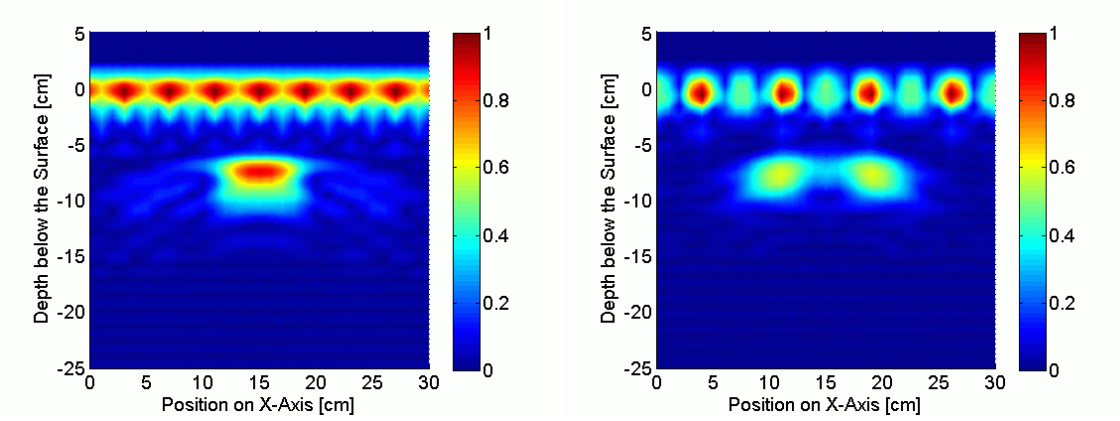

(a) rough surface model 1 (b) rough surface model 2

Figure 4.58: Results of the simulation with surface roughnesses.

4.7 Modified Bujanov Loop Antenna

4.7.1 Design and Development

As an alternative approach for the application of common principles for the construction of wideband antennas a loop structure has been reported in [KB+01; KA+03] has been analyzed using 3D field simulation techniques. In order to stabilize the radiation pattern and the position of the phase center the original design has been modified [BA+07]. Hence, the antenna will be referred to as modified Bujanov loop antenna. This type of antenna is very lightweight, low cost, easy to fabricate and shows an extremely wide bandwidth. Fig. 4.59 illustrates the shape and the design of such a modified Bujanov antenna. The antenna is made of a single thin metallic sheet as shown in Fig. 4.60 which is bended to form a spiral. A standard 50 Ohm SMA connector is used for the feeding of the antenna. The first part of the antenna consists of a loop formed by a metallic sheet and the second part consists of a TEM horn which is formed by further extending and flaring of the loop part. The antenna radiates a linearly polarized field, has a medium gain and a wide band of operating frequencies which can be changed by proper scaling of the structure.

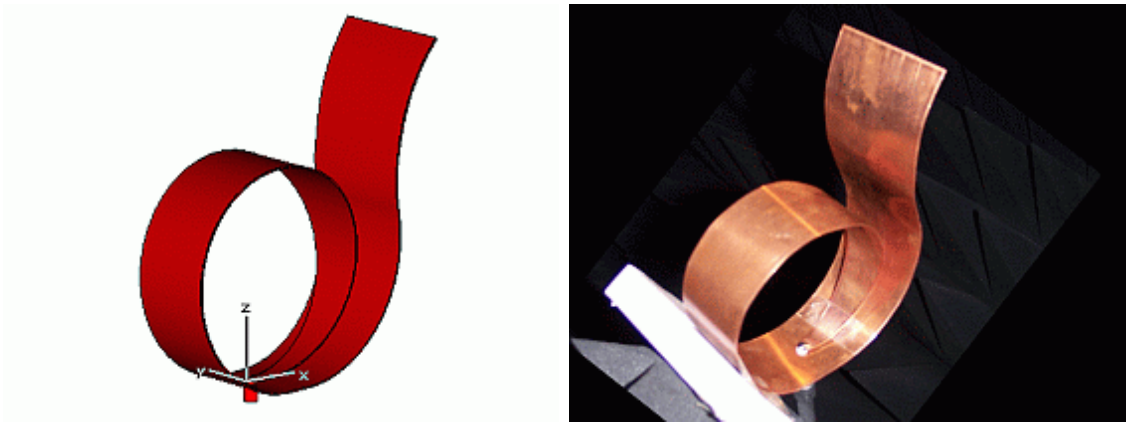

(a) MWS model (b) prototype

Figure 4.59: Modified Bujanov loop antenna with spiral shape.

In the following the modified structure of the Bujanov antenna will be explained. The shape of the metallic sheet which is used for the fabrication of the antenna is shown in Fig. 4.60. The tapered portion a along with some part of the straight portion b of the metal sheet is bent to form a loop. The rest of the straight portion

of the metallic sheet is flared outwards to form the shape of a horn antenna. The small hole at the center of the metallic sheet is used to connect the SMA connector at the tip of the tapered section for feeding the antenna. The diameter of the circular hole is the same as the diameter of the SMA connector. The cross section of the Bujanov antenna and the feeding SMA connector are shown in Fig. 4.61. The input impedance is determined by the SMA connector which has been chosen to be 50 Ohm. The dimensions of the antenna itself are depending on the dimensions of the parts a, b, c and the width w of the metallic sheet, respectively.

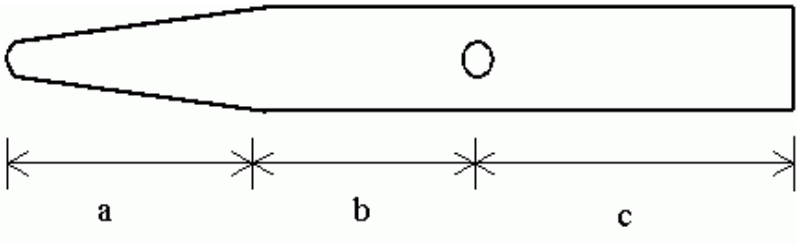

Figure 4.60: Thin metallic sheet outlines of the modified Bujanov antenna.

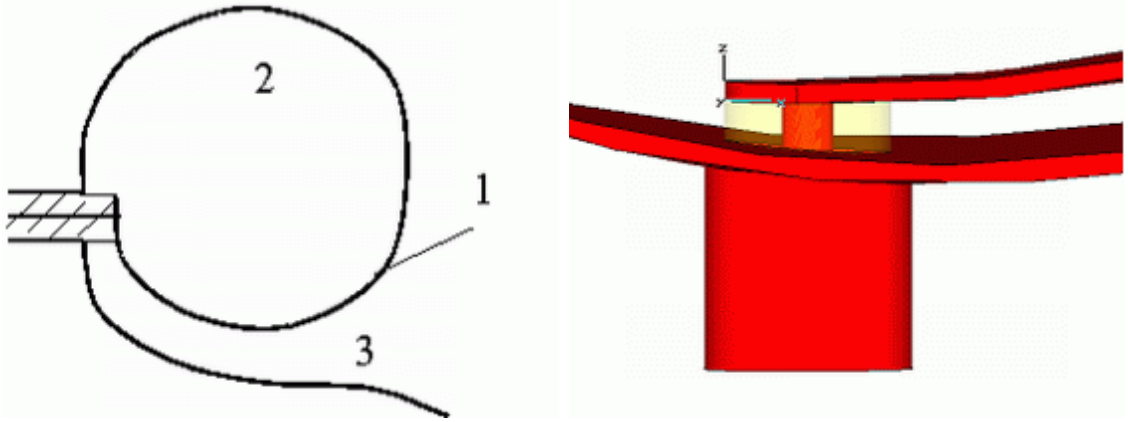

(a) cross section

(b) SMA connector

Figure 4.61: Further design specifications of the modified Bujanov antenna.

In [KB+01] it has been proposed that the antenna can be viewed as a combination of an electric monopole (1), a magnetic dipole (2) and a TEM horn (3) as shown in Fig. 4.61(a). However, further investigations revealed that this assumption does not hold true [BA+07]. The aim of the loop part is basically to stabilize the antenna. In order to increase the stability and, thus, fix the radiation pattern of the antenna it is placed inside foam or thermocol with a relative permittivity of $\epsilon_r = 1$.

4.7.2 Antenna Characteristics

The simulated and the measured return loss of the modified Bujanov antenna are compared in Fig. 4.62. As it can be seen the return loss of the antenna is less than -14 dB in the operating frequency range of 1 GHz to 18 GHz with a moderate agreement between the simulated results and the the results of the measurement. However, it can be concluded that the measured return loss is higher for frequencies between 6 GHz and 10 GHz and smaller than the simulated one for frequencies above 10 GHz exactly as it has been observed in previous simulations. This phenomena can be explained with the assumption of PEC material for the 3D field simulation. However, metal losses which are indirectly improving the return loss of the antenna are not taken into account because they can lead to unwanted instabilities of the simulation software. Additional modifications of the shape of the horn part and an optimization of various parameters like the feeding or the width and the shape of the metal yield further improvements of the antenna characteristics. The radiation pattern of the modified Bujanov antenna has been investigated by 3D EM field simulation for different frequencies as it is shown in Fig. 4.63. Size and direction of the main lobe remain almost constant for frequencies between 1 GHz and 16 GHz and the directivity of the fabricated prototype varies between 5 and 23.

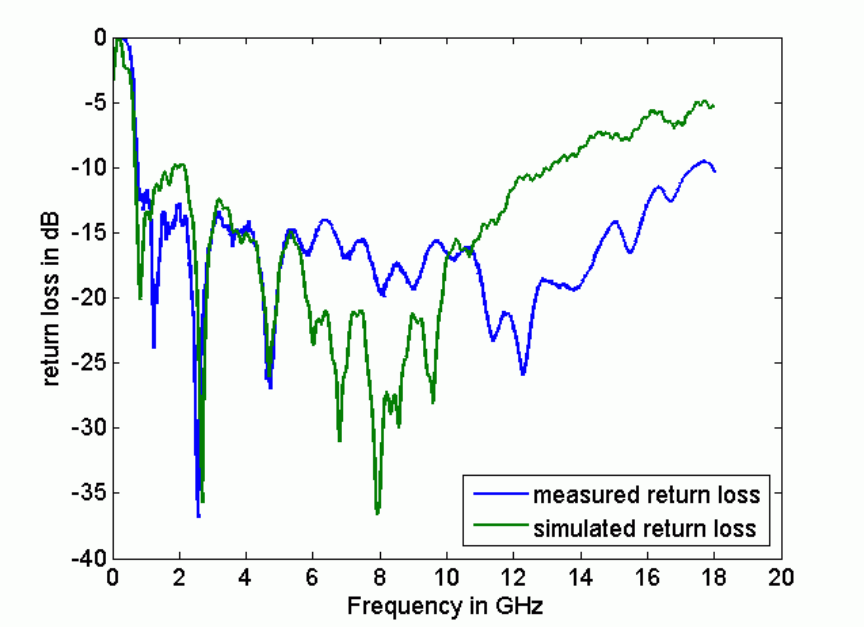

Figure 4.62: Simulated and measured return loss of the Bujanov loop antenna.

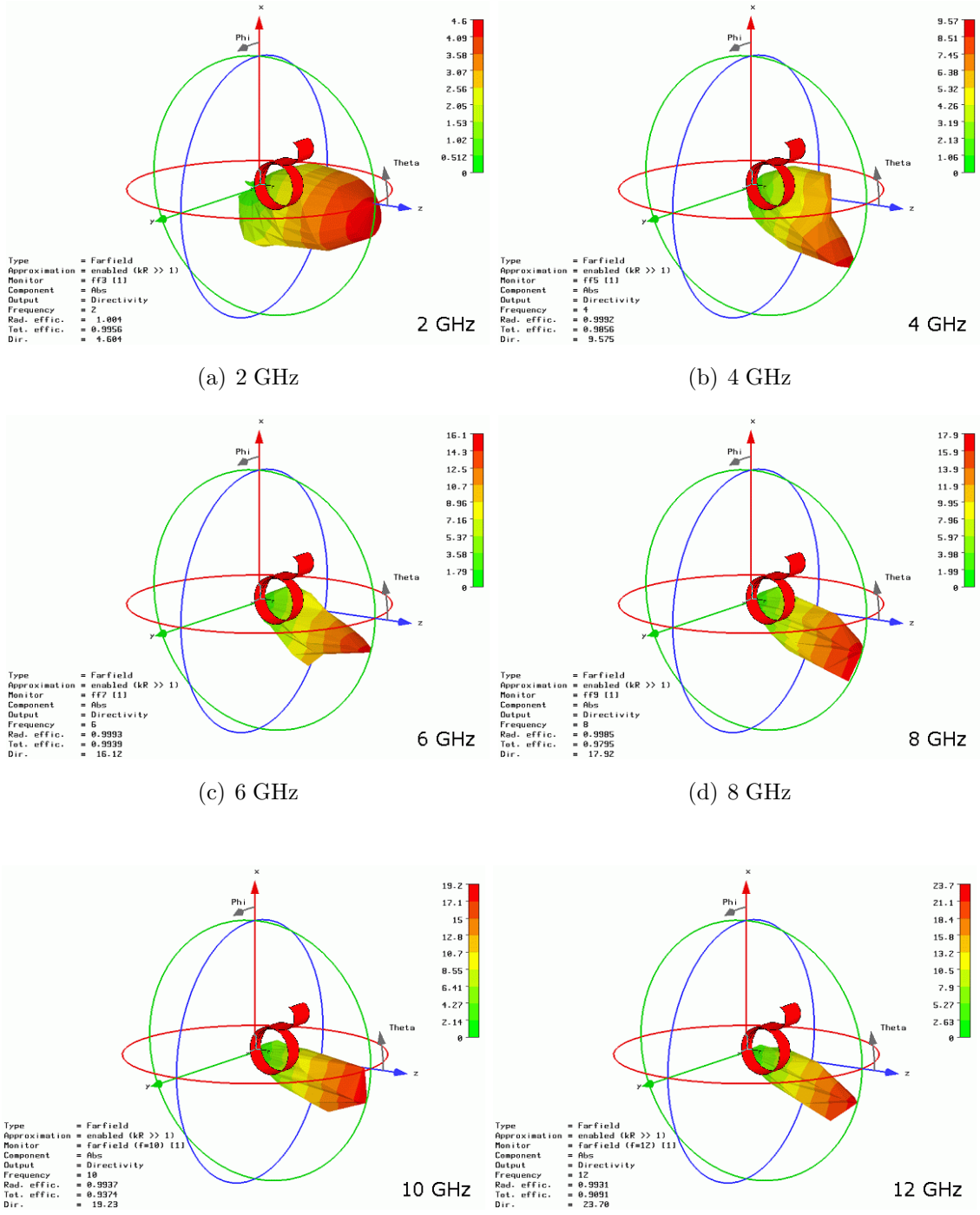

(a) 2 GHz

(b) 4 GHz

(c) 6 GHz

(d) 8 GHz

(e) 10 GHz

(f) 12 GHz

Figure 4.63: Radiation pattern of the modified Bujanov loop antenna.

4.7.3 GPR Simulation Results

As it has been the case with the other antennas that have been investigated in the context of this thesis the modified Bujanov loop antenna has been integrated in the simulation of a GPR environment. The corresponding model is illustrated in Fig. 4.64. The antenna has been placed in a distance of 10 cm above the surface of the homogeneous soil brick with dimensions of d_x=70 cm, d_y=20 cm and d_z=20 cm. For the soil material the properties of dry sand, namely, a permittivity of $\epsilon_r = 2.5$ with a loss tangent of 0.01 have been assumed. It should be noted, that the center of the radiated energy beam reveals a spacial offset of 10 cm along the x-axis from the center of the loop which must be taken into account for the simulation.
The cylindrical target object with a diameter of 10 cm and a height of 3 cm has been aligned parallel to the surface in a depth of 7 cm. For the simulation of a B-scan with 31 antenna positions on the x-axis across the center of the object two scenarios have been taken into account. The first case utilizes an air-filled object with a permittivity of $\epsilon_r = 1.0$, whereas the second scenario represents the case of a similar object with a permittivity of $\epsilon_r = 3.5$. An operating frequency range from 1 GHz to 10 GHz has been chosen for the simulation. The corresponding results that are illustrated in Figs. 4.45 and 4.46 have been normalized with respect to the maximum of the amplitude in Fig. 4.45 which allows to compare both cases.

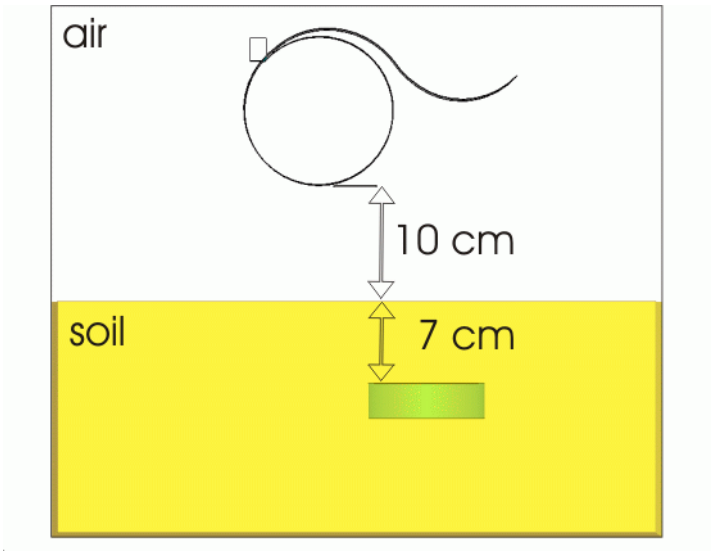

Figure 4.64: Simulation model of a GPR with a modified Bujanov antenna.

It shows, that the position of the target objects can be recognized even without a further background subtraction. The reflections at the upper and lower interface between the target object and the surrounding soil can be distinguished which indicates a large lateral resolution. In comparison to other antennas the amplitude of the reflected signals is smaller which means that parts of the reflected energy have not been received by the antenna. This effect can be explained by the frequency dependent inclination of the radiated energy beam. Moreover, a background reflection in a depth of 5 cm can be identified which is overlapping the reflection from the buried object for both scenarios. Due to the systematic nature of this reflection it can be, however, removed completely by the background subtraction.

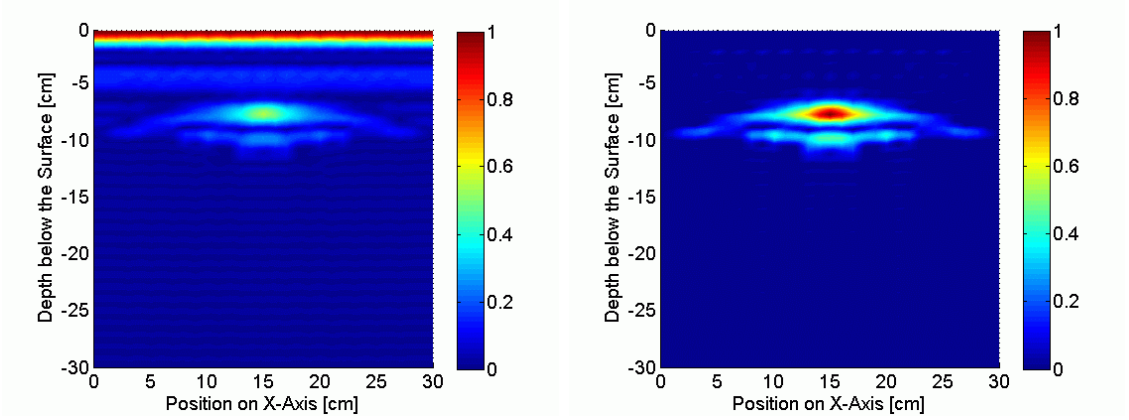

(a) object 1 ($\epsilon_r = 1.0$), no processing (b) additional background subtraction

Figure 4.65: Modified Bujanov antenna above cylindrical object ($\epsilon_r = 1.0$).

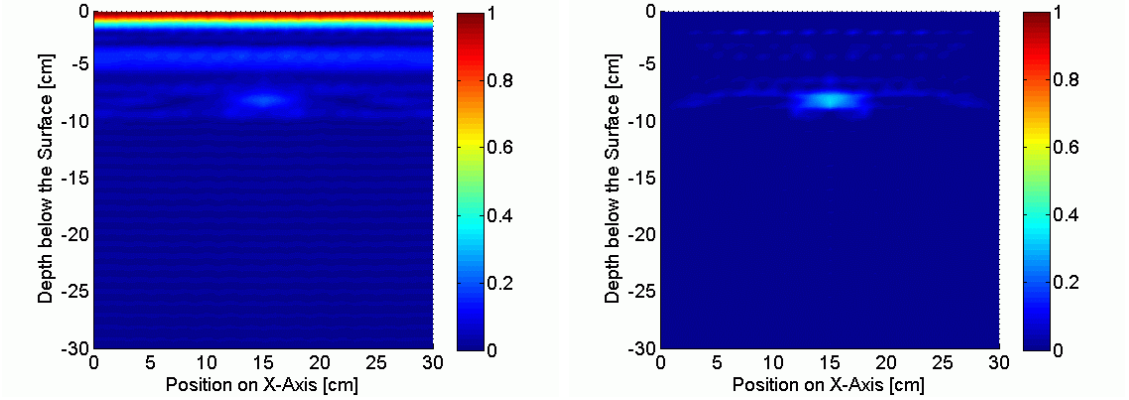

(a) object 2 ($\epsilon_r = 3.5$), no processing (b) additional background subtraction

Figure 4.66: Modified Bujanov antenna above cylindrical object ($\epsilon_r = 3.5$).

Chapter 5

Focusing by Synthetic Apertures

5.1 Introduction

The important problem of forming subsurface images from monostatic or bistatic ground penetrating radar (GPR) systems has been addressed frequently. In this chapter it will be shown how the resolution of GPR images can be improved significantly by means of synthetic aperture radar (SAR) focusing. While many of the suggested focusing concepts still suffer from unpredictable reflection, refraction and dispersion effects the proposed SAR focusing technique not only handles these problems but turns them into advantages that decrease the computational effort significantly. The fast SAR focusing technique that will be investigated allows for reducing the 3D problem which is encountered when an image of a subsurface target is to be reconstructed to a 2D one by focusing only on a single layer of the corresponding data stack. In order to estimate the influence of different antenna characteristics and array parameter on the performance of the SAR focusing a method for the calculation of the EM field distribution of antenna arrays which utilizes both, dipole elements and realistic GPR antenna characteristics, will be considered.
The simulation results for the dipole arrays are obtained analytically whereas the other calculations are done using 3D field simulation. By means of applying this array simulation technique the influence of different parameter such as the number of elements in the synthetically generated array, the distance between these elements, the position of the focusing point, the distance between the antenna and the layer on which to focus on will be addressed and discussed. Moreover, different strategies for a further optimization of the SAR focusing will be investigated.

5.2 Common Processing Techniques

5.2.1 Fundamental SAR Processing

The concept of synthetic aperture radar (SAR) was first introduced by Carl Wiley [Wil54]. He assumed that every antenna that has a sufficiently wide beam width in the along-track direction is illuminating a given target or area from different positions. Hence, the ensemble of different locations of the antenna constitute the synthetic aperture of the system. The distance from the sensor to the target is called range. The concept of SAR basically consists of a signal processing that combines the received reflections of a specific target from different illuminating positions into a well-focused, high-resolution image. For the processing of the SAR focusing the differences of the phase signal of the individual signals which have been taken into account are corrected for a given point on the surface. Subsequently the individual signal contributions are combined by constructive and destructive interference. This yields an effective aperture which is significantly larger than the antenna itself resulting in the terminology synthetic aperture radar as illustrated in Figs. 5.1.

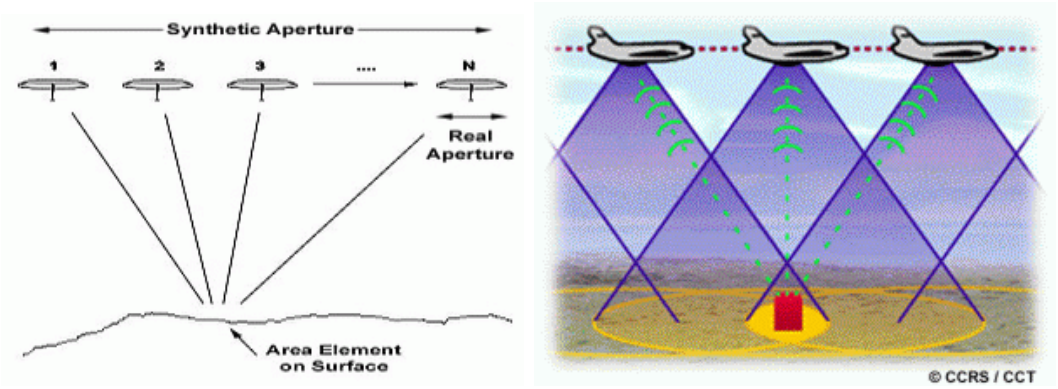

Figure 5.1: Concept of a SAR data acquisition [Var05e].

Combining the series of observations as if they would have done with one large antenna requires significant computational resources. The resulting focused reflectivity distribution contains amplitude and phase. The phase information, however, is often discarded for basic applications. The amplitude contains information about the ground structure similar to a photographic picture of the observed area. However, the interpretation of radar images is not that simple, wherefore the experimental results are often compared with measurements over known ground structures.

The maximum range of a SAR system is limited, as the received signal to noise ratio decreases with an increasing range. The basic concept of SAR processing can be enhanced in various ways to collect more information and in the following a brief review of common SAR techniques will be given according to [Sou99; Che02; CB06].

5.2.2 Doppler Beam Sharpening

The so-called Doppler Beam Sharpening (DBS)is a commonly used technique for SAR applications. If the real aperture of the antenna is small in comparison to the wavelength which is utilized, the emitted radar energy spreads over a wide area. The Doppler Beam Sharpening processing takes advantage of the so-called Doppler effect. Thus, targets ahead of the platform return a Doppler up-shifted signal and targets behind the platform return a Doppler down-shifted signal. The amount of shift varies with the angle forward or backward from the normal direction.
If the speed of the platform is known, the returned target signal can be placed in a specific angle so that the size of the radar beam reduces significantly. Based on the ability to distinguish smaller Doppler shifts the system can have many very tight beams concurrently. DBS dramatically improves the angular resolution of the SAR picture. However, it is more difficult to take advantage of this technique for improving the estimation of the range resolution. Moreover, for a GPR system the radar platform usually does not move during the data acquisition.

5.2.3 Polarimetric SAR Processing

Radar waves have a certain polarization and different materials reflect these waves with different intensities, but anisotropic materials such as grass often reflect different polarizations with different intensities. Some materials will also convert one polarization into another. By emitting a mixture of polarizations and using receiving antennas with a specific polarization, several different images can be collected from the same target object. Often three different images are used as the three color channels in a synthesized image. When all linear polarization combinations are utilized, the complete scattering properties of a radar target can be determined considering a specific frequency, incidence angle and azimuth direction. Computerized information extraction, such as terrain classification, is an important component of polarimetry and the interpretation of the resulting colors requires significant testing

of known materials. New developments include the utilization of changes in the random polarization returns of some surfaces such as grass or sand, between two images of the same location at different points in time. Thus, a polarimetric SAR system allows to detect changes which are not visible to optical systems [CKB98].

5.2.4 Interferometric SAR Processing

Rather than discarding the phase information of the SAR image as it done for the basic SAR processing, additional information can be extracted from it. If two observations of exactly the same terrain from two different positions are available, an aperture synthesis can be performed which provides the resolution performance that would be given by a radar system with dimensions equal to the separation of the two measurements. This technique is called interferometric SAR (InSAR). If two samples are obtained simultaneously by placing two antennas on the same carrier, some distance apart, any phase difference will contain information about the angle from which the radar echo returned. Combining this with the distance information, it is possible to determine the position in three dimensions of the image pixel.
Thus, it is possible to extract terrain altitude as well as radar reflectivity, producing a digital elevation model with a single pass. If the two measurement samples are separated in time, perhaps from two different flights over the same terrain, then there are two possible sources of phase shift. The first is terrain altitude, as discussed above. The second is terrain motion. A terrain which has shifted between observations will return a different phase and the amount of shift required to cause a significant phase difference is on the order of the wavelength used. InSAR processing offers a powerful tool in geological remote sensing as it is shown in Fig. 5.2.

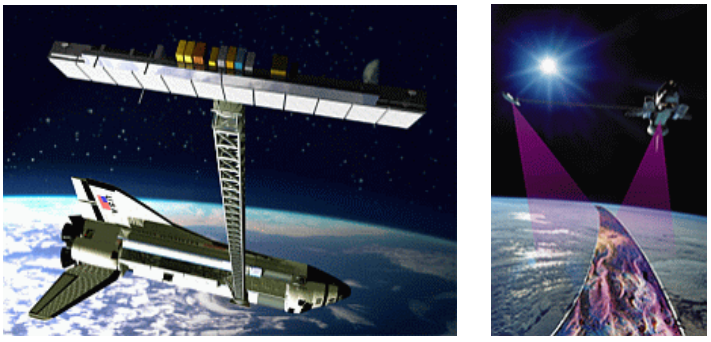

Figure 5.2: Shuttle Radar Topography Mission using InSAR [Var05b].

5.3 Synthetic Aperture Radar for GPR

5.3.1 Formulation of the Focusing Problem

Under the influence of humidity and inhomogeneities, the soil medium introduces absorption, refraction and reflection, which degrade the quality of the raw GPR data. The complexity of the problem makes it difficult to derive a precise mathematical description of a GPR. In chapter 1.4.4 different inversion schemes and focusing techniques for GPR are discussed. In the context of this thesis a SAR focusing concept has been adapted which has been proposed in [YS$^+$04]. The corresponding scattering problem has been formulated according to [HJ00]. The proposed technique employs the Born approximation and a plane-wave expansion of the dyadic Green's function for the interface problem. Thus, the initial model which describes the interaction of waves with ground inhomogeneities can be simplified which increases the computational efficiency. It is assumed that transmitting and receiving antenna are identical, that they have a wide radiation pattern and that they are located in the upper half-space above the air-soil interface as it is illustrated in Fig. 5.3.
The positions of the transmitting and receiving antenna are denoted by $\mathbf{r}_t = (x_t, y_t, h)$, respectively, $\mathbf{r}_r = (x_r, y_r, h)$. A fixed offset d in the x-direction between the antennas is assumed, so that $\mathbf{r}_t = \mathbf{r}_r + \mathbf{r}_\Delta$ with constant $\mathbf{r}_\Delta = (d, 0, 0)$. The position of the ground inhomogeneities which exist due to a buried object in the lower half-space V is denoted by $\mathbf{r}' = (x', y', z')$ assuming that z' equals the target depth $-D$.

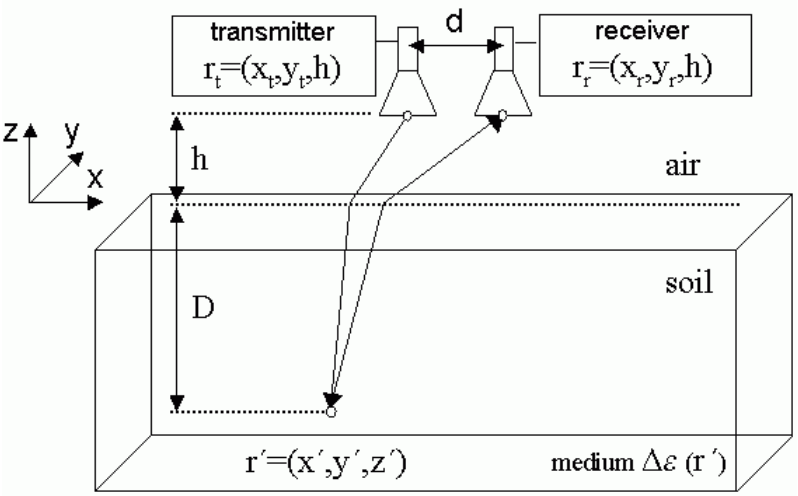

Figure 5.3: Geometrical model of a bistatic ground penetrating radar.

For the formulation of the scattering problem the transmitting and the receiving antenna are assumed to be infinite small dipoles. The unit vectors $\hat{\mathbf{p}}_t$ and $\hat{\mathbf{p}}_r$ point along the axis of the transmitting and receiving dipole, respectively. In this case, the transmitting dipole has a moment $\overline{Il}$ parallel to the unit vector $\hat{\mathbf{p}}_t$ whereas the receiving dipole determines the $\hat{\mathbf{p}}_r$-component of the electric field. The electric field at the receiving antenna can be expressed by the following equation:

$$\hat{\mathbf{p}}_r^T \mathbf{E}\left(\mathbf{r}_r, \mathbf{r}_t\right) = \hat{\mathbf{p}}_r^T \mathbf{E}_B\left(\mathbf{r}_r, \mathbf{r}_t\right) + \hat{\mathbf{p}}_r^T \mathbf{E}_S\left(\mathbf{r}_r, \mathbf{r}_t\right) \tag{5.1}$$

Herein, $\mathbf{E}_B\left(\mathbf{r}_r, \mathbf{r}_t\right)$ denotes the so-called background field at the receiver which is obtained if there are no buried objects and $\mathbf{E}_S\left(\mathbf{r}_r, \mathbf{r}_t\right)$ is the scattered field which is caused by the buried objects at $\mathbf{r}'$. The background field $\mathbf{E}_B\left(\mathbf{r}_r, \mathbf{r}_t\right)$ does not change when the radar is moved laterally. The contribution from the buried object $\hat{\mathbf{p}}_r^T \mathbf{E}_S\left(\mathbf{r}_r, \mathbf{r}_t\right)$ can be expressed as formulated in equation (5.2).

$$\hat{\mathbf{p}}_r^T \mathbf{E}_S\left(\mathbf{r}_r, \mathbf{r}_t\right) = j\omega\mu_0 \int_V \hat{\mathbf{p}}_r^T \bar{\mathbf{G}}\left(\mathbf{r}_r, \mathbf{r}'\right) \mathbf{E}\left(\mathbf{r}', \mathbf{r}_t\right) O(\mathbf{r}')\, dV' \tag{5.2}$$

In equation (5.2) the inhomogeneities of the permittivity due to the buried object are taken into account by the object function $O(\mathbf{r}')$. Herein ϵ_B defines the permittivity of the soil. The inhomogeneities of the conductivity of the soil which are typically much smaller than the permittivity variations are neglected for this analysis.

$$O(\mathbf{r}') = j\omega\left[\epsilon(\mathbf{r}') - \epsilon_B\right] = j\omega\Delta\epsilon(\mathbf{r}') \tag{5.3}$$

The term $\mathbf{E}\left(\mathbf{r}', \mathbf{r}_t\right)$ in equation (5.2) denotes the total electric field and the integration has to be extended over the entire region V in which the product $\mathbf{E}\left(\mathbf{r}', \mathbf{r}_t\right) O(\mathbf{r}')$ cannot be neglected. $\bar{\mathbf{G}}\left(\mathbf{r}_r, \mathbf{r}'\right)$ is the dyadic Green's function for a planar interface with constant permeability as it has been assumed for the analysis. When the observation point $\mathbf{r}_r$ is above the air-soil interface and the source point $\mathbf{r}'$ is below the interface the expansion of a spherical wave which penetrates the lower half-space can be expressed in terms of plane waves as described in equation (5.4).

Herein, the term $\bar{\mathbf{F}}(k_x, k_y)$ denotes the dyadic function with respect to the planar air-soil interface. This function can be derived if the transmission matrix that contains the x and y components of the plane wave spectrum of a Hertzian dipole is applied [HJ00] and a 2D Fourier transformation from the spectral domain to the spatial domain is utilized [GC99]. The propagation vectors for the plane waves are given by $\mathbf{k}_0 = k_x\hat{\mathbf{x}} + k_y\hat{\mathbf{y}} + k_z\hat{\mathbf{z}}$ and $\mathbf{k}_1 = k_x\hat{\mathbf{x}} + k_y\hat{\mathbf{y}} + k_{z\eta}\hat{\mathbf{z}}$ wherein k_z and $k_{z\eta}$ are denoting the z component in the upper and lower halfspace, respectively.

$$\bar{\mathbf{G}}(\mathbf{r}_r, \mathbf{r}') = \frac{j}{4\pi^2} \int_{-\infty}^{+\infty}\int_{-\infty}^{+\infty} \bar{\mathbf{F}}(k_x, k_y)\, e^{-j(\mathbf{k}_0\cdot\mathbf{r}_r - \mathbf{k}_1\cdot\mathbf{r}')}\, dk_x\, dk_y \tag{5.4}$$

If the total field $\mathbf{E}(\mathbf{r}', \mathbf{r}_t)$ in the region V which contains the buried object was known, it would be possible to determine the scattered field $\mathbf{E}_S(\mathbf{r}_r, \mathbf{r}_t)$ above the interface exactly. However, the field $\mathbf{E}(\mathbf{r}', \mathbf{r}_t)$ is unknown in V. This problem can be solved if the first Born approximation is utilized in order to obtain a simpler equation for the scattered field. The Born approximation allows to modify equation (5.2) and replace $\mathbf{E}(\mathbf{r}', \mathbf{r}_t)$ by the background field $\mathbf{E}_B(\mathbf{r}', \mathbf{r}_t)$. The illumination is provided by the $\hat{\mathbf{p}}_t$-directed transmitting dipole so that the background field denotes as

$$\mathbf{E}_B(\mathbf{r}', \mathbf{r}_t) = j\omega\mu_0\overline{Il}\, \bar{\mathbf{G}}_{\mathbf{inv}}(\mathbf{r}', \mathbf{r}_t)\, \hat{\mathbf{p}}_t \tag{5.5}$$

In A.2 it will be shown how the general reciprocity relation can be utilized in order to replace the inverse dyadic Greens's function $\bar{\mathbf{G}}_{\mathbf{inv}}(\mathbf{r}', \mathbf{r}_t)$ with the term $\bar{\mathbf{G}}^T(\mathbf{r}_t, \mathbf{r}')$. Thus, it is possible to express the background field in terms of a dyadic Green's function with its observation point $\mathbf{r}_t$ above the air-soil interface and its source point $\mathbf{r}'$ below the interface so that the formulation of the dyadic Green's function in equation (5.4) can also be utilized for the formulation of equation (5.6).

$$\bar{\mathbf{G}}(\mathbf{r}_t, \mathbf{r}') = \frac{j}{4\pi^2} \int_{-\infty}^{+\infty}\int_{-\infty}^{+\infty} \bar{\mathbf{F}}(k_x, k_y)\, e^{-j(\mathbf{k}_0\cdot\mathbf{r}_t - \mathbf{k}_1\cdot\mathbf{r}')}\, dk_x\, dk_y \tag{5.6}$$

Inserting equation (5.6) into the relation for the scattered field (5.2) yields

$$\begin{aligned}\hat{\mathbf{p}}_r^T \mathbf{E}_S(\mathbf{r}_r, \mathbf{r}_t) &= (j\omega)^2 \mu_0^2 \overline{Il} \int_V \hat{\mathbf{p}}_r^T \bar{\mathbf{G}}(\mathbf{r}_r, \mathbf{r}') \bar{\mathbf{G}}^T(\mathbf{r}_t, \mathbf{r}') \hat{\mathbf{p}}_t O(\mathbf{r}')\, dV' \\ &= (j\omega)^3 \mu_0^2 \overline{Il} \int_V \hat{\mathbf{p}}_r^T \bar{\mathbf{G}}(\mathbf{r}_r, \mathbf{r}') \bar{\mathbf{G}}^T(\mathbf{r}_t, \mathbf{r}') \hat{\mathbf{p}}_t \Delta\epsilon(\mathbf{r}')\, dV' \end{aligned} \tag{5.7}$$

A more convenient formulation of equation (5.7) can be derived if it is reformulated with respect to the center position between the transmitting and the receiving antenna $\mathbf{r}_c = \mathbf{r}_r + \mathbf{r}_\Delta/2 = \mathbf{r}_t - \mathbf{r}_\Delta/2$. It shows, that the position of the transmitting and the receiving antenna can be determined by the distance between both antennas $\mathbf{r}_\Delta$ and the corresponding center position $\mathbf{r}_c$. Thus it is possible to substitute $\mathbf{r}_r = \mathbf{r}_c - \mathbf{r}_\Delta/2$, respectively, $\mathbf{r}_t = \mathbf{r}_c + \mathbf{r}_\Delta/2$ and equation (5.7) reads as

$$\hat{\mathbf{p}}_r^T \mathbf{E}_S(\mathbf{r}_c) = \int_V \mathbf{K}(\mathbf{r}_c, \mathbf{r}')\, \Delta\epsilon(\mathbf{r}')\, dV' \tag{5.8}$$

Herein, the term $\mathbf{K}(\mathbf{r}_c, \mathbf{r}')$ has been utilized as a substitute for the dyadic Green's function block in order to increase the convenience which reads as follows.

$$\mathbf{K}(\mathbf{r}_c, \mathbf{r}') = (j\omega)^3 \mu_0^2 \overline{Il}\, \hat{\mathbf{p}}_r^T \bar{\mathbf{G}} \left(\mathbf{r}_c - \frac{\mathbf{r}_\Delta}{2}, \mathbf{r}'\right) \bar{\mathbf{G}}^T \left(\mathbf{r}_c + \frac{\mathbf{r}_\Delta}{2}, \mathbf{r}'\right) \hat{\mathbf{p}}_t \tag{5.9}$$

Equation (5.7) is a solution of the forward problem which determines the field caused by a certain distribution of inhomogeneities in the soil. However, for the focusing of GPR data the inverse problem has to be solved, which means that inhomogeneities have to be detected from the measured field. Consequently, it is necessary to invert equation (5.8). The two-dimensional focusing of the scattered field $\hat{\mathbf{p}}_r^T \mathbf{E}_S(\mathbf{r}_c)$ with respect to a focusing point $\mathbf{r}_f = (x_f, y_f, 0)$ yields the following equation. The position of the focusing point at $z = 0$, namely, at the surface of the air-soil interface has been chosen in order to simplify the focusing procedure. The length of the traveling path is calculated using the three-dimensional Pythagoras' Theorem.

$$U(\mathbf{r}_f, k) = \int_{\mathbf{r}_c} e^{jk\left(\left|\mathbf{r}_c - \frac{\mathbf{r}_\Delta}{2} - \mathbf{r}_f\right| + \left|\mathbf{r}_c + \frac{\mathbf{r}_\Delta}{2} - \mathbf{r}_f\right|\right)} \hat{\mathbf{p}}_r^T \mathbf{E}_S(\mathbf{r}_c)\, d\mathbf{r}_c \tag{5.10}$$

The formulation of the backscattered field in equation (5.8) is inserted.

$$U\left(\mathbf{r}_f, k\right) = \int\limits_{\mathbf{r}_c} e^{jk \cdot l_{cor}(\mathbf{r}_c, \mathbf{r}_f)} \int\limits_{V} \mathbf{K}\left(\mathbf{r}_c, \mathbf{r}'\right) \Delta\epsilon(\mathbf{r}')\, dV'\, d\mathbf{r}_c \tag{5.11}$$

Herein, $l_{cor}(\mathbf{r}_c, \mathbf{r}_f)$ is used to substitute the calculation of the path length as follows:

$$l_{cor}(\mathbf{r}_c, \mathbf{r}_f) = \left|\mathbf{r}_c - \frac{\mathbf{r}_\Delta}{2} - \mathbf{r}_f\right| + \left|\mathbf{r}_c + \frac{\mathbf{r}_\Delta}{2} - \mathbf{r}_f\right| \tag{5.12}$$

Then, the order of integration is changed so that the resulting equation reads as

$$U\left(\mathbf{r}_f, k\right) = \int\limits_{V} \Delta\epsilon(\mathbf{r}') \int\limits_{\mathbf{r}_c} \mathbf{K}\left(\mathbf{r}_c, \mathbf{r}'\right) e^{jk \cdot l_{cor}(\mathbf{r}_c, \mathbf{r}_f)}\, d\mathbf{r}_c\, dV' \tag{5.13}$$

For the analysis it is convenient to separate the three-dimensional vectors $\mathbf{r}$ into a two-dimensional transverse component which will be denoted by $\boldsymbol{\nu} = (x, y)$ and a longitudinal z-component so that $\mathbf{r}_c = (\boldsymbol{\nu}_c, h)$, $\mathbf{r}_f = (\boldsymbol{\nu}_f, 0)$ and $dV' = d^2\boldsymbol{\nu}'\, dz$.

$$U\left(\boldsymbol{\nu}_f, k\right) = \int\limits_{-\infty}^{+\infty} \int\limits_{-\infty}^{+\infty} \int\limits_{-\infty}^{+\infty} \Delta\varepsilon\left(\nu', z'\right) Q\left(\nu', z', \boldsymbol{\nu}_f, k\right)\, d^2\boldsymbol{\nu}'\, dz' \tag{5.14}$$

The term $Q\left(\nu', z', \boldsymbol{\nu}_f, k\right)$ denotes the so-called transfer function of the investigated system which is a mathematical substitute for the expression in equation (5.15). It should be noted that the initial three-dimensional integration over $\mathbf{r}_c$ reduces to a two-dimensional one over $\boldsymbol{\nu}_c$ because the height of the transmitting and the receiving antenna h is constant and, thus, the integration over z_c can be omitted.

$$\begin{aligned} Q\left(\nu', z', \boldsymbol{\nu}_f, k\right) = {} & (j\omega)^3 \mu_0^2 \overline{Il} \int\limits_{\boldsymbol{\nu}_c} e^{jk\left(\sqrt{\left(\boldsymbol{\nu}_c - \frac{\boldsymbol{\nu}_\Delta}{2} - \boldsymbol{\nu}_f\right)^2 + h^2} + \sqrt{\left(\boldsymbol{\nu}_c + \frac{\boldsymbol{\nu}_\Delta}{2} - \boldsymbol{\nu}_f\right)^2 + h^2}\right)} \\ & \cdot \hat{\mathbf{p}}_r^T \bar{\mathbf{G}}\left(\boldsymbol{\nu}_c - \frac{\boldsymbol{\nu}_\Delta}{2}, z_c, \nu', z'\right) \bar{\mathbf{G}}^T\left(\boldsymbol{\nu}_c + \frac{\boldsymbol{\nu}_\Delta}{2}, z_c, \nu', z'\right) \hat{\mathbf{p}}_t\, d^2\boldsymbol{\nu}_c \end{aligned} \tag{5.15}$$

In the focusing region the phase distribution of the field is similar to the phase distribution of a plane wave which propagates perpendicularly to the air-soil interface and if the permittivity of the soil is large enough a wave refraction nearly perpendicular to this interface can be assumed which allows to approximate $k_{z\eta} \approx k\eta$ without a significant error. The illuminating field propagates in the $-z$-direction leading to a phase factor of $e^{-jk\eta(-z')} = e^{jk\eta z'}$. Thus, the transformation of the function $Q(\nu', z', \boldsymbol{\nu}_f, k) \approx Q(\nu', 0, \boldsymbol{\nu}_f, k)\, e^{j2k\eta z'}$ yields equation (5.16).

$$U(\boldsymbol{\nu}_f, k) = \int_{-\infty}^{+\infty}\int_{-\infty}^{+\infty}\int_{-\infty}^{+\infty} \Delta\varepsilon(\nu', z')\, Q(\nu', 0, \boldsymbol{\nu}_f, k)\, e^{j2k\eta z'}\, d^2\nu'\, dz' \tag{5.16}$$

An inverse Fourier transformation is applied in order to perform the transformation of equation (5.16) from the wavenumber domain to the spatial domain as follows.

$$\begin{aligned}\tilde{U}(\boldsymbol{\nu}_f, z) &= \frac{1}{2\pi}\int_{-\infty}^{+\infty} U(\boldsymbol{\nu}_f, k)\, e^{-jkz} dk \\ &= \int_{-\infty}^{+\infty}\int_{-\infty}^{+\infty}\int_{-\infty}^{+\infty} \Delta\varepsilon(\nu', z')\, q(\nu', 2\eta z' - z)\; d^2\nu'\, dz'\end{aligned} \tag{5.17}$$

Herein, the utilized kernel function $q(\nu', 2\eta z' - z)$ reads as follows.

$$q(\nu', 2\eta z' - z) = \frac{1}{2\pi}\int_{-\infty}^{+\infty} Q(\nu', 0, \boldsymbol{\nu}_f, k)\, e^{jk(2\eta z' - z)}\, dk \tag{5.18}$$

In 5.4.3 it is verified that this time domain representation of the kernel function can be assumed to be highly localized in the cross section and extended in the depth below the focusing point as it is illustrated in Fig. 5.4. Thus, it is possible to reduce the initial three-dimensional problem of focusing on every point within a certain volume to a two-dimensional one for which only focusing points on the air-soil interface plane are taken into account which increases the computational efficiency of the algorithm significantly. In [YS+04] it is shown that the kernel function $q(\nu', 2\eta z' - z)$ tends to be the delta function, namely, $\delta(\nu' - \boldsymbol{\nu}_f) \cdot \delta\left(z' - \frac{z}{2\eta}\right)$.

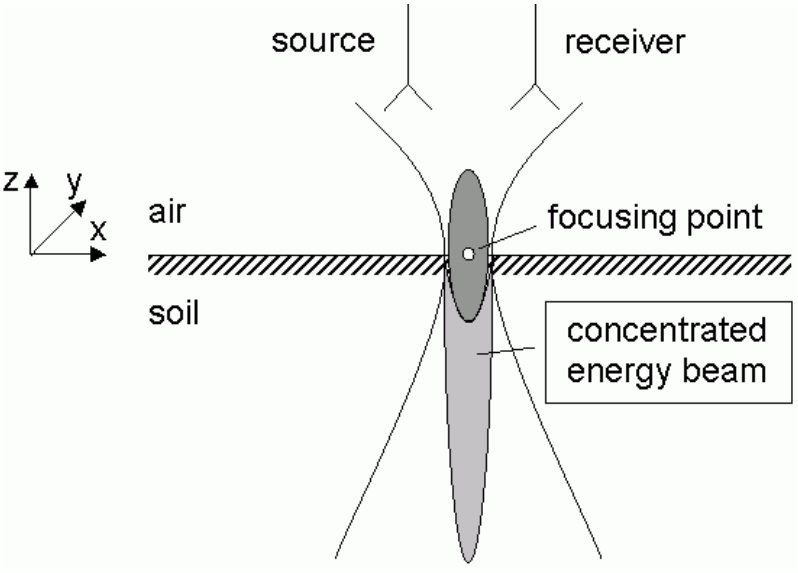

Figure 5.4: Energy concentration in the region below the focusing point.

Consequently, a first approximation of equation (5.17) is suggested in equation (5.19).

$$\tilde{U}\left(\boldsymbol{\nu}_f, z\right) \;\approx\; \Delta\varepsilon\left(\boldsymbol{\nu}_f, \frac{z}{2\eta}\right) \int_{-\infty}^{+\infty}\int_{-\infty}^{+\infty}\int_{-\infty}^{+\infty} q\left(\nu', 2\eta z' - z\right)\; d^2\nu'\, dz' \tag{5.19}$$

Hence, the heterogeneous distribution of the permittivity can be reconstructed by

$$\Delta\varepsilon\left(\boldsymbol{\nu}_f, \frac{z}{2\eta}\right) \approx \tilde{U}\left(\boldsymbol{\nu}_f, z\right) \cdot \left[\int_{-\infty}^{+\infty}\int_{-\infty}^{+\infty}\int_{-\infty}^{+\infty} q\left(\nu', 2\eta z' - z\right)\; d^2\nu'\, dz'\right]^{-1} \tag{5.20}$$

However, it is important to note, that for a complete inversion algorithm, namely, the calculation of the real value for the distribution of the inhomogeneous permittivity in the subsurface it is necessary to solve equation (5.17). If the utilization of the Born approximation should be avoided so-called iterative methods can be found from the literature, see 1.4.4, which allow to solve the inverse problem by continuous calculation of the forward problem with iteratively varied input data. However, the focused backscattered field $\tilde{U}\left(\boldsymbol{\nu}_f, z\right)$ already represents the underlying distribution of the inhomogeneous permittivity in the lower half-space, which yields essential information for the detection of buried objects such as AP landmines.

5.3.2 Implementation of the SAR Focusing

After the mathematical background of the SAR focusing has been discussed, the resulting implementation of the algorithm will be explained. At first, the results of the GPR measurement are acquired forming a complex data matrix $S(x, y, f)$.

$$S(x, y, f) = \frac{1}{2\pi} \int_{-\infty}^{+\infty} s(x, y, t)\, e^{-j\omega t}\, dt \tag{5.21}$$

In order to apply the phase correction the double-integral in equation (5.22) has to be solved. Later, chapter 5.3.2 demonstrates how the time-consuming calculation of new focusing matrices for every point (x_F, y_F) can be replaced by an equivalent convolution which utilizes only one matrix for the SAR focusing of all positions.

$$U(x_F, y_F, f) = \int_{-\infty}^{+\infty}\int_{-\infty}^{+\infty} S(x, y, f)\, H(x - x_F, y - y_F, f)\; dx\, dy \tag{5.22}$$

Herein, the focusing matrix $H(x, y, f)$ contains the phase correction for every considered antenna position with respect to a certain focusing point (x_F, y_F). It can be formulated for the bistatic, respectively, the monostatic case ($d = 0$) as follows.

$$H(x, y, f) = \begin{cases} e^{jk\left(\sqrt{\left(x-\frac{d}{2}\right)^2+y^2+h^2}+\sqrt{\left(x+\frac{d}{2}\right)^2+y^2+h^2}\right)} \\ e^{j2k\left(\sqrt{x^2+y^2+h^2}\right)} \text{ for the case } d = 0 \end{cases} \tag{5.23}$$

Finally, the inverse Fourier transform is utilized in order to calculate the time-domain representation of the SAR focused data as it is formulated in equation (5.24).

$$\tilde{U}(x_F, y_F, t) = \int_{-\infty}^{+\infty} U(x_F, y_F, f)\, e^{j\omega t}\, df \tag{5.24}$$

The SAR focused data set $\tilde{U}(x_F, y_F, t)$ corresponds to the distribution of the permittivity in the soil at the soil position (x_F, y_F). This results are either illustrated directly or further processed to prepare detection and classification approaches.

Unfortunately, it turns out that a straight-forward implementation of the proposed SAR focusing requires a long processing time because 4 hierarchical loops, namely over the x-axis and the y-axis of the data matrix $S(x, y, f)$ and the focusing matrix $H(x, y, f)$ have to be taken into account. Therefore, an alternative technique has been derived in the context of this thesis, that basically replaces the 4 hierarchical loops by a convolution of $H(x, y, f)$ and $S(x, y, f)$. The left-hand side of the diagram in Fig. 5.5 illustrates such a focusing matrix, which has been calculated for a single focusing point, namely, the white point in the center of the two-dimensional focusing matrix on the left hand side is shifted across the data matrix with respect to the axial stepwidth `dx`, respectively, `dy`. Thus, the proposed SAR focusing is applied for all considered points of the matrix $S(x, y, f)$. At the same time the convolution concept allows to reduce the computational efforts significantly.
The size of $H(x, y, f)$ on the x-axis and the y-axis needs to be twice the size of $S(x, y, f)$ to ensure, that even for the maximum shifting, e.g. for a focusing point position in the lower left corner of $S(x, y, f)$, the phase relations for all considered antenna element can be calculated. Moreover, data matrix and phase relation matrix must utilize the same geometrical distance between their element even though in reality the step size between the antenna readings may vary from the chosen step size between the focusing points. Therefore, $S(x, y, f)$ has to be interpolated, so that the distance between the antenna elements `dx`, respectively, `dy` equals the chosen distance between different focusing points `dxf`, respectively, `dyf`. As long as the number of elements in $H(x, y, f)$ is a multiple of the number of elements in $S(x, y, f)$ intermediate zeros can be added to fill the empty elements.

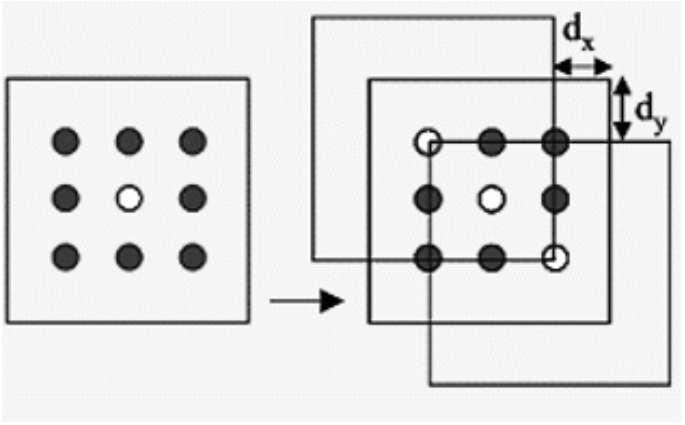

Figure 5.5: Convolution of phase relation matrix and data matrix.

5.4 Investigation of the SAR Processing

5.4.1 Simulation of an Array of Dipoles

A fundamental question which arises is how the geometrical dimensions of the antenna array will effect the results of the proposed SAR processing. In the context of this thesis this problem has been studied considering an array of elementary dipoles located in free space because the field simulation for this setup is numerically efficient which is very important since a large variety of array parameter has been taken into account for the analysis. The field of a single dipole is known analytically and the results for a single element can be extended to the virtual antenna array by a technique which is similar to the process of convolution. In this way each individual antenna contributes to the resulting field of the entire array. The individual elementary dipoles will be located parallel to the y-axis of the global right-handed Cartesian coordinate system as it is illustrated in Fig. 5.6(a). This orientation has been chosen, because for an elementary dipole the main lobe of radiation will propagate perpendicular to the direction of orientation. In order to retrieve the field distribution on a x-y-plane in a certain distance below the antenna array the electromagnetic field radiated by an elementary dipole needs to be calculated first. It is given analytically by the following equations which can be found from textbooks. However, these equations require that the dipole is orientated in the z'-direction of the corresponding local spherical coordinate system (Fig. 5.6(b)). The quantities of r, θ and ϕ are calculated according to the well-known geometrical relations.

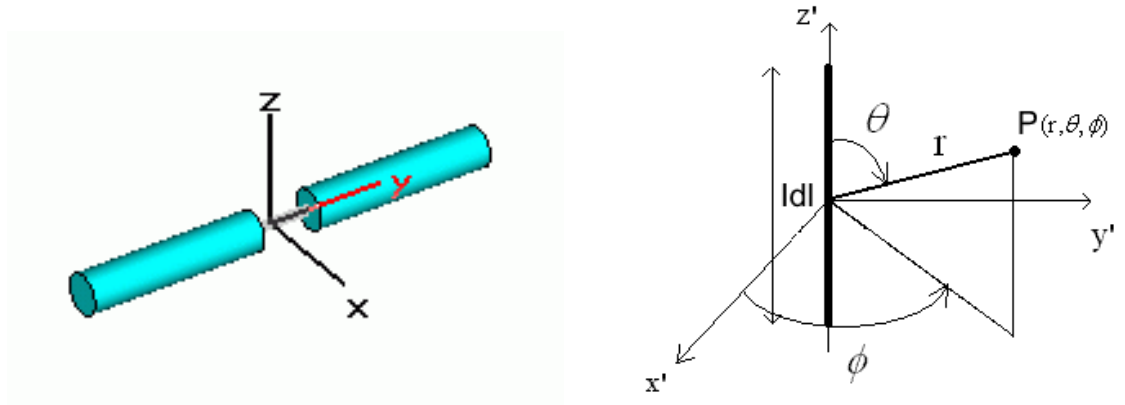

(a) Global coordinate system (b) Local coordinate system

Figure 5.6: Orientation of elementary dipoles in global and local coordinates.

$$E_\phi = H_r = H_\theta = 0 \tag{5.25}$$

$$E_r = 2kZ_0 Idle^{-jkr} \cdot \frac{1}{4\pi r} \cdot \cos\theta \cdot \left(\frac{1}{kr} - j\frac{1}{(kr)^2} \right) \tag{5.26}$$

$$E_\theta = jkZ_0 Idle^{-jkr} \cdot \frac{1}{4\pi r} \cdot \sin\theta \cdot \left(1 - j\frac{1}{kr} - \frac{1}{(kr)^2} \right) \tag{5.27}$$

$$H_\phi = jkIdle^{-jkr} \cdot \frac{1}{4\pi r} \cdot \sin\theta \cdot \left(1 - j\frac{1}{kr} \right) \tag{5.28}$$

The quantity Idl represents the amplitude of the single element excitation current, k the wavenumber and Z_0 the wave impedance of a plane wave in free space. It is important to note, that for the proposed calculation no farfield approximations have been assumed. The total field at a certain point in space can be obtained by summing all contributing field components at that specific location. However, the intention of the proposed method is the calculation of the electromagnetic field distribution of a complete antenna array. In order to superimpose the contributions of the individual dipoles it is convenient to transform the spherical field components given by the above equations into Cartesian ones using the well-known equations (5.29) - (5.34) which can be found from various textbooks and denote as follows.

$$E_{x'} = \sin\theta\cos\phi \cdot E_r + \cos\theta\cos\phi \cdot E_\theta - \sin\phi \cdot E_\phi \tag{5.29}$$

$$E_{y'} = \sin\theta\sin\phi \cdot E_r + \cos\theta\sin\phi \cdot E_\theta + \cos\phi \cdot E_\phi \tag{5.30}$$

$$E_{z'} = \cos\theta \cdot E_r - \sin\theta \cdot E_\theta \tag{5.31}$$

$$H_{x'} = \sin\theta\cos\phi \cdot H_r + \cos\theta\cos\phi \cdot H_\theta - \sin\phi \cdot H_\phi \tag{5.32}$$

$$H_{y'} = \sin\theta\sin\phi \cdot H_r + \cos\theta\sin\phi \cdot H_\theta + \cos\phi \cdot H_\phi \tag{5.33}$$

$$H_{z'} = \cos\theta \cdot H_r - \sin\theta \cdot H_\theta \tag{5.34}$$

The magnitude of the electric, respectively, the magnetic field of a single dipole element which is illustrated in Fig. 5.7 is calculated using a summation of the Cartesian field components with respect to a temporary averaged field strength according to equations (5.35) and (5.36). Therefore, the field components have to be transformed from local coordinates to global ones. Consequently, the index substitutions

$E_x = E_{x'}$, $E_y = E_{z'}$, $E_z = E_{y'}$, respectively, $H_x = H_{x'}$, $H_y = H_{z'}$, $H_z = H_{y'}$ have to be applied. The electromagnetic field components are illustrated in Fig. 5.8.

$$E = \sqrt{0.5 \cdot \left(|E_x|^2 + |E_y|^2 + |E_z|^2\right)} \tag{5.35}$$

$$H = \sqrt{0.5 \cdot \left(|H_x|^2 + |H_y|^2 + |H_z|^2\right)} \tag{5.36}$$

The size of the calculation plane has been chosen large enough to ensure that the field energy level has decreased completely towards the edges of the plane. Thus, the electromagnetic field distribution of a complete array of elementary dipoles with m by n elements and a distance `dx` between the elements on the x-axis, respectively, a distance `dy` on the y-axis can be calculated by using only the analytically given field distribution of a single dipole element which is shifted to all considered antenna positions in order to contribute to the total field of the resulting antenna array. One of the major contributions of the proposed technique is the fact, that this processing can be done with enormous computational efficiency. It is obvious, that due to this concept of superimposing the contributions of the individual array elements the interaction between different antennas is neglected completely. However, this assumption is valid because for GPR applications the individual measurements are performed with monostatic or bistatic antenna configurations which will be combined by further processing techniques to form synthetic arrays of antennas.

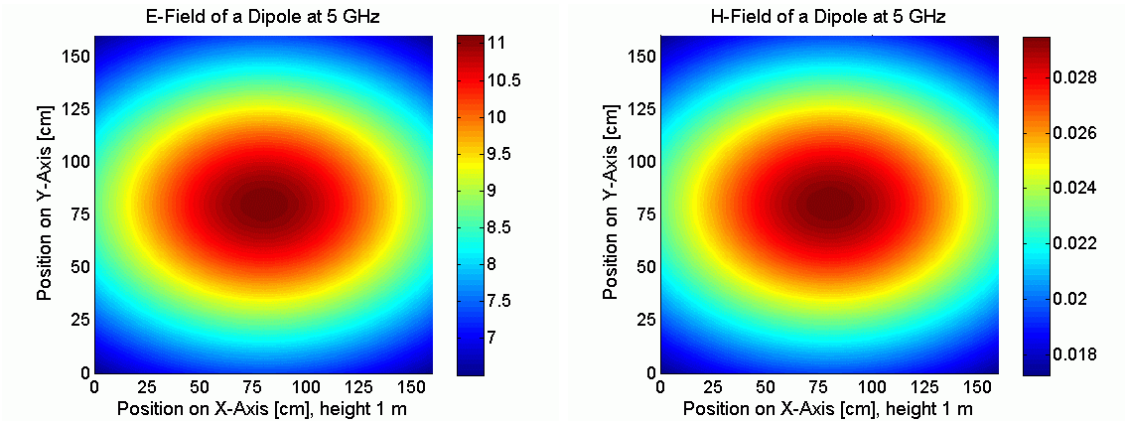

(a) E-field of a single dipole

(b) H-field of a single dipole

Figure 5.7: E-field and H-field of a dipole element at 5 GHz.

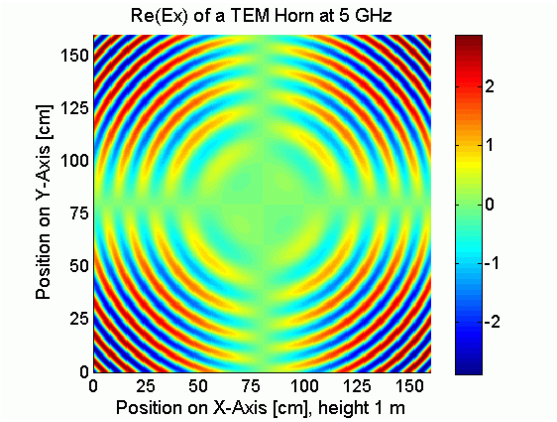

(a) E_x component

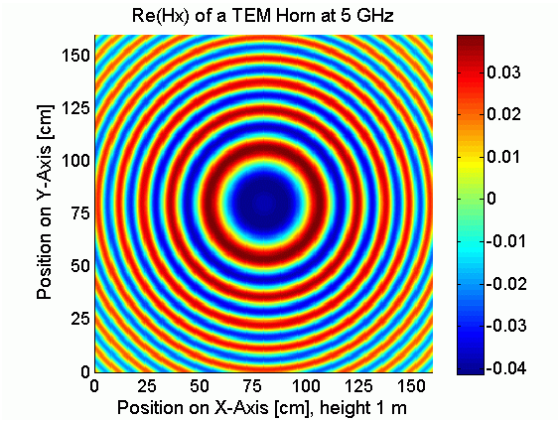

(b) H_x component

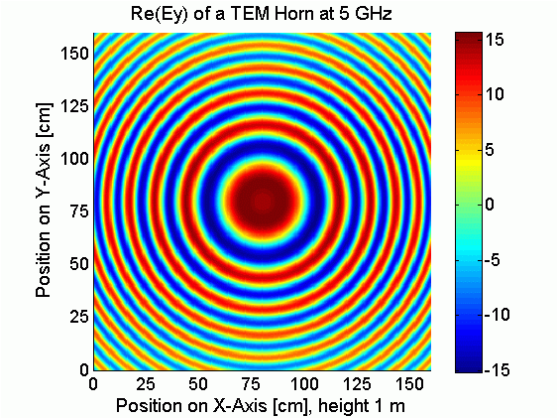

(c) E_y component

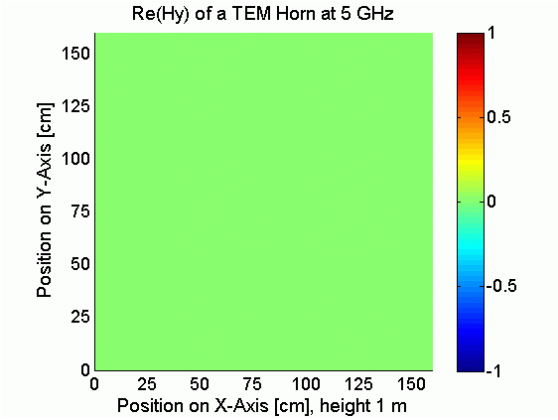

(d) H_y component

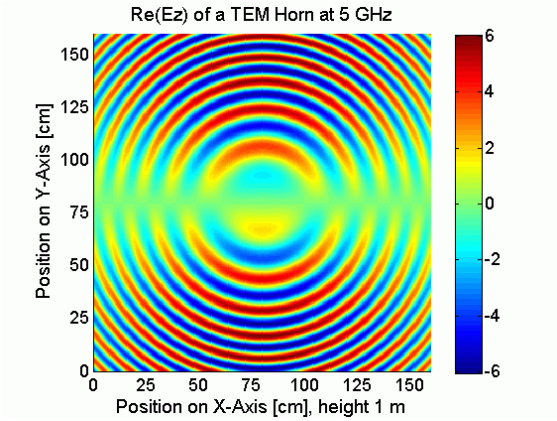

(e) E_z component

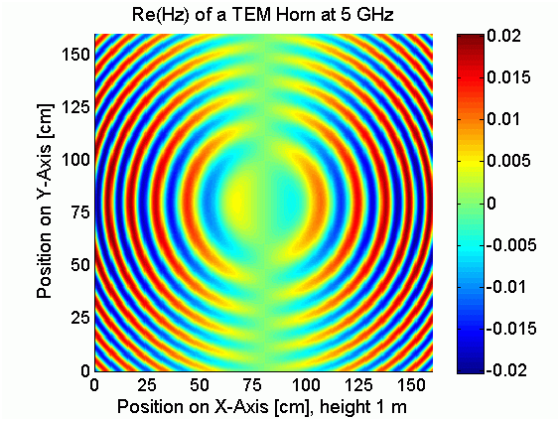

(f) H_z component

Figure 5.8: Field components of an elementary dipole antenna at 5 GHz. The dipole is located at the origin of the coordinate system and orientated in the y-direction.

Using the proposed method the electric and magnetic field of a dipole array with 21 by 21 elements and a grid step size of 5 cm has been simulated for a frequency of 5 GHz in a depth of 1 m below the antenna array. Fig. 5.9 shows the corresponding field distribution on this x-y-plane below the antenna array. Without any further processing all dipole elements of the antenna array are propagating in different directions and the electric, respectively, the magnetic field is not concentrated. In comparison Fig. 5.10 illustrates the results of the SAR focusing. For the investigation only one focusing point in the center of the array has been selected. It shows, that the electric field is concentrated completely at the chosen focus point position and the energy density is much higher than in the case without focusing.

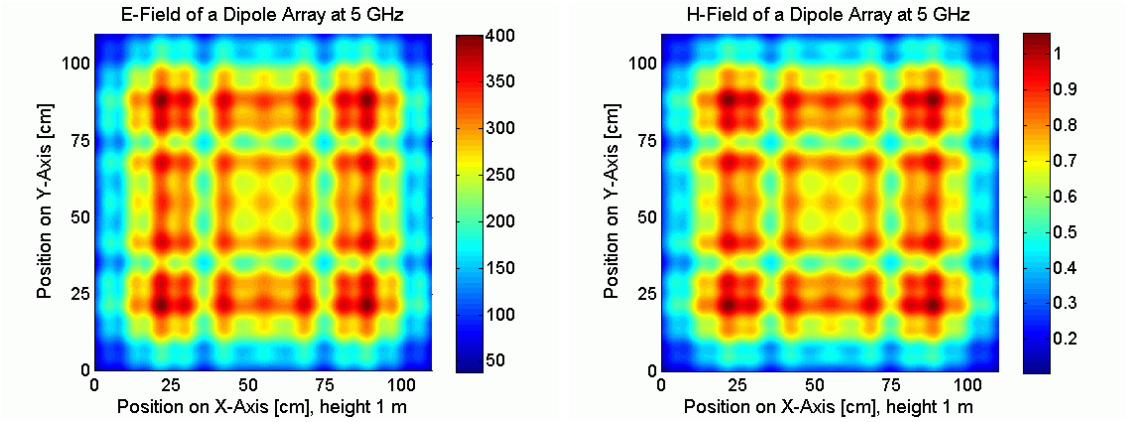

(a) E-field of a dipole array (b) H-field of a dipole array

Figure 5.9: E-field and H-field of a 21 by 21 dipole array at 5 GHz.

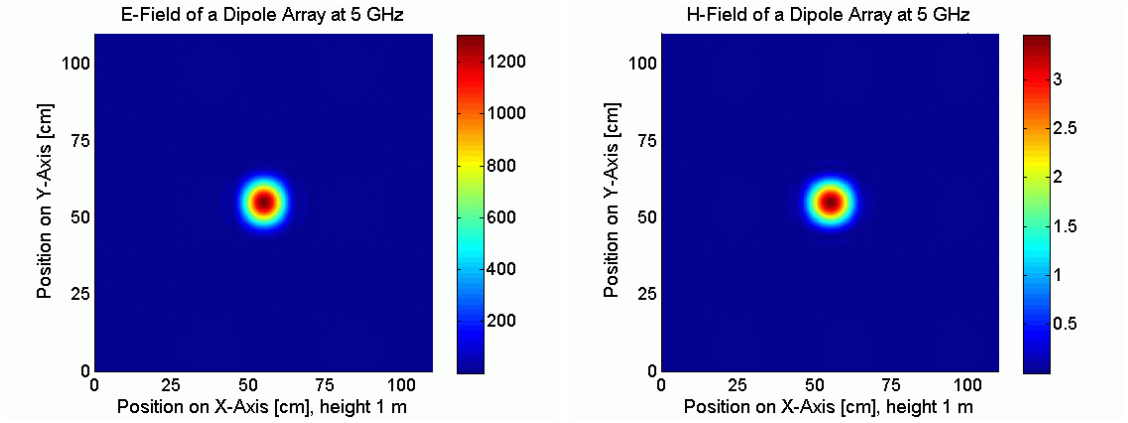

(a) E-field of a dipole array (b) H-field of a dipole array

Figure 5.10: E-field and H-field of a 21 by 21 dipole array at 5 GHz.

From Figs. 5.9 and 5.10 can be revealed, that the electric and magnetic field pattern of the antenna array are almost identical. Therefore, the resulting E-field characteristics will be taken into account exclusively for the further investigation of the influence of varied array parameters on the quality of the SAR focusing. At first the distance between the elements of the 21 by 21 dipole array will be varied from 5 cm to 40 cm and the SAR focusing will be applied for a frequency of 10 GHz according to equation 5.22. Again, only one focusing point in the center of the array in a depth of 1 m has been selected. The results for a grid step size of 5 cm which are illustrated in Fig. 5.11(a) reveal, that the electric field is concentrated completely at the chosen focus point position. Except for minor artifacts on both axis through the focus point which will be discussed in 5.4.4 no grating lopes are visible.
If now the distance between the elements of the virtual array is increased from 5 cm to 10 cm and the SAR focusing is applied an important effect can be obtained. As shown in Fig. 5.11(b) systematic interferences occur that would decrease the quality of the SAR focusing, whereas for a step width of 5 cm only the focus point at the center of the array is illuminated. If the grid steps between the elements is further increased the interference becomes stronger (Fig. 5.11(c) and 5.11(d)). The original array with 21 by 21 elements and a distance of 5 cm between the elements has also been simulated for a frequency of 20 GHz. Fig. 5.12 reveals that for a step size of 5 cm, respectively, 10 cm almost the same interference phenomena occur that could be obtained at 10 GHz for a step size of 10 cm, respectively, 20 cm. Hence, the obtained interference depends on the relation between the utilized wavelength and the distance between the elements. For the determination of the maximum allowed step size between the GPR measurements the highest operating frequency must be taken into account in order to avoid a decreased performance of the focusing.
Another aspect which has been investigated using the proposed method is the influence of the number of array elements on the energy density and the distribution of the focusing spot. Therefore, the size of the antenna array has been increased in steps from 5 by 5 up to 41 by 41 and one focusing point in the center of the array in a depth of 1 m has been selected. For all cases same frequency has been utilized and a similar cutout of the resulting field pattern has been illustrated in Figs. 5.13 and 5.14. It can be obtained, that for the given the characteristic of an ideal dipole the energy density at the focusing point increases continuously, while the spot size becomes smaller if more antennas are considered for the SAR processing.

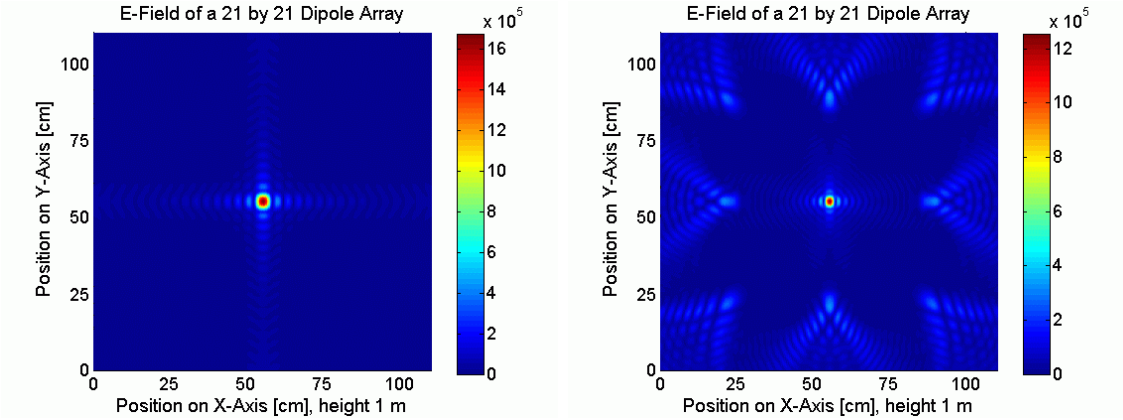

(a) 5 cm element step size

(b) 10 cm element step size

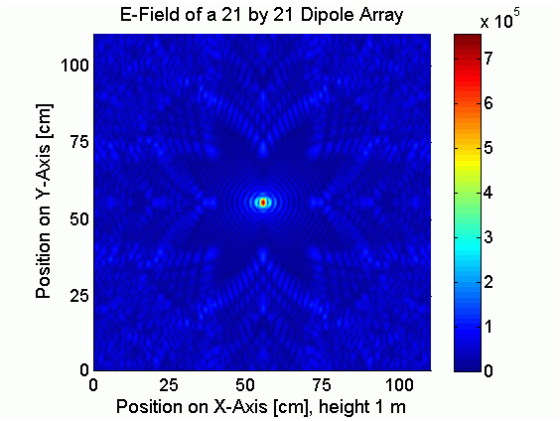

(c) 20 cm element step size

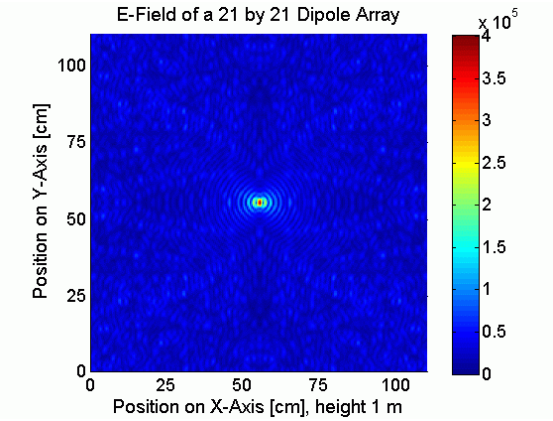

(d) 40 cm element step size

Figure 5.11: 21 by 21 dipole array with varied element step size at 10 GHz.

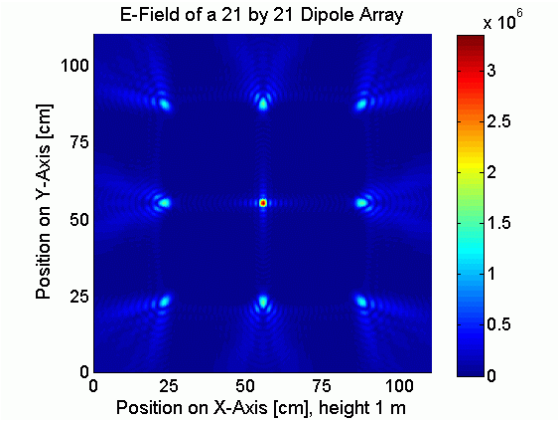

(a) 5 cm element step size

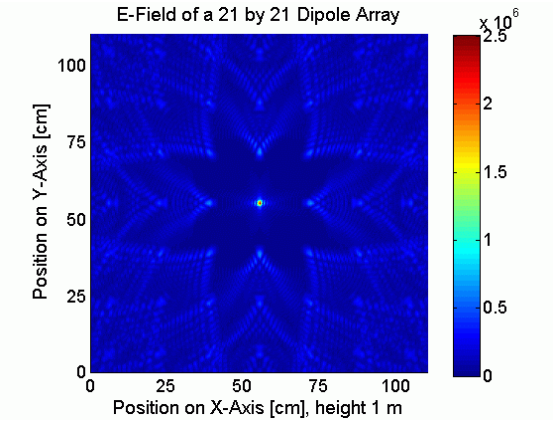

(b) 10 cm element step size

Figure 5.12: 21 by 21 dipole array with varied element step size at 20 GHz.

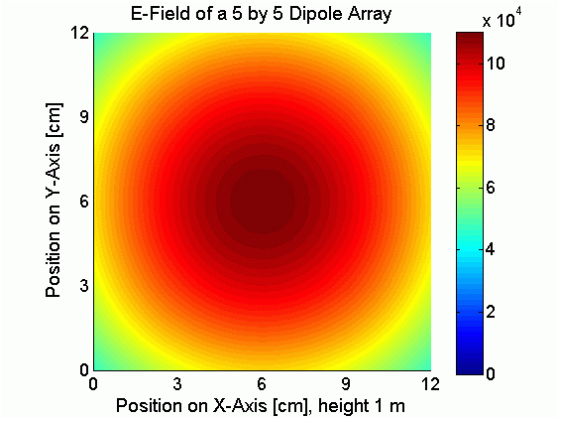

(a) 5 by 5 dipole elements

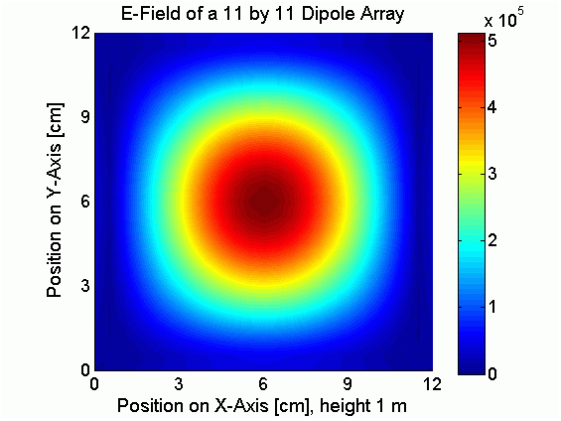

(b) 11 by 11 dipole elements

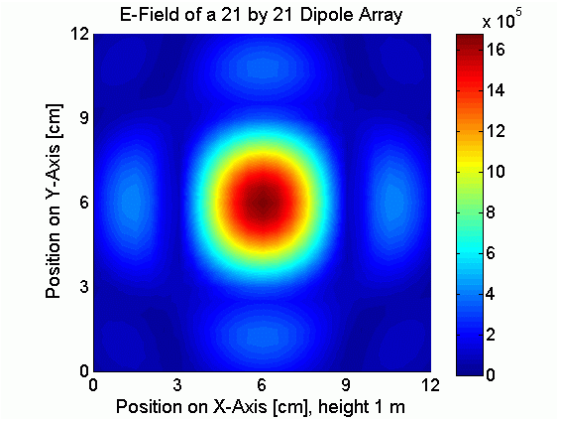

(c) 21 by 21 dipole elements

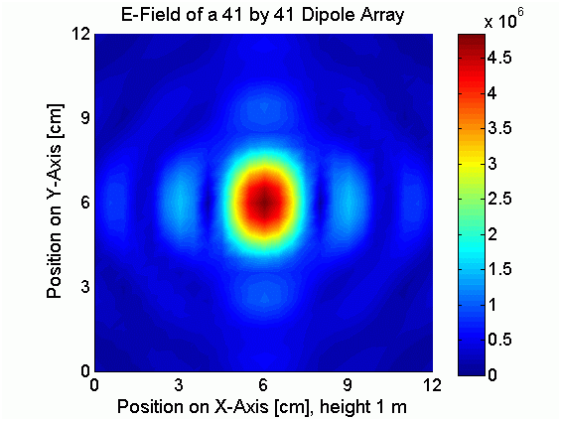

(d) 41 by 41 dipole elements

Figure 5.13: Dipole array with varied number of dipole elements at 10 GHz.

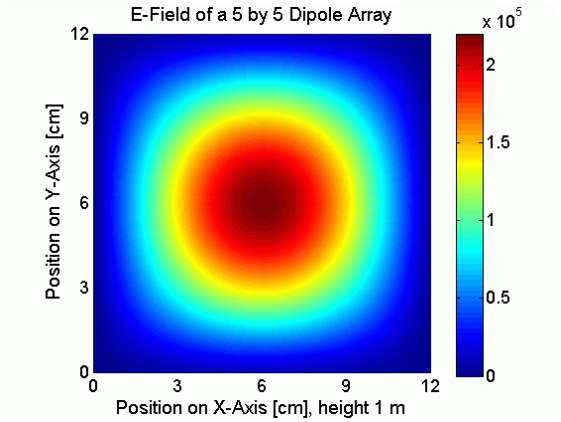

(a) 5 by 5 dipole elements

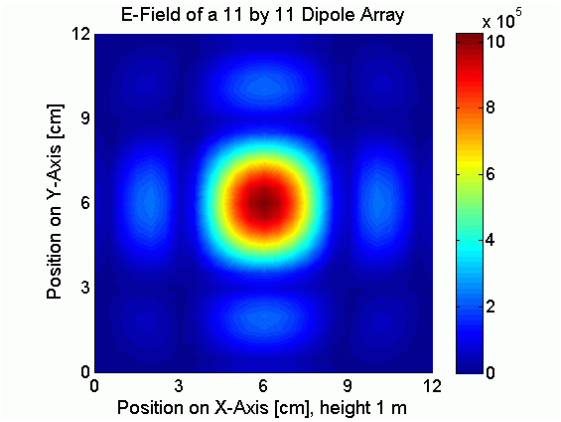

(b) 11 by 11 dipole elements

Figure 5.14: Dipole array with varied number of dipole elements at 20 GHz.

5.4.2 Realistic Antenna Characteristics

The analytical generation of dipole arrays turned out to be a versatile tool for the investigation of fundamental relations of the SAR focusing technique. However, the underlying principles should be investigated in a more realistic environment that takes into account the simulated radiation characteristics of real GPR antennas. As an example, the fields of a TEM double ridged horn antenna which cannot be calculated analytically, are imported from the 3D field simulation of a GPR environment as it has been introduced in chapter 3 which employs a highly sophisticated finite integration technique. The antenna has been chosen for the analysis because of their ability to be used for a GPR according to chapter 4, namely, a reasonable bandwidth and an almost frequency independent radiation pattern. However, it is possible to integrate any kind of antenna and even new design approaches in order to anticipate the behavior of this antenna in the context of a SAR focusing. Moreover, the resulting field distribution of the antenna array can be obtained not only in air but also in the subsurface because the utilized 3D EM field simulation allows to consider the presence of a soil brick below the array, e.g. with a relative permittivity of $\epsilon_r = 2.45$ which has been chosen similar to that of dry sand. Thus, the quality of the SAR focusing can be investigated and the underlying assumptions can be verified.
The distribution of the electric and magnetic field of the TEM double-ridged horn antenna has been recorded for different frequencies between 2 GHz and 10 GHz, which corresponds to the band of operating frequencies for this type of antenna. So-called field monitors which allow for recording of the components of electromagnetic field at a certain plane inside the soil have been defined for a number of frequencies in steps of 10 mm on the z-axis below the aperture of the antenna. The plane size of 1.6 m by 1.6 m, which has been chosen similar to the case of the dipole array to ensure, that the field energy level has decreased almost completely towards the edges of the simulated plane. The simulated field components for a single TEM double-ridged antenna are illustrated in Fig. 5.15. The method to calculate the overall field distribution of the antenna array by summing up the field contributions of the individual elements remains the same and the total field of a single TEM double-ridged horn antenna which has been calculated using equations (5.35) and (5.36) is illustrated in Fig. 5.16 whereas Fig. 5.17 illustrates electric and magnetic field of the corresponding array with 21 by 21 elements and a stepwidth of 5 cm between the elements in both directions which has been simulated for a frequency of 5 GHz.

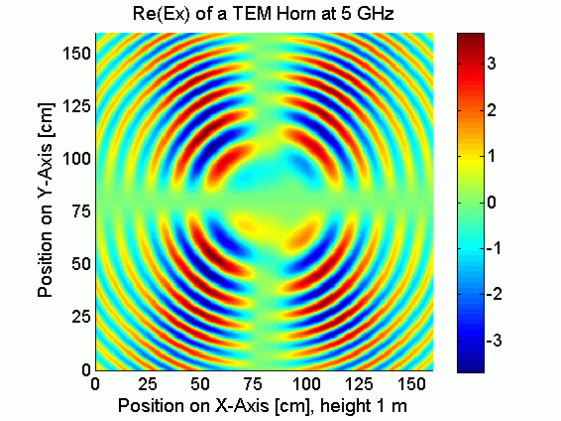

(a) E_x component

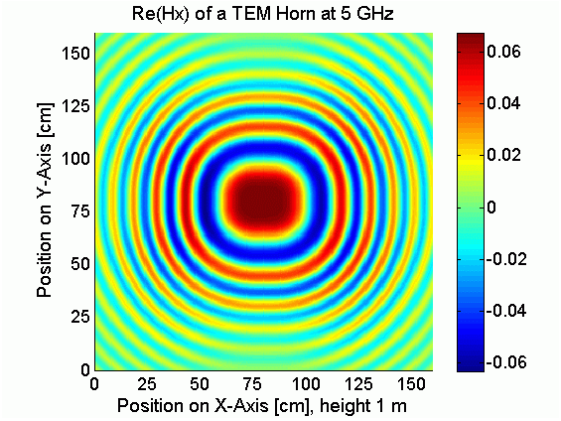

(b) H_x component

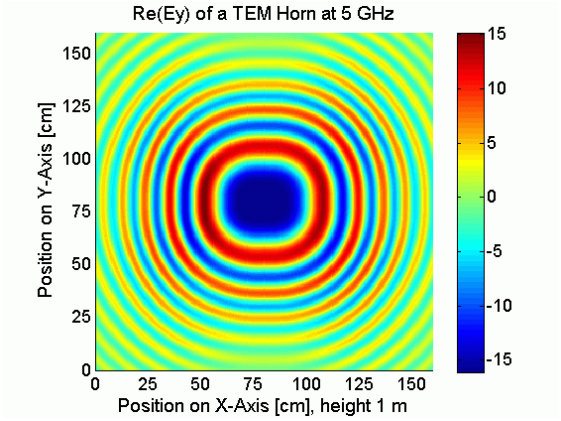

(c) E_y component

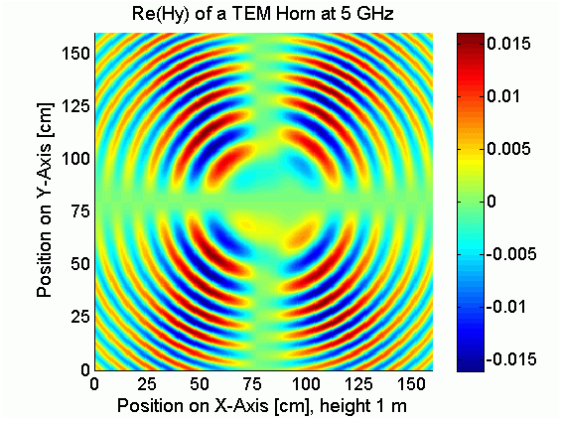

(d) H_y component

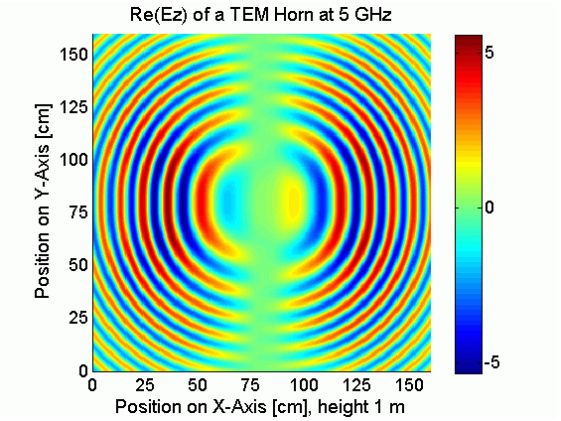

(e) E_z component

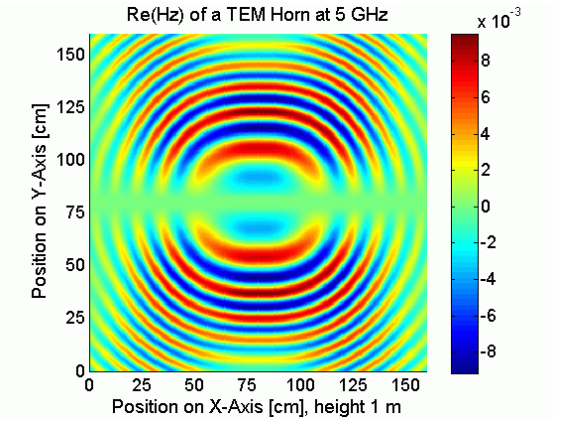

(f) H_z component

Figure 5.15: Field components of the TEM double-ridged horn at 5 GHz. The TEM horn is orientated with the two ridges along the x-axis of the coordinate system.

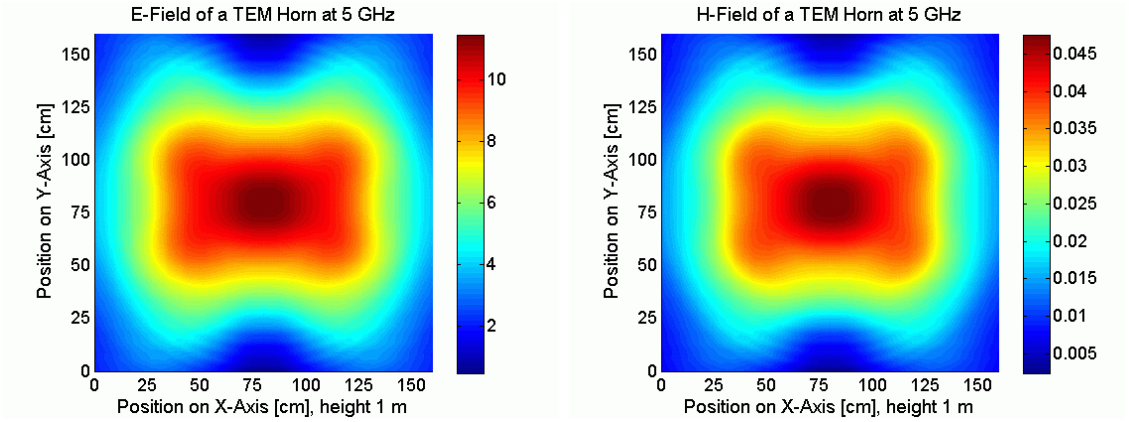

(a) E-field of a single TEM horn (b) H-field of a single TEM horn

Figure 5.16: E-field and H-field of a single TEM horn antenna at 5 GHz.

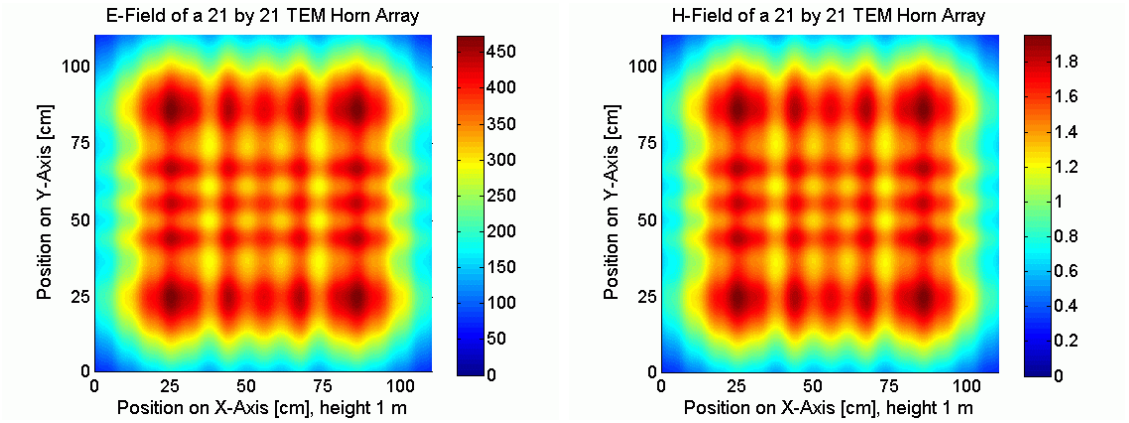

(a) E-field of a TEM horn array (b) H-field of a TEM horn array

Figure 5.17: E-field and H-field of a 21 by 21 TEM horn array at 5 GHz.

For both cases, the analytically calculated field patterns and the ones that utilize a numerically generated, realistic antenna characteristic, almost the same behavior can be obtained after the proposed SAR focusing is applied. Moreover, the comparison between the electric and the magnetic field of the TEM horn array for different geometrical configurations as it is illustrated in Figs. 5.18 and 5.19 and that of a similar dipole array configuration in Figs. 5.11 and 5.12 reveals the same dependencies. The quality of the focusing and the appearance of the discussed interference phenomena can be predicted precisely for the array of TEM horn antennas similar to the case of the dipole array. Hence, it is possible to anticipate the behavior of any given antenna designs in the context of a synthetically generated focusing array.

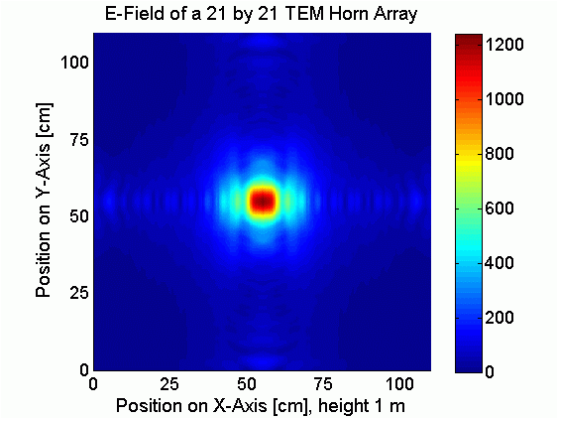

(a) 5 cm element step size

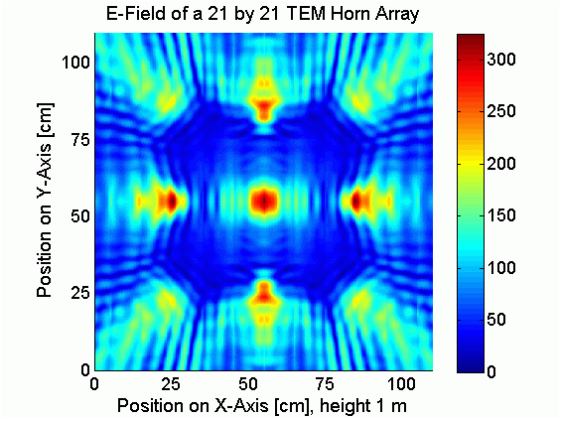

(b) 10 cm element step size

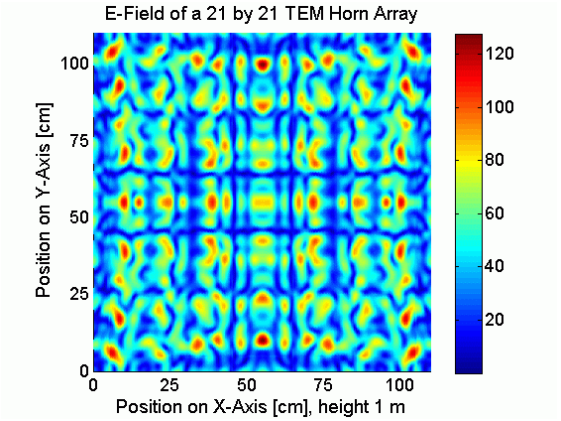

(c) 20 cm element step size

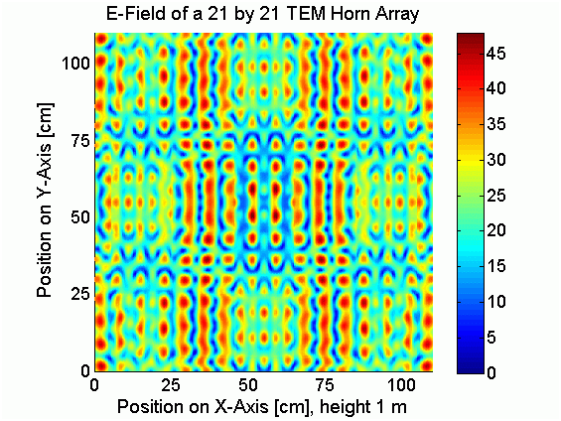

(d) 40 cm element step size

Figure 5.18: 21 by 21 TEM horn array with varied element step size at 5 GHz.

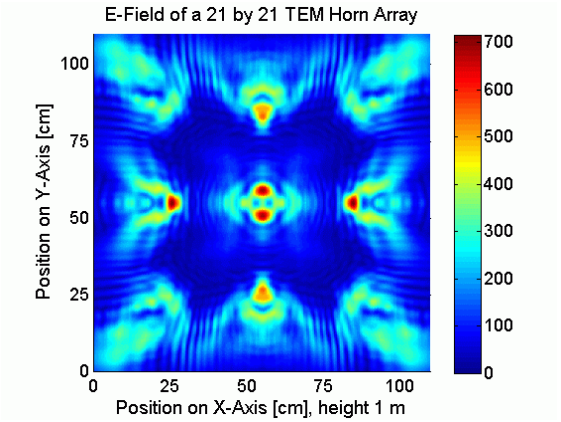

(a) 5 cm element step size

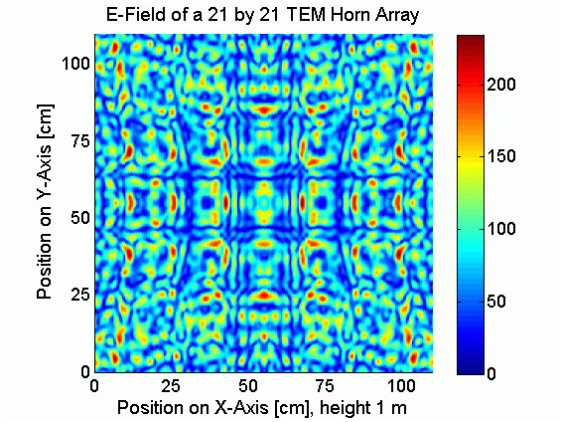

(b) 10 cm element step size

Figure 5.19: 21 by 21 TEM horn array with varied element step size at 10 GHz.

5.4.3 Verification of the Energy Beam

The major assumption of the proposed SAR focusing algorithm is a well-focused energy beam inside the soil as it is illustrated in Fig. 5.4. In this context beam means that the small spot size of the energy distribution is kept over large distances in the direction normal to the surface of the soil. The E-field distribution which is shown in Fig. 5.20 has been obtained for a TEM horn array with 21 by 21 elements, a step size of 5 cm between the elements for a frequency of 5 GHz. It is located 1 m above the soil with a permittivity of $\epsilon_r = 3$. Focusing point positions in the center, respectively, at the left edge of the array have been utilized. Fig. 5.21 illustrates that for both cases the energy beam remains well-focused for depth layers up to 30 cm. Hence, it is possible to reduce the 3D focusing problem to a 2D one.

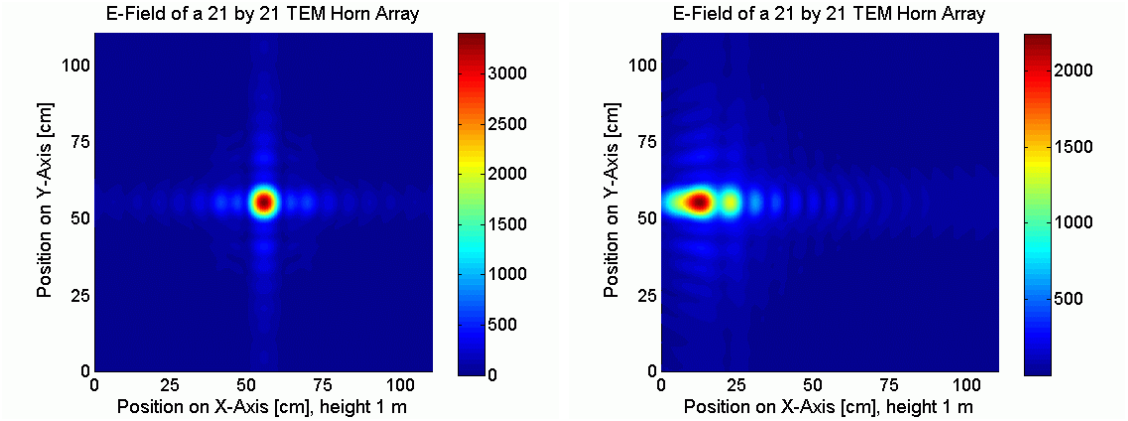

(a) Focusing at the center (b) Focusing at left edge

Figure 5.20: E-field at the surface of the soil for different focusing points.

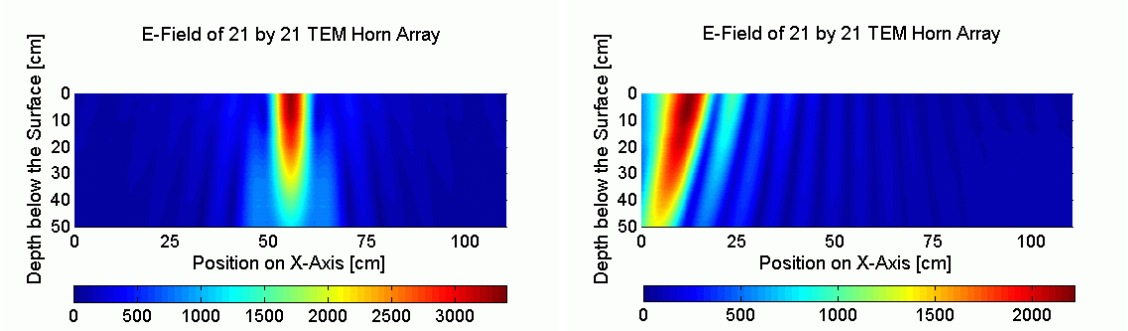

(a) Focusing at the center (b) Focusing at left edge

Figure 5.21: E-field up to 50 cm below the surface for this focusing points.

5.4.4 Gaussian Amplitude Weighting

In the previous section it has been explained, how the so-called grating lopes, namely the secondary focusing points, can be avoided completely if the grid step size of the synthetic antenna array is chosen with respect to the illuminated area and the highest operating frequency. However, e.g. Figs. 5.11(a) or 5.20(a) reveal minor interference structures on both coordinate axis through the focusing point. It is well-known that the farfield distribution of the array is given by Fourier transformation of the aperture loading. Consequently, the Fourier transformation of a rectangular aperture loading creates the sinc-modulation of the corresponding field which has been observed. It showed that a Gaussian weighting of the aperture loading can compensate for this effect although the field distribution is observed in the nearfield region. The suggested technique modifies the aperture loading in such a way, that it appears to be Gauss shaped. Hence, the corresponding field distribution will also be Gauss shaped and the sinc-modulation can be reduced significantly. The weighting equation which has been taken from [Har78] returns an α-valued N-point Gaussian window. Herein N is given by the number of antenna elements on the x-axis, respectively the y-axis and α is defined as the reciprocal of the standard deviation. As α increases, the width of the window will decrease and elements which are located closer to the edges of the antenna array will be attenuated. Fig. 5.22 illustrates the improved focusing quality of a 21 by 21 dipole array with grid steps of 5 cm and an operating frequency of 5 GHz considering a weighting with α=2.

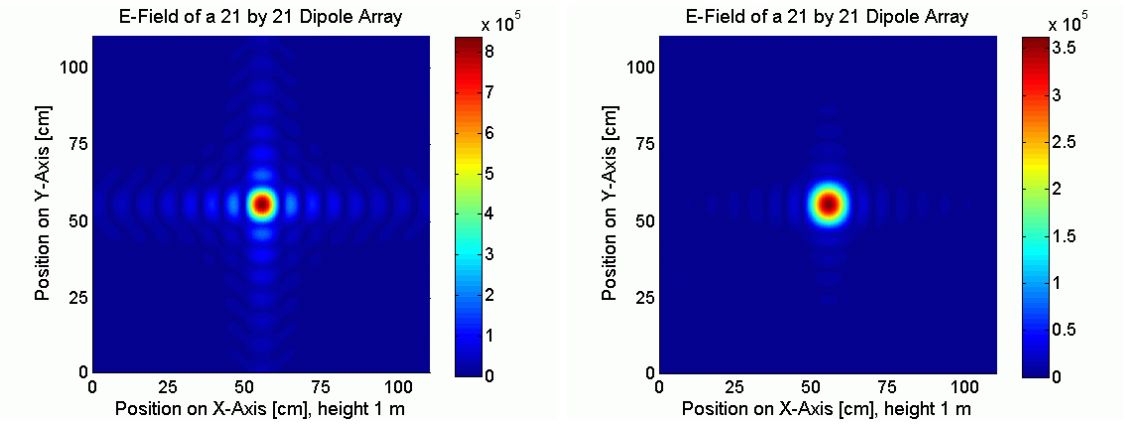

(a) No weighting

(b) With weighting

Figure 5.22: Gaussian weighting for a 21 by 21 dipole array at 5 GHz.

Fig. 5.22(b) clearly illustrates the ability of the proposed Gaussian amplitude weighting to reduce the unwanted interference phenomena significantly. In comparison to Fig. 5.22(a), however, it shows, that the diameter of the focusing spot has been increased while the energy density has been decreased, because the SAR focusing utilizes an array with smaller effective dimensions which is due to the Gaussian weighting. If α is increased further the interference phenomena could be removed completely, but the SAR focusing would yield a spot size similar to that of a much smaller synthetic array without any weighting. Therefore, a suitable value for the weighting factor α has to be determined as a trade off between the suppression of the unwanted interference phenomena and the resolution of the SAR array.
As another example the E-field distribution of a linear dipole array with 51 elements and a step size of 2 cm between the elements which is operated at a frequency of 5 GHz should be investigated. The focusing point has been chosen in the center of the array. For the investigation three different focusing depths have been taken into account, namely, 25 cm, 50 cm and 100 cm below the aperture of the antenna array. As it is shown in Fig. 5.23 for all three cases the discussed interferences can be obtained if no further amplitude weighting is applied. Fig. 5.24 illustrates how different values of α modify the results of the SAR focusing. While for α=2 some of the interference structures still remain visible they are removed completely for a value of α=4. However, the energy concentration has already been decreased significantly and decreases further, if higher values such as α=6 are utilized.

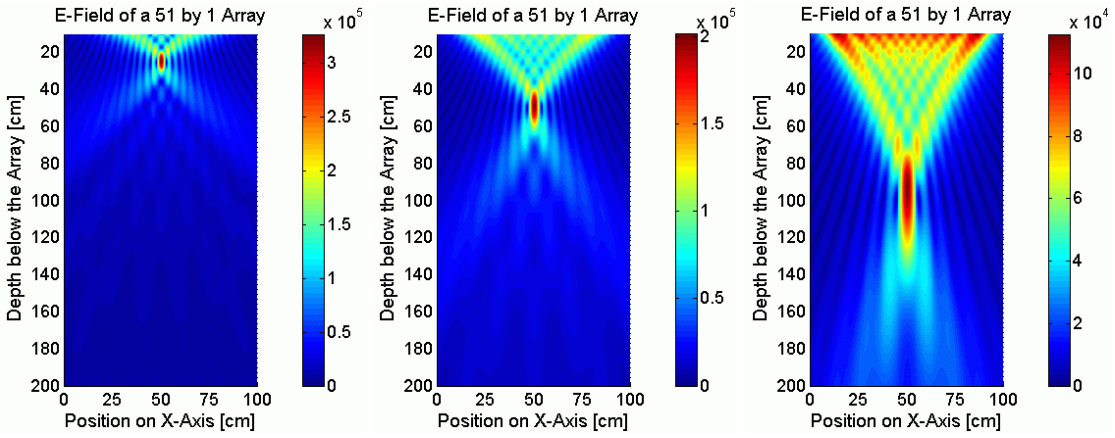

(a) $h_{foc} = 25\,cm$ (b) $h_{foc} = 50\,cm$ (c) $h_{foc} = 100\,cm$

Figure 5.23: E-field distribution for different depths of focusing.

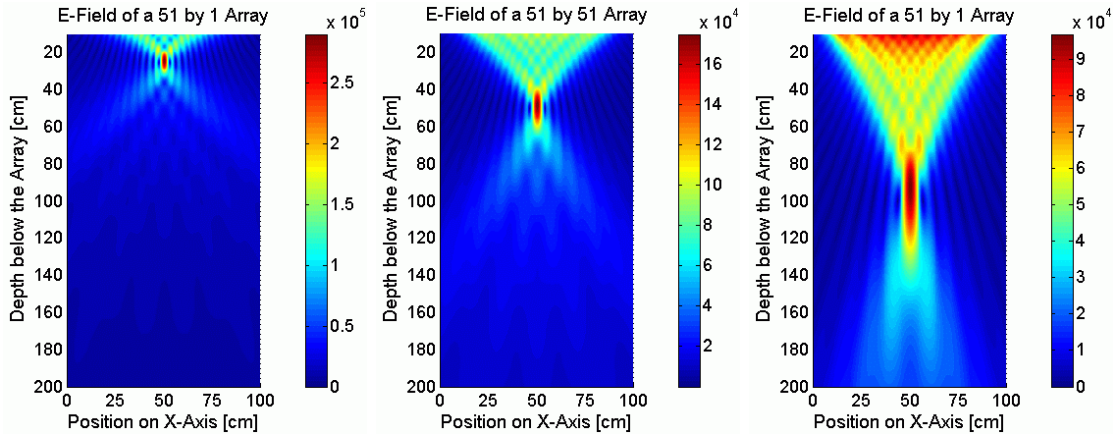

(a) $h_{foc} = 25\,cm$ (b) $h_{foc} = 50\,cm$ (c) $h_{foc} = 100\,cm$

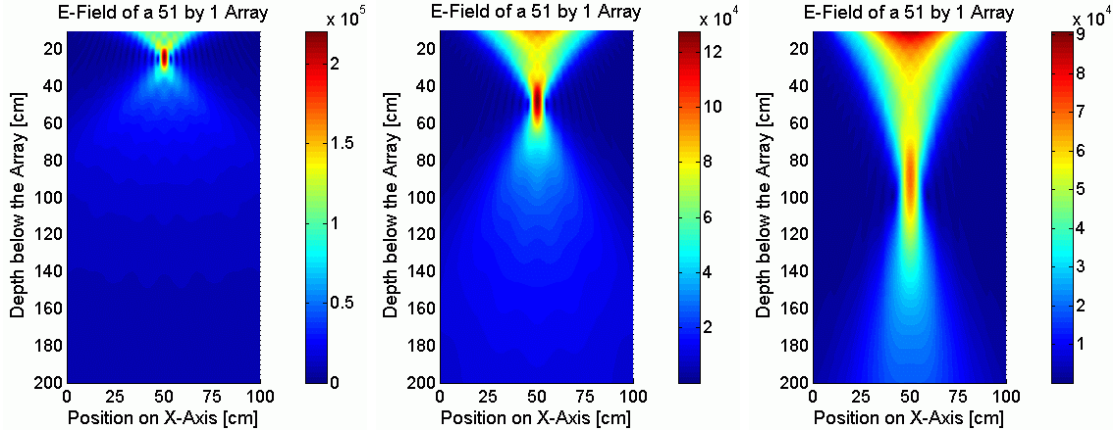

(d) $h_{foc} = 25\,cm$ (e) $h_{foc} = 50\,cm$ (f) $h_{foc} = 100\,cm$

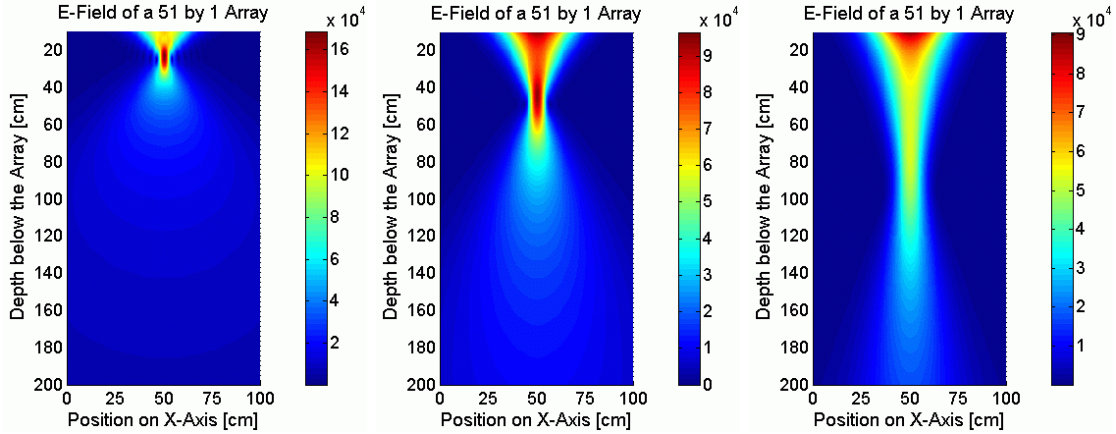

(g) $h_{focus} = 25\,cm$ (h) $h_{focus} = 50\,cm$ (i) $h_{focus} = 100\,cm$

Figure 5.24: Amplitude weighting for α=2 (a)-(c), α=4 (d)-(f) and α=6 (g)-(i).

5.5 Verification of the SAR Focusing

5.5.1 Resolution Capabilities of SAR

In order to verify the proposed concept of SAR focusing a first experimental measurement at the laboratory GPR setup, see 7.2, has been accomplished. The SFCW measurement is done using a vector network analyzer which is remotely controlled via the GBIP interface from a control PC. The same PC also provides the control of the automated antenna positioning system. The two C-scan measurements which have been performed utilize 41 by 41 antenna positions that have been distributed with a stepwidth of 1 cm. For the experiment a monostatic antenna configuration has been chosen and a TEM double-ridged horn antenna is utilized. It has been placed in a distance of 30 cm above the surface of the soil, which consists of homogeneously distributed dry sand with a permittivity of $\epsilon_r = 2.5$ and a loss tangent of 0.01. The measurement utilizes a frequency range from 2 GHz to 10 GHz.
For the investigation two differently shaped objects have been buried in a depth of 8 cm below the surface of the soil in the center of the soil area. The objects are made from foam material with electromagnetic properties of air, namely, a permittivity of $\epsilon_r = 1$ and negligible losses. Object 1, which will be referred to as stair-shaped, is illustrated in Fig. 5.25(a), whereas Fig. 5.25(b) illustrates object 2, which will be referred to as H-shaped. Both objects utilize a characteristic length of all edges of 5 cm which has been chosen to fit the operating wavelength at the center frequency, namely, 6 GHz. Thus, it should be possible to determine the achievable spatial resolution of the GPR for the case with and without the SAR focusing.

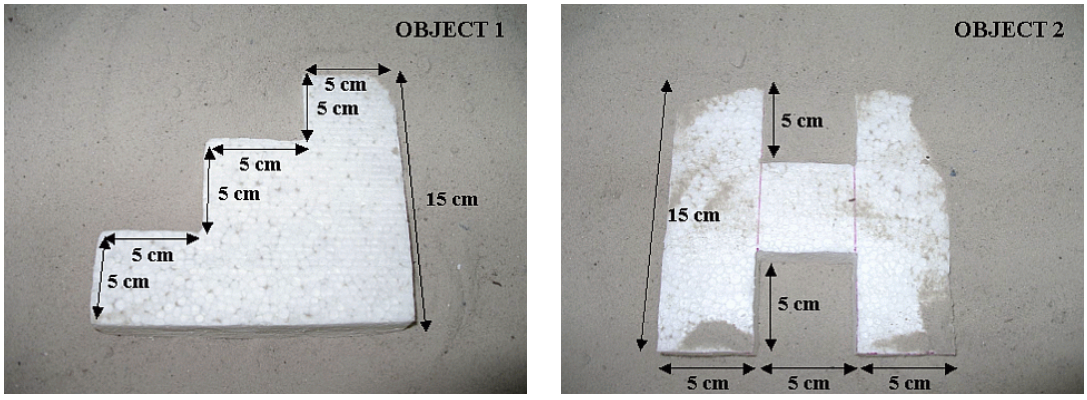

Figure 5.25: Test objects which have been made from foam material ($\epsilon_r = 1$).

After the measurements have been completed the resulting data sets are transformed to the time domain. Figs. 5.26(a) and 5.26(b) illustrate the results of the measurement without any further processing of the raw data set. It is obvious, that the shape of the objects cannot be determined correctly. Moreover, the resulting image of object 2 is suggesting a wrong object shape which is basically the result of constructive interference at the where the antenna footprint covers both sides of the H-shaped body. However, Figs. 5.26(c) and 5.26(d) clearly verify, that the spatial imaging resolution of the GPR can be improved significantly if the proposed SAR focusing is applied. The resulting images reveal the shapes of the buried target objects which clearly indicates that the achieved spatial resolution of the GPR is significantly better than the edge length of these target objects, namely, 5 cm.

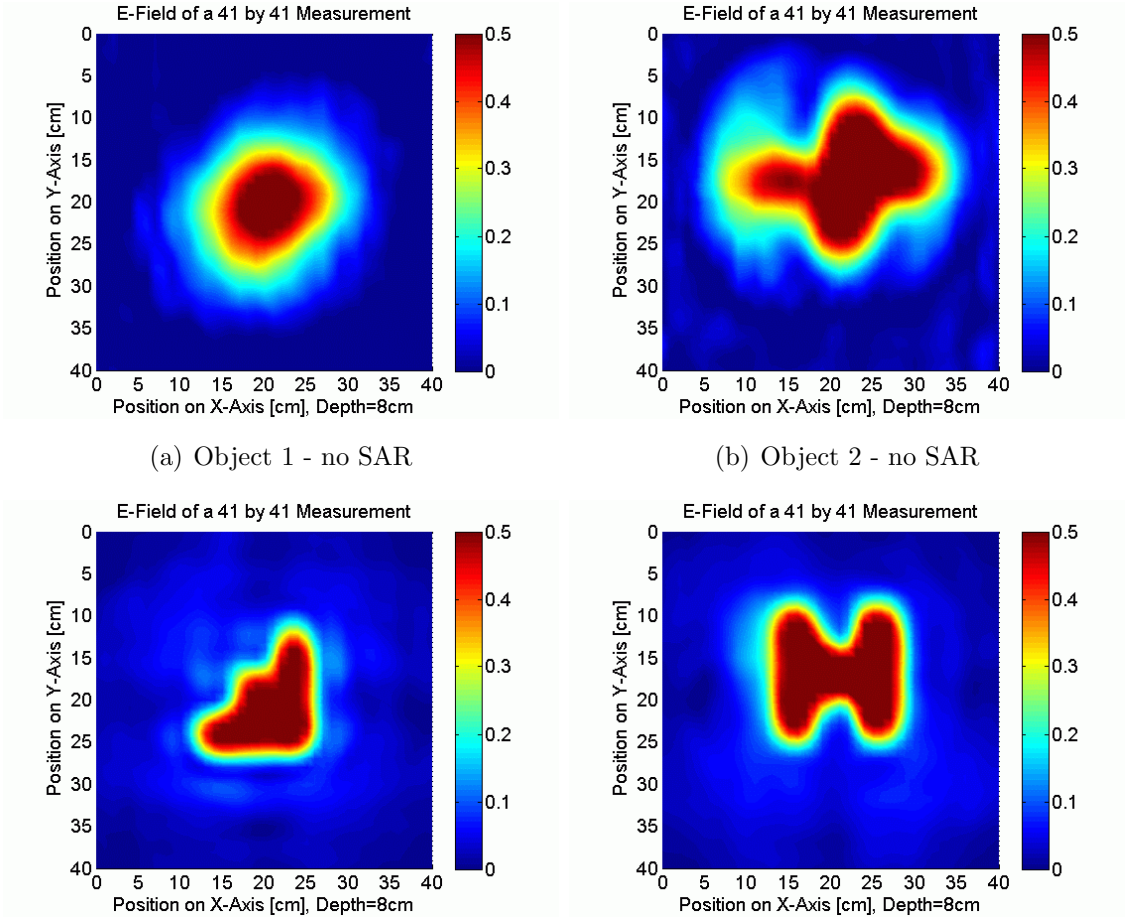

(a) Object 1 - no SAR

(b) Object 2 - no SAR

(c) Object 1 - with SAR

(d) Object 2 - with SAR

Figure 5.26: Measurement results without (a)-(b) and with SAR focusing (c)-(d).

5.5.2 Using an Independent Imaging Grid

For all previous investigations it has been assumed that the SAR focusing has been applied to exactly the same locations at which the antenna measurements are taken. In other words, the imaging or focusing grid has implicitly been assumed to be identical to the measurement grid which has not to be necessarily the case. In order to illustrate the consequences of such an equal grid distribution, the number of antenna positions for the experimental GPR configuration with object 2 has been decreased without changing any additional parameters of the measurement. Figs. 5.27(a) and 5.27(b) illustrate the results of the SAR focusing considering only 21 by 21 antenna elements with an axial distance of 2 cm, respectively, 11 by 11 antenna elements in a distance of 4 cm that both cover the same area which has been illustrated previously using 41 by 41 antenna elements in a distance of 1 cm.

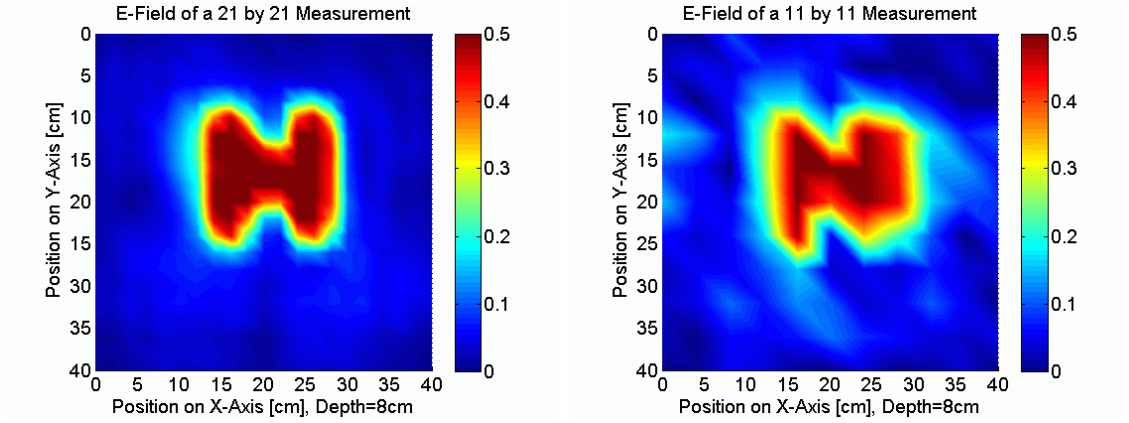

(a) 21 by 21 positions, 2 cm distance

(b) 11 by 11 positions, 4 cm distance

Figure 5.27: SAR focusing results without independent imaging grid.

It shows, that the resolution is decreased in comparison to Fig. 5.26(d). While an axial distance of 2 cm between the antenna elements still allows to recognize the correct shape of target object 2 it is no longer possible to identify the characteristic H-shape if a distance of 4 cm between the antenna elements is utilized. However, the distribution of the points for which the SAR focusing is applied does not depend on the distribution of the antenna measurements. Therefore, a reasonable imaging grid has been found as a trade-off between achievable imaging resolution and computational efforts. It showed, that the imaging resolution starts to converge for an axial distance of 1 cm and that further improvements can be neglected.

As a verification the previous GPR configurations with different axial distances between the antenna elements have been investigated and a constant axial focusing points distance of 1 cm has been utilized. It shows, that the quality of the results with 21 by 21 antenna elements has been increased and is almost identical to the case with 41 by 41 elements. Moreover, even with 11 by 11 antenna elements, see Fig. 5.28(c), the target object can clearly be identified. However, the better quality of the SAR images reveals first grading lobe effects which have been discussed in 5.4. They are related to the axial distance between the antenna elements. Consequently, the quality of the focusing decreases significantly if the axial antenna distance is increased beyond a certain limit as it has been illustrated for the case with 6 by 6 antenna elements and an axial antenna distance of 8 cm in Fig. 5.28(d).

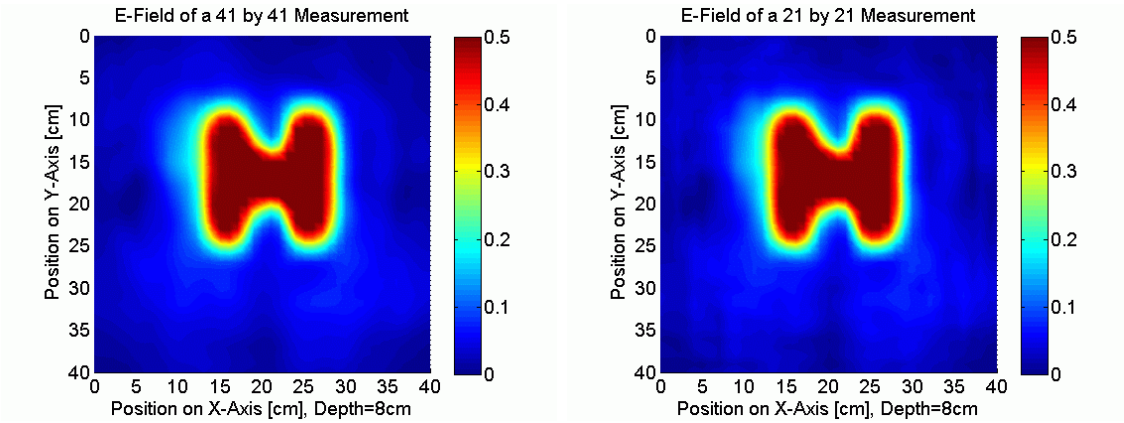

(a) 41 by 41 positions, 1 cm distance

(b) 21 by 21 positions, 2 cm distance

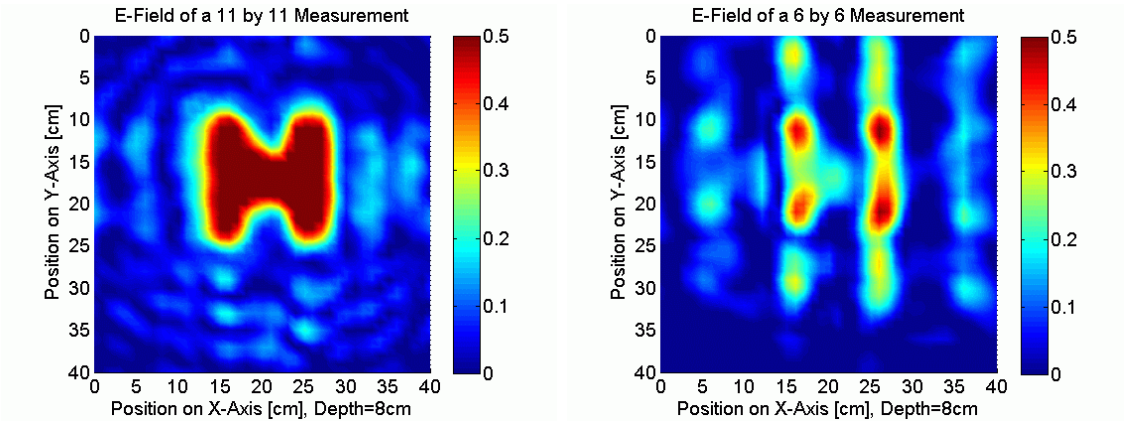

(c) 11 by 11 positions, 4 cm distance

(d) 6 by 6 positions, 8 cm distance

Figure 5.28: SAR focusing results with 1 cm imaging grid resolution.

5.5.3 Real-Time Implementation of SAR

Some GPR field applications require a real-time processing of the measurement results. The implementation of the SAR algorithm by means of FPGA processing can already improve the computational efficiency significantly. Nonetheless, the size of the synthesized array should be as small as possible in order to increase the processing speed further. On the one hand the total size of the synthesized antenna array is directly effecting the resolution of the SAR focusing. However, for certain SAR array dimensions additional elements are no longer contributing to the focusing which allows to define the maximum size of the synthesized antenna array.
In the context of this thesis different methods have been investigated, that allow to split the total array in subarrays so that the SAR processing can be applied immediately after the measurements have been carried out for this subarray. Again, the 41 by 41 elements measurement of target object 2 has been utilized and Fig. 5.29(a) illustrates the results of a SAR focusing for which the 41 by 41 elements array is split in 41 arrays with the dimension 41 by 1 along the x-axis. The results in Fig. 5.29(b) represent the case where the 41 by 41 elements array is split in 4 subarrays with 21 by 21 elements. After the SAR focusing has been applied the subarray results are recombined. For both cases some object features are lost due to the limited size of the focusing array. The H-shape of the buried object, however, can still be anticipated from the images. Further investigations revealed that smaller subarrays give only inferior results exactly as it has been predicted theoretically.

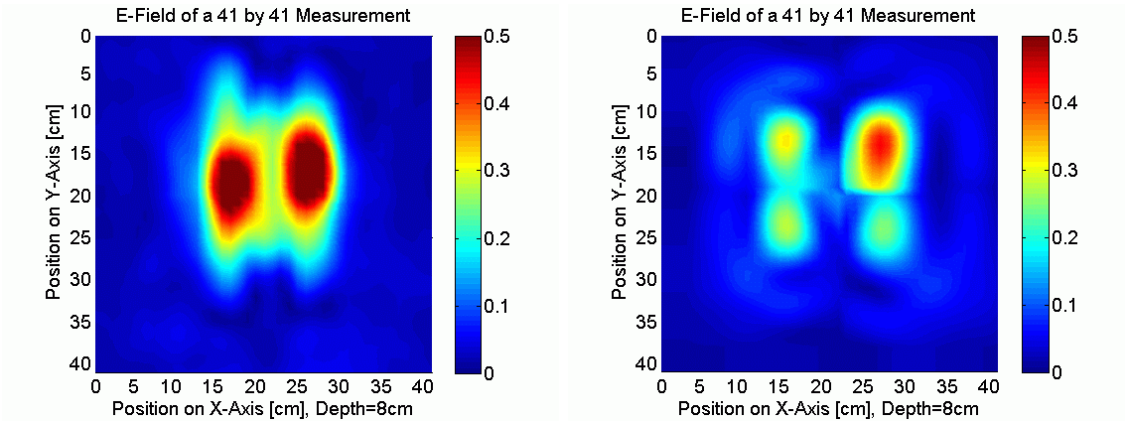

(a) Processing of 41 (41 by 1) arrays

(b) Processing of 4 (21 by 21) arrays

Figure 5.29: SAR focusing results for different subarray configurations.

Chapter 6

Focusing with Dielectric Lenses

6.1 Introduction

An appropriate imaging of GPR has to provide a resolution which is sufficient for the detection and classification of target objects either by post-processing or as hardware implementation. The concept of focusing waves using lenses such as in Fig. 6.1 is well-known and has already been utilized for microwave applications before, e.g. [KM02]. However, to the author's knowledge the successful realization of a lens focused GPR has not been reported yet. In [Man05] it has even been stated, that a dielectric lens it is not suitable for focusing the radiation of a rectangular horn antenna. Nonetheless, a biconvex dielectric lens in which is supposed to increase the imaging resolution of a GPR has been designed and experimentally investigated. For the design of the lens a full 3D field simulation has been used which properly models the feeding horn antenna, the lens itself as well as the ground in which a target object is buried. The performance of the lens approach is assessed by investigating the imaging resolution for a certain buried target object.

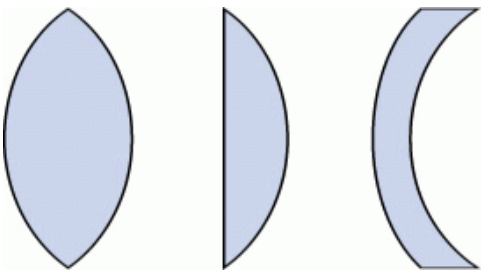

Figure 6.1: Different shapes for the design of a focusing lens.

6.2 Design of a Dielectric Lens

At first the structural shape of the lens has to be defined. A lens is constructed either traditionally as a solid shape or as a so-called zoned lens which has been introduced first by Augustin Fresnel in 1822 [Var06c]. Hence it is also referred to as Fresnel lens. It reduces the amount of material required compared to a conventional spherical lens by breaking the lens into a set of concentric annular sections known as Fresnel zones. For each of these zones, the overall thickness of the lens is decreased, chopping the continuous surface of a standard lens into a set of surfaces of the same curvature, with discontinuities between them. This allows a substantial reduction in thickness, weight and volume of the lens, at the expense of reducing its quality. Although zoned lenses have been used in many different applications (Fig. 6.2) the resulting image is not nearly as good as that from a continuous lens. Moreover, for broadband microwave applications it is not possible to compensate the different path lengths for all considered frequencies. Hence, a Fresnel lens is not suitable for the broadband focusing of an antenna in the context of subsurface radar.

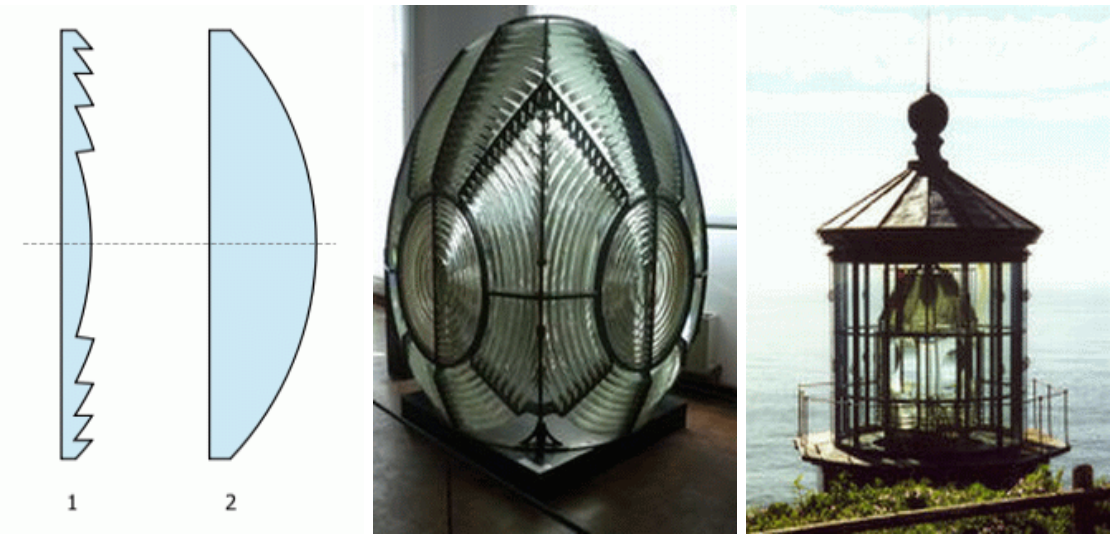

Figure 6.2: Concept and application of a Fresnel lens [Var06c].

For the construction of a biconvex lens as it is proposed for the focusing of a ground penetrating radar two independent plano-convex lenses have to be designed, which will be combined at the planar wave front interface. Therefore, two different focusing problems are taken into account, namely, the problem of an upper lens which focuses

on the phase center of the antenna and the problem of a lower lens that allows for focusing on the surface of the ground as it has been illustrated in Fig. 6.3. Both plano-convex lenses are designed and optimized individually and combined afterwards in order to achieve the desired biconvex dielectric lens. The actual design of the lens should take the following points into account. At first, it should not be located too close to the feeding antenna in order to avoid disturbance of the feeding antenna which would degrade the overall system performance. A properly designed lens should be illuminated uniformly. An oversized lens leads to a bulky design and a considerable power loss in the lens itself. Furthermore, the refraction index of the dielectric material should not be too large in order to avoid large reflections.

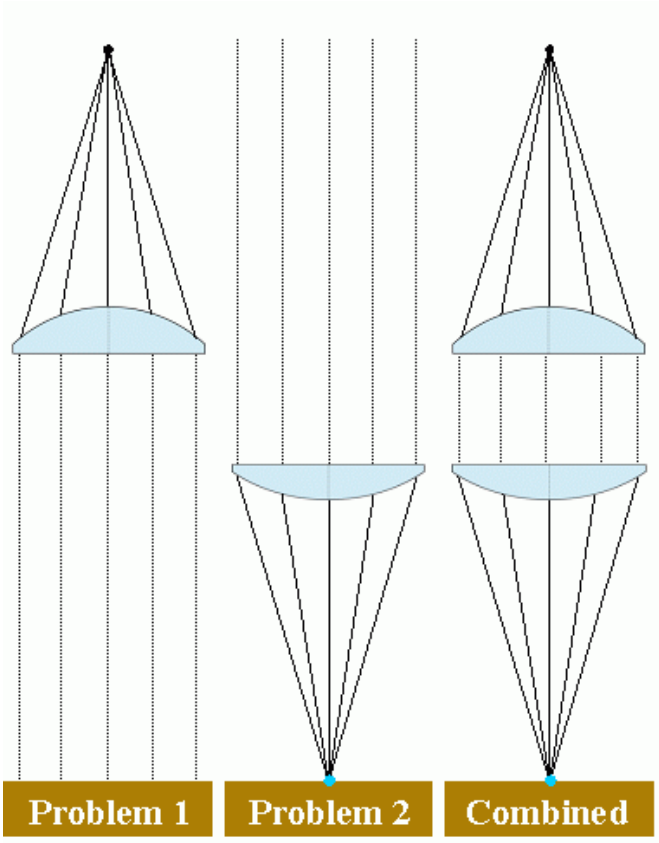

Figure 6.3: Combination of two independently designed plano-convex lenses.

The shapes of both plano-convex lenses have been designed using the well-known lens equation (6.1) which can be found in various textbooks such as [KM02]. By some algebraic modifications it can be transformed into equation (6.2) which allows for computing the shape of a plano-convex lens considering the underlying geometry.

$$R = \frac{(\eta - 1) \cdot L}{\eta \cdot \cos\theta - 1} \tag{6.1}$$

$$z' = -\frac{L}{\eta + 1} \pm \sqrt{\frac{x^2}{\eta^2 - 1} + \left(\frac{L}{\eta + 1}\right)^2} \tag{6.2}$$

The specific geometrical relations for the design procedure, e.g. the distance to the focusing point L and the refraction index of the dielectric material η are defined according to the model of a plano-convex lens setup as it is shown in Fig. 6.4.

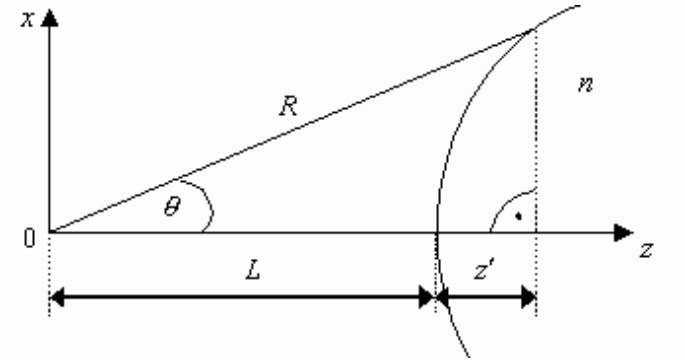

Figure 6.4: Geometrical relations for the design of a plano-convex lens.

The prototype of the dielectric lens is made of 'artificial wood'. This material seems to be ideal for the intended application because it is cheap, light-weight and can easily be shaped on a machine. Furthermore, it reveals an almost frequency independent relative permittivity of $\epsilon_r \approx 2.1$ and reasonable losses, exactly as it has been demanded. The resulting material parameter which were determined by a precision broadband measuring method [JMO03; AJO07] are illustrated in Fig. 6.5.

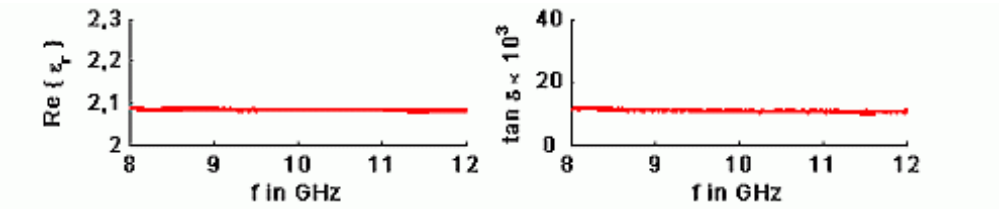

Figure 6.5: Measurement results of relative permittivity and loss tangent.

The final design of the two plano-convex focusing lenses has been determined by optimization as follows. The upper plano-convex lens has been designed for a distance of 15 cm between the center of the lens surface and the aperture of the feeding 20 dB standard gain horn. Taking into account that the phase center of the feeding rectangular horn is located 12 cm behind its aperture, the lens has been designed for a focal length of 27 cm. For the lower plano-convex lens a corresponding focal length of 20 cm has been assumed as it is shown in Fig. 6.6.

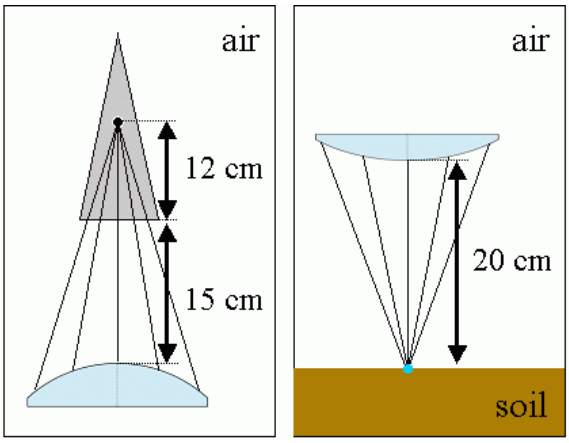

Figure 6.6: Considered positioning of upper and lower plano-convex lens.

The biconvex lens in Fig. 6.7 which consists of the combined plano-convex lenses has been shaped on a CNC milling machine. It has a diameter of 28 cm and a thickness of around 15 cm. For the practical realization a plastic holder has been constructed, which is supposed not to affect the propagation performance of the system.

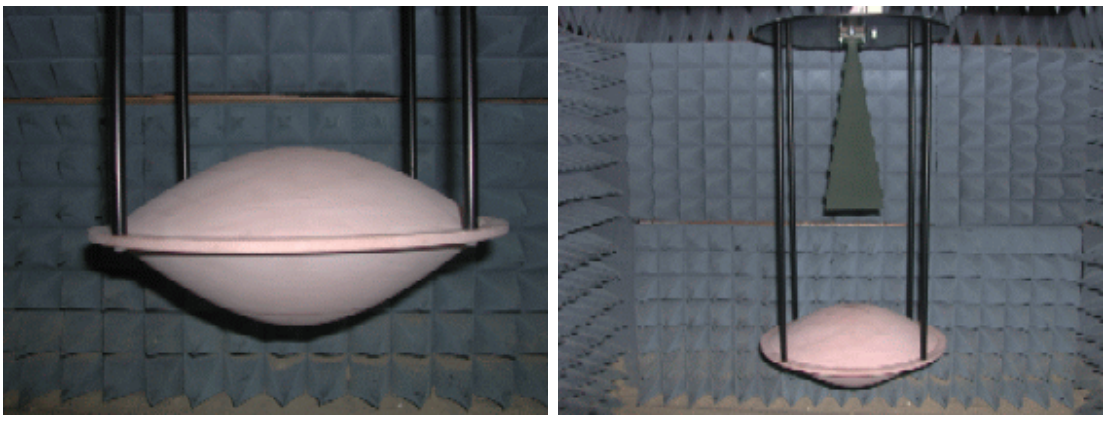

Figure 6.7: Dielectric lens with plastic holder and feeding horn antenna.

6.3 Verification of the Lens Concept

The simulation of the GPR environment that includes the antenna, the lens, the homogeneous soil and the buried target objects has been implemented utilizing the remote control technique which has been discussed in 3.6. A 20 dB standard gain horn antenna, see 4.2, has been used as feed. For this configuration the distance between the antenna and the lens has been chosen by optimization to be 15 cm while the distance between the lens and the surface of the ground has been set to 16 cm. This distance has been found as a good compromise between different lens positions (Fig. 6.8) and yields an optimum field distribution inside of the soil.

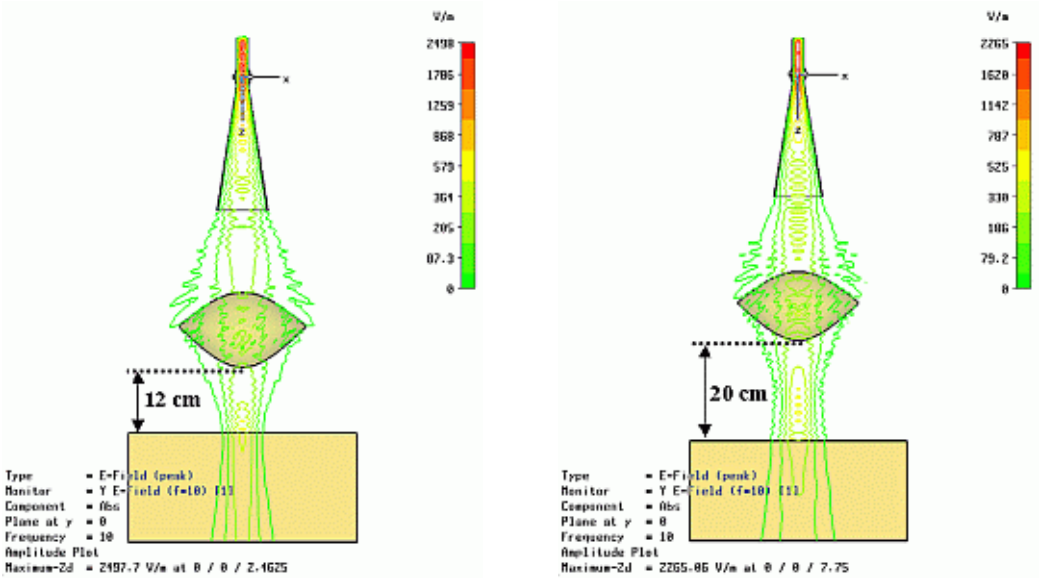

(a) 12 cm distance between lens and soil (b) 20 cm distance between lens and soil

Figure 6.8: Resulting E-field distribution for a frequency of 10 GHz.

The resulting concentration of the energy at the surface which describes the quality of the focusing has been obtained for both, the proposed antenna system utilizing a dielectric lens and different positions of the horn antenna without lens. The first configuration without a lens considers the 20 dB horn antenna at the original height above the ground and yields the worst result (Fig. 6.9(a)). But also for an antenna position of 16 cm above the surface, which corresponds to the position of the lens (Fig. 6.9(b)) and at only 2 cm above the surface of the soil (Fig. 6.9(c)) the horn antenna cannot outperform the lens focused configuration (Fig. 6.9(d)).

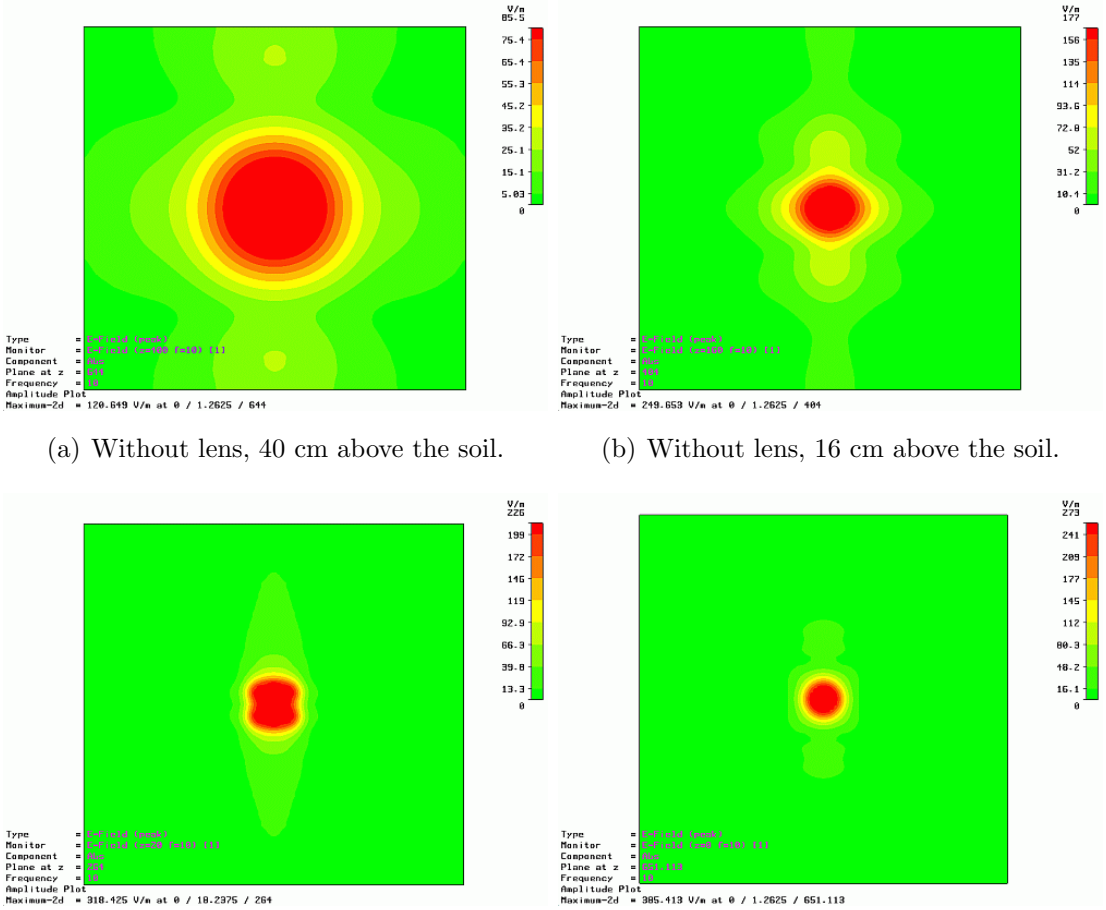

(a) Without lens, 40 cm above the soil.

(b) Without lens, 16 cm above the soil.

(c) Without lens, 2 cm above the soil.

(d) With proposed lens configuration.

Figure 6.9: Amplitude of the E-field at 10 GHz at the surface of the soil.

However, the 2 cm case of Fig. 6.9(c) cannot be used in GPR due to the large disturbance of the feeding antenna by the soil. For focusing a GPR for landmine detection the energy beam has to remain concentrated for at least 20 cm below the surface and the best height of the lens above the soil must reveal a concentrated field for all layers within this region. Figs. 6.10(a) - 6.10(b) illustrates the best results of the antenna without lens placed 2 cm above the surface. The application of the lens 20 cm above the surface significantly improves the the concentration of the energy (Figs. 6.10(c) - 6.10(d)), but the resolution can be increased if the focus point which is located in a fixed distance of 20 cm is placed below the surface. An optimum position of the lens has been obtained 16 cm above the surface (Figs. 6.10(e) - 6.10(f)), which corresponds to a focus point 4 cm below the surface.

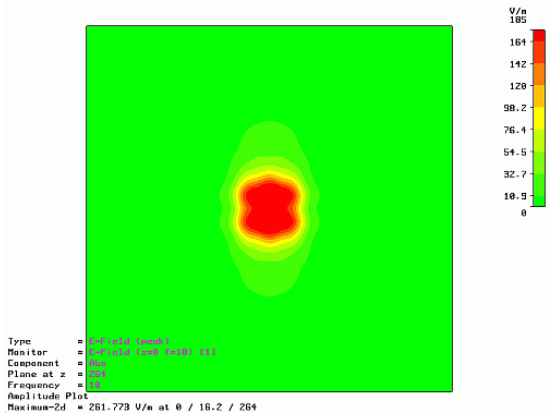

(a) surface layer without a lens

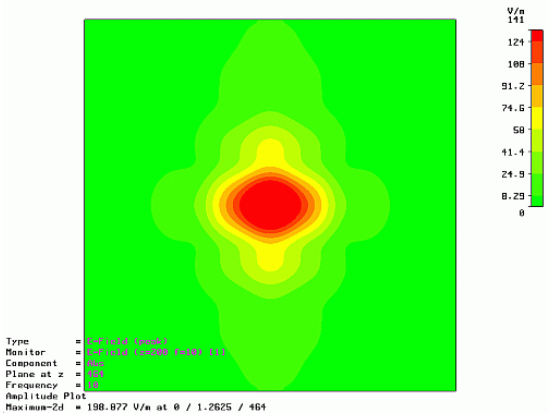

(b) depth of 20 cm without lens

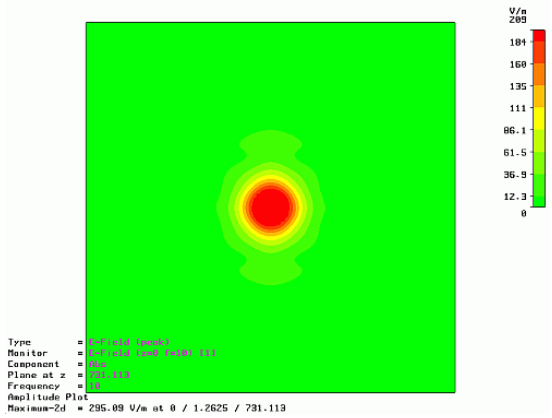

(c) surface layer for '20 cm setup'

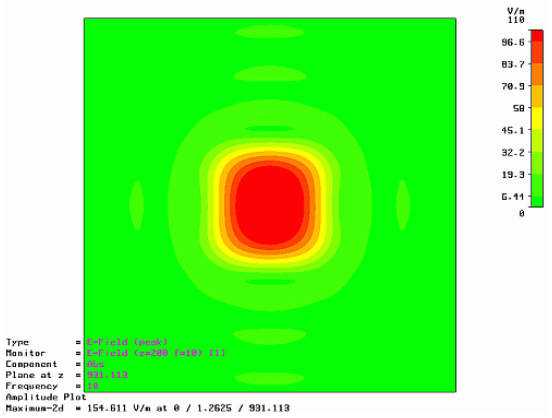

(d) depth of 20 cm for '20 cm setup'

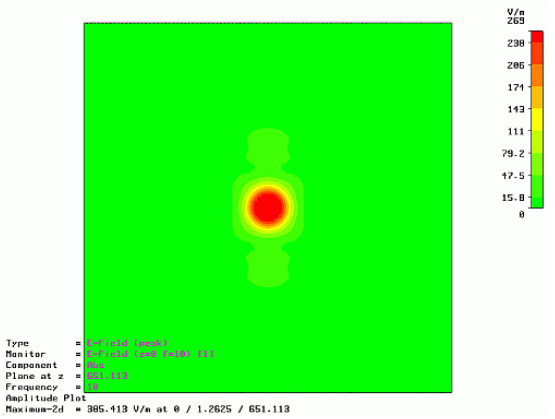

(e) surface layer for '16 cm setup'

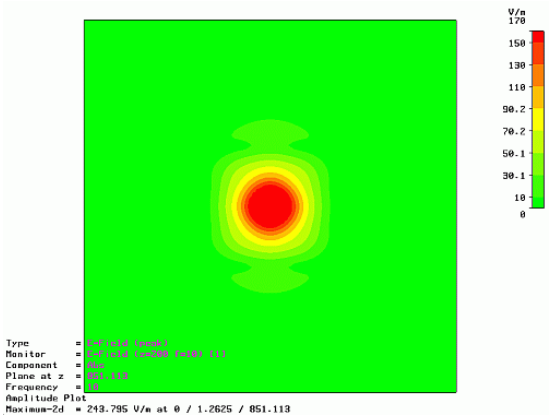

(f) depth of 20 cm for '16 cm setup'

Figure 6.10: E-field at 10 GHz with 20 dB horn for different configurations.

The resolution of a GPR with and without lens will be obtained utilizing 3D field simulations of two B-scans with 31 steps and a step size of 1 cm (Fig. 6.11). In order to obtain the ability of the proposed lens focused GPR system to distinguish between closely located scatterers two air-filled target objects with a relative permittivity of 1 and dimensions of 5 cm by 5 cm by 20 cm have been placed in a distance of 5 cm and in a depth of 7 cm below the surface of the soil as it is illustrated in Fig. 6.12. The B-scan axis has been chosen perpendicular to the orientation of the target objects in order to determine the ability of the system to distinguish between both. For the soil material the permittivity of dry sand, namely, 2.5 with a loss tangent of 0.01 has been assumed. These values have also been obtained by the broadband method which utilizes waveguide measurements [JMO03; AJO07]. The simulation utilizes a frequency range from 8 GHz to 12 GHz which corresponds to the frequency range for which the feeding horn antenna has been designed, namely, the X-band frequency range. Moreover, two B-scan measurements with and without lens with 31 steps and an identical step size of 1 cm have been made. The distances between antenna, lens and surface, the size and the orientation of the target objects which are made of foam material with a relative permittivity of $\epsilon_r = 1$ are exactly as they have been chosen for the field simulation. The experiments have been conducted using the laboratory GPR, see 7.2, which is illustrated in Figs. 6.13 and 6.14 and the same operating frequency range from 8 GHz to 12 GHz has been utilized.
The results of the 3D field simulations (Figs. 6.15(a) - 6.15(d)) and measurements (Figs. 6.16(a) - 6.16(d)) reveal, that a dielectric lens is suitable for the focusing of a subsurface radar and that the agreement between simulation and experimental results is excellent. The buried target objects which have been placed in a distance of only 5 cm can clearly be distinguished as separated objects whereas for the case without lens they appear to be merged and, even worse, form a phantom object with the strongest reflection in the middle between both objects. The measurement also shows that even a small surface roughness is effecting the reflection which leads to slightly different images of the left and the right object. From the right hand side of Figs. 6.15 and 6.16 it can be concluded that the contrast of the buried target objects can significantly be enhanced if a simple background subtraction is applied, which basically subtracts the ground reflection from the actual one. In conclusion the imaging resolution of a subsurface radar system can be enhanced significantly using the proposed dielectric lens setup which has been presented and verified.

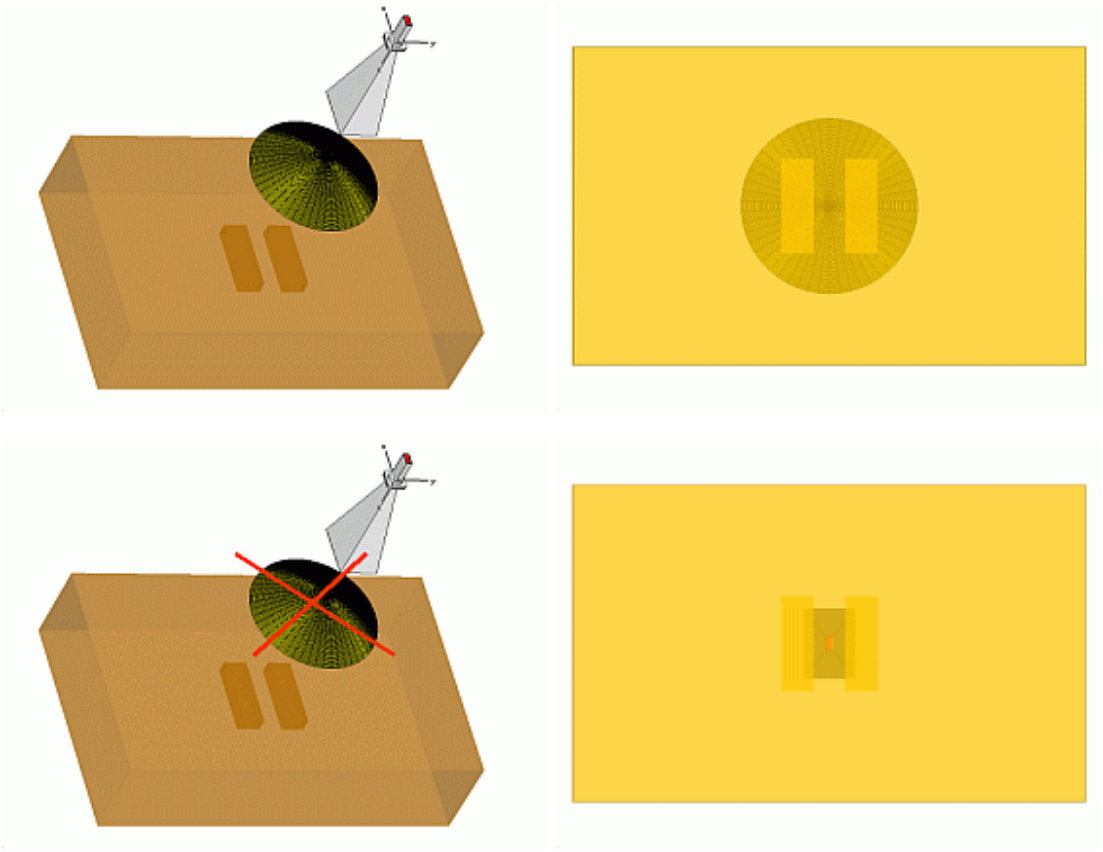

Figure 6.11: 3D simulation model for a GPR with and without focusing lens.

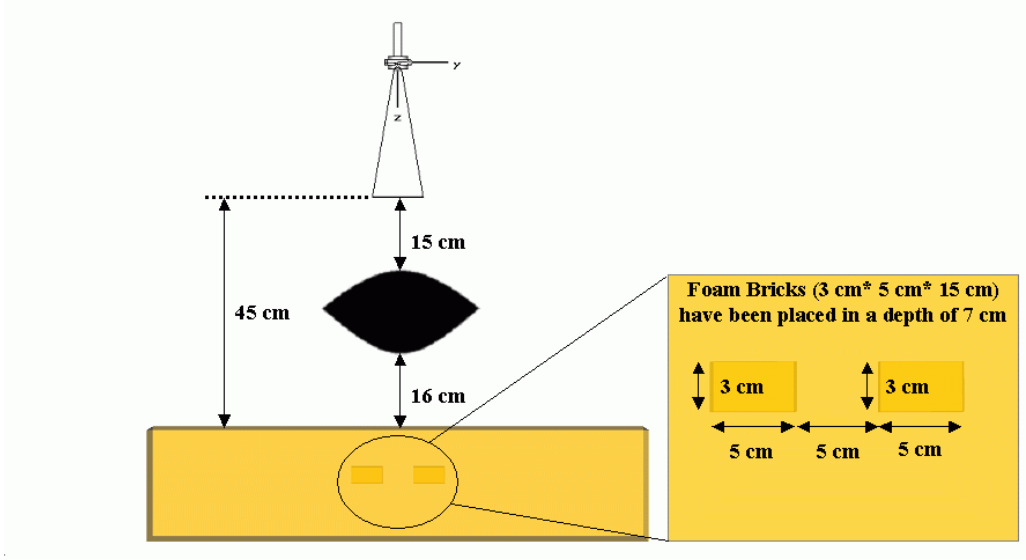

Figure 6.12: Positioning of target objects and lens setup for the simulations.

However, the resolution of the focusing lens can only be evaluated if it is compared to the results of the SAR focusing technique which has been introduced in 5.3. Therefore the B-scan results without lens have been corrected using this focusing technique. The corresponding images which have been obtained by simulations and measurements are presented in Figs. 6.15(e) and 6.15(f) and Figs. 6.16(e) and 6.16(f), respectively. Once again, they illustrate the outstanding capability of the proposed focusing technique. Even without the application of a background subtraction the target objects can clearly be distinguished and the correct depth of these objects can be obtained, whereas they are merged without SAR.

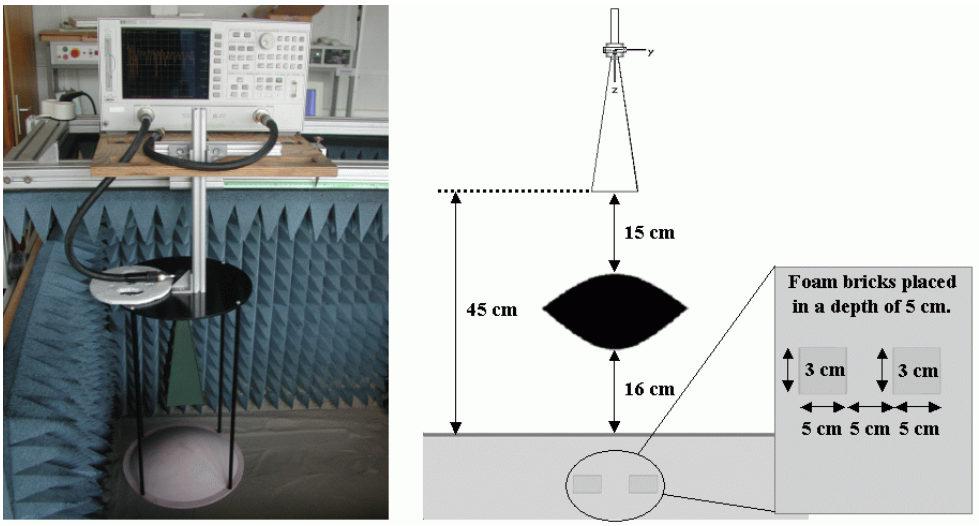

Figure 6.13: Positioning of target objects and lens setup for the measurements.

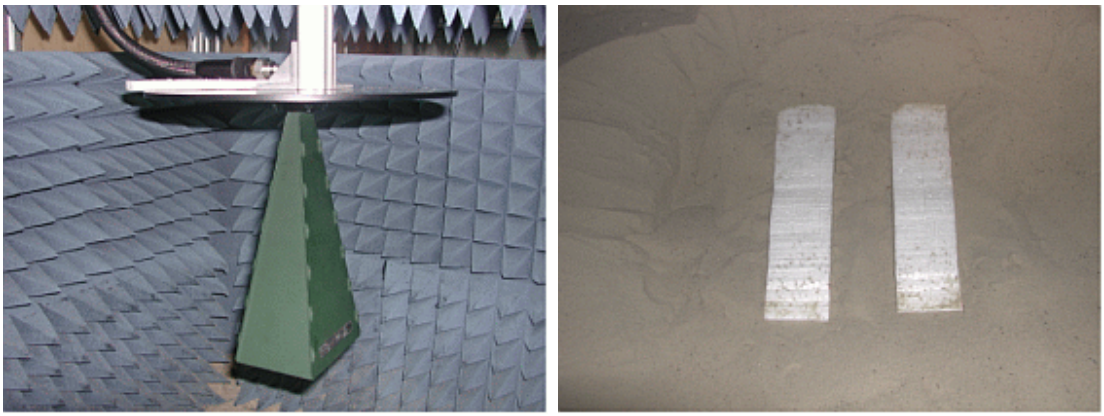

Figure 6.14: Feeding horn antenna without lens and target objects in the soil.

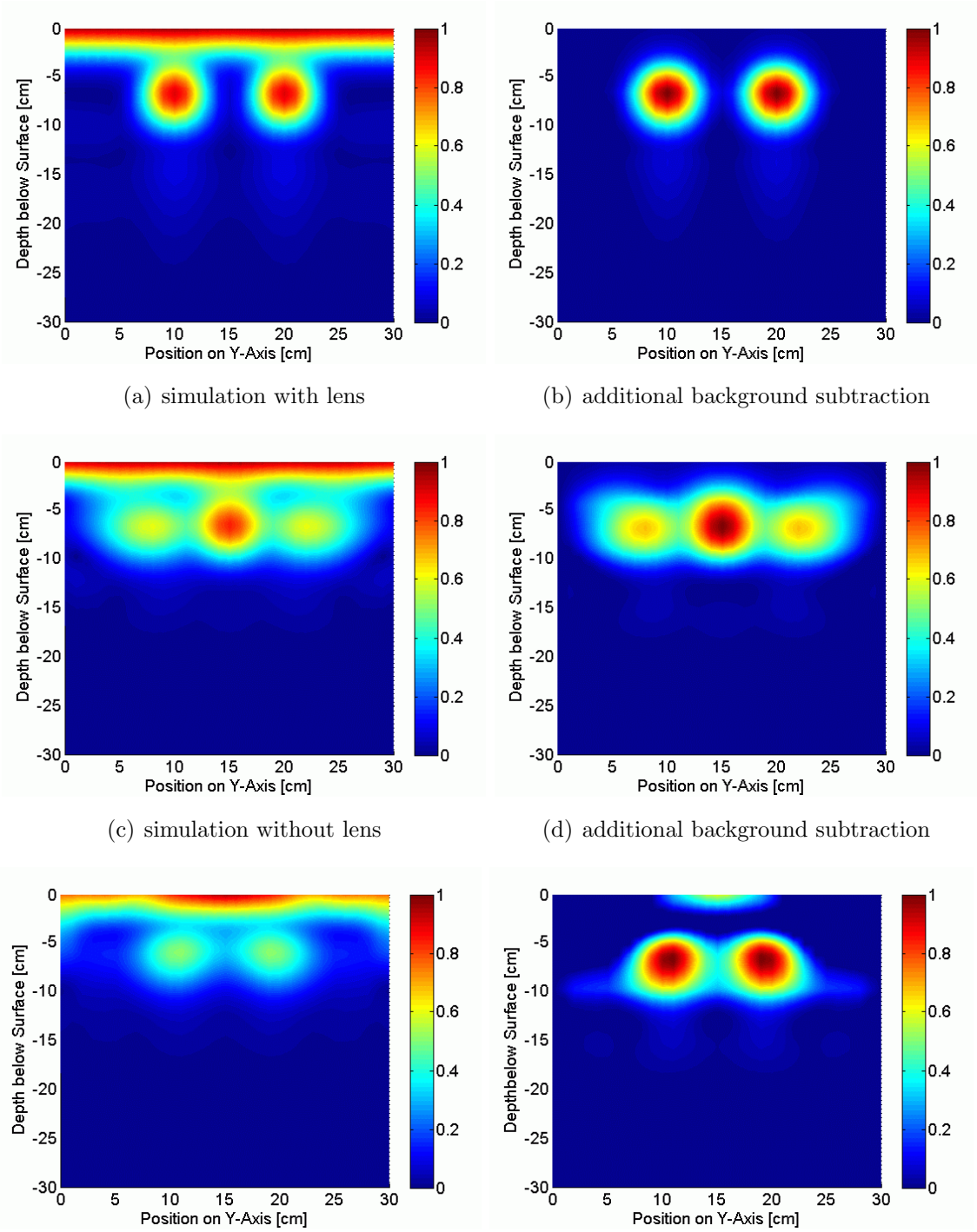

(a) simulation with lens

(b) additional background subtraction

(c) simulation without lens

(d) additional background subtraction

(e) simulation SAR without lens

(f) additional background subtraction

Figure 6.15: Results of the simulation with and without focusing lens.

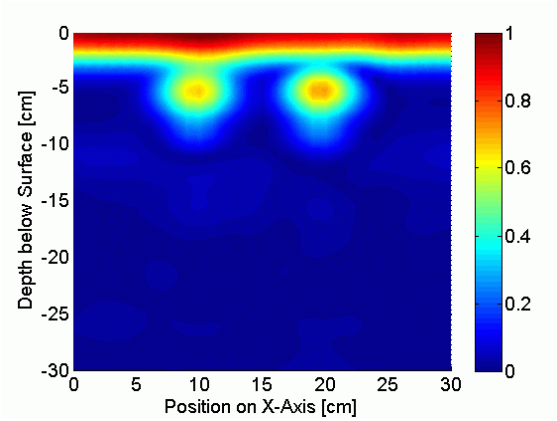

(a) measurement with lens

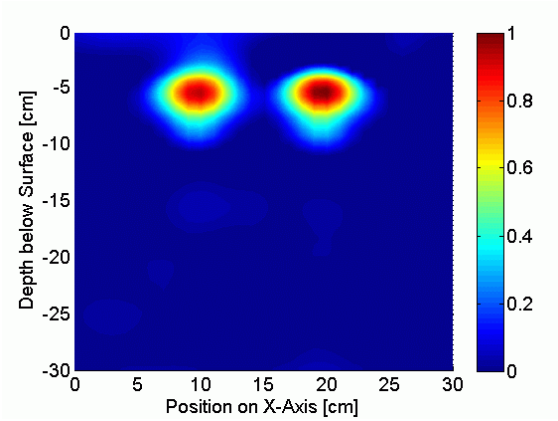

(b) additional background subtraction

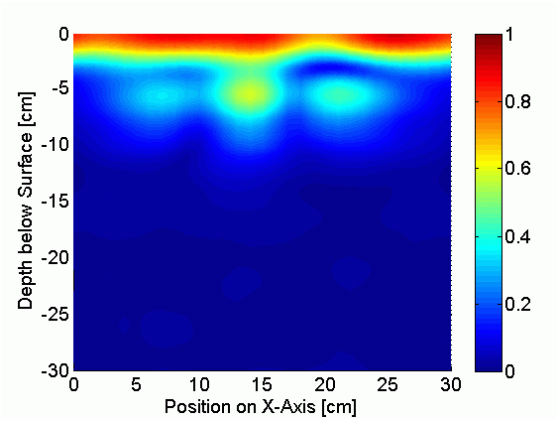

(c) measurement without lens

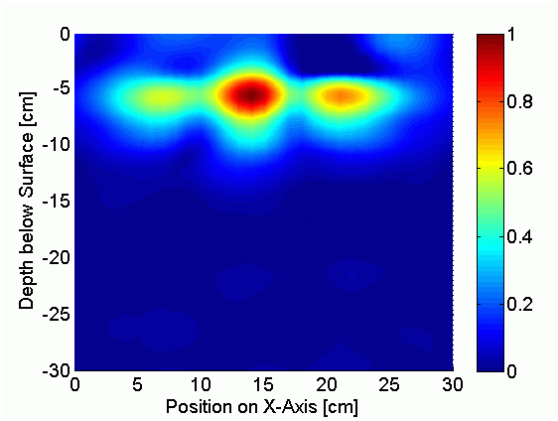

(d) additional background subtraction

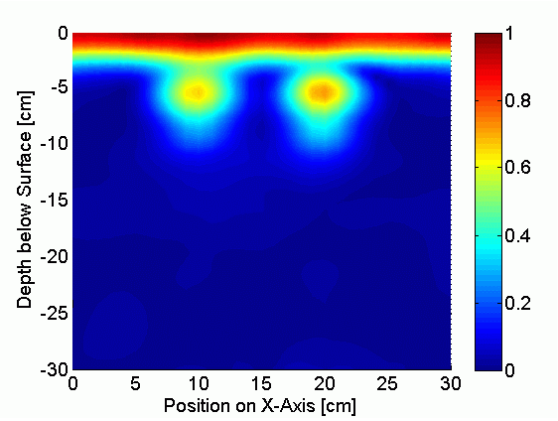

(e) measurement SAR without lens

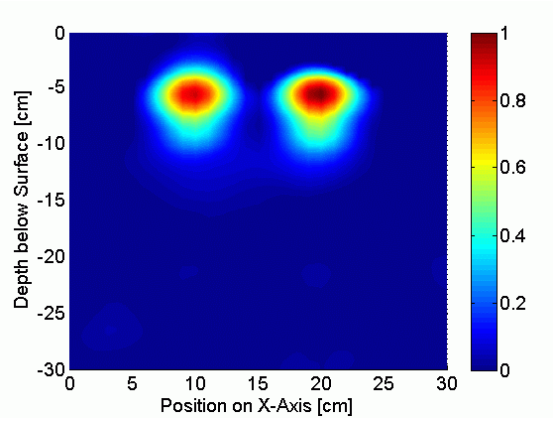

(f) additional background subtraction

Figure 6.16: Results of the measurement with and without focusing lens.

6.4 Adaptation of Additional Antennas

The existing lens configuration can easily be adapted to the new antenna, which is important, because it is easier to fabricate a new set of holding rods instead of another lens. For a given lens the best position for the 10 dB standard gain horn antenna (see 4.2) has been obtained by simulation. The best focusing results could be obtained for a distance of 20 cm between the aperture of the antenna and the surface of the dielectric lens. This means that the phase center of the antenna is located 27 cm away from the upper surface of the lens. The MWS simulation model and the resulting E-field distribution at 10 GHz are illustrated in Fig. 6.17.

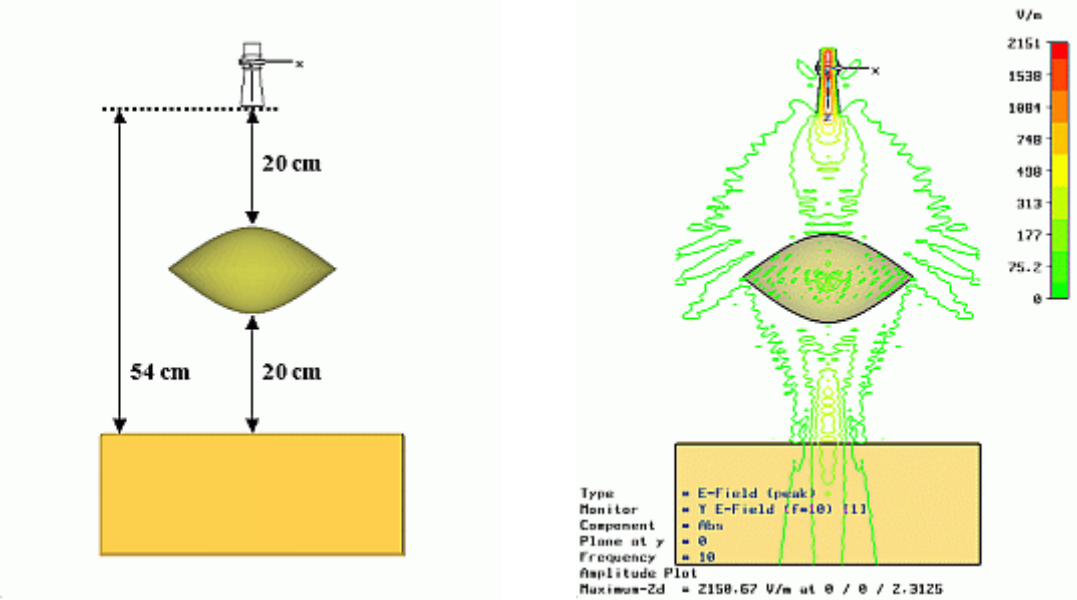

(a) 10 dB horn with lens and soil

(b) E-field distribution at 10 GHz

Figure 6.17: MWS model of the lens setup and resulting E-field distribution.

In order to verify the quality of the focusing at first the E-field distribution has been obtained for a 10 dB horn without lens which has been located in a distance of 2 cm above the surface of the soil (Figs. 6.18(a) and 6.18(b)). Again, the energy concentration at the surface and inside of the soil can be improved significantly if the proposed lens configuration is applied (Figs. 6.18(c) and 6.18(d)) and the degree of focusing can be further enhanced, if the focus point is moved 4 cm below the surface (Figs. 6.18(e) and 6.18(f)). For both cases a higher degree of focusing could be achieved in comparison to the setup which uses the 20 dB standard gain horn.

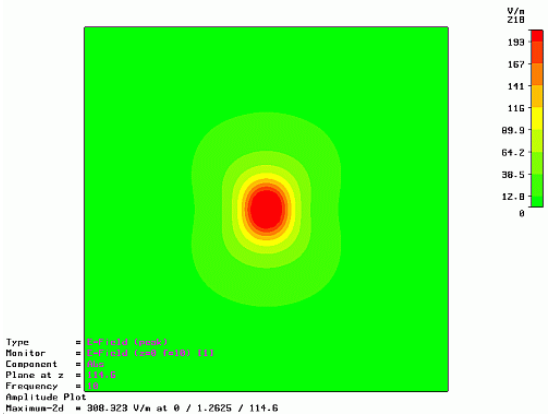

(a) surface layer without lens

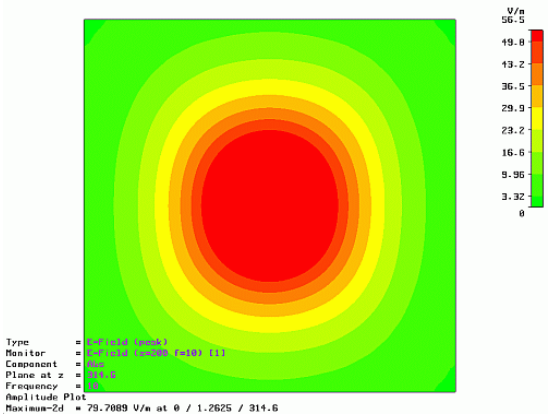

(b) depth of 20 cm without lens

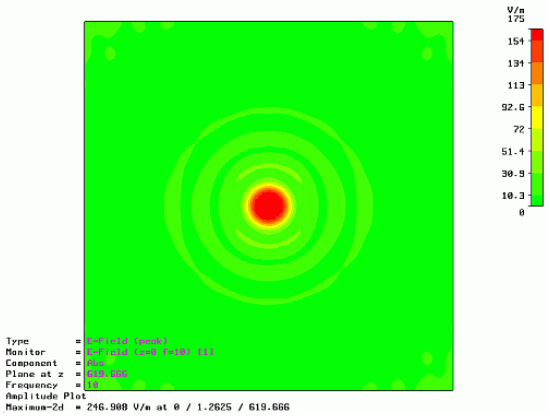

(c) surface layer for '20 cm setup'

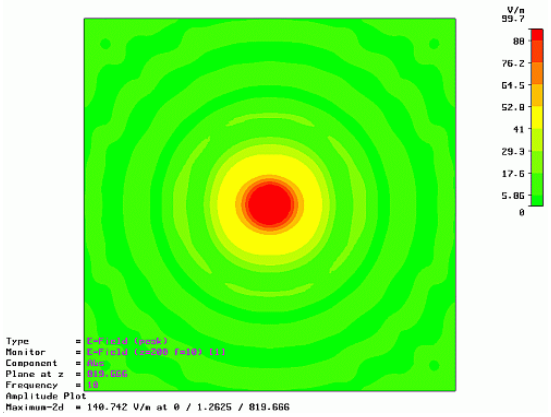

(d) depth of 20 cm for '20 cm setup'

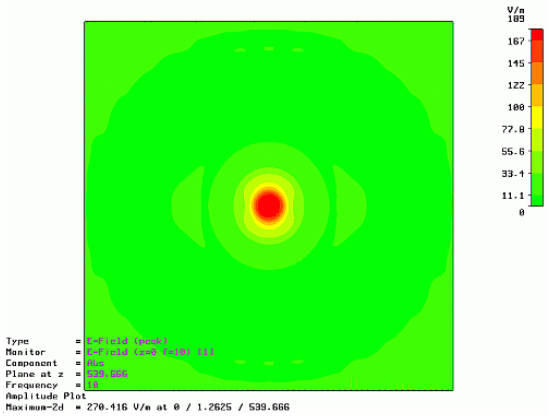

(e) surface layer for '16 cm setup'

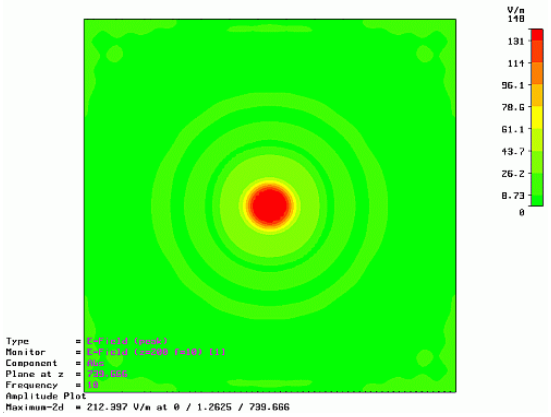

(f) depth of 20 cm for '16 cm setup'

Figure 6.18: E-field at 10 GHz with 10 dB horn for different configurations.

6.5 Discussion of the Lens Concept

In conclusion, the lens focusing approach should be compared with the SAR processing. On the one hand the lens focusing yields a precise lateral resolution and no further processing is needed to obtain the results for a certain A-scan measurement, whereas it is more complicated to implement a real-time SAR processing, which can only be done with much higher computational effort. However, every new antenna configuration requires an adaption of the lens setup and especially large lenses seem to be not suitable for any kind of mobile applications, whereas the SAR processing can be applied very flexible and completely without enlarging the measurement equipment. Moreover, the high directivity of the lens focused beam reveals another almost paradox drawback. The problem can occur, that the so-called pencil beam radiation pattern (small black spot in Fig. 6.19(a)) might simply miss smaller objects (white circular shapes) if the antenna is not placed directly above them.
Therefore, one of the advantages of the proposed SAR technique is the ability to reconstruct a complete area, even though the antenna has been placed only above a limited number of coordinates (large black areas in Fig. 6.19(b)) for which the position must be determined precisely in order to ensure correct results. Hence, none of the techniques dominates the other one completely and the specific application determines how the imaging resolution of the GPR should be increased.

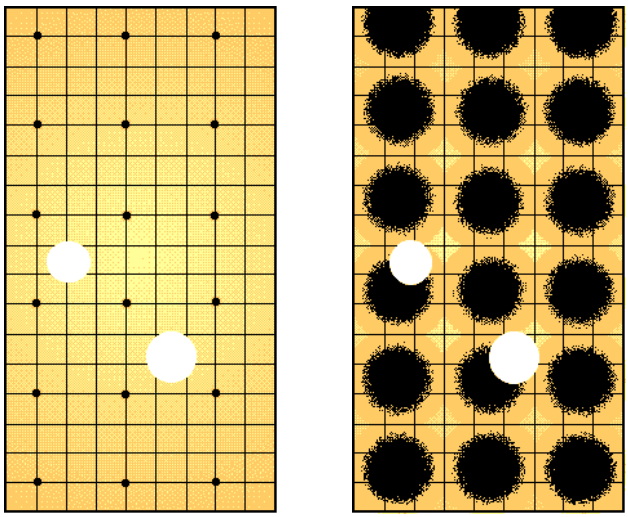

(a) with lens (b) without lens

Figure 6.19: Distribution of antenna footprints (black spots) on the surface.

Chapter 7

Experimental GPR Systems

7.1 Introduction

The previous chapters of this thesis have already taken into account several important aspects of a mine detecting GPR system, e.g. the investigation of antenna concepts for GPR or the proper focusing of the obtained radar images. In the following chapter the practical realization of a GPR system will be addressed. Therefore, the development of two PC-controlled GPR system for automated GPR measurements, namely, a laboratory GPR test facility, see Fig. 7.1(a) and a prototype of a mobile GPR systems for outdoor applications will be addressed. Both systems have been employed for GPR experiments using either real AP mines or other test objects, see Fig. 7.1(b), and different important results will be discussed.

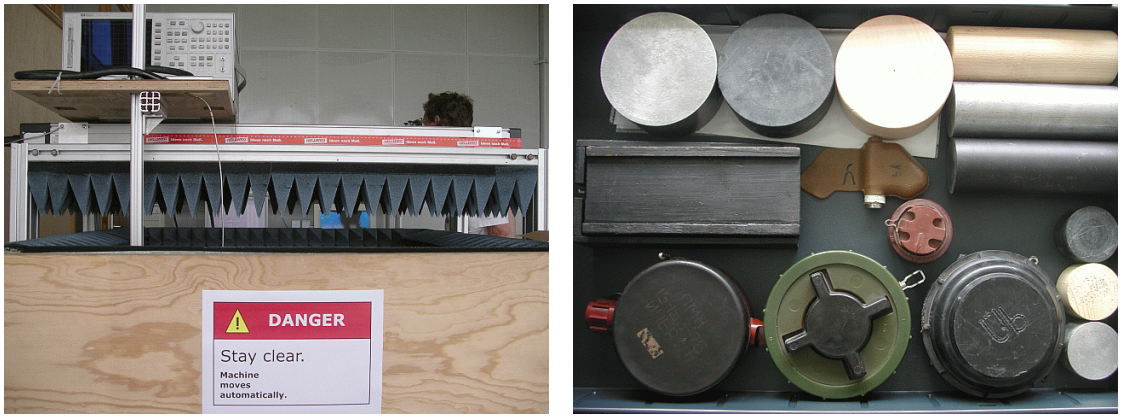

(a) automated GPR test facility (b) AP mines and test objects

Figure 7.1: Test facility and accessories for experimental GPR measurements.

7.2 Laboratory GPR Investigations

7.2.1 Configuration of the GPR System

The laboratory GPR test facility, see Fig. 7.2, which has been developed in the context of this thesis allows to perform very large GPR experiments such as C-scan measurements with many antenna positions automatically. The wooden box with transverse dimensions of 1.2 m by 1.2 m has been assembled with absorber material and is filled with 0.4 m of homogeneous sandy soil. In order to perform stepped frequency GPR measurements a vector network analyzer (VNA) has been mounted on top of an automatic positioning system (APS) which has been constructed in such a way that the utilized antenna can reach every point above the surface.

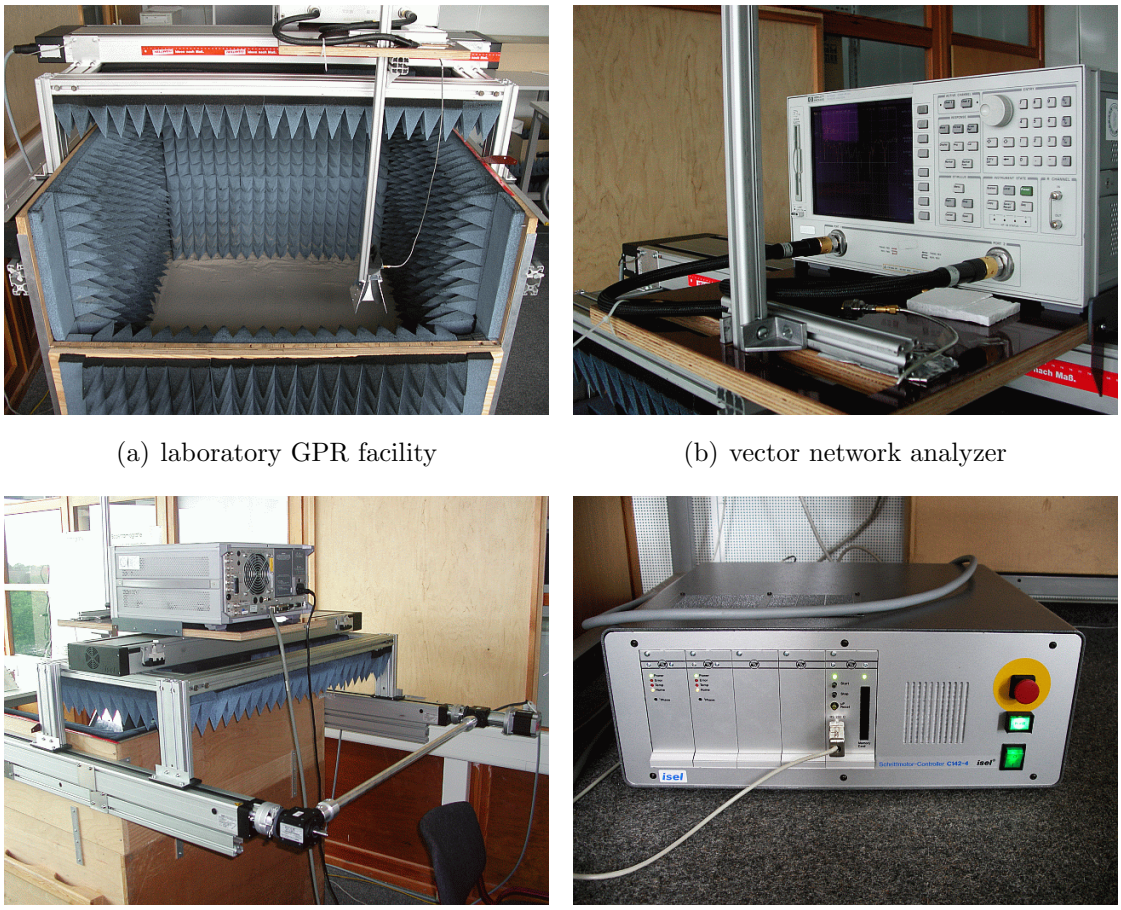

(a) laboratory GPR facility

(b) vector network analyzer

(c) linear stepper motors

(d) stepper motor controller

Figure 7.2: Assembly of the fully automated laboratory GPR system.

All antennas which have been investigated in 4 can be used together with the proposed system. Mechanical manipulations of the feeding cable which can influence the results of the measurements at higher frequencies can be avoided completely because the VNA is moved together with the antenna system. The APS consists of two linear stepper motors which are connected to a controller. Thus, it is possible to move the VNA platform along the x-axis and the y-axis, respectively.
The complete GPR scan procedure which can consist of many individual A-scan measurements at different antenna positions is controlled by a central program which has been realized using Visual Basic (VB). The program is based on a state machine that simultaneously controls all external devices. It allows to take the unpredictable time behavior of APS and VNA into account without losing any information. After the dimensions of the C-scan along both axis have been defined the system starts to move the antenna to the first considered position. The VNA measurement is performed and the results of the measurement are stored on the control PC under a predefined name while the antenna is already moved to the next position. Fig. 7.3 illustrates the utilized user interface. Herein, the green and red bars on the left upper corner are indicating the current state of all connected subsystems.

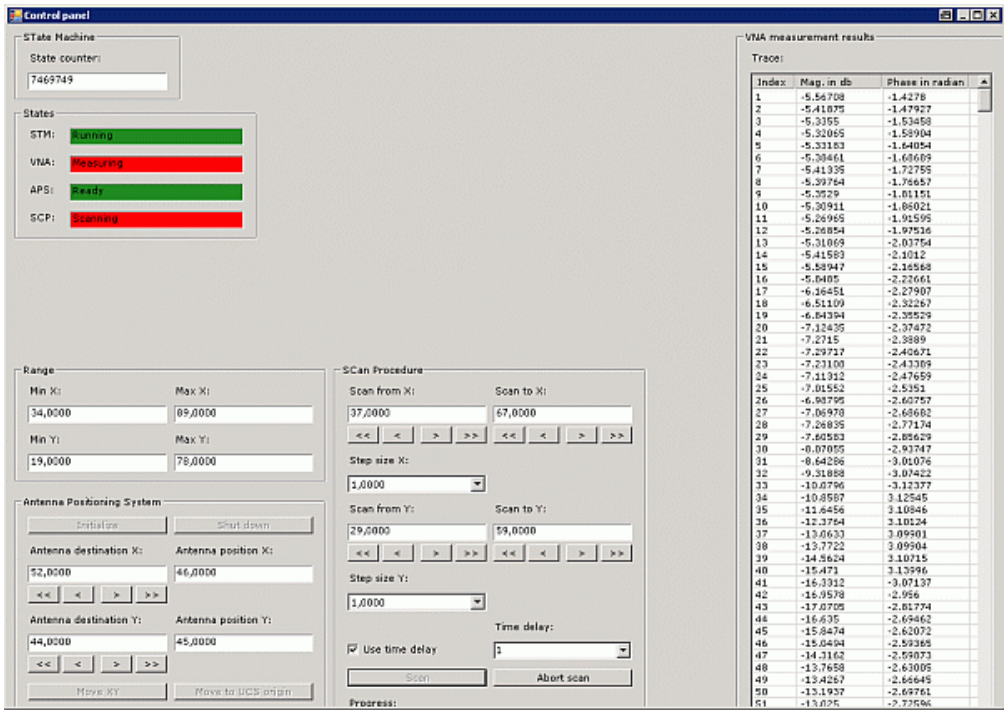

Figure 7.3: Control panel of the infinite state machine.

7.2.2 Influence of the Antenna Height

The height of the transmitting antenna above the surface of the soil is often defined without any further explanation. Therefore, the laboratory GPR test facility has been utilized for a systematic investigation of the relation between the height of the antenna and the imaging resolution of the corresponding SAR focused GPR. A double-ridged TEM horn antenna, see 4.5, has been placed in a distance of 15 cm, 30 cm, 45 cm and 60 cm above the surface of the soil, see Fig. 7.4(a). The H-shaped foam object which is illustrated in Fig. 7.4(b) has been placed in a depth of 7 cm below the surface. In 5.5 it has already been verified, that the proposed focusing techniques can improve the resolution of the resulting image significantly.
For every height a C-scan measurement with 41 by 41 antenna positions and an axial distance of 1 cm has been done. The frequency range has been chosen from 2 GHz to 10 GHz. Fig. 7.5 illustrates the corresponding B-scan results across the center of the buried H-object. Without any focusing the spreading of the objects reflection signature increases if the height of the antenna increases, exactly as it has been predicted theoretically. However, it has been found that the application of the SAR focusing yields more or less identical results which have been illustrated in Fig. 7.6. It should be noted, that all images have been normalized using an identical reference value. Thus, it is possible to compare the results of the C-scans. It shows, that the amplitude of the reflected energy increases if the height of the antenna increases because more antennas are contributing to the SAR focusing.

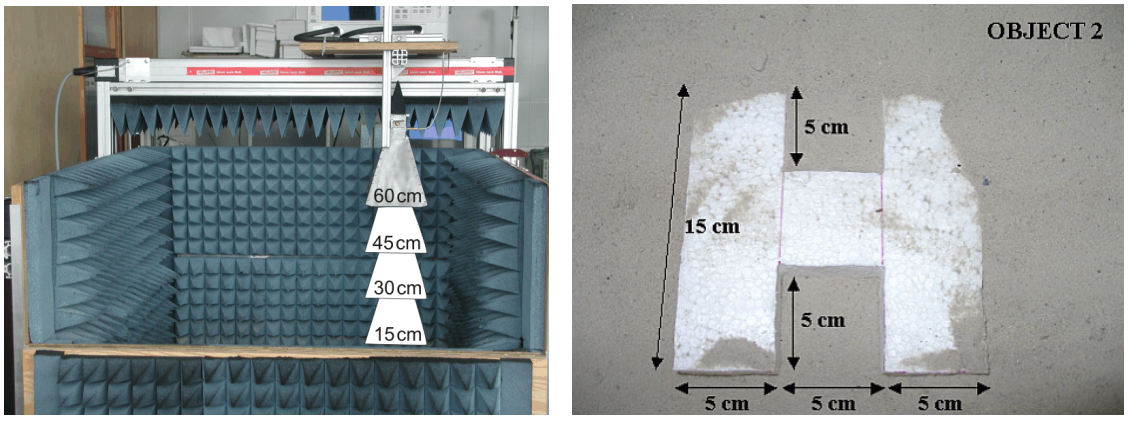

(a) height of the TEM horn antenna

(b) buried foam object ($\epsilon_r = 1.0$)

Figure 7.4: Configuration of the experimental GPR measurement.

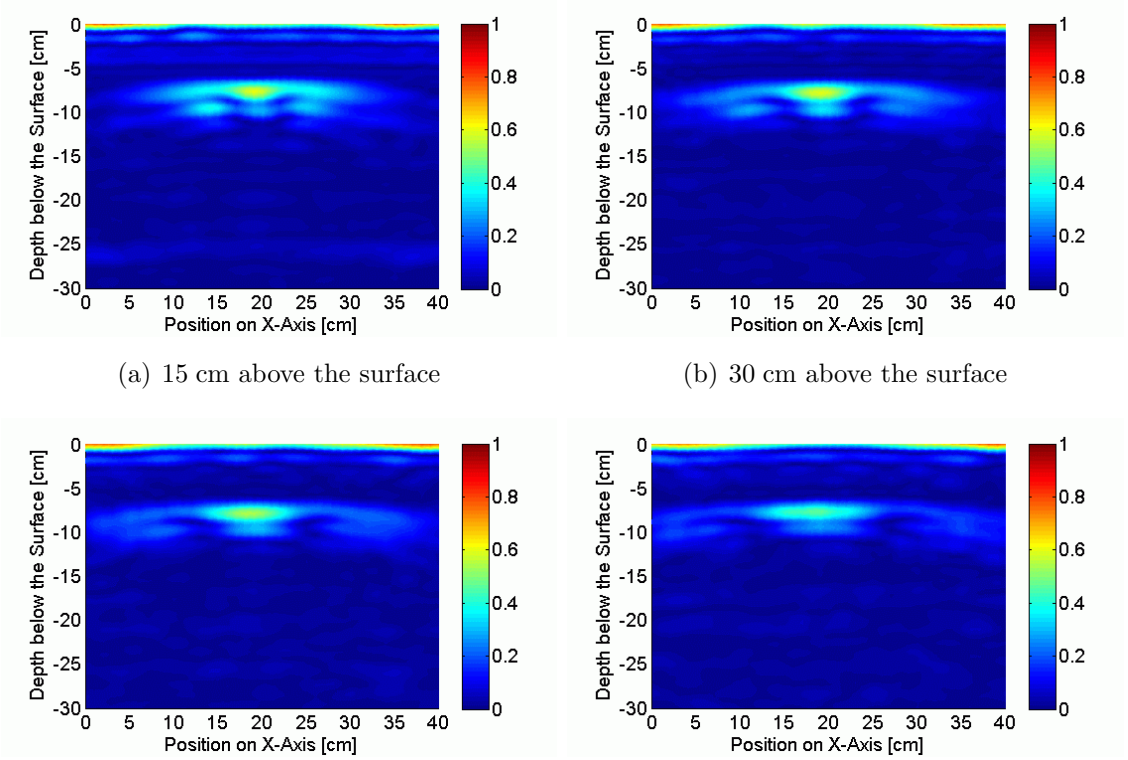

(a) 15 cm above the surface

(b) 30 cm above the surface

(c) 45 cm above the surface

(d) 60 cm above the surface

Figure 7.5: B-scan results without any additional processing.

As long as the SAR focusing is applied for the complete array the H-shape of the buried target object can be identified for every antenna height. Significant differences, however, can be obtained if the SAR focusing is only applied for a subarray, e.g. the central part of the C-scan with 21 by 21 antenna positions. Fig. 7.7 illustrates, that the H-shape of the target object can clearly be identified if the antenna is placed 15 cm above the surface of the soil, whereas it is lost completely for an antenna height of 60 cm which indicates, that the subarray with 21 by 21 contributing antennas is too small for a complete compensation of the energy spreading.
In order to verify the obtained results the same experiment has been conducted for the small version of the double-ridged TEM horn antenna, see 4.6. Fig. 7.8 illustrates the results of the SAR focusing. In comparison to the case with the standard-sized TEM horn antenna the small version of this antenna yields slightly better results, which can be explained by a smaller footprint of this antenna. Nonetheless, the results of the subarray focusing in Fig. 7.9 clearly verify the previous ones.

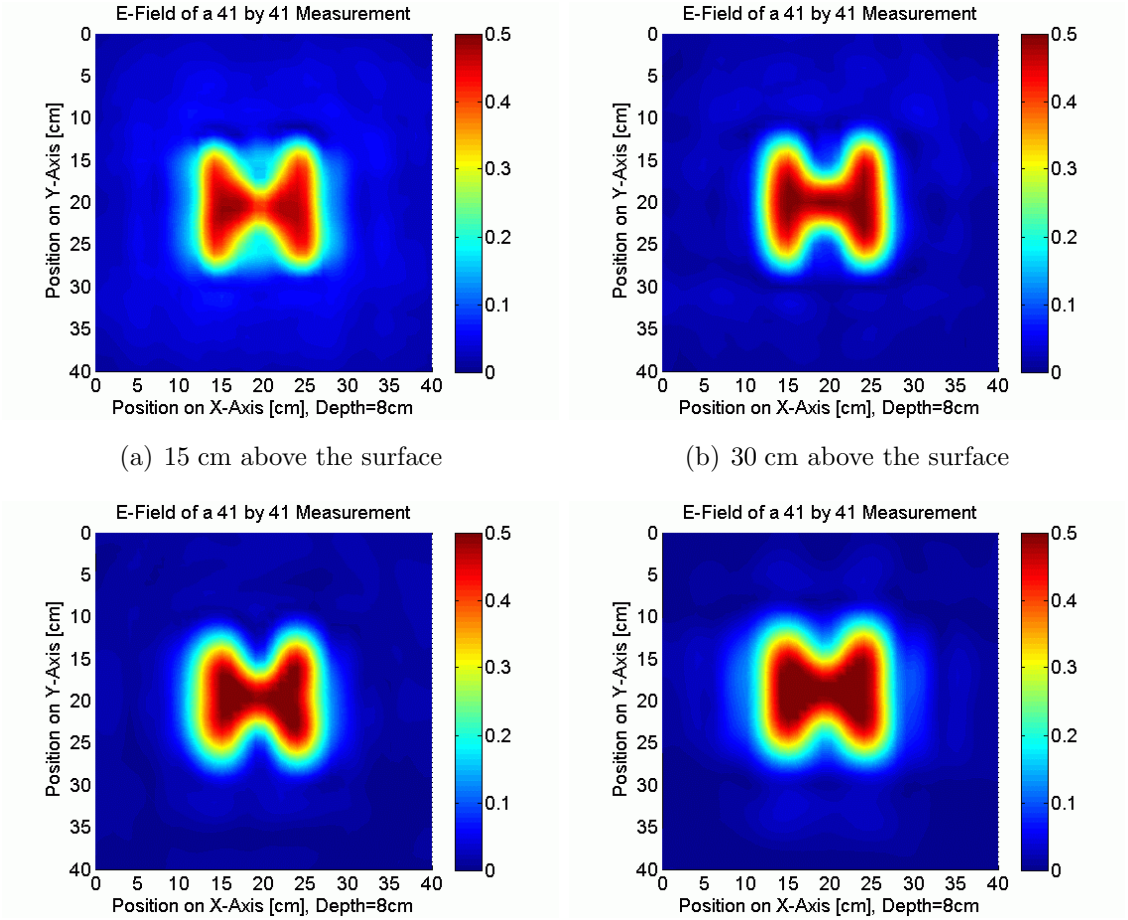

(a) 15 cm above the surface

(b) 30 cm above the surface

(c) 45 cm above the surface

(d) 60 cm above the surface

Figure 7.6: SAR focusing results for the double-ridged TEM horn antenna.

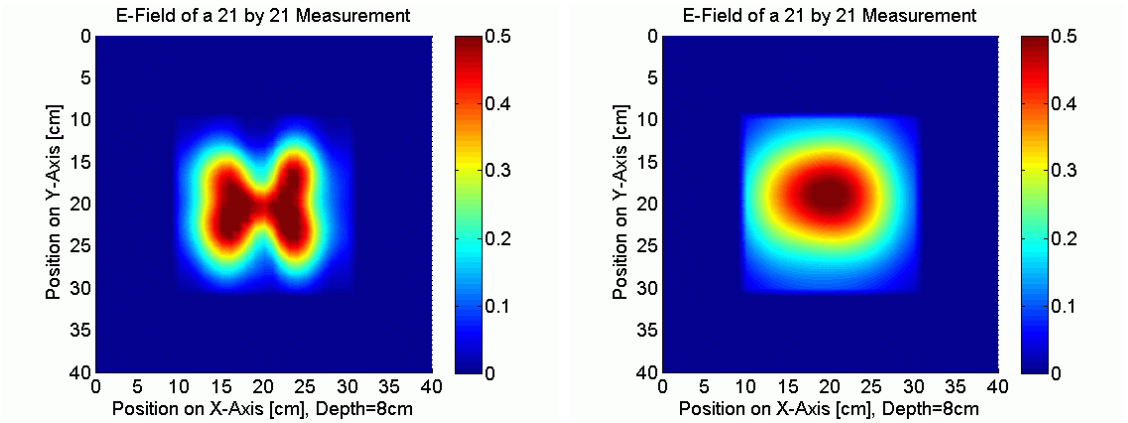

(a) 15 cm above the surface

(b) 60 cm above the surface

Figure 7.7: SAR focusing results for the double-ridged TEM horn antenna.

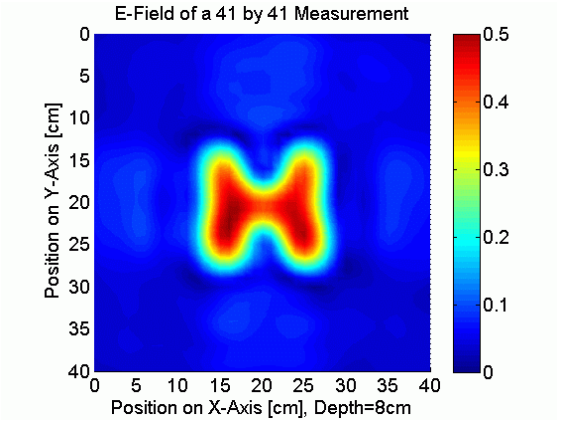

(a) 15 cm above the surface

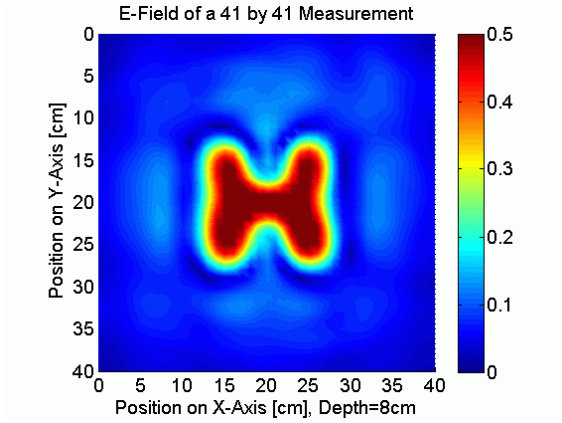

(b) 30 cm above the surface

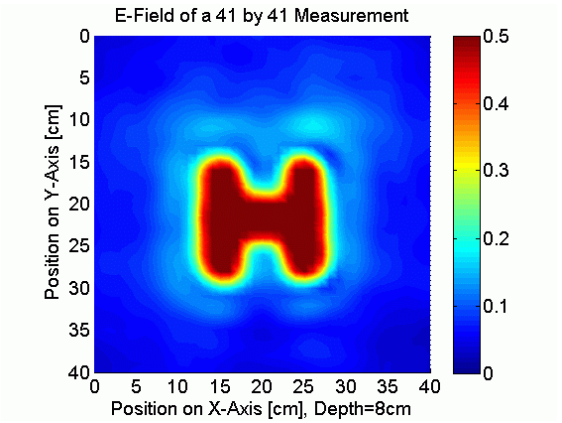

(c) 45 cm above the surface

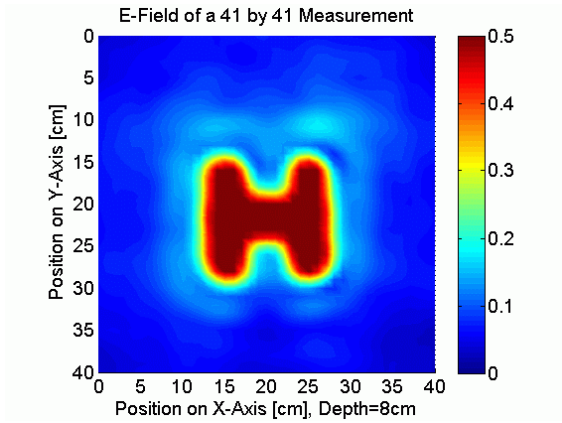

(d) 60 cm above the surface

Figure 7.8: SAR focusing results for the small double-ridged TEM horn.

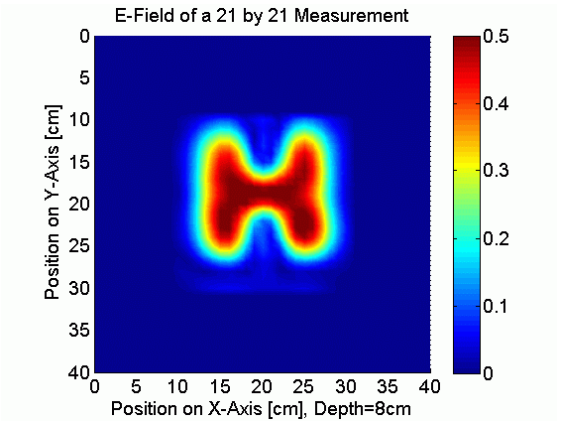

(a) 15 cm above the surface

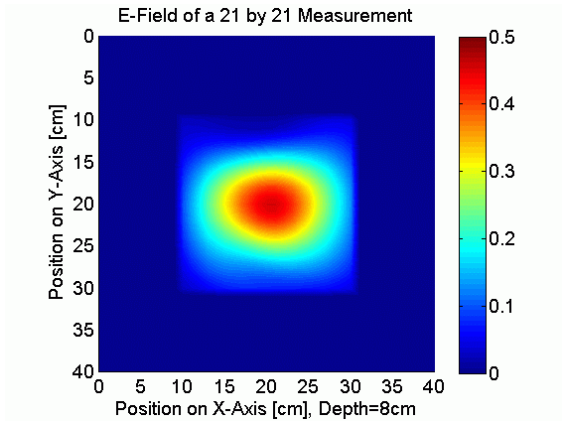

(b) 60 cm above the surface

Figure 7.9: SAR focusing results for the small double-ridged TEM horn.

7.2.3 Comparison of Different Antennas

For a setup with multiple target objects, see Fig. 7.10(a), which are buried in a depth of 7 cm the Orion-type IRA (Fig. 7.10(b)), the double-ridged TEM horn antenna (Fig. 7.10(c)) and the modified Bujanov antenna (Fig. 7.10(d)) are utilized in the same frequency range from 1 GHz to 10 GHz in order to compare the results. A SAR focusing has been applied for the double-ridged TEM horn and the Bujanov antenna, whereas for the case of the Orion-type IRA only a simple background subtraction is utilized. The results of two B-scan measurements which are indicated by dotted lines in Fig. 7.10(a) are illustrated in Figs. 7.11-7.13. B-scan 1 represents a measurement across the metal cylinder and the PPM mine, whereas B-scan 2 illustrates the measurement parallel to B-scan 1 across a second PPM mine.

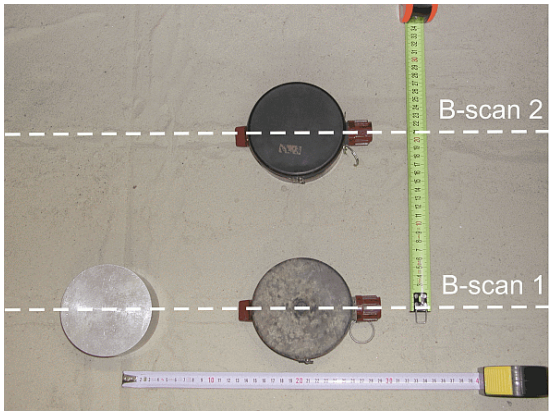

(a) positioning of the targets

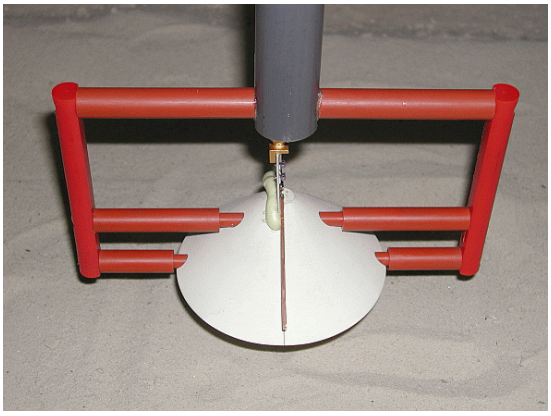

(b) mounted Orion-type IRA

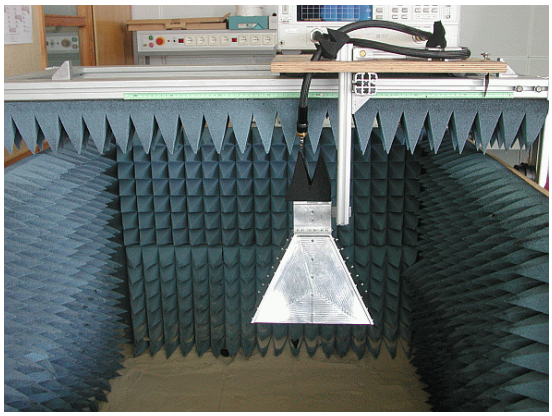

(c) mounted TEM horn antenna

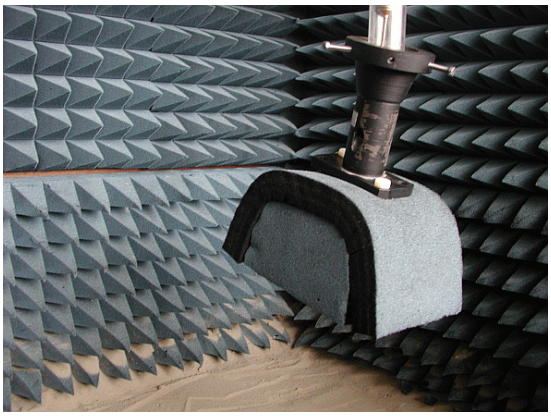

(d) mounted Bujanov antenna

Figure 7.10: Configuration of the experimental GPR measurement.

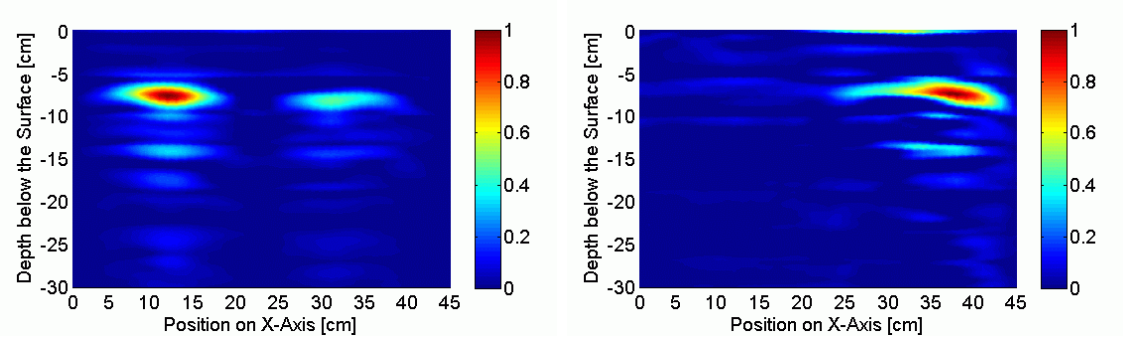

(a) Orion-type IRA, B-scan 1

(b) Orion-type IRA, B-scan 2

Figure 7.11: Experimental B-scan results for the Orion-type IRA.

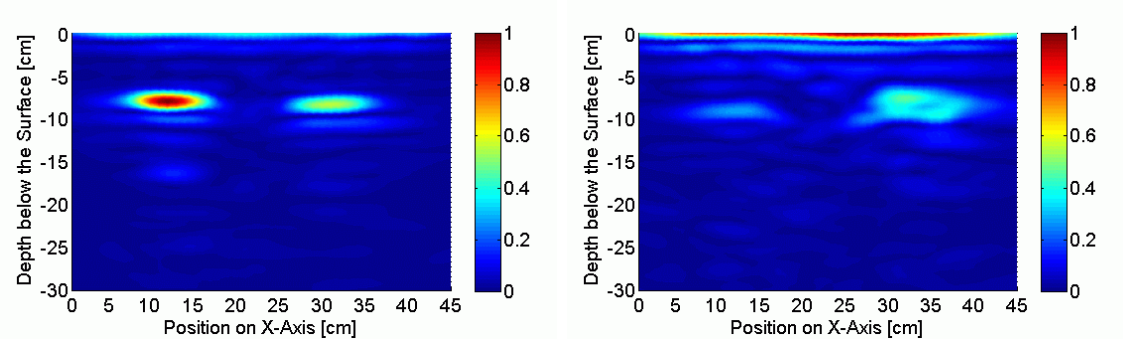

(a) TEM horn antenna, B-scan 1

(b) TEM horn antenna, B-scan 2

Figure 7.12: Experimental B-scan results for the TEM horn antenna.

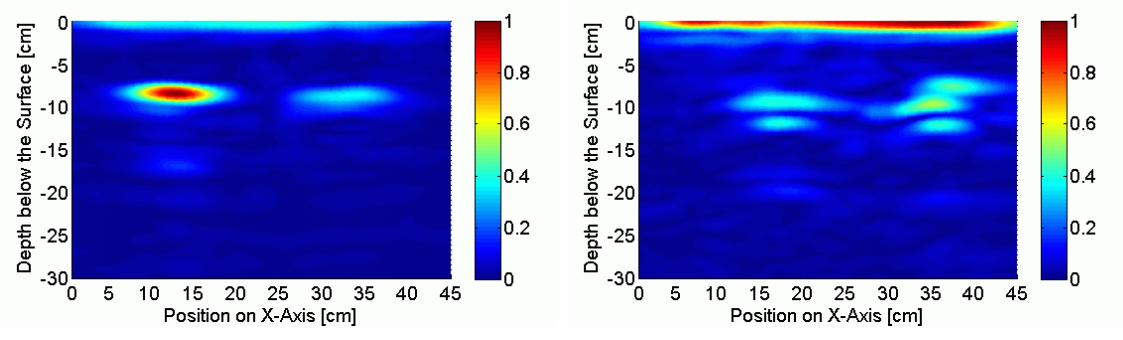

(a) Bujanov antenna, B-scan 1

(b) Bujanov antenna, B-scan 2

Figure 7.13: Experimental B-scan results for the Bujanov antenna.

It shows that the different antennas yield almost similar results and that the reflection of the metal cylinder in B-scan 1 is much stronger than that of the PPM mine which can be explained by different electromagnetic properties of metal and PVC. The reflection on the left-hand side of B-scan 2 also indicates the strong presence of the metal cylinder. Moreover, it shows that the PPM mines are not completely identical, which could also be related to the presence of the metal cylinder.
For a second experiment two completely different antennas have been placed with their phase center about 50 cm above the surface, see Fig. 7.14. One antenna is the double-ridged TEM horn which utilizes a frequency range from 1.5 GHz to 18 GHz, whereas the second one, a standard gain Ka-band antenna [Var05d], can be utilized in the frequency range from 26.5 GHz to 40 GHz. Figs. 7.15(a) and 7.15(c) illustrate the results of a B-scan across the center of a M14 mine which has been buried in a depth of 18 cm. Two typical reflections, namely, at the top and the bottom of the of the M14 mine can be obtained. The results of a similar B-scan across the center of a metal cylinder with a diameter of 5 cm which has been buried in a depth of 16 cm are illustrated in Figs. 7.15(b) and 7.15(d). Herein, a much stronger single response represents the total reflection at the surface of the object. Both antennas allow to detect the buried target objects. Therefore, it can be concluded that the depth of penetration is sufficient even for frequencies higher than 25 GHz.
In addition to the previous experiments a text has been written on the surface of the soil, see Fig. 7.16(a). The resulting C-scan of this structure which is illustrated in Fig. 7.16(b) demonstrates the high resolution of the Ka-band setup.

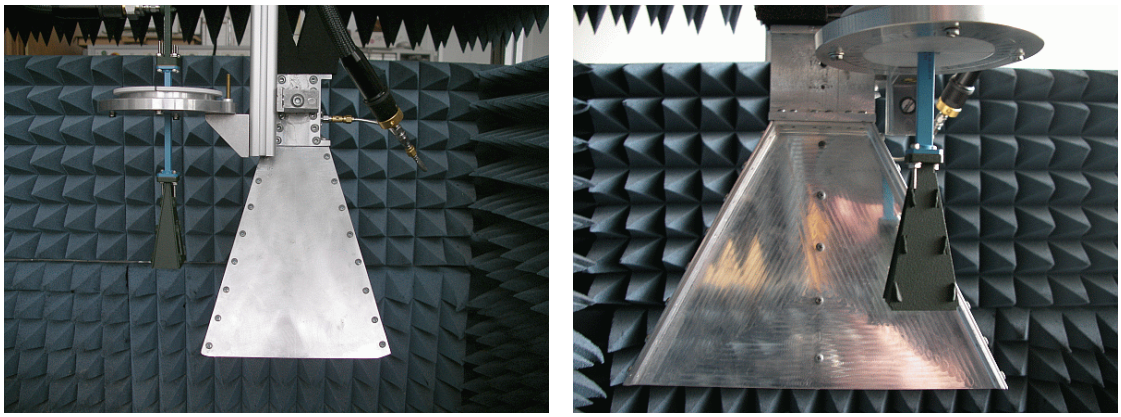

(a) front view (b) side view

Figure 7.14: Comparison of Ka-band horn and double-ridged TEM horn.

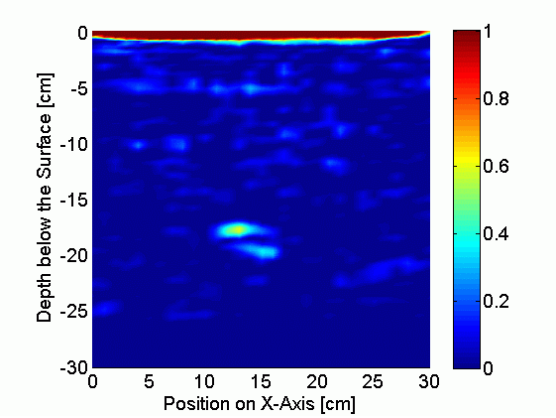

(a) M14 mine with TEM horn antenna

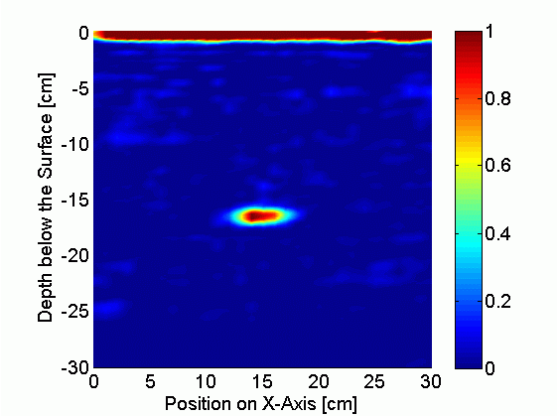

(b) cylinder with TEM horn antenna

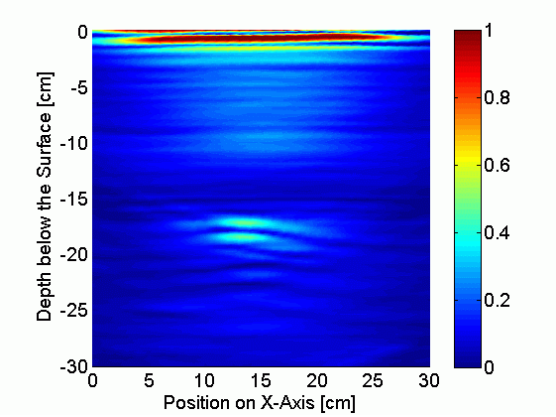

(c) M14 mine with Ka-band antenna

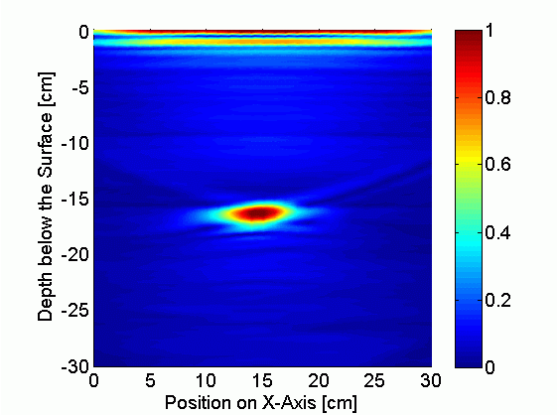

(d) cylinder with Ka-band antenna

Figure 7.15: B-scan results for the TEM horn antenna and the Ka-band antenna.

(a) text on the surface

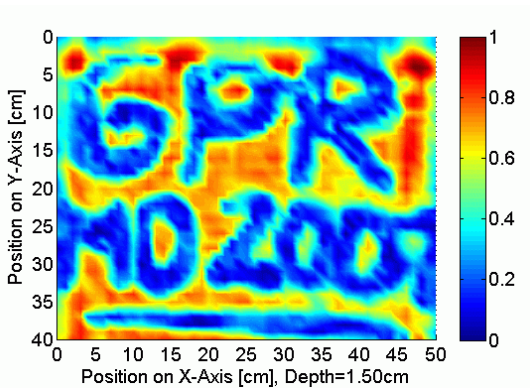

(b) resulting GPR image

Figure 7.16: Imaging a text structure on the surface of the soil.

7.2.4 Influence of Surface Roughness

In order to investigate the influence of periodic surface structures which have been discussed in 3.3.3 a double-ridged TEM horn antenna has been placed in a distance of 45 cm above the surface and the operating frequency range has been chosen from 2 GHz to 10 GHz. A PPM-2 AP mine has been placed in a depth of 10 cm and three different surface scenarios, namely, a flat surface, small waves with λ=3 cm (Fig. 7.17) and large waves with λ=6 cm (Fig. 7.18) have been investigated. The B-scan and C-scan results in Fig. 7.19 clearly indicate, that the reflection signature of the buried object is only affected for the case of very large surface waves.

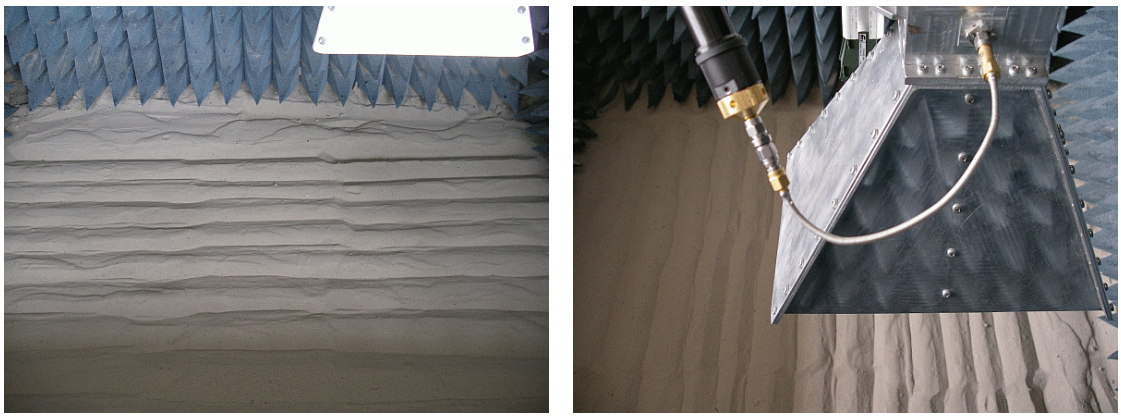

(a) small waves, front view (b) small waves, side view

Figure 7.17: Experimental GPR setup with small periodic surface waves.

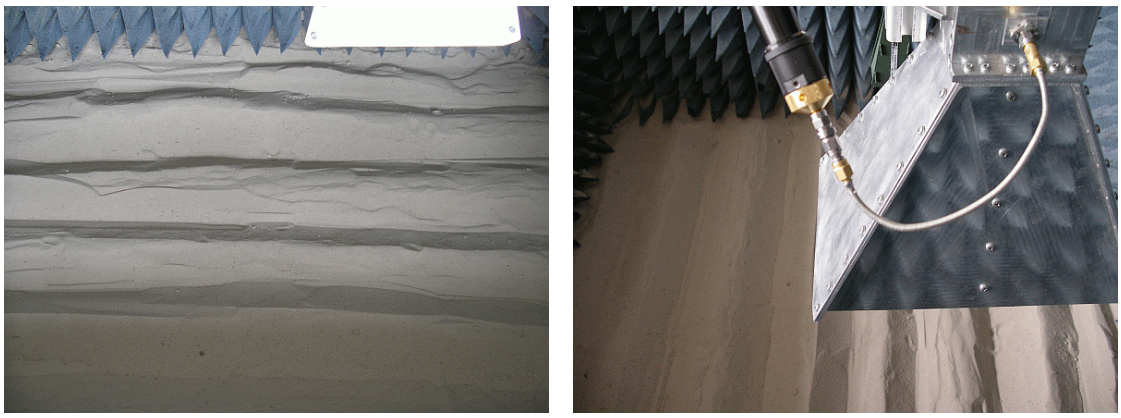

(a) large waves, front view (b) large waves, side view

Figure 7.18: Experimental GPR setup with large periodic surface waves.

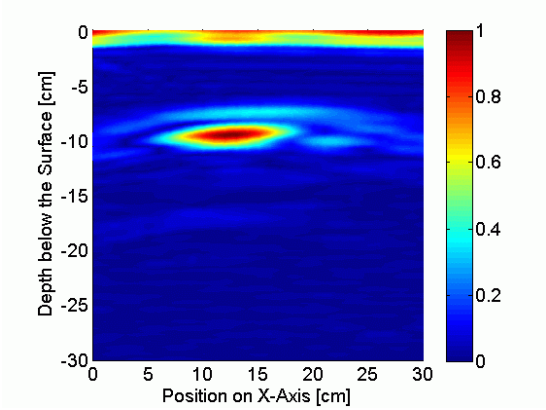

(a) flat surface (B-scan)

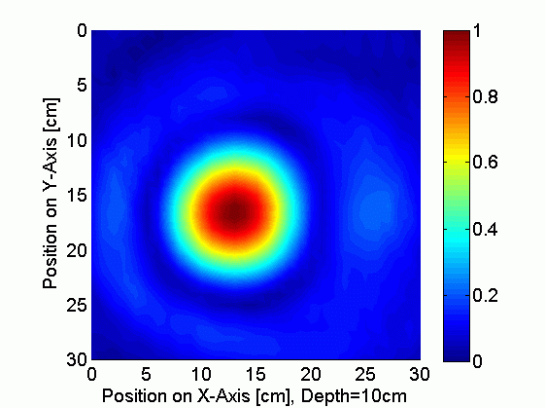

(b) flat surface (C-scan)

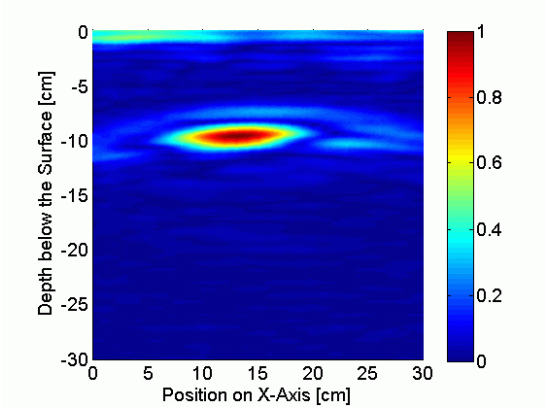

(c) small surface waves (B-scan)

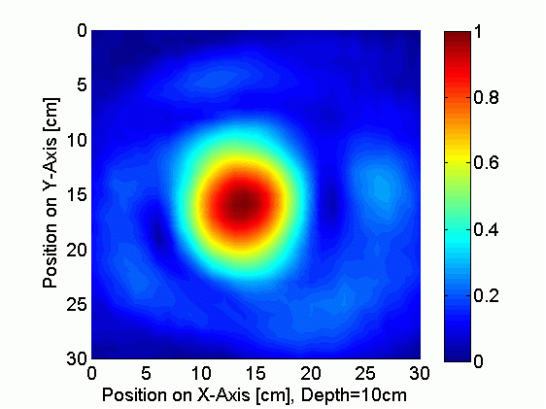

(d) small surface waves (C-scan)

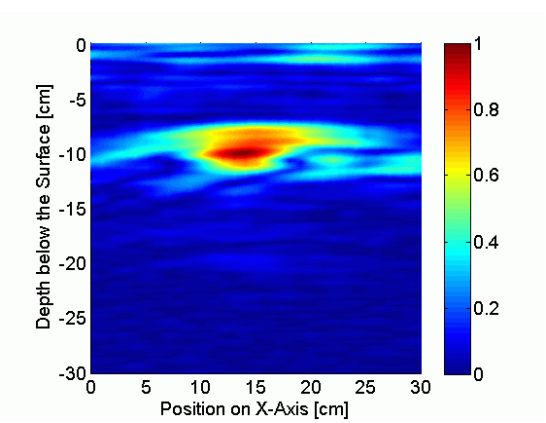

(e) large surface waves (B-scan)

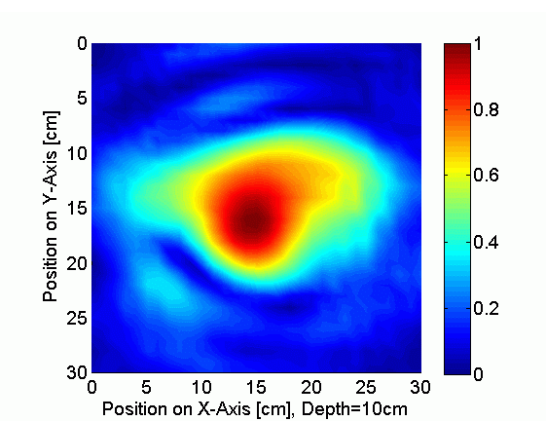

(f) large surface waves (C-scan)

Figure 7.19: GPR results for three different surface roughness scenarios.

For a second experiment the double-ridged TEM horn antenna has been placed again in a distance of 45 cm above the surface and the operating frequency range has been chosen from 2 GHz to 10 GHz. For this experiment the well-known H-object with a permittivity of $\epsilon_r = 1.0$ has been placed in a depth of 7 cm below the surface which is covered with large natural stones, see Fig. 7.20. The C-scan results with 41 by 41 measurement positions in Fig. 7.21 reveal, that the H-shape of the buried target object can no longer be reconstructed correctly, because the stones cover almost the complete buried target object and, thus, prevent a proper focusing of the subsurface region. Nonetheless, the presence of a buried object still can be recognized.

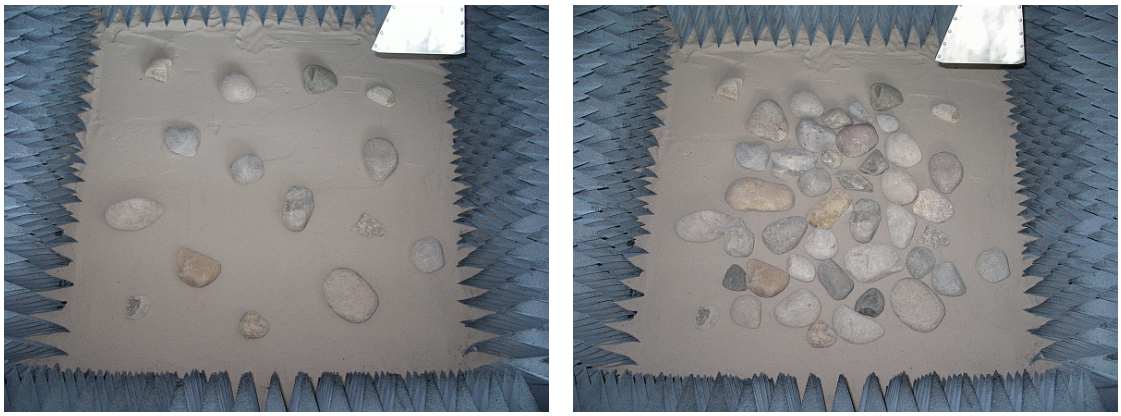

(a) stone configuration 1 (b) stone configuration 2

Figure 7.20: Two experimental GPR scenarios with stones on the surface.

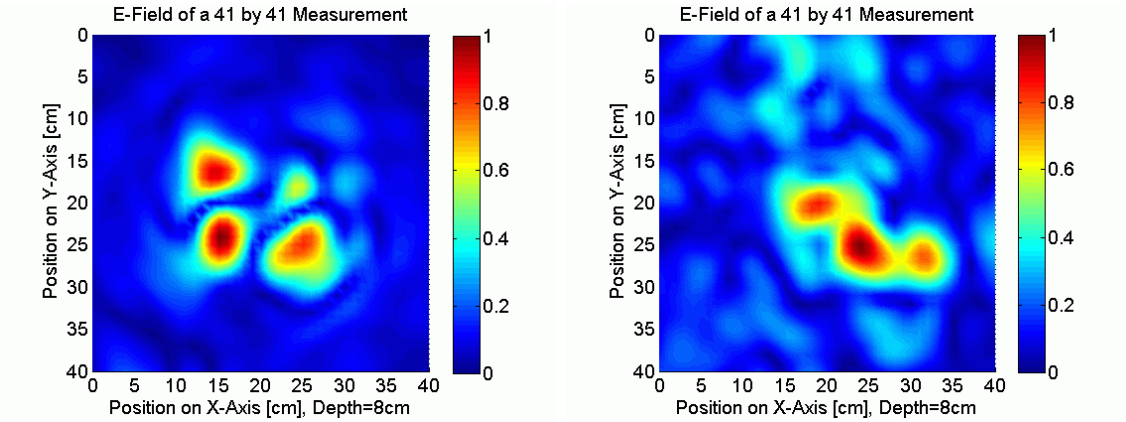

(a) stone configuration 1 (b) stone configuration 2

Figure 7.21: B-scan results for the setup with stones on the surface.

7.3 Development of a Mobile GPR

7.3.1 Portable Vector Network Analyzer

The R&S FSH series which is illustrated in Fig. 7.22(a) has been introduced as a portable and low-cost mobile spectrum analyzer and utilizes the frequency range from 10 MHz up to 3 GHz for the case of the R&S FSH3, respectively, 6 GHz for the R&S FSH6 [Var05c]. In combination with an internal tracking generator and an optional VSWR bridge, see Fig. 7.22(b), the R&S FSH series can be used e.g. for distance-to-fault or cable loss measurements. More important for GPR applications is, however, its capability to be used as a one-port vector network analyzer.
Thus, the R&S FSH3 allows to perform mobile stepped-frequency GPR measurements. As a first step the accuracy of the vector network analysis should be verified using a precise laboratory Anritsu VNA as a reference. Therefore, a double-ridged TEM horn antenna, see 4.5, has been placed in a height of 50 cm above a layer of absorbing material, respectively a metal plate and the corresponding complex return loss has been measured using both, the R&S FSH3 and the Anritsu VNA. A very good agreement between the results of the amplitude of S_{11} can be found from Figs. 7.23(a) and 7.23(b) whereas Figs. 7.24(a) and 7.24(b) indicate differences of the phase. Nonetheless, the obtained results indicate a good agreement, because the nearly linear slope of the phase differences in Figs. 7.24(c) and 7.24(d) can be explained by the length difference of the utilized VNA connector cables.

(a) mobile VNA - R&S FSH3 (b) VSWR Bridge - R&S FSH-Z2

Figure 7.22: Mobile VNA R&S FSH3 and VSWR Bridge R&S FSH-Z2.

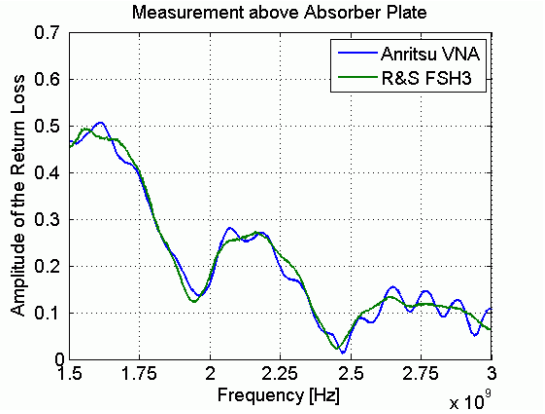

(a) Measurement above Absorber

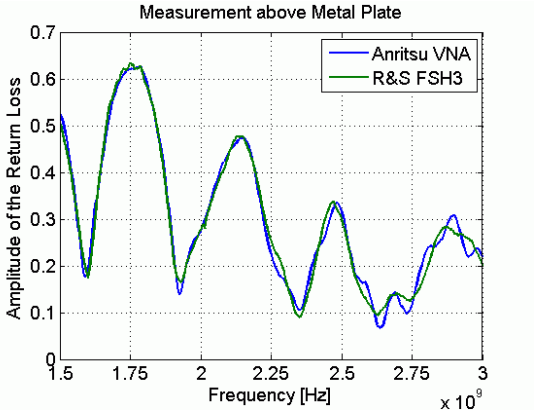

(b) Measurement above Metal Plate

Figure 7.23: Amplitude measurement with R&S FSH3 and Anritsu VNA.

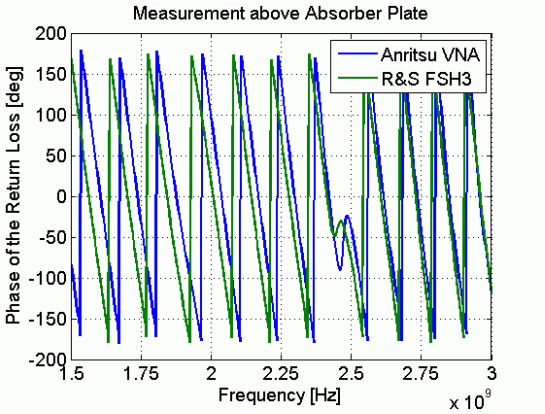

(a) Measurement above Absorber

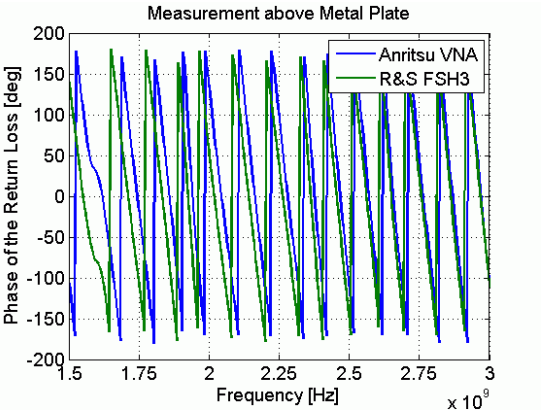

(b) Measurement above Metal Plate

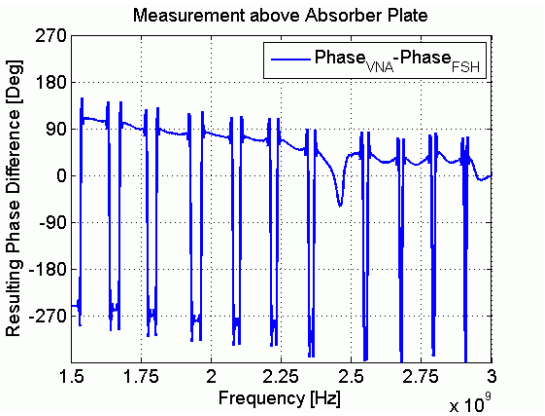

(c) Measurement above Absorber

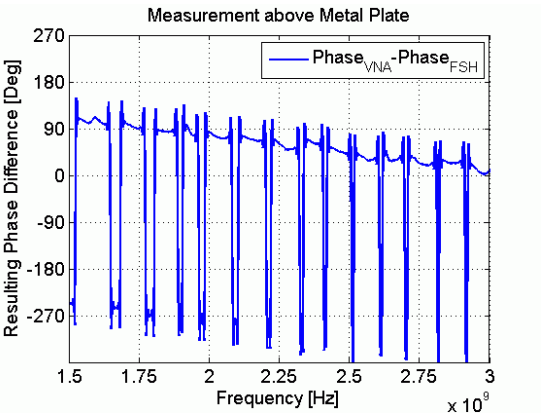

(d) Measurement above Metal Plate

Figure 7.24: Phase measurement with R&S FSH3 and Anritsu VNA.

7.3.2 Preliminary System with R&S FSH3

After the accuracy of the portable vector network analyzer has been verified a preliminary prototype of a mobile GPR system has been constructed. The resulting system which is illustrated in Fig. 7.25 allows to place the R&S FSH3 on top of a frame structure which also holds the GPR antenna, namely, the modified double-ridged TEM horn, see 4. The metal parts of the structure have been shielded with absorbing material in order to avoid interactions with the transmitted signal.
The ability of the preliminary setup to detect AP landmines in a realistic environment has been investigated by an outdoor B-scan measurement for which a PPM-2 AP mine has been placed in a depth of 5 cm below the surface, see Fig. 7.26.

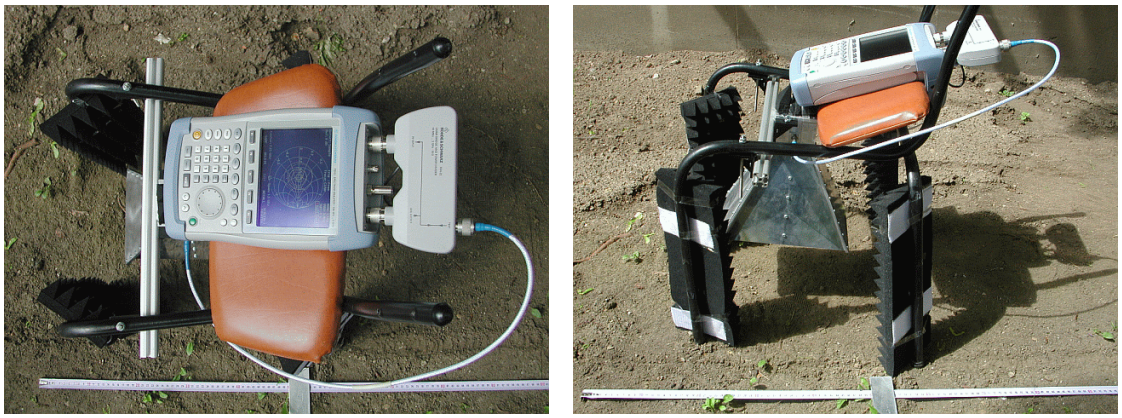

(a) mobile R&S FSH3 system (b) mounted TEM horn antenna

Figure 7.25: Assembly of the preliminary mobile GPR with R&S FSH3.

(a) manual movement of the setup (b) placement of the PPM-2 mine

Figure 7.26: Experimental outdoor measurement with R&S FSH3 setup.

In order to perform a B-scan measurement the preliminary GPR setup has to be moved by hand from one position to the next one. The positioning itself is controlled by a measuring tape before the corresponding A-scan measurement is started.
Fig. 7.27(a) illustrates the results of a B-scan measurement above unmodified soil whereas the B-scan results shown in Fig. 7.27(b) have been obtained after the mine has been placed. For both measurements 46 positions in a stepwidth of 1 cm are taken into account. The mine signature is masked almost completely by strong surface reflections. Nonetheless, it can be identified if a background subtraction is utilized. The subtraction of the mean value of Fig. 7.27(b) yields Fig. 7.27(c) whereas the real subtraction of the B-scans with and without object yields Fig. 7.27(d). In conclusion, however, it has been found that the frequency range from 1.5 GHz to 3 GHz yields a poor depth resolution and is insufficient for GPR applications.

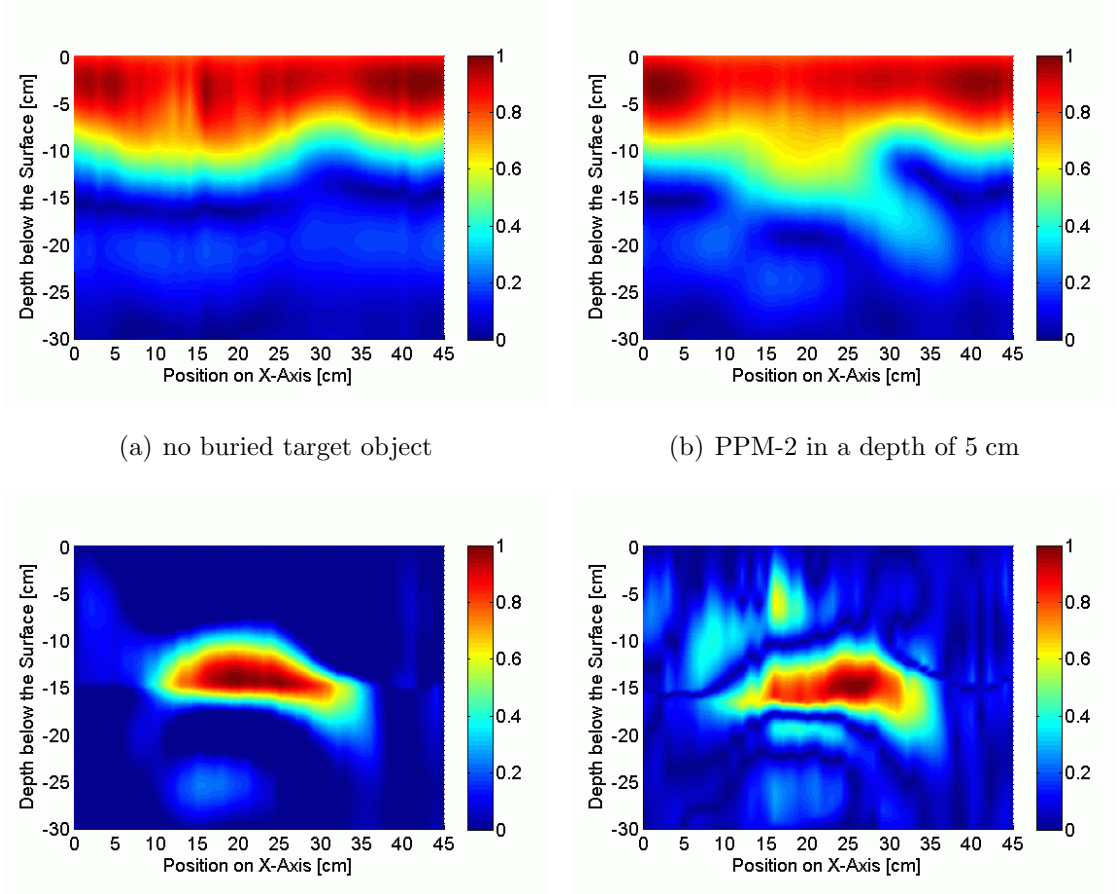

(a) no buried target object

(b) PPM-2 in a depth of 5 cm

(c) mean background subtraction

(d) real background subtraction

Figure 7.27: Results of a GPR measurement with the mobile FSH3 setup.

7.3.3 Advanced System with R&S FSH6

The R&S FSH6 model of the FSH series is the extended version of the R&S FSH3 and supports frequencies from 10 MHz up to 6 GHz. As soon as the corresponding VSWR Bridge R&S FSH-Z3 was available the applicability of the new device for GPR applications could be investigated. At first two measurements have been performed using the laboratory GPR facility in combination with the portable VNA in order to determine the influence of an increased frequency range, see Fig. 7.28.
As it is illustrated in Fig. 7.29 two different target objects, namely, a PPM-2 AP mine and a cylindrical metal object with a diameter of 10 cm and a height of 3 cm have been placed in a depth of 4 cm below the surface of the dry sandy soil.

(a) R&S FSH6 with VSWR Bridge (b) shielded Bujanov antenna

Figure 7.28: Configuration of the laboratory GPR measurement setup.

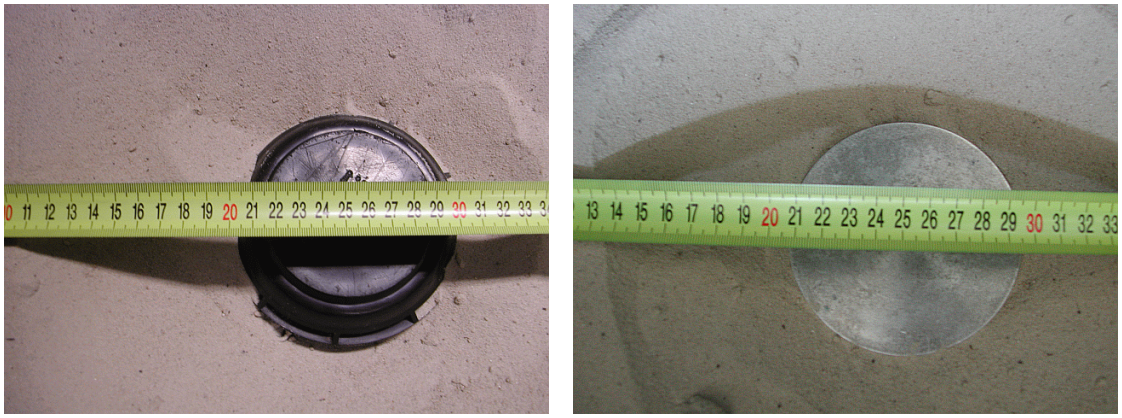

(a) PPM-2 AP mine, depth 4 cm (b) metal cylinder, depth 4 cm

Figure 7.29: Placement of the target objects in a depth of 4 cm.

The corresponding B-scan measurements along the center of the buried objects take 51 positions with a stepwidth of 1 cm into account. The frequency range has been chosen from 1.5 GHz to 3 GHz (R&S FSH3 case), respectively, from 1.5 GHz to 6 GHz (R&S FSH6 case). The results shown in Fig. 7.30 clearly indicate, that the larger frequency range of the R&S FSH6 increases the depth resolution significantly in comparison to the R&S FSH3, exactly as it has been predicted, see 2.2.6. Consequently, the R&S FSH6 has been employed for the development of an advanced mobile GPR system which utilizes an automation for the movement of the antenna along one axis. The system consists of the VNA itself, a standard notebook, a laser distance meter and a double-ridged TEM horn antenna that is connected to a linear stepper motor, see Fig. 7.31. It is mounted on top of a four-wheel trolley which has been modified in order to carry the linear stepper motor on its front side.

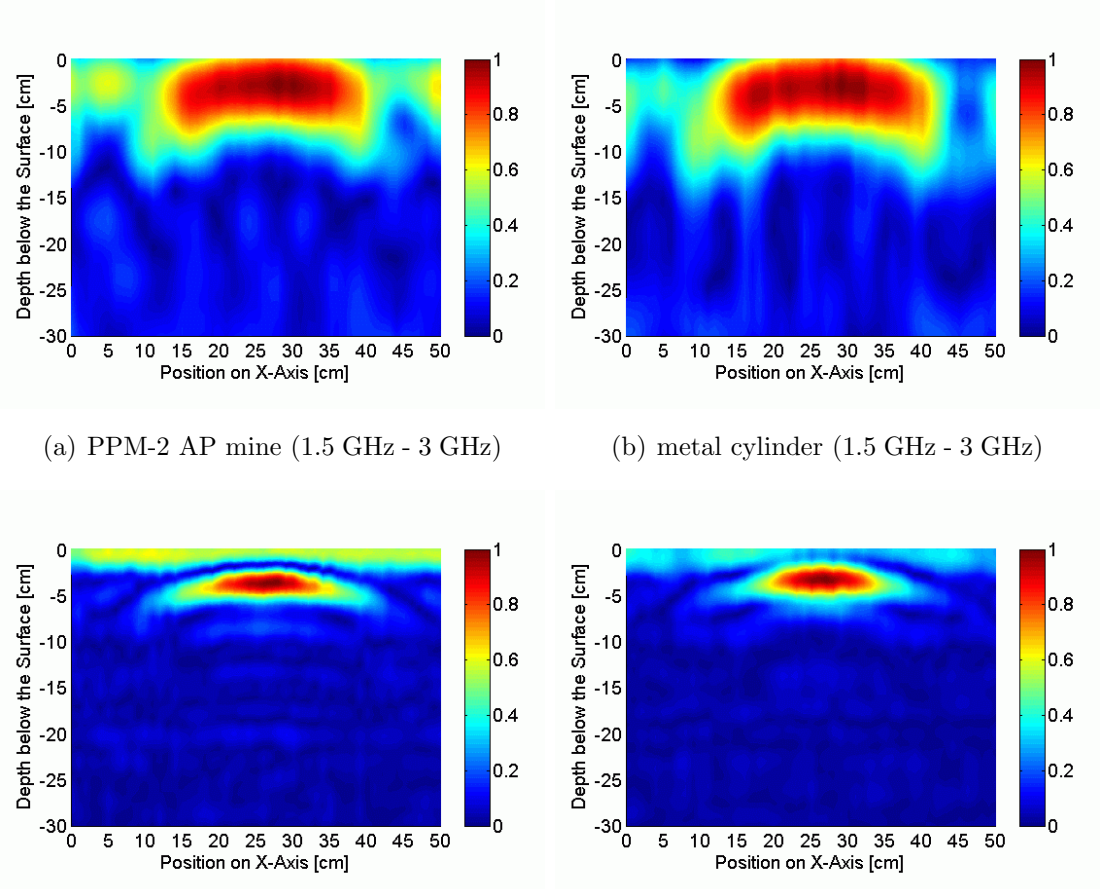

(a) PPM-2 AP mine (1.5 GHz - 3 GHz)

(b) metal cylinder (1.5 GHz - 3 GHz)

(c) PPM-2 AP mine (1.5 GHz - 6 GHz)

(d) metal cylinder (1.5 GHz - 6 GHz)

Figure 7.30: Results of laboratory GPR measurement with R&S FSH6.

The automatic positioning system has been designed in such a way that the linear stepper motor carries both, the mounted transceiving antenna and the R&S FSH6. Thus, the bending of the connector cable which might influence the results of the measurements can be neglected completely. The antenna position on the x-axis is controlled by a precise linear stepper motor system. However, the trolley is moved manually in the normal direction. The corresponding distance is measured using a laser distance meter which allows to determine precisely the distance towards a reference plane (±0.1 mm). The laser guided positioning of the trolley, the movement of the linear stepper motor and the VNA remote access is controlled by a Visual Basic software that has been installed on a standard notebook. The software is basically the same as the one that is used for the laboratory GPR test facility.

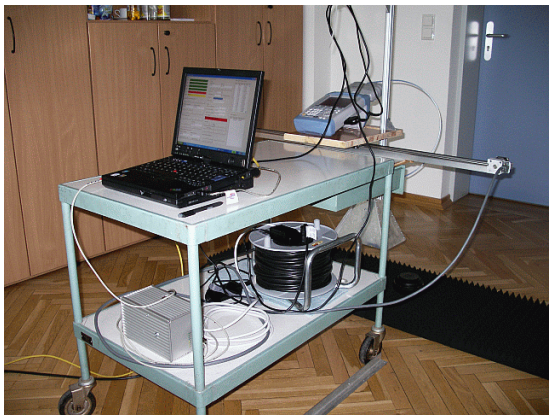

(a) mobile GPR with R&S FSH6

(b) mounted TEM horn antenna

(c) laser distance meter

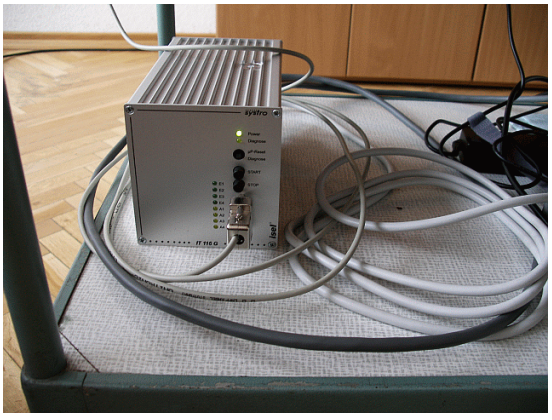

(d) stepper motor controller

Figure 7.31: Assembly of the preliminary mobile GPR with R&S FSH6.

7.3.4 Indoor Verification of the Setup

After the assembly of the advanced GPR system has been completed two experimental indoor setups have been investigated, see Fig. 7.32. For setup 1 a PPM-2 mine and a PMN mine have been placed in a distance of 30 cm whereas setup 2 consists of two cylindrical test objects which are made of PVC and metal. The relevant area on the floor has been covered with absorbing material in order to avoid unwanted reflections and the double-ridged TEM horn antenna has been mounted in a height of 18 cm above the absorber, respectively, 13 cm above the top of the objects.

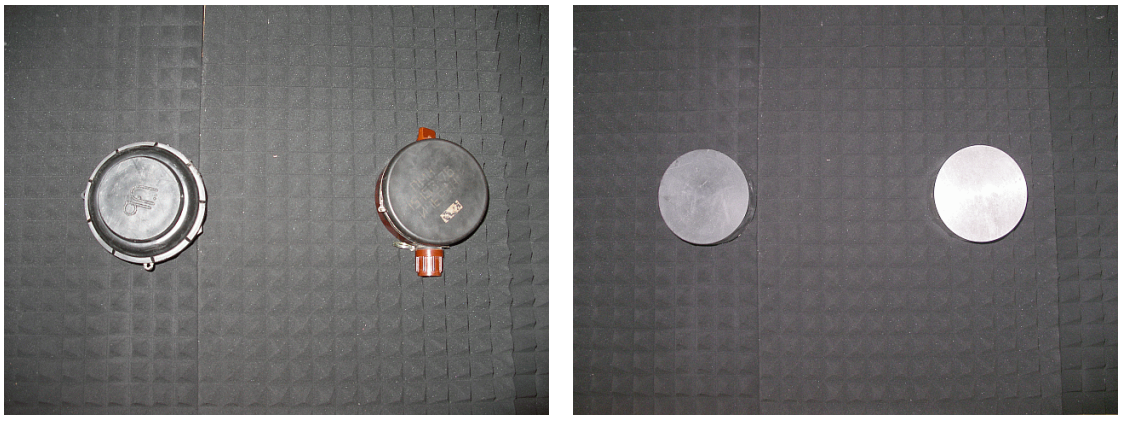

(a) setup 1: PPM-2 and PMN mine (b) setup 2: PVC and metal cylinder

Figure 7.32: Placement of the target objects at the absorber material.

For both GPR experiments 31 by 8 measurement positions with an axial stepwidth of 2 cm have been taken into account. The results of the complete C-scan are illustrated in Figs. 7.33(a) and 7.34(a) for the layer in a depth of 13 cm below the aperture of the antenna, whereas Figs. 7.33(b) and 7.34(b) illustrate the results of a B-scan directly above the center of the target objects. Dotted white lines indicate the utilized cutting planes. Moreover, it is important to note, that the depth in both B-scan images refers to the distance below the aperture of the antenna.
It shows that the target objects can be clearly identified and that the amplitude of the reflection in the B-scans immediately reveals their position in the subsurface. The reflection signatures of the AP mines in setup 1 are almost similar, whereas the signature of the metal cylinder is much stronger than that of the plastic one which can be explained by different electromagnetic properties of PVC and metal.

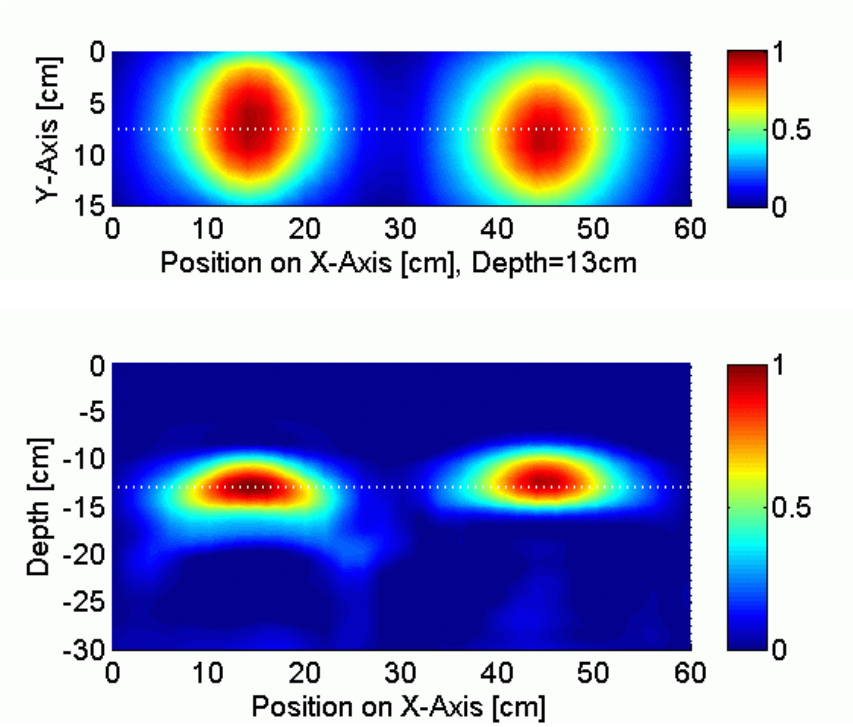

Figure 7.33: C-scan (top) and B-scan (bottom) results of setup 1.

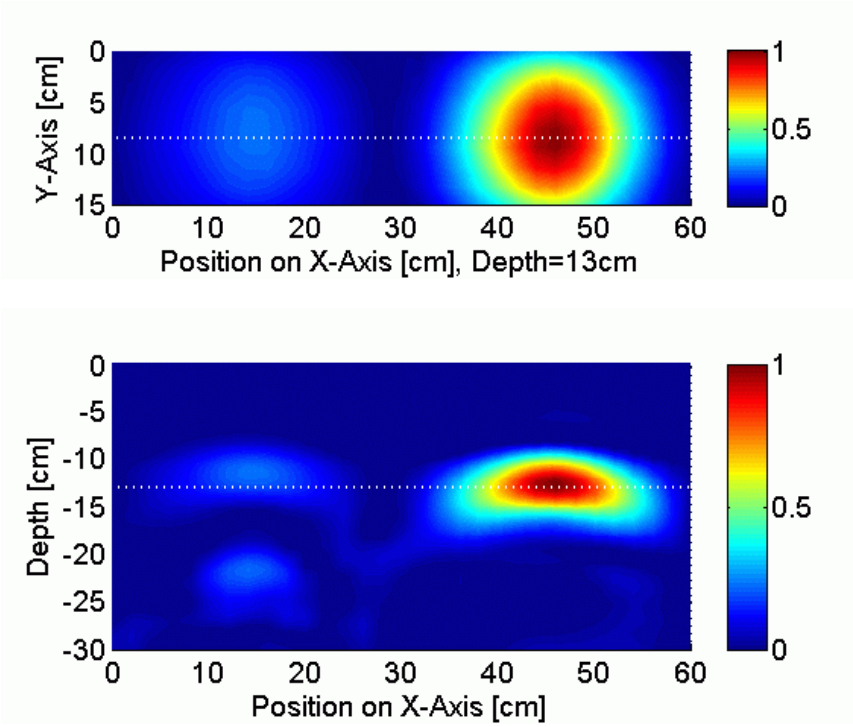

Figure 7.34: C-scan (top) and B-scan (bottom) results of setup 2.

7.3.5 Outdoor Verification of the Setup

In addition to the previous investigations the the proposed mobile GPR system has been utilized for an outdoor GPR survey under realistic conditions, see Fig. 7.35. So far the power supply is realized by an extension cable, which, however, allows for a stand-off distance of more than 50 m. The soil which has been chosen for the experiment consists of mold with stones up to a size of a few cm and was covered with grass and leafs. The overall roughness of the surface was in the range of ±2 cm. For the GPR measurement experiment two well-known AP landmines, namely, the PPM-2 mine and the PMN mine, have been buried one after another at the same position in a typical depth of 6 cm below the surface of the soil, see Fig. 7.36.

(a) mobile GPR with R&S FSH6 (b) operation of the GPR system

Figure 7.35: Experimental outdoor measurement with R&S FSH6 setup.

(a) PPM-2 AP mine, depth 6 cm (b) PMN AP mine, depth 6 cm

Figure 7.36: Placement of two different AP landmines inside of the soil.

In advance, two additional B-scan surveys have been completed above different areas of the soil in order to investigate the influence of the surface roughness. The results of the measurement are illustrated in Figs. 7.37(a) and 7.37(c) and reveal considerable variations of the reflection at the surface. However, the results in Figs. 7.37(b) and 7.37(d) indicate that even for real surfaces a large portion of this unwanted reflection can be removed if a mean value background subtraction is applied.
Finally, the C-scan GPR experiments with 31 by 8 measurement positions and an axial stepwidth of 2 cm have been accomplished. Because the target objects are buried inside of the soil the proposed SAR focusing algorithm has been utilized with an axial stepwidth of 1 cm, see 5. The B-scan and C-scan results of the PPM-2 mine case are illustrated in Fig. 7.38, whereas Fig. 7.39 illustrates the corresponding results of the PMN mine case. Again, a dotted line in the C-scan image indicates the cutting plane of the B-scan and vice versa. Both target objects can clearly be distinguished from the background and yield almost similar reflection signatures exactly as it has been obtained as a result of the indoor GPR experiment.

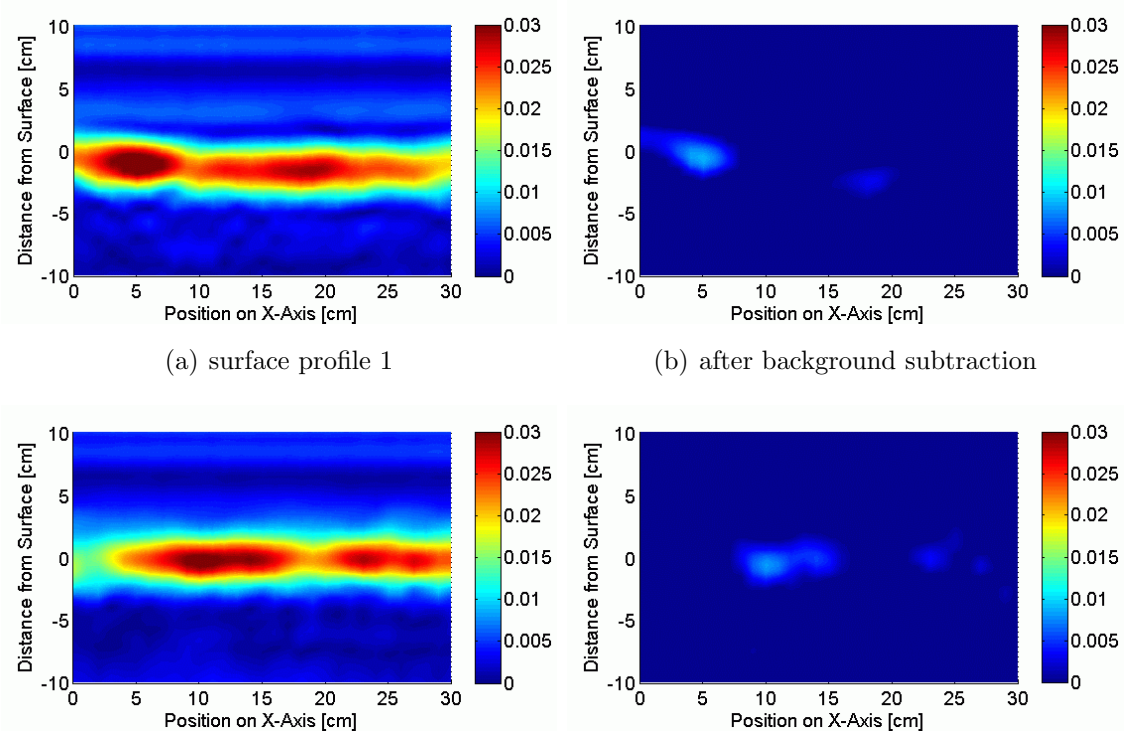

(a) surface profile 1

(b) after background subtraction

(c) surface profile 2

(d) after background subtraction

Figure 7.37: B-scan measurements above natural surface profiles.

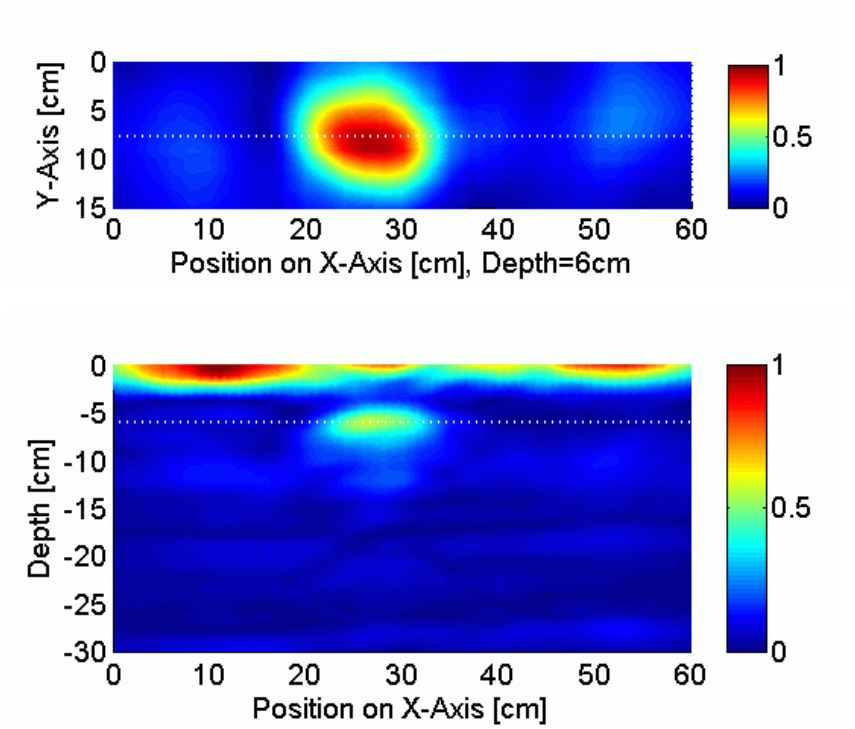

Figure 7.38: C-scan (top) and B-scan (bottom) results of PPM-2 setup.

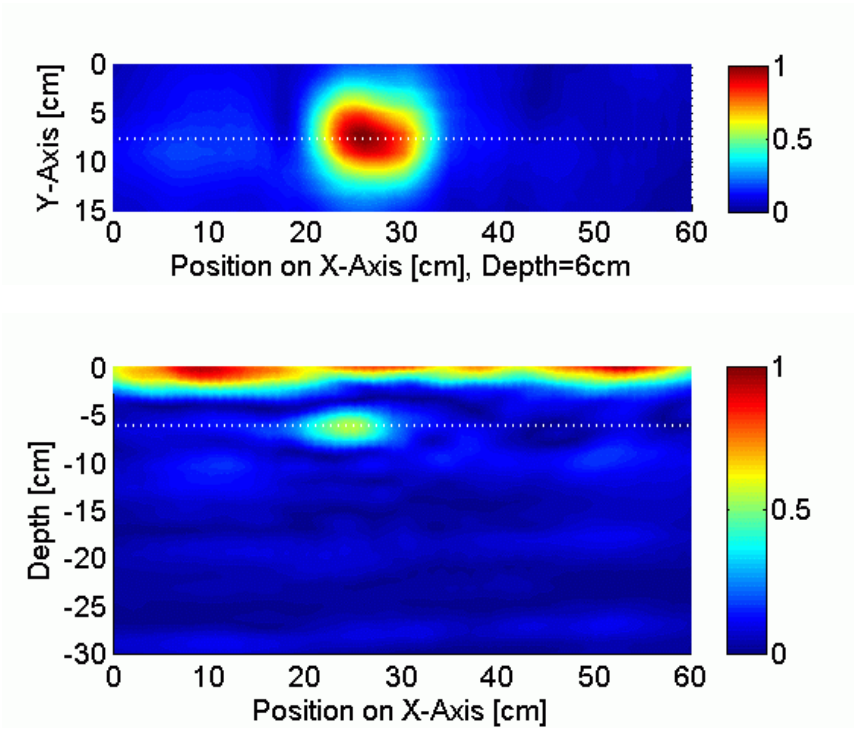

Figure 7.39: C-scan (top) and B-scan (bottom) results of PMN setup.

Chapter 8

Summary and Conclusion

The aim of the research work which has been presented in the context of this thesis was the systematic investigation of the imaging capabilities of ground penetrating radar (GPR) which is supposed to be utilized for the detection of buried nonmetallic Anti-Personnel (AP) landmines. Starting with a state of the art review three major objectives have been addressed, namely, the need for a 3D EM field simulation of a complete GPR environment, which includes the transmitting and the receiving antenna system, the soil structure and a target object that is buried in the subsurface, secondly, the investigation of suitable antenna designs in the context of GPR applications and, last but not least, the improvement of the imaging resolution using either synthetic aperture radar(SAR) techniques or a biconvex dielectric lens.
The novel method for the systematic simulation of a complete GPR environment which has been presented uses all features of the commercial 3D EM field simulation package CST Microwave Studio (MWS). The large number of varying geometries during a complete GPR scan demands for an automation of the GPR simulation which has been realized by means of an ActiveX server control. Thus, the whole functionality of the simulation tool can be controlled from an external Win32 application providing a possibility for the automation of the GPR simulation. The definition of electromagnetic soil parameter in the simulation of the GPR has been addressed and the implementation of realistic physical soil properties such as the texture, the structure or the roughness of the surface have been discussed. Moreover, the flexible integration of different antenna systems and the utilization of different target objects have been illustrated. The quality and the accuracy of the proposed 3D EM simulation of a GPR environment have been verified successfully.

Another important issue which has been addressed is the antenna design for GPR applications. In the context of this thesis different promising antennas designs have been discussed. Important antenna parameters such as the bandwidth of operating frequencies and the radiation pattern have been taken into account right from the beginning of the investigation. Different antenna designs such as the log-periodic dipole antenna, the standard gain horn antenna, the double-ridged TEM horn antenna, the Bujanov antenna or the Orion-type impulse radiating antenna have been investigated using both, 3D field simulations and real measurement experiments. All antennas have been integrated in the proposed simulation environment right from the beginning of the optimization process so that their behavior in the context of a GPR survey could be predicted prior to the fabrication of a first prototype.
The third objective of this thesis has addressed the imaging resolution. It has been demonstrated that SAR focusing can be utilized in order to improve the resolution of GPR images significantly. The fast SAR focusing technique that has been investigated allows for reducing the 3D problem which is encountered when an image of a subsurface target is to be reconstructed to a 2D one by focusing only on a single layer of the corresponding data stack. The influence of different parameter such as the number of elements in the array, the distance between these elements, the position of the focusing point or the position of the antenna have been investigated using both, analytical and numerical simulation and experimental measurements. Thus, the physical limitations of the SAR focusing method have been identified and can be taken into account. In addition, a biconvex dielectric lens for the focusing of a GPR has been designed and compared with the proposed SAR focusing.
Moreover, two prototype GPR systems which have been designed, constructed and verified experimentally, namely, a fully automated laboratory GPR and a mobile GPR setup for outdoor measurements. Both systems have been utilized for various experimental GPR measurements, e.g. for the verification of the proposed SAR focusing concept, the investigation of the dielectric lens focusing approach or the comparison of different antennas. It has been found, that GPR is a versatile tool for the detection of buried nonmetallic objects. The best imaging resolution can be achieved, if the transmitting antenna system and, thus, its radiation pattern, the utilized range of operating frequencies, and the placement of the antenna above the soil are all taken into account. Furthermore the theoretically and practically defined limitations of the proposed SAR focusing technique have been discussed.

Appendix A

Electromagnetic Derivations

A.1 One-Port Calibration Procedure

When a vector network analyzer (VNA) is utilized for one-port measurements the measured reflection coefficient Γ_m can differ from the actual reflection coefficient Γ significantly unless the VNA is properly calibrated. According to the well-know error-model Γ is related to the corresponding measured quantity Γ_m by a bilinear transformation which can be described by equations (A.1).

$$\Gamma = \frac{\Gamma_m - E_D}{E_R + E_S\left(\Gamma_m - E_D\right)} \tag{A.1}$$

The directivity error E_D, the source match error E_S and the frequency response error E_R represent system errors which can be calculated if three independent calibration standards are taken into account, e.g. a match, a short and an offset short. The equivalent error model has been illustrated in Fig. A.1. In order to derive a convenient description of the one-port calibration problem which can be solved using matrix inversion techniques equation A.1 needs to be reformulated as follows.

$$\begin{aligned} \Gamma_m - E_S\Gamma\Gamma_m &= E_D\left(1 - E_S\Gamma\right) + E_R\Gamma \\ &= E_D - E_D E_S\Gamma + E_R\Gamma \qquad \text{(A.2)} \\ \Gamma_m &= E_D + \left(E_R - E_D E_S\right)\Gamma + E_S\Gamma\Gamma_m \qquad \text{(A.3)} \end{aligned}$$

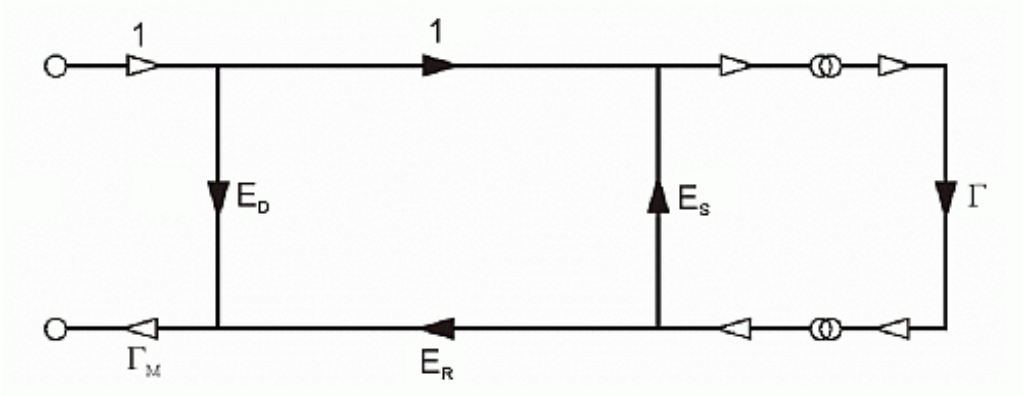

Figure A.1: Full one-port error model.

Finally, the term $(E_R - E_D E_S)$ in equation A.3 is substituted by E_X in order to increases the convenience of the formulation. If now three known calibration standards Γ_1, Γ_2 and Γ_3 are connected to the measurement system which is supposed to be calibrated the corresponding reflection coefficients Γ_{m1}, Γ_{m2} and Γ_{m3}, respectively, can be measured and the calibration problem can be formulated as follows.

$$\begin{bmatrix} 1 & \Gamma_1 & \Gamma_{m1}\Gamma_1 \\ 1 & \Gamma_2 & \Gamma_{m2}\Gamma_2 \\ 1 & \Gamma_3 & \Gamma_{m3}\Gamma_3 \end{bmatrix} \begin{bmatrix} E_D \\ E_X \\ E_S \end{bmatrix} = \begin{bmatrix} \Gamma_{m1} \\ \Gamma_{m2} \\ \Gamma_{m3} \end{bmatrix} \tag{A.4}$$

A simple matrix inversion allows to calculated the desired error coefficients.

$$\begin{bmatrix} E_D \\ E_X \\ E_S \end{bmatrix} = \begin{bmatrix} 1 & \Gamma_1 & \Gamma_{m1}\Gamma_1 \\ 1 & \Gamma_2 & \Gamma_{m2}\Gamma_2 \\ 1 & \Gamma_3 & \Gamma_{m3}\Gamma_3 \end{bmatrix}^{-1} \begin{bmatrix} \Gamma_{m1} \\ \Gamma_{m2} \\ \Gamma_{m3} \end{bmatrix} \tag{A.5}$$

Knowing E_X, E_D and E_S, E_R can be calculated as $E_R = E_X + E_D E_S$. Thus, the system errors of the measurement setup can be corrected using equation A.1. It is important to note, that this error correction has to be applied for every spectral component individually. However, the determination of the error coefficients has to be done only once as long as the measurement setup is not changed.

A.2 Analysis of the Half-space Problem

In order to describe the propagation of electromagnetic waves in the presence of a flat interface between air and a homogeneous medium two different problems have to be analyzed, namely, the propagation from soil to air and the propagation in the opposite direction, see Fig. A.2. For the first problem a source in the soil is assumed which is described by the polarization current $\mathbf{J}_1(\mathbf{r}') = \overline{Il}\,\delta(\mathbf{r}' - \mathbf{r}_s)\,\hat{\mathbf{p}}_\mathbf{s}$.

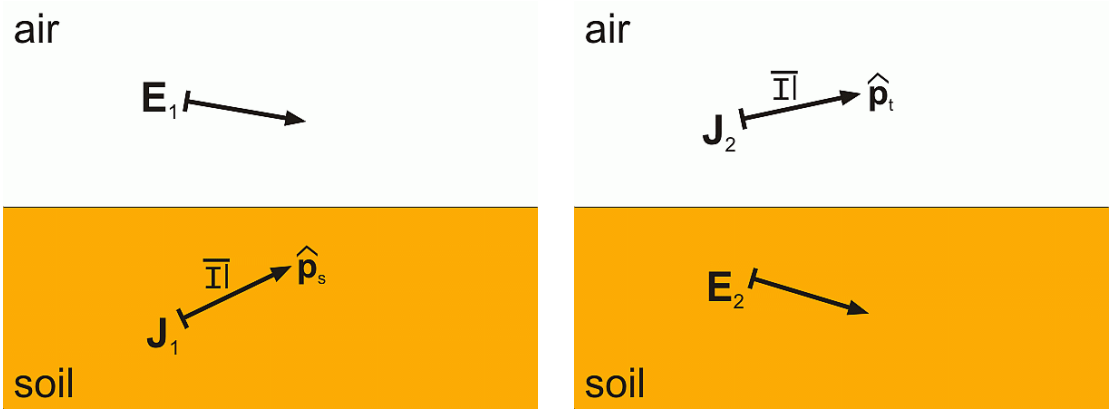

(a) problem 1: from soil to air (b) problem 2: from air to soil

Figure A.2: Propagation in the presence of a flat air-soil interface.

Thus, the scattered field $\mathbf{E}_1(\mathbf{r}_r)$ which can be received in the air denotes as

$$\begin{aligned}
\mathbf{E}_1(\mathbf{r}_r) &= j\omega\mu_0 \int_V \bar{\mathbf{G}}(\mathbf{r}_r, \mathbf{r}')\,\mathbf{J}_1(\mathbf{r}')\; d\mathbf{r}' \\
\mathbf{E}_1(\mathbf{r}_r) &= j\omega\mu_0 \int_V \bar{\mathbf{G}}(\mathbf{r}_r, \mathbf{r}') \cdot \left(\overline{Il}\,\delta(\mathbf{r}' - \mathbf{r}_s)\,\hat{\mathbf{p}}_\mathbf{s}\right)\; d\mathbf{r}' \\
\mathbf{E}_1(\mathbf{r}_r) &= j\omega\mu_0 \overline{Il}\,\bar{\mathbf{G}}(\mathbf{r}_r, \mathbf{r}_s) \cdot \hat{\mathbf{p}}_\mathbf{s} \qquad \text{(A.6)}
\end{aligned}$$

For the second propagation problem a source in the air is assumed which can be understood as a transmitting antenna that is described as $\mathbf{J}_2(\mathbf{r}') = \overline{Il}\,\delta(\mathbf{r}' - \mathbf{r}_t)\,\hat{\mathbf{p}}_\mathbf{t}$. The corresponding observation point which is now located inside of the soil and described by the field $\mathbf{E}_2(\mathbf{r}_s)$. For the calculation of $\mathbf{E}_2(\mathbf{r}_s)$ the general reciprocity relation has been utilized. Thus, it is possible to determine the relation between $\mathbf{E}_2(\mathbf{r}_s)$ and $\mathbf{J}_2(\mathbf{r}')$ using the known relation between $\mathbf{E}_1(\mathbf{r}_r)$ and $\mathbf{J}_1(\mathbf{r}')$.

$$\begin{aligned}
\int_V \mathbf{E}_2^T(\mathbf{r}') \cdot \mathbf{J}_1(\mathbf{r}')\ d\mathbf{r}' &= \int_V \mathbf{E}_1^T(\mathbf{r}') \cdot \mathbf{J}_2(\mathbf{r}')\ d\mathbf{r}' \\
\int_V \mathbf{E}_2^T(\mathbf{r}') \cdot \left(\overline{Il}\,\delta(\mathbf{r}' - \mathbf{r}_s)\,\hat{\mathbf{p}}_\mathbf{s}\right)\ d\mathbf{r}' &= \int_V \mathbf{E}_1^T(\mathbf{r}') \cdot \left(\overline{Il}\,\delta(\mathbf{r}' - \mathbf{r}_t)\,\hat{\mathbf{p}}_\mathbf{t}\right)\ d\mathbf{r}' \\
\mathbf{E}_2^T(\mathbf{r}_s) \cdot \hat{\mathbf{p}}_\mathbf{s}\,\overline{Il} &= \mathbf{E}_1^T(\mathbf{r}_t) \cdot \hat{\mathbf{p}}_\mathbf{t}\,\overline{Il}
\end{aligned}$$

In the above equation the term $\mathbf{E}_2^T(\mathbf{r}_s) \cdot \hat{\mathbf{p}}_\mathbf{s}$ can be replaced with its transpose $\left(\mathbf{E}_2^T(\mathbf{r}_s) \cdot \hat{\mathbf{p}}_\mathbf{s}\right)^T = \hat{\mathbf{p}}_\mathbf{s}^\mathbf{T} \cdot \mathbf{E}_2(\mathbf{r}_s)$ because it is a scalar. Furthermore, $\mathbf{E}_1^T(\mathbf{r}_t)$ on the left-hand side of the equation is substituted according to equation A.6.

$$\begin{aligned}
\left(\mathbf{E}_2^T(\mathbf{r}_s) \cdot \hat{\mathbf{p}}_\mathbf{s}\right)^T \overline{Il} &= \left(j\omega\mu_0 \overline{Il}\,\bar{\mathbf{G}}(\mathbf{r}_r, \mathbf{r}_s)\,\hat{\mathbf{p}}_\mathbf{s}\right)^T \cdot \hat{\mathbf{p}}_\mathbf{t}\,\overline{Il} \\
\hat{\mathbf{p}}_\mathbf{s}^\mathbf{T} \cdot \mathbf{E}_2(\mathbf{r}_s)\,\overline{Il} &= j\omega\mu_0 \overline{Il}^2\ \left(\hat{\mathbf{p}}_\mathbf{s}^\mathbf{T} \cdot \bar{\mathbf{G}}^\mathbf{T}(\mathbf{r}_t, \mathbf{r}_s)\right) \cdot \hat{\mathbf{p}}_\mathbf{t} \\
\mathbf{E}_2(\mathbf{r}_s) &= j\omega\mu_0 \overline{Il}\,\bar{\mathbf{G}}^T(\mathbf{r}_t, \mathbf{r}_s) \cdot \hat{\mathbf{p}}_\mathbf{t} \qquad \text{(A.7)}
\end{aligned}$$

The unit vector $\hat{\mathbf{p}}_s^T$ has been dropped, because the analysis is valid for every selected field component in the soil. The scattered field $\mathbf{E}_S(\mathbf{r}_r, \mathbf{r}_t)$ which considers a transmitter and a receiver above the interface could be determined exactly if the total field $\mathbf{E}(\mathbf{r}')$ in the subsurface region was known. It has already been shown, that the first Born approximation can be utilized so that the term for the total field $\mathbf{E}(\mathbf{r}')$ can be replaced by the one of the background field $\mathbf{E}_B(\mathbf{r}')$. The illumination is provided by the $\hat{\mathbf{p}}_t$-directed transmitting dipole so that the background field denotes as

$$\mathbf{E}_B(\mathbf{r}') = j\omega\mu_0 \overline{Il}\,\bar{\mathbf{G}}_\mathbf{inv}(\mathbf{r}', \mathbf{r}_t) \cdot \hat{\mathbf{p}}_t \qquad \text{(A.8)}$$

Comparing equation (A.7) with equation (A.8) it can be concluded that $\bar{\mathbf{G}}_\mathbf{inv}(\mathbf{r}', \mathbf{r}_t)$ is equal to $\bar{\mathbf{G}}^T(\mathbf{r}_t, \mathbf{r}')$. Thus, only one dyadic Green's function is required for the complete description of the propagation problem at the the air-soil interface.

Appendix B

Anti-Personnel Landmines

B.1 Introduction

The Convention on Conventional Weapons defines an anti-personnel (AP) landmine as a mine designed to be exploded by the presence, proximity or contact of a person. The explosion of such a mine will incapacitate, injure or kill one or more persons. These hidden, indiscriminate weapons continue to kill and maim for decades after wars have ended. According to the International Campaign to Ban Landmines (ICBL), more than 350 different kinds of anti-personnel landmines have been produced by more than 50 countries. It is assumed that 60-70 million active AP landmines exist in at least 70 countries throughout the world, with more landmines being deployed every day. AP landmines act to injure or kill victims either by the explosive blast or by bounding, respectively, directional fragmentation of metal debris projected upon detonation. Placed on the surface or in a depth up to 20 cm below the surface AP landmines are often 12 cm or less in diameter.
They are much harder to detect and to remove than Anti-Tank (AT) landmines and are activated only by the weight of a foot. Many types of AP landmines were designed and constructed with very little or none metallic content. Their packages can be made of various materials such as plastic, wood, fiberglass, bakelite, ceramic, cardboard, neoprene, resin and even glass. Five common types of anti-personnel landmines that have been employed for different measurement experiments in the context of this thesis will be introduced according to [Smi06]. The dimension, composition, construction and the type and amount of explosive material that these mines utilize will be explained and illustrated in the following chapter.

B.2 M14

The M14 is a small AP blast mine manufactured in the USA. It has been found in Angola, Cambodia, Chad, Chile, El Salvador, Eritrea, Ethiopia, Iran, Iraq, Jordan, Laos, Lebanon, Malawi, Mozambique, Somalia, Vietnam, Zambia. The mine is usually colored olive green, but also other colors are reported. The cylindrical plastic body has a height of 40 mm, a diameter of 56 mm and a minimum metal content of approximately 2.36 g in the firing pin. The M14 is fired when pressure is applied to the top surface. The main charge is 28.35 g of tetryl. The design was chosen because of logistical considerations. Because of their small size, a soldier can carry several M14 mines. This is a minimum metal mine and is very hard to detect. When U.S. forces use the M14 in Korea metal washers have been added in order to meet detectability requirements of the Ottawa Convention on Conventional Weapons.

Figure B.1: M14 Anti-Personnel Mine [Smi06].

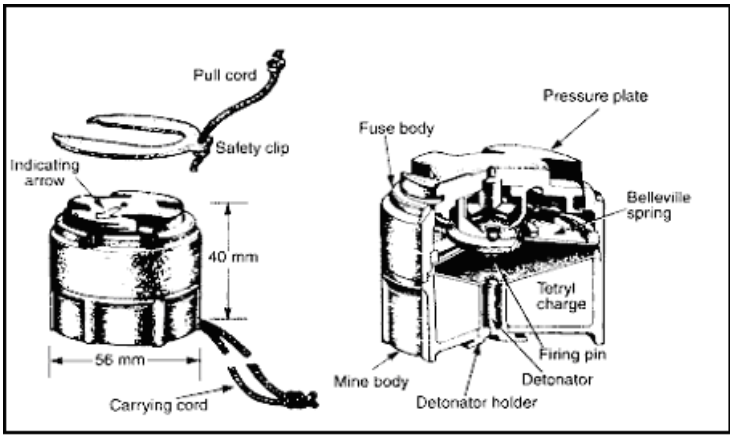

Figure B.2: Schematics of the M14 Anti-Personnel Mine [Var06b].

B.3 PPM-2

The PPM-2 is a plastic-cased, pressure operated, AP blast mine made in the former East Germany. It has been found in Angola, Cambodia, Chad, Eritrea, Ethiopia, Lebanon, Mozambique, Namibia and Somalia. Moreover, it was the last land mine to be placed in service along the Iron Curtain in the eastern part of Germany. Made of a softer, more pliable plastic than it's predecessors, the PPM-2 began appearing in the late 1970's. Its dimensions are a height of 60 mm and a diameter of 134 mm and it is usually black. The main explosive charge of 110 g TNT has a piezo-electric initiation mechanism in connection with an electric detonator.

Figure B.3: PPM-2 Anti-Personnel Mine [Smi06].

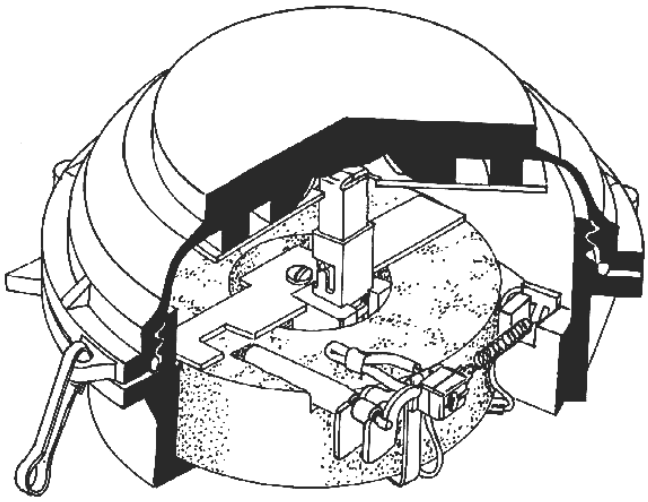

Figure B.4: Schematics of the PPM-2 Anti-Personnel Mine [Smi06].

B.4 PMN

The PMN anti-personnel mine is a bakelite-cased, pressure operated, anti-personnel blast mine, which is sometimes called the 'Black-widow'. Made in the former Soviet Union, it has been found in Afghanistan, Angola, Azerbaijan, Cambodia, Egypt, Eritrea, Ethiopia, Georgia, Honduras, Iraq, Kurdistan, Laos, Lebanon, Libya, Mozambique, Namibia, Nicaragua, Rwanda, Somalia, Sudan, Tajikistan, Vietnam and Yemen. The mine has a body that is usually reddish-brown bakelite with a black rubber top with a height of 56 mm and a diameter of 112 mm. The main charge consist of 240 g TNT in combination with a stab-sensitive MD-9 detonator. The Chinese Type 58 AP mine is reported to be an identical copy of the PMN.

Figure B.5: PMN Anti-Personnel Mine [Smi06].

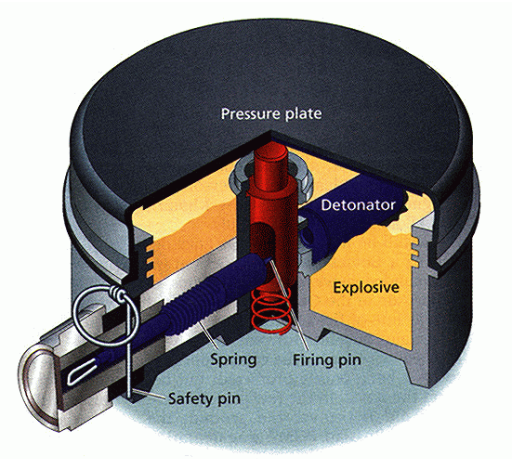

Figure B.6: Schematics of the PMN Anti-Personnel Mine [Tab06].

B.5 PMN-2

The PMN-2 is a plastic-cased, pressure operated, anti-personnel blast mine including a complex arming-delay and blast resistance mechanism. Made in the former Soviet Union, it has been found in Afghanistan, Angola, Azerbaijan, Cambodia, Chechnya, Eritrea, Ethiopia, Georgia, Honduras, Lebanon, Mozambique, Nicaragua, Tajikistan and Thailand. The mine has a body with a height of 53 mm and a diameter of 120 mm. That PMN-2 is usually of green plastic with a black rubber cross on top. The main charge consists of 100 g TNT. The PMN-2 detonator is integral but the booster charge screws into the base. The primary high explosive charge is entirely on the side of the mine opposite the arming pin. Although a very complex mine the PMN-2 remains functional in most grounds for many years.

Figure B.7: PMN-2 Anti-Personnel Mine [Smi06].

Figure B.8: Disassembled PMN-2 Anti-Personnel Mine [Smi06].

References

[ACR91] Annan, A. P., Cosway, S. W., and Redman, J. D., "Water Table Detection with Ground Penetrating Radar," *Annual Meeting of the Society of Exploration Geophysicists*, vol. 61, pp. 494–496, 1991. 9

[AG+02] Andrieu, M., Gallais, F., Mallepeyre, V., and Jecko, B., "Landmine Detection with an Ultra-Wideband SAR System," *Proc. of SPIE Vol. 4742 – Detection and Remediation Technologies for Mines and Minelike Targets VII*, pp. 237–247, 2002. 13

[AJO07] Anis, M., Jöstingmeier, A., and Omar, A. S., "Introduction of an Effective Waveguide Width in Transmission/Reflection Methods for Dielectric Measurements," *in Proc. 2007 IEEE Antennas and Propagation Society International Symposium*, pp. 281–284, Honolulu, Hawaii, June 10-15, 2007. 41, 71, 146, 151

[BA+07] Bandyopadhyay, A. K., Anis, M., Jöstingmeier, A., Meyer, T., and Omar, A. S., "Analysis of a Compact Ultra-Wideband Antenna for Radio Frequency Applications," *in Proc. 2007 IEEE Antennas and Propagation Society International Symposium*, Honolulu, Hawaii, June 10-15, 2007. 103, 104

[Bau99] Baum, C. E., *Detection and Identification of Visually Obscured Targets.* Philadelphia: Taylor and Francis, 1999. 4

[BE98] Brunzell, H. O. and Ericsson, A., "Dual-Antenna Impulse Radar for Improved Detection of Buried Landmines," *Proc. of SPIE Vol. 3392 – Detection and Remediation Technologies for Mines and Minelike Targets III*, pp. 725–734, 1998. 15

[BEH00] Binningsboe, J., Eide, E., and Hjelmstad, J. F., "3D migration of GPR Array-Antenna Data," *in Proc. Eighth International Conference on GPR*, pp. 459–463, Gold Coast, Australia, May 23-26, 2000. 16

[BF+04] Baumann, D., Fumeaux, C., Leuchtmann, P., and Vahldieck, R., "Finite-Volume Time-Domain (FVTD) Modeling of a Broadband Double-Ridged Horn Antenna," *International Journal of Numerical Modeling*, vol. 17, pp. 285–298, 2004. 88, 90

[BG97] Bruschini, C. and Gros, B., "A Survey of Current Sensor Technology Research for the Detection of Landmines," *in Proc. of the International Workshop on Sustainable Humanitarian Demining*, Zagreb, Croatia, September 29-30, 1997. 3

[BGJ03] Burkholder, R. J., Gupta, I. J., and Johnson, J. T., "Comparison of Monostatic and Bistatic Radar Images," *IEEE Antennas and Propagation Magazine*, vol. 45, pp. 41–50, 2003. 26

[BLV03] Bruns, C., Leuchtmann, P., and Vahldieck, R., "Analysis and Simulation of a Broadband Double-Ridged Horn Antenna," *IEEE Trans. on Electromagnetic Compability*, vol. 45, pp. 55–60, 2003. 88, 90

[BMN98] Botelho, M. A., Mufti, I. R., and Neto, V. P., "Multishot Prestack Depth Migration − An Application on Real Wide-angle Reflection and Refraction GPR Data," *Annual Meeting of the Society of Exploration Geophysicists*, vol. 68, pp. 1393–1396, 1998. 9

[BO91] Beck, R. and Osborn, J., "Three Dimensional Migration and Forward Modeling of Ground Penetrating Radar Data," *Report CMU-RI-TR-91-12, Robotics Institute, Carnegie Mellon University*, 1991. 16

[Bro77] Brookner, E., *Radar Technology*. Norwood: Artech House, 1977. 10

[BS96] Bourgeois, J. M. and Smith, G. S., "A Fully Three-Dimensional Simulation of a Ground-Penetrating Radar: FDTD Theory Compared with Experiment," *IEEE Transactions on Geoscience and Remote Sensing*, vol. 34, pp. 36–44, 1996. 14

[BS98] Bourgeois, J. M. and Smith, G. S., "A Complete Electromagnetic Simulation of the Separated-Aperture Sensor for Detecting Buried Land Mines," *IEEE Transactions on Antennas and Propagation*, vol. 46, pp. 1419–1426, 1998. 14

[BSC99] Breejen, E., Schutte, K., and Cremer, F., "Sensor Fusion for Anti-Personnel Landmine Detection − A Case Study," *Proc. of SPIE Vol. 3710 − Detection and Remediation Technologies for Mines and Minelike Targets IV*, pp. 215–222, 1999. 13

[BW+00] Bradley, M., Witten, T., McCummins, R., and Duncan, M., "Mine Detection with a Ground Penetrating Synthetic Aperture Radar," *Proc. of SPIE Vol. 4038 − Detection and Remediation Technologies for Mines and Minelike Targets V*, pp. 1001–1007, 2000. 13

[BW+02] Bradley, M., Witten, T., McCummins, R., and Duncan, M., "Mine Detection with Ground Penetrating Synthetic Aperture Radar," *Proc. of SPIE Vol. 4742 − Detection and Remediation Technologies for Mines and Minelike Targets VII*, pp. 248–258, 2002. 13

[Cas01] Casey, K. F., "Rough Surface Effects on Subsurface Target Detection," *Proc. of SPIE Vol. 4394 − Detection and Remediation Technologies for Mines and Minelike Targets VI*, pp. 754–763, 2001. 44

[CB+04] Clark, W., Burns, B., Dieguez, E., and Ralston, J., "Comparison of three Wideband Antennas for Ground Penetrating Radar," *Proc. of SPIE Vol. 5415 − Detection and Remediation Technologies for Mines and Minelike Targets IX*, pp. 433–446, 2004. 15

[CB06] Claerbout, J. F. and Black, J. L., *Basic Earth Imaging − Online Version*. http://www.stanford.edu, retrieved Apr. 10, 2006. 111

[Che02] Cheney, M., "Introduction to Synthetic Aperture Radar (SAR) and SAR Interferometry," *Approximation Theory X: Wavelet, Splines and Applications, Vanderbilt University Press*, pp. 167–177, 2002. 111

[CJ+06] Chen, Y., Joines, W., Xie, Z., Shi, G., Liu, Q., and Carin, L., "Double-Sided Exponentially Tapered GPR Antenna and Its Transmis-

sion Line Feed Structure," *IEEE Transactions on Antennas and Propagation*, vol. 54, pp. 2615–2623, 2006. 15

[CKB98] Carin, L., Kapoor, R., and Baum, C. E., "Polarimetric SAR Imaging of Buried Landmines," *IEEE Transactions on Geoscience and Remote Sensing*, vol. 36, pp. 1985–1988, 1998. 112

[Col92] Collin, R. E., *Foundations for Microwave Engineering.* New York: McGraw-Hill Book Company, 2nd ed., 1992. 20, 21, 22

[Cur98] Curtis, J. O., "Site Characterization Investigations in Support of UXO Technology Demonstrations, Jefferson Proving Ground Indiana," *Technical report, U.S. Army Corps of Engineers*, 1998. 43

[DA89] Davis, J. L. and Annan, A. P., "Ground Penetrating Radar for High-Resolution Mapping of Soil and Rock Stratigraphy," *Geophysical Prospecting*, vol. 37, pp. 531–551, 1989. 9, 41

[Dan00] Daniels, J. J., "Ground Penetrating Radar for Imaging Archaeological Objects in the Subsurface," *in Proc. of the New Millennium International Forum on Conservation of Cultural Property*, pp. 247–265, Kongju, Korea, December 5-8, 2000. 9

[Dan04] Daniels, D. J., *Ground Penetrating Radar.* London: IEE Press, 2004. 9, 31, 32, 33, 34, 41

[DBT78] Dolphin, L. T., Beatty, W. B., and Tanzi, J. D., "Radar Probing of Victorio Peak, NM," *Geophysics*, vol. 43, pp. 441–448, 1978. 9

[Dea01] Dean, J. T., "MINETEST − Testing of Sensors and Systems in Support to Humanitarian Demining," *European Commission, Joint Research Center, Institute for Protection and Security*, 2001. 13

[Dev02] Devillers, J., *Honey Bees: Estimating the Environmental Impact of Chemicals.* New York: Taylor & Francis, 2002. 8

[ECS07] Engle, C. F., Cogger, C. G., and Stevens, R. G., *Clean Water for Washington: Role of Soil in Groundwater Protection.* http://cru.cahe.wsu.edu, retrieved Jan. 10, 2007. xix, 40

[Edd93] Edde, B., *Radar – Principles, Technology, Applications.* Englewood Cliffs: PTR Prentice Hall, 1993. 10, 26

[Eid00] Eide, E. S., "Ultra-Wideband Transmit / Receive Antenna Pair for Ground Penetrating Radar," *IEE Proc. on Microwaves, Antennas and Propagation*, vol. 147, pp. 231–235, 2000. 15

[ES+05] Eide, E., Sandnes, P. A., Nilssen, B., and Tjora, S., "Airfield Runway Inspection Using 3-Dimensional GPR," *in Proc. of the 3rd International Workshop on Advanced Ground Penetrating Radar*, pp. 87–92, Delft, Netherlands, May 2-3, 2005. 9

[FB01] Farr, E. G. and Bowen, L. H., "Impulse Radiating Antennas for Anti-Personnel Mine Detection," *Proc. of SPIE Vol. 4394 – Detection and Remediation Technologies for Mines and Minelike Targets VI*, pp. 680–691, 2001. 15, 70

[FBM00] Fischer, R., Burlage, R., and Maston, M., "UXO and Mine Detection Using Laser Induced Fluorescence Imagery and Genetically Engineered Microbes," *Army AL&T July-August*, pp. 10–12, 2000. 8

[FCK00] Feng, H., Castation, D. A., and Karl, W. C., "A Statistical Approach to Rough Surface Underground Imaging," *in Proc. of 2000 International Conference on Image Processing*, vol. 1, pp. 705–708, Vancouver, Canada, September 10-13, 2000. 44

[FG02] Fortuny-Guasch, J., "A Novel 3-D Subsurface Radar Imaging Technique," *IEEE Transactions on Geoscience and Remote Sensing*, vol. 40, pp. 443–452, 2002. 17

[GB+01] Garroway, A. N., Buess, M. L., Miller, J. B., Suits, B. H., Hibbs, A. D., Barrall, G. A., and Burnett, L. J., "Remote Sensing by Nuclear Quadrupole Resonance (NQR)," *IEEE Transactions on Geoscience and Remote Sensing*, vol. 39, pp. 1108–1118, 2001. 7

[GC99] Geng, N. and Carin, L., "Wide-Band EM Scattering from a Dielectric BOR Buried in a Layered Lossy Dispersive Medium," *IEEE Transactions on Antennas and Propagation*, vol. 47, pp. 610–619, 1999. 115

[GD+00] Guy, E. D., Daniels, J. J., Radzevicius, S. J., and Vendl, M. A., "Demonstration of Using Crossed Dipole Antenna for Site Characterization," *Geophysical Research Letters*, vol. 26, pp. 3421–3424, 2000. 15

[GG+04] Gomez Martin, R., Godoy Rubio, R., Gonzalez Garca, S., Fernandez Pantoja, M., and Rubio Bretones, A., "Simulation of a Ground Penetrating Radar Using an ADI-FDTD/MOMTD Hybrid Method," *in Proc. 2004 URSI EMTS International Symposium on Electromagnetic Theory*, pp. 203–205, Pisa, Italy, May 23-27, 2004. 14

[GH+04] Gross, R., Horstmeyer, H., Green, A. G., and Begg, J., "Geometry of the Wellington Fault (New Zealand) Defined by 3-D Georadar Data," *in Proc. Tenth International Conference on Ground Penetrating Radar*, pp. 559–562, Delft, Netherlands, June 21-24, 2004. 9

[GHM04] Gordon, G., Heyman, E., and Mazar, R., "Gaussian Beam Summation Formulation of Rough Surface Scattering," *in Proc. 2004 URSI EMTS International Symposium on Electromagnetic Theory*, pp. 1077–1079, Pisa, Italy, May 23-27, 2004. 44

[GO00] Gürel, L. and Oguz, U., "Three-dimensional FDTD Modeling of a Ground Penetrating Radar," *IEEE Transactions on Geoscience and Remote Sensing*, vol. 38, pp. 1513–1521, 2000. 14

[GO01] Gürel, L. and Oguz, U., "Simulations of Ground Penetrating Radars over Lossy and Heterogeneous Grounds," *IEEE Transactions on Geoscience and Remote Sensing*, vol. 39, pp. 1190–1197, 2001. 14

[GPR04] Galagedara, L., Parkin, G., and Redman, D., "Measuring and Modeling of GPR Ground Wave Depth Penetration Under Transient Soil Moisture Conditions," *in Proc. Tenth International Conference on GPR*, pp. 505–508, Delft, Netherlands, June 21-24, 2004. 9

[GS84] Gazdag, J. and Sguazerro, P., "Migration of Seismic Data by Phase-Shift plus Interpolation," *Geophysics*, vol. 49, pp. 124–131, 1984. 16

[Gue97] Guerlac, H., *Radar in World War II.* Berlin: Springer, 1997. 10

[Har78] Harris, F. J., "On the Use of Windows for Harmonic Analysis with the DFT," *in Proc. of the IEEE*, vol. 66, pp. 51–83, 1978. 135

[HJ00] Hansen, T. B. and Johansen, P. M., "Inversion Scheme for Ground Penetrating Radar That Takes into Account the Planar Air-Soil Interface," *IEEE Transactions on Geoscience and Remote Sensing*, vol. 48, pp. 496–506, 2000. 113, 115

[HS00] Holzrichter, M. W. and Sleefe, G. E., "Resolution Enhancement of Landmines in Ground-Penetrating Radar Images," *Proc. of SPIE Vol. 4038 − Detection and Remediation Technologies for Mines and Minelike Targets V*, pp. 1160–1170, 2000. 17

[HU+85] Hallikainen, M. T., Ulaby, F. T., Dobson, M. C., and El-Rayes, M. A., "Microwave Dielectric Behavior of Wet Soil − Part I: Empirical Models and Experimental Observations," *IEEE Transactions on Geoscience and Remote Sensing*, vol. 23, pp. 25–34, 1985. 41

[Hue04] Huelsmeyer, C., *Verfahren, um entfernte metallische Gegenstände mittels elektrischer Wellen einem Beobachter zu melden.* Deutsches Patent Nr. 165 546, 1904. 10

[HvD+03] Hendrickx, J. M., van Dam, R. L., Borchers, B., Curtis, J., Lensen, H. A., and Harmon, R., "Worldwide Distribution of Soil Dielectric and Thermal Properties," *Proc. of SPIE Vol. 5089 − Detection and Remediation Technologies for Mines and Minelike Targets VIII*, pp. 1158–1168, 2003. 41

[IY+07] Iskander, M. F., Yun, Z., Youn, H., Kim, W., and Celik, N., "On the Feasibility of Using GPR Technology for the UXO Detection and Discrimination in the Volcanic Soil of Hawaii," *in Proc. 2007 IEEE Antennas and Propagation Society International Symposium*, pp. 4949–4952, Honolulu, Hawaii, June 10-15, 2007. 41

[JB04] Johnson, J. T. and Burkholder, R. J., "A Study of Scattering From an Object Below a Rough Surface," *IEEE Transactions on Geoscience and Remote Sensing*, vol. 42, pp. 59–66, 2004. 44

[JLM96] Jao, J. K., Lee, C. F., and Merchant, B. L., "Synthetic Aperture Radar Performance in Detecting Shallow Buried Targets," *Proc. of SPIE Vol. 2765 − Detection and Remediation Technologies for Mines and Minelike Targets*, pp. 275–286, 1996. 17

[JM94] Johansson, E. M. and Mast, J. E., "Three-dimensional Ground-Penetrating Radar Imaging Using Synthetic Aperture Time-Domain Focusing," *Proc. of SPIE Vol. 2275 − Advanced Microwave and Millimeter-Wave Detectors*, pp. 205–214, 1994. 17

[JMO03] Jöstingmeier, A., Meyer, T., and Omar, A. S., "Material Measurements of Absorbers with Magnetic Losses," *in Proc. 2003 IEEE Antennas and Propagation Society International Symposium*, vol. 4, p. 66, Columbus, Ohio, June 22-27, 2003. 41, 71, 146, 151

[Joh02] Johnson, J. T., "A Numerical Study of Scattering From an Object Above a Rough Surface," *IEEE Transactions on Antennas and Propagation*, vol. 50, pp. 1361–1367, 2002. 44

[KA+03] Koshelev, V. I., Andreev, Y. A., Buyanov, Y. I., Plisko, V. V., and Sukhushin, K. N., "Ultra-Wideband Transmitting Antenna, Arrays, and High-Power Radiation Sources," *Ultra-Wideband Short Pulse Electromagnetics 6*, pp. 357–367, 2003. 103

[KB+01] Koshelev, V. I., Buyanov, Y. I., Andreev, Y. A., Plisko, V. V., and Sukhushin, K. N., "Ultra-Wideband Radiators of High-Power Pulses," *in Proc. 2001 IEEE Pulsed Power Plasma Science*, vol. 2, pp. 1661–1664, Las Vegas, Nevada, June 17-22, 2001. 103, 104

[KB04] Koh, G. and Ballard, J. R., "Disturbed Soil Signatures for Mine Detection," *in Proc. of the 24th Army Science Conference*, Orlando, Florida, November 29 − Dec. 2, 2004. 14

[KC99] Knoll, M. D. and Clement, W. P., "Vertical Radar Profiling to Determine Dielectric Constant, Water Content, and Porosity Values at Well Locations," *Symp. on the Application of Geophysics to Engineering and Environmental Problems*, Oakland, California, March 14-18, 1999. 9

[KE90] Knight, R. and Endres, A., "A New Concept in Modeling the Dielectric Response of Sandstones: Defining a Wet Rock and Bulk Water System," *Geophysics*, vol. 55, pp. 586–594, 1990. 9, 43

[KJ02] Kim, H. and Johnson, J. T., "Radar Images of Rough Surface Scattering: Comparison of Numerical and Analytical Models," *IEEE Trans. on Antennas and Propagation*, vol. 50, pp. 94–100, 2002. 44

[KM02] Kraus, J. D. and Marhefka, R. J., *Antennas for all Applications*. Boston: McGraw-Hill, 3rd ed., 2002. 143, 145

[Kno96] Knoll, M. D., *Petrophysical Basis for Ground Penetrating Radar and Very Early Time Electromagnetics, Electrical Properties of Sand-Clay Mixtures*. PhD thesis, University of British Columbia, 1996. 43

[KS+99] Kenton, A. C., Schwartz, C. R., Horvath, R., Cederquist, J. N., Nooden, L. S., Twede, D. R., Nunez, J. A., John, W., and Montavon, K., "Detection of Land Mines with Hyperspectral Data," *Proc. of SPIE Vol. 3710 − Detection and Remediation Technologies for Mines and Minelike Targets IV*, pp. 917–928, 1999. 5

[KW+03] Kruk, J., Wapenaar, C. P., Fokkema, J. T., and van den Berg, P. M., "Improved Three-dimensional Image Reconstruction Technique for Multi-Component Ground Penetrating Radar Data," *Subsurface Sensing Technologies and Applications*, vol. 4, pp. 61–99, 2003. 16

[KWR02] Kosmas, P., Wang, Y., and Rappaport, C., "Three-dimensional FDTD Model for Ground Penetrating Radar Detection of Objects Buried in Realistic Dispersive Soil," *Proc. of SPIE Vol. 4742 − Detection and Remediation Technologies for Mines and Minelike Targets VII*, pp. 330–338, 2002. 14, 44

[LC+03] Lacko, P. R., Clark, W. W., Sherbondy, K., and Ralston, J. M., "Studies of Ground Penetrating Radar Antennas," *2nd International Workshop on Advanced GPR*, pp. 24–29, Delft, Netherlands, May 14-16, 2003. 15

[LH01] Lampe, B. and Hollinger, K., "Numerical Modeling of a Complete GPR System," *Proc. of SPIE Vol. 4491 – Subsurface and Subsurface Sensing Technologies and Applications III*, pp. 99–110, 2001. 14

[LI01] Langman, A. and Inggs, M. R., "Pulse versus Stepped Frequency Continuous Wave Modulation for Ground Penetrating Radar," *in Proc. 2001 IEEE International Geoscience and Remote Sensing Symposium*, vol. 3, pp. 1533–1535, Sidney, Australia, 9-13 July 2001, 2001. xix, 32

[LIF94] Langman, A., Inggs, M. R., and Flores, B. C., "Improving the Resolution of Stepped Frequency Continuous Wave Ground Penetrating Radar," *Proc. of SPIE Vol. 2275 – Advanced Microwave and Millimeter-Wave Detectors*, pp. 146–155, 1994. 32

[Lim03] Lim, T. Y., *A Broadband Counter-Wound Spiral Antenna For Subsurface Radar Applications*. BA thesis, Naval Postgraduate School Monterey, California, 2003. 15

[LL10] Loewy, H. and Leimbach, G., *Verfahren zur systematischen Erforschung des Erdinnern gröerer Gebiete mittels elektrischer Wellen*. Deutsches Patent DE237944, 1910. 12

[LL11] Loewy, H. and Leimbach, G., *Verfahren zum Nachweis unterirdischer Erzlager und Grundwasserspiegel mittels elektrischer Wellen*. Deutsches Patent DE254517, 1911. 12

[LL95] Liner, C. L. and Liner, J. L., "Ground Penetrating Radar – A Near-face Experience from Washington County, Arkansas," *The Leading Edge*, vol. 14, pp. 17–21, 1995. 9

[Loe10] Loewy, H., "Eine elektrodynamische Methode zur Erforschung des Erdinneren," *Physikalische Zeitschrift*, vol. 11, pp. 697–705, 1910. 12

[LS02] Liu, S. and Sato, M., "Electromagnetic Logging Technique Based on Borehole Radar," *IEEE Transactions on Geoscience and Remote Sensing*, vol. 40, pp. 2083–2092, 2002. 12

[Lud02] Ludloff, A., *Praxiswissen Radar und Radarsignalverarbeitung*. Braunschweig: Vieweg Verlagsgesellschaft, 3. Auflage, 2002. 28

[Lun01] Lundberg, M., *Electro-Optical Land Mine Detection.* BA thesis, University of Lund, Department of Engineering, 2001. 5

[LY+05] Liye, L., Yi, S., Chunlin, H., and Junjie, M., "Study about the Radiation Properties of an Antenna for Ground-Penetrating Radar," *in Proc. IEEE International Symposium on Microwave, Antenna, Propagation and EMC Technologies for Wireless Communications*, vol. 1, pp. 391–394, Beijing, China, August 8-12, 2005. 15

[LYL00] Lestari, A. A., Yarovoy, A. G., and Ligthart, L. P., "Capacitively-Tapered Bowtie Antenna," *in Proc. 2000 Conference on Antennas and Propagation*, Davos, Switzerland, April 9-14, 2000. 15

[LYL01] Lestari, A. A., Yarovoy, A. G., and Ligthart, L. P., "An Efficient Ultra-Wideband Bow-Tie Antenna," *in Proc. 31st European Microwave Conference*, London, UK, September 25-27, 2001. 15

[LYL04] Lestari, A. A., Yarovoy, A. G., and Ligthart, L. P., "Ground Influence on the Input Impedance of Transient Dipole and Bow-Tie Antennas," *IEEE Transactions on Antennas and Propagation*, vol. 52, pp. 1970–1975, 2004. 16

[LYL05] Lestari, A. A., Yarovoy, A. G., and Ligthart, L. P., "Adaptive Wire Bow-Tie Antenna for Ground Penetrating Radar," *in Proc. 2005 IEEE International Geoscience and Remote Sensing Symposium*, vol. 1, pp. 368–371, Seoul, Korea, July 25-29, 2005. 16

[Mai00] Maierhofer, C., "Radaranwendungen im Bauwesen," *ZfP-Zeitung der Deutschen Gesellschaft für Zerstörungsfreie Prüfung*, vol. 72, pp. 43–50, 2000. 9

[Mal06] Mallow, J., *Optimierung einer TEM Double-ridged Hornantenne zur Vergröerung der nutzbaren Bandbreite und zur Nebenkeulenunterdrückung.* BA thesis, University of Magdeburg, Department of Electronics, Signal Processing and Communications, 2006. 96

[Man05] Mansor, M. F. B., *Dielectric Lens for an H-Plane Waveguide Horn.* BA thesis, University of Duisburg-Essen, Department of Engineering and Microwave Techniques, 2005. 143

[Max65] Maxwell, J. C., "A Dynamical Theory of the Electromagnetic Field," *Philosophical Transactions of the Royal Society of London*, vol. 155, pp. 459–512, 1865. 19

[MB01] Martinez, A. and Byrnes, A. P., "Modeling Dielectric-constant Values of Geologic Materials: An Aid to Ground-Penetrating Radar Data Collection and Interpretation," *Current Research in Earth Sciences, Bulletin 247, part 1*, 2001. 33, 37, 41, 43

[MF+03] McFee, J. E., Faust, A., Andrews, H. R., Clifford, T., Ing, H., Cousins, T., and Haslip, D., "The Feasibility of Neutron Moderation Imaging for Land Mine Detection," *Journal of Subsurface Sensing Technologies and Applications*, vol. 4, pp. 209–240, 2003. 7

[MH04] Meincke, P. and Hansen, T. B., "Planar Near-Field Measurements of Ground Penetrating Radar Antennas," *in Proc. 2004 URSI EMTS International Symposium on Electromagnetic Theory*, pp. 105–107, Pisa, Italy, May 23-27, 2004. 15

[MJ94] Mast, J. E. and Johansson, E. M., "Three-dimensional Ground-Penetrating Radar Imaging Using Multifrequency Diffraction Tomography," *Proc. of SPIE Vol. 2275 – Advanced Microwave and Millimeter-Wave Detectors*, pp. 196–203, 1994. 32, 33

[MJO02] Meyer, T., Jöstingmeier, A., and Omar, A. S., "Three-Dimensional Microwave Resonator Tomography Using Spectral Expansion of the Object Function," *in Proc. 2002 IEEE Antennas and Propagation Society International Symposium*, vol. 2, pp. 706–709, San Antonio, Texas, June 16-21, 2002. 50

[ML+03] MacDonald, J., Lockwood, J. R., McFee, J., Altshuler, T., Broach, T., Carin, L., Rappaport, C., Scott, W. R., and Weaver, R., *Alternatives for Landmine Detection.* Santa Monica: RAND, 2003. 3, 9

[MLM98] McMechan, G. A., Loucks, R. G., and Mescher, P., "Ground Penetrating Radar Imaging of a Collapsed Paleocave System in the Ellen-

burger Dolomite, Central Texas," *Journal of Applied Geophysics*, vol. 39, pp. 1–10, 1998. 9

[MN98] Magg, M. and Nitsch, J., "Mine Detection with Microwaves," *RTO Lecture Series: Advanced Pattern Recognition Techniques*, 1998. 15, 17, 25, 33

[Mol86] Moler, R. B., *Workshop Report: Nuclear Techniques for Mine Detection Research, Lake Luzerne, NY, July 22-25*. Fort Belvoir: Army Belvoir Research and Development Center, 1986. 7

[Mor74] Morey, R. M., "Continuous Subsurface Profiling by Impulse Radar," *in Proc. of the Engineering Foundations Conference on Subsurface Exploration for Underground Excavation and Heavy Constructions*, pp. 213–232, Henniker, New Hampshire, August 11-16, 1974. 12

[MS99] Montoya, T. P. and Smith, G. S., "Land Mine Detection Using a GPR Based on Resistively Loaded Vee Dipoles," *IEEE Transactions on Antennas and Propagation*, vol. 47, pp. 1795–1806, 1999. 15

[MvG02] Morrow, I. L. and van Genderen, P., "Effective Imaging of Buried Dielectric Objects," *IEEE Transactions on Geoscience and Remote Sensing*, vol. 40, pp. 943–949, 2002. 17

[MY02] Milisavljevic, N. and Yarovoy, A. G., "An Effective Algorithm for Subsurface SAR Imaging," *in Proc. 2002 IEEE Antennas and Propagation Society International Symposium*, vol. 4, pp. 314–317, San Antonio, Texas, June 16-21, 2002. 17

[NR68] Nicolson, A. M. and Ross, G. F., "Measurement of the Intrinsic Properties of Materials by Time Domain Techniques," *IEEE Trans. on Instrumentation and Measurement*, vol. 17, pp. 395–402, 1968. 41

[Olh88] Olhoeft, G. R., "Selected Bibliography on Ground Penetrating Radar," *in Proc. of the Symposium on the Applications of Geophysics to Engineering and Environmental Problems*, pp. 462–520, Golden, Colorado, March 28-31, 1988. 10

[OLL04] Ozdemir, C., Lim, S., and Ling, H., "An Algorithm for Ground Penetration Imaging Using Synthetic Aperture Radar Concept," *in Proc. 2004 URSI EMTS International Symposium on Electromagnetic Theory*, pp. 1098–1100, Pisa, Italy, May 23-27, 2004. 17

[Par01] Parnadi, I. W., *Kennwert-Schätzung aus Georadar-Transmissionsdaten.* PhD thesis, University of Freiberg, Department of Geoscience and Civil Engineering, 2001. 33

[Pee98] Peebles, P., *Radar Principles.* New York: John Wiley, 1998. 26, 28

[PL99] Plumb, R. G. and Leuschen, C., "A Class of Migration Algorithms for Ground-Penetrating Radar Data," *in Proc. 1999 IEEE International Geoscience and Remote Sensing Symposium*, vol. 5, pp. 2519–2521, Hamburg, Germany, June 28 − July 2, 1999. 16

[PM93] Pratt, B. R. and Miall, A. D., "Anatomy of a Bioclastic Grainstone Megashoal Revealed by Ground Penetrating Radar," *Geology*, vol. 21, pp. 223–226, 1993. 9

[PO04] Powers, M. H. and Oden, C. P., "Migration of Dispersive GPR Data," *in Proc. Tenth International Conference on Ground Penetrating Radar*, pp. 1–4, Delft, Netherlands, June 21-24, 2004. 16

[Pow97] Powers, M. H., "Modeling frequency-dependent GPR," *The Leading Edge*, vol. 16, pp. 1657–1662, 1997. 20

[RB+02] Rodacy, P. J., Bender, S. F., Bromenshenk, J. J., Henderson, C. B., and Bender, G., "The Training and Deployment of Honeybees to Detect Explosives and Other Agents of Harm," *Proc. of SPIE Vol. 4724 − Detection and Remediation Technologies for Mines and Minelike Targets VII*, pp. 474–481, 2002. 8

[RGD00] Radzevicius, S. J., Guy, E. D., and Daniels, J. J., "Pitfalls in GPR Data Interpretation: Differentiating Stratigraphy and Buried Objects from Periodic Antenna and Target Effects," *Geophysical Research Letters*, vol. 27, pp. 3393–3396, 2000. 15

[Rol06] Rolke, W., *Design of a Log-periodic Dipole Antenna (LPDA).* http://www.wolfgang-rolke.de, Mar. 10, 2006. xx, 80, 82

[Rot02] Rothe, M., "HOPE – Final Report," *European Commission, Joint Research Center, HOPE Research Group*, 2002. 13

[Rus02] Russel, K., "September 2001 Test Results of an Acoustic Instrumented Prodder," *in Proc. of the UXO/Countermine Forum*, Orlando, Florida, September 5, 2002. 3

[RZG98] Rhebergen, J., Zwamborn, A., and Giri, D., "Design of an Ultra-Wideband Ground-Penetrating Radar System Using Impulse Radiating Antennas," *IEE Conference Publication No. 458 – Detection of Abandoned Landmines*, pp. 45–49, Edinburgh, UK, October 12-14, 1998. 15

[Sac04] Sachs, J., "DEMAND – Final Report," *European Commission, Joint Research Center, DEMAND Research Group*, 2004. 13

[Sch96] Schon, J. H., *Physical Properties of RocksFundamentals and Principles of Petrophysics.* Tarrytown: Pergamon Press, 1996. 41

[SD+98] Sachs, J., Dvoracek, J., Schneider, A., Friedrich, J., and Zetik, R., "Ground Penetrating Radar – Probleme und Perspektiven," *in Proc. 43rd International Scientific Colloquium*, Illmenau, Germany, September 21-24, 1998. 32, 33

[SD+00] Sullivan, A., Damarla, T. R., Geng, N., Dong, Y., and Carin, L., "Detection of above Ground and Subsurface Unexploded Ordnance Using Ultra-Wideband (UWB) Synthetic Aperture Radar (SAR) and Electromagnetic Modeling Tools," *Proc. of SPIE Vol. 4038 – Detection and Remediation Technologies for Mines and Minelike Targets V*, pp. 983–992, 2000. 13, 17

[SD+01] Sachs, J., Dvoracek, J., Schneider, A., Friedrich, J., and Zetik, R., "Ultra-Wideband Methods Applied for Moisture and Liquid Sensing," *in Proc. 4th Conference on EM Wave Interaction with Water and Moist Substances*, Weimar, Germany, May 13-16, 2001. 9

[SF05] Sato, M. and Feng, X., "GPR Migration Algorithm for Landmines Buried in Inhomogeneous Soil," *in Proc. 2005 IEEE Antennas and Propagation Society International Symposium*, vol. 1A, pp. 206–209, Washington, D.C., July 3-8, 2005. 17

[SH99] Storm, J. and Haugsted, B., "Detection of Buried Land Mines Facilitated by Actively Provoked IR Signatures," *Proc. of SPIE Vol. 3710 – Detection and Remediation Technologies for Mines and Minelike Targets IV*, pp. 167–172, 1999. 5

[SK04] Sato, M. and Kobayashi, T., "Imaging of Buried Landmines by SAR-GPR," *in Proc. 2004 URSI EMTS International Symposium on Electromagnetic Theory*, pp. 215–217, Pisa, Italy, May 23-27, 2004. 16

[Sko90] Skolnik, M. I., *Radar Handbook*. New York: McGraw-Hill Book Company, 2nd ed., 1990. 10

[Smi06] Smith, A., *Landmines and Humanitarian Mine Action: Anti-Personnel Blast Mines*. http://www.nolandmines.com, retrieved Jul. 06, 2006. xxiv, 191, 192, 193, 194, 195

[Sou99] Soumekh, M., *Synthetic Aperture Radar Signal Processing*. New York: John Wiley & Sons, Inc., 1999. 111

[SS+72] Simmons, G., Strangway, D. W., Bannister, L., Baker, R., Cubley, D., Torraca, G. L., and Watts, R., "The Surface Electrical Properties Experiment," *Lunar Geophysics, Z. Kopal and D. W. Strangway, eds.*, pp. 258–271, 1972. 12

[Ste29] Stern, W., "Versuch einer elektrodynamischen Dickenmessung von Gletschereis," *Beitrag zur Geophysik*, vol. 23, pp. 292–333, 1929. 12

[Ste30] Stern, W., "Grundlagen, Methodik und bisherige Ergebnisse elektrodynamischer Dickenmessung von Gletschereis," *Gletscherkunde*, vol. 15, pp. 24–42, 1930. 12

[Sto78] Stolt, R., "Migration by Fourier Transform," *Geophysics*, vol. 43, pp. 23–48, 1978. 16

[SvD+03] Schoolderman, A. J., van Dijk, S., Deurloo, D., and Russell, K., "Instrumented Prodder: Preliminary Results of the Technology Demonstrator Evaluation," *in Proc. 2003 Conference on Requirements and Technologies for the Detection, Removal and Neutralization of Landmines and UXO*, Brussels, Belgium, September 15-18, 2003. 3

[Swo86] Swords, S. S., *Technical History of the Beginnings of Radar*. London: Peter Peregrinus Ltd, 1986. 10

[SX99] Sabatier, J. M. and Xiang, N., "Laser-Doppler Based Acoustic-to-Seismic Detection of Buried Mines," *Proc. of SPIE Vol. 3710 – Detection and Remediation Technologies for Mines and Minelike Targets IV*, pp. 215–222, 1999. 6

[SX01] Sabatier, J. M. and Xiang, N., "Anti-Personnel Mine Detection Using Acoustic-to-Seismic Coupling," *Proc. of SPIE Vol. 4394 – Detection and Remediation Technologies for Mines and Minelike Targets IV*, pp. 535–541, 2001. 6

[Tab06] Tabak, E., *Some Landmines, Demining Research at the University of Western Australia*. http://www.mech.uwa.edu.au/jpt/demining, retrieved Oct. 22, 2006. xxiv, 194

[TJ05] Thaysen, J. and Jakobsen, K. B., "Wideband Cavity Backed Spiral Antenna for Stepped Frequency Ground Penetrating Radar," *in Proc. 2005 IEEE Antennas and Propagation Society International Symposium*, vol. 1B, pp. 418–421, Washington, D.C., July 3-8, 2005. 15

[TR+98] Tsihrintzis, G. A., Rappaport, C. M., Winton, S. C., and Johansen, P. M., "Statistical Modeling of Rough Surface Scattering for Ground Penetrating Radar Applications," *Proc. of SPIE Vol. 3392 – Detection and Remediation Technologies for Mines and Minelike Targets III*, pp. 735–744, 1998. 44

[Tra96] Trang, A., "Simulation of Mine Detection over Dry Soil, Snow, Ice, and Water," *Proc. of SPIE Vol. 2765 – Detection and Remediation Technologies for Mines and Minelike Targets*, pp. 430–440, 1996. 14, 54

[UB+90] Ulaby, F. T., Bengal, T. H., Dobson, M. C., East, J. R., Garvin, J. B., and Evans, D. L., "Microwave Dielectric Properties of Dry Rocks," *IEEE Transactions on Geoscience and Remote Sensing*, vol. 28, pp. 325–336, 1990. 41

[Ulr82] Ulriksen, C. P., *Application of Impulse Radar to Civil Engineering*. PhD thesis, University of Lund, Department of Engineering, 1982. 9, 41

[Var98] Various, *Hidden Killers: The Global Landmine Crisis*. Washington: U.S. Department of State, Bureau of Political-Military Affairs, Office of Humanitarian Demining Programs, 1998. 2

[Var02] Various, "Rules Regarding Ultra-Wideband Transmission Systems," *Federal Communications Commission, Report 02-48*, 2002. 13

[Var04] Various, *Cuming Microwave Corporation: C-Stock AK4 Datasheet*. http://www.cumingmw.com, retrieved Oct. 06, 2004. 70

[Var05a] Various, *Marshall Legacy: Dogs for the Detection of Landmines*. http://www.marshall-legacy.org, retrieved Apr. 12, 2005. 8

[Var05b] Various, *National Aeronautic and Space Agency: SRTM Shuttle Mission 2000*. http://www.nasa.gov, retrieved Aug. 12, 2005. xxii, 112

[Var05c] Various, *R&S FSH-Series Handheld Spectrum Analyzer: FSH Data Sheet*. http://www.rohde-schwarz.com, retrieved Dez. 16, 2005. 173

[Var05d] Various, *Flann Microwave Inc.: Standard Gain Horns Data Sheet*. http://www.flann.com, retrieved Sep. 12, 2005. xx, 62, 168

[Var05e] Various, *Natural Resources Canada: Radar Systems in Remote Sensing*. http://ccrs.nrcan.gc.ca, retrieved Sep. 20, 2005. xxii, 110

[Var06a] Various, *Microwave Studio Online Help - Version 5.1.1*. CST GmbH, Darmstadt, Germany, retrieved Aug. 16, 2006. xix, 38

[Var06b] Various, *Field Medical Service School Manual, Camp Pendelton, California: Antipersonnel Devices*. http://www.brooksidepress.org, retrieved Mar. 20, 2006. xxiv, 192

[Var06c] VARIOUS, *Wikipedia — The Free Encyclopedia: Concept of a Fresnel Lens*. http://www.wikipedia.org, retrieved Nov. 18, 2006. xxii, 144

[Var06d] VARIOUS, *Aviation During World War Two: World War Two Radar*. http://www.century-of-flight.net, retrieved Oct. 28, 2006. xix, 11

[Var06e] VARIOUS, *Flensburger Fahrzeugbau GmbH: Minebreaker Clearance Vehicle*. http://www.ffg-flensburg.de, retrieved Sep. 14, 2006. 3

[Var06f] VARIOUS, *Minewolf Systems AG: Minewolf Mine Clearance Vehicle*. http://www.minewolf.com, retrieved Sep. 14, 2006. 4

[Var07a] VARIOUS, *The International Campaign to Ban Landmines (ICBL)*. http://www.icbl.org, retrieved Feb. 26, 2007. 2, 5

[Var07b] VARIOUS, *United Nations Electronic Mine Information Network*. http://www.mineaction.org, retrieved Feb. 26, 2007. 1

[Var07c] VARIOUS, *European Union in Humanitarian Demining (EUDEM)*. http://www.eudem.vub.ac.be, retrieved Mar. 07, 2007. 6

[vG03] VAN GENDEREN, P., "Multi-Waveform Stepped Frequency Continuous Wave (SFCW) Radar," *in Proc. 2003 European Microwave Week*, pp. 849–852, Munich, Germany, October 6-10, 2003. 32

[vGS00] VAN GESTEL, J. P. and STOFFA, P., "Migration Using Multi-Configuration GPR Data," *in Proc. Eighth International Conference on GPR*, pp. 448–452, Gold Coast, Australia, May 2326, 2000. 16

[Wei03] WEIGHTMAN, G., *Signor Marconi's Magic Box: The Most Remarkable Invention of the 19th Century & the Amateur Inventor whose Genius Sparked a Revolution*. Cambridge: Da Capo Press, 2003. 10

[WH04] WHITING, B. M. and HACKENBERGER, S., "Using 3D GPR to Determine the Extent of Possible 17th and 18th Century Graves Beneath a Concrete Driveway: Bridgetown Synagogue, Bridgetown, Barbados," *in Proc. Tenth International Conference on Ground Penetrating Radar*, pp. 475–478, Delft, Netherlands, June 21-24, 2004. 9

[Wil54] Wiley, C., *Pulsed Doppler Radar Method and Means*. US Patent No. 3.196.436, 1954. 110

[WM+93] Warhus, J. P., Mast, J. E., Johansson, E. M., Nelson, S. E., and Lee, H., "Advanced Ground Penetrating Radar Imaging Radar for Bridge Inspection," *in Proc. 12th Review of Progress in Quantitative Nondestructive Evaluation*, Brunswick, Maine, August 1-6, 1993. 9

[Yar04] Yarovoy, A. G., "Adaptive Bow-Tie Antenna for GPR," *in Proc. Tenth International Conference on Ground Penetrating Radar*, vol. 1, pp. 121–124, Delft, Netherlands, June 21-24, 2004. 15

[YC05] Youn, H. and Chen, C. C., "Special GPR Antenna Developments for Landmine and UXO Surveys," *in Proc. 2005 IEEE Antennas and Propagation Society International Symposium*, vol. 3B, pp. 100–103, Washington, D.C., July 3-8, 2005. 15

[YJL98a] Yarovoy, A. G., Jongh, R. V., and Ligthart, L., "IRCTR Activities in Modeling of Electromagnetic Wave Transmission Through an Air-Ground Interface," *in Proc. 1998 Electromagnetics Research Symposium*, pp. 449–454, Nantes, France, July 13-17, 1998. 44

[YJL98b] Yarovoy, A. G., Jongh, R. V., and Ligthart, L., "Transmission of Electromagnetic Fields Through an Air-Ground Interface in the Presence of Statistical Roughness," *in Proc. 1998 IEEE International Geoscience and Remote Sensing Symposium*, vol. 3, pp. 1463–1465, Seattle, USA, July 6-10, 1998. 44

[YL00] Yarovoy, A. G. and Ligthart, L. P., "Ultra-Wideband Antennas for Ground Penetrating Radar," *in Proc. International Symposium on Antennas for Radar Earth Observation*, pp. 1–5, Delft, Netherlands, June 8-9, 2000. 15, 88

[YS+04] Yakubov, V. P., Suhanov, D. Y., Omar, A. S., and Spiliotis, N. G., "New Fast SAR Method for 3-D Subsurface Radiotomography," *in Proc. Tenth International Conference on Ground Penetrating Radar*, pp. 103–106, Delft, Netherlands, June 21-24, 2004. 113, 118